National Library
of Canada

Bibliothèque nationale
du Canada

Canadian Theses Service

Service des thèses canadiennes

Ottawa, Canada
K1A 0N4

NOTICE

The quality of this microform is heavily dependent upon the quality of the original thesis submitted for microfilming. Every effort has been made to ensure the highest quality of reproduction possible.

If pages are missing, contact the university which granted the degree.

Some pages may have indistinct print especially if the original pages were typed with a poor typewriter ribbon or if the university sent us an inferior photocopy.

Reproduction in full or in part of this microform is governed by the Canadian Copyright Act, R.S.C. 1970, c. C-30, and subsequent amendments.

AVIS

La qualité de cette microforme dépend grandement de la qualité de la thèse soumise au microfilmage. Nous avons tout fait pour assurer une qualité supérieure de reproduction.

S'il manque des pages, veuillez communiquer avec l'université qui a conféré le grade.

La qualité d'impression de certaines pages peut laisser à désirer, surtout si les pages originales ont été dactylographiées à l'aide d'un ruban usé ou si l'université nous a fait parvenir une photocopie de qualité inférieure.

La reproduction, même partielle, de cette microforme est soumise à la Loi canadienne sur le droit d'auteur, SRC 1970, c. C-30, et ses amendements subséquents.

NL-339 (r. 88/04) c

Canada

UNIVERSITY OF ALBERTA

METAMORPHISM, DEFORMATION, UPLIFT AND THEIR TECTONIC IMPLICATIONS IN THE HORSERANCH RANGE, NORTH-CENTRAL BRITISH COLUMBIA

BY

© HEATHER ELIZABETH PLINT

A THESIS

SUBMITTED TO THE FACULTY OF GRADUATE STUDIES AND RESEARCH

IN PARTIAL FULFILLMENT OF THE REQUIREMENTS FOR THE DEGREE OF

DOCTOR OF PHILOSOPHY

DEPARTMENT OF GEOLOGY

EDMONTON, ALBERTA

FALL, 1991

National Library of Canada
Bibliothèque nationale du Canada

Canadian Theses Service
Service des thèses canadiennes

Ottawa, Canada
K1A 0N4

The author has granted an irrevocable non-exclusive licence allowing the National Library of Canada to reproduce, loan, distribute or sell copies of his/her thesis by any means and in any form or format, making this thesis available to interested persons.

The author retains ownership of the copyright in his/her thesis. Neither the thesis nor substantial extracts from it may be printed or otherwise reproduced without his/her permission.

L'auteur a accordé une licence irrévocable et non exclusive permettant à la Bibliothèque nationale du Canada de reproduire, prêter, distribuer ou vendre des copies de sa thèse de quelque manière et sous quelque forme que ce soit pour mettre des exemplaires de cette thèse à la disposition des personnes intéressées.

L'auteur conserve la propriété du droit d'auteur qui protège sa thèse. Ni la thèse ni des extraits substantiels de celle-ci ne doivent être imprimés ou autrement reproduits sans son autorisation.

ISBN 0-315-69961-2

Canadä

UNIVERSITY OF ALBERTA

RELEASE FORM

NAME OF AUTHOR: Heather E. Plint

TITLE OF THESIS: Metamorphism, Deformation and Uplift and Their Tectonic Implications in the Horseranch Range, North-Central British Columbia

DEGREE: Doctor of Philosophy

YEAR THIS DEGREE GRANTED:

Fall, 1991

Permission is hereby granted to The University of Alberta Library to reproduce single copies of this thesis and to lend or sell such copies for private, scholarly or scientific research purposes only.

The author reserves other publication rights, and neither the thesis nor extensive extracts from it may be printed or otherwise reporduced without the author's written permission.

Heather Plint

656 Sixteen Road,
R.R.#1, Ridgeville,
Ontario, Canada
L0S 1MO

DATE July 16, 1991

UNIVERSITY OF ALBERTA

FACULTY OF GRADUATE STUDIES AND RESEARCH

The undersigned certify that they have read, and recommend to the Faculty of Graduate Studies and Research for acceptance, a thesis entitled "Metamorphism, Deformation, Uplift and their Tectonic Implications in the Horseranch Range, north-central British Columbia" submitted by Heather E. Plint in partial fulfillment of the requirements for the degree of Doctorate of Philosophy in Geology.

Philippe Erdmer

Dr. P. Erdmer

H. Baadsgaard

~~Dr. P. Cavell for~~ Dr H. Baadsgaard

R St J Lambert

Dr. R. St. J. Lambert

C. Evenchick

Dr. C. A. Evenchick

E R Kanasewich

Dr. E. Kanasewich

DATE: 24 June, 1991

This thesis is dedicated to my parents who taught me that a good education and a lot of hard work leads to success, to Jeremy who unknowingly taught me that life is too short to spend it all at a desk, and to Dale who helped me find the balance.

ABSTRACT

A geological study of the Horseranch Range in the Omineca Belt of north-central British Columbia, was carried out to determine the structural, thermal and uplift history and the regional tectonic significance of the area.

Exposed in the range are an Upper Proterozoic(?), garnet- to sillimanite-orthoclase-grade schist complex, Lower Paleozoic quartzite, phyllite and carbonate rocks, late Early Cretaceous and Eocene granites, and Eocene (?) ultramafic to mafic intrusions. The eastern contact of the complex is not exposed. On the west side, high-grade rocks of the complex are juxtaposed against overlying low-grade rocks along a northwest-striking, moderately to steeply southwest-dipping ductile mylonite zone. Regional metamorphism to 650 °C and 5-7 kb in the complex outlasted northerly trending, tight to isoclinal, recumbent, syn-metamorphic folding of S_1 and development of axial planar S_2. Monazite U-Pb crystallization ages (ca. 113 Ma) for a syn- to post-S_2 granite limit the regional metamorphic peak in sillimanite-orthoclase schist to late Early Cretaceous or younger. Gentle to tight, upright to steeply inclined, post-metamorphic folding of S_2 about subhorizontal to moderately plunging, northwest-trending hinges was followed by moderate-temperature (ca. 350°C) mylonitization. Kinematic indicators in mylonite record dextral, oblique-normal strike-slip displacement and in one locality, dextral strike-slip displacement. Zircon and monazite U-Pb crystallization ages (ca. 50 Ma), $^{40}Ar/^{39}Ar$ hornblende, muscovite and biotite cooling ages (ca. 45 Ma to 40 Ma) and apatite fission track ages (ca. 44 Ma) and track lengths record Eocene mylonitization and rapid cooling (48°C/m.y.) of the complex. The mylonite zone is interpreted to be a Riedel shear or splay fault associated with the mid-Cretaceous (105 to 100 Ma) dextral strike-slip Kechika fault. Late Cretaceous and/or Early Tertiary northeast-directed shortening caused oblique-normal strike-slip along the zone and coincident rapid uplift and cooling in the complex. Uplift by oblique-slip distinguishes the range from metamorphic core complexes. Tertiary uplift and cooling of the range contrasts with the nearby Swannell and Sifton Ranges indicating diachronous uplift in the northern Omineca Belt.

ACKNOWLEDGEMENTS

I would like to thank Dr. Hugh Gabrielse for originally suggesting the thesis topic and Dr. Philippe Erdmer for his guidance, enthusiasm and friendship throughout this study and for his generosity, which allowed me to attend conferences and helped in the production of this thesis. Thanks are due to Dr. H. Bud Baadsgaard for use of his mineral separation facilities, for guidance with the U-Pb data and for critically reading the thesis and to Dr. Richard Lambert for help with thin sections and for critically reading the thesis. Thanks also to Dr. Pat Cavell for her help numerous times during the course of the mineral separations and the geochronometry study. Dr. Randall Parrish is thanked for doing the U-Pb analyses and for critically assessing my interpretations of these data. Thanks to Dr. Peter Reynolds for permitting me to use the Dalhousie University argon laboratory and patiently answering all my questions. Sandy Grist is thanked for expertly carrying out the fission track analyses. Thanks are due to Dr. Ron Burwash for the use of his microscope and help with the thin section photography and to K. Hegarty for permission to use the GEOTRACK model.

Funding for this study by the British Columbia Ministry of Engineering, Mining and Petroleum Resources and the National Sciences and Engineering Research Council of Canada are gratefully acknowledged. I benefited from the technical help cheerfully provided by John Machachek (University of Calgary) and Paul Wagner (University of Alberta) during microprobing, by Keith Taylor during the argon analyses and by Frank Dimitrov during the photography. Don Resultay is thanked for his excellent and efficient work on the thin sections. Capable field assistance by Dorthe "Bro" Jakobsen and Karen Krey is greatly appreciated. Personal grants from the "Travelling Metamorphic Petrologist's Fund" and "Third Daughters of Eminent Physicists Association" are gratefully acknowledged.

Last, but not least, I would like to thank Suzan Atkinson, Karen Krey, Ralph Rushton, Bob Shaw, Jennifer Smith, Jackie Staveley and Paul Wagner for the fun and games over the years and Barb Henderson, Rob Stevens and Agnes Koffyberg for being cheery additions to the gang in the final part of the saga, Darlene Syrotuik and the after work aerobics gang for helping me maintain my mental and physical fitness, Hilary Plint for helping to colour the maps and for the much needed rap sessions and Dr. Dale Issler for help with the fission track modelling and mostly, for hanging in there with me.

TABLE OF CONTENTS

CHAPTER 1: INTRODUCTION AND GEOLOGICAL SETTING

1.1. Regional Tectonic Setting and Purpose of Study 1

1.2. Location, Access and Exposure 3

1.3. General Geology and Previous Work 3

1.4. Approach 8

CHAPTER 2: ROCK TYPES, FIELD RELATIONS, PETROGRAPHY, STRATIGRAPHIC CORRELATIONS AND METAMORPHIC MINERAL ASSEMBLAGES AND ZONES

2.1. Introduction 9

2.2. Metamorphic Rocks 9

2.2.1. Schist Complex 9

(i) Moderate- to High-Grade Schist 10
(ii) Phlogopite Marble 12
(iii) Chlorite-Muscovite-Garnet Schist 13

2.2.2. Homogeneous Quartzite and Phyllite 13

2.2.3. Regional Correlation of Metamorphic Rocks and Depositional Environment 14

2.3. Sedimentary Rocks 17

2.3.1. Dolostone and Dolomitic Limestone 17

2.3.2. Polymictic Conglomerate 17

2.4. Intrusive Rocks 18

2.4.1. Granite and Quartz Monzonite 18

2.4.2. Mafic and Ultramafic Rocks 22

2.5. Mylonite Zone 22

2.6. Metamorphic Mineral Assemblages 23

2.6.1. Prograde Mineral Assemblages and Mineral Zones 23

2.6.2. Retrograde Metamorphic Mineral Assemblages 25

2.6.3. Contact Metamorphic Mineral Assemblages 26

CHAPTER 3: STRUCTURE

3.1. Introduction 33

3.2. Structure of the Schist Complex 33

3.2.1. Macroscopic Folds and Planar Fabircs 33

3.2.2. Lineations 36

3.2.3. Microstructures and Porphyroblast-Matrix Relations 42

3.3. Structure of the Low-Grade Rocks 55

3.3.1. Macroscopic Planar Fabrics and Folds 55

3.3.2. Microstructure 55

3.4. Structure and Kinematics in the Mylonite Zone 58

3.4.1. Folds, Planar Fabrics and Microstructures 58

(i) Granitic Protomylonite to Mylonite 58
(ii) Dioritic to Gabbroic Protomylonite to Mylonite 60
(iii) Metacarbonate Mylonite to Ultramylonite 63
(iv) Quartzite Mylonite and Mylonitic Schist 65

3.4.2. Lineations and Kinematic Indicators 65

3.5. Brittle Faults 71

3.6. Relative Timing of Deformation and Metamorphism 73

3.7. Comparison with Other High-Grade Anticlinoria in Northern British Columbia 74

3.7.1. Regional Metamorphism and Folds 74

3.7.2. Granitic Basement and Intrusive Rocks 75

3.8. Summary 76

CHAPTER 4: MINERAL CHEMISTRY AND EQUILIBRIUM ASSESSMENT

4.1.Introduction 77

4.2. Mineral Chemistry 77

4.2.1. Muscovite 77

4.2.2. Plagioclase and Orthoclase 84

4.2.3. Garnet 89

(i) Type I Garnet Zoning 89
(ii) Type II Garnet Zoning 99
(iii) Type III Garnet Zoning 99

4.2.4. Biotite 102

4.2.5. Staurolite 110

4.2.6. Al_2SiO_5 Polymorphs 110

4.2.7. Opaque Minerals 113

4.3. Assessment of Equilibrium 113

4.3.1. Textural Disequilibrium 113

4.3.2. Chemical Disequilibrium 113

4.4. Summary 121

CHAPTER 5: P-T CONDITIONS OF METAMORPHISM AND MYLONITIZATION

5.1. Introduction 123

5.2. Phase Equilibria and Mineral Isograds 124

5.2.1. Biotite Zone 124

5.2.2. Staurolite-Garnet Zone and Biotite-Garnet ± Kyanite Zone 124

5.2.3. Sillimanite-Orthoclase-Muscovite Zone and Partial Melting 128

5.3. Isograd Map Pattern 132

5.4. Contact Metamorphism 132

5.5. Geothermobarometry 132

5.5.1. Introduction 132

5.5.2. Garnet-Biotite Geothermometry 135

5.5.3. Garnet-Plagioclase-Al_2SiO_5-Quartz Geobarometry 139

5.5.4. Plagioclase-Biotite-Garnet-Muscovite Geobarometry 141

5.6. Summary Matamorphic P-T Conditions 141

5.7. P-T Conditions of Mylonitization and Magnitude of Displacement 144

CHAPTER 6: GEOCHRONOLOGY

6.1. Introduction 147

6.2. Analytical Methods and Closure/Annealing Temperatures 147

6.2.1. U-Pb Method 149

6.2.2. ^{40}Ar-^{39}Ar Method 149

6.2.3. Fission Track Method 151

6.3. Results 152

6.3.1. U-Pb 152

(i) Granite in the Schist Complex 157
(ii) Granitic Mylonites 160
(iii) Usefulness of the ^{230}Th Disequilibrium Correction 162

6.3.2. ^{40}Ar-^{39}Ar 163

6.3.3. Fission Track 166

6.4. Implications of Age Data and Fission Track Lengths 166

6.5. Cooling Rates and Uplift Rates 169

6.6. Track Length Modelling 171

CHAPTER 7: TECTONIC IMPLICATIONS

7.1. Preamble 176

7.2. Regional Cretaceous and Tertiary Tectonics in the Northern Omineca Belt 176

7.3. An Oblique-Normal Strike-Slip Model for the Horseranch Range 177

7.4. The Horseranch Range as a Metamorphic Core Complex 180

7.5. Nature and Timing of Uplift in the Northern Omineca Belt 183

7.5.1. Sifton Range 183

7.5.2. Swannell Ranges 184

(i) Chase Mountain Area 184
(ii) Ingenika Range 184
(iii) Manson Creek-Germansen Landing Area 184

7.5.3. Mount Mackinnon area 185

7.5.4. South-Central Yukon.. 185

7.5.5. Discussion.. 186

CHAPTER 8: CONCLUSIONS AND REMAINING QUESTIONS

8.1. Conclusions.. 187

8.2. Remaining Questions.. 187

REFERENCES.. 190

APPENDIX 1: Locations and detailed descriptions of samples analysed for mineral chemistry and geochronometry.. 209

APPENDIX 2: Analytical methods.. 229

A2.1. Electron Microprobe.. 229
A2.2. Geochronometry.. 229
A2.3. Neutron Activation (INAA).. 261

APPPENDIX 3: Numerical expressions for geothermometry and geobarometry....... 263

LIST OF TABLES

Table 3.1: Relative timing of metamorphism and deformation 34

Table 4.1: Summary of mineral phases analysed by microprobe 78

Table 4.2: Microprobe analyses of muscovite 80

Table 4.3: Microprobe analyses of plagioclase and orthoclase 85

Table 4.4: Microprobe analyses of garnet 90

Table 4.5: Microprobe analyses of biotite 103

Table 4.6: Microprobe analyses of staurolite 111

Table 4.7: Microprobe analyses of Al_2SiO_5 polymorphs 112

Table 4.8: Microprobe analyses of ilmenite and rutile 114

Table 4.9: Log Mn/Fe ratios for garnet rims versus $(K_D^{\text{gt rim-bi}})_{\text{Fe-Mg}}$ in pelites 122

Table 5.1: Definitions of mole fractions used in geothermobarometry calculations 134

Table 5.2: Temperatures calculated using the garnet-biotite geothermometer 137

Table 5.3: (a) Values of parameters used in garnet-plagioclase-Al_2SiO_5-quartz geobarometry. (b) Calculated activities and pressures using garnet-plagioclase-Al_2SiO_5-quartz geobarometer 140

Table 5.4: Pressures calculated using plagioclase-biotite-garnet-muscovite geobarometer 142

Table 5.5: $\delta^{18}O$ temperatures for quartz-hornblende, quartz-muscovite and quartz-biotite pairs 145

Table 6.1: Summary of mineral phases analysed and methods used 148

Table 6.2: Description of zircons and monazites analysed by the U-Pb method 150

Table 6.3: U-Pb analytical data 153

Table 6.4: U-Pb dates for zircon and monazite 159

Table 6.5: Summary of fission track count data and ages 167

Table 6.6: Input data for fission track length models 173

Table A1.1: Mineral assemblages for pelitic, psammitic, calcareous and mafic schist 219

Table A1.2: Mineral assemblages for granite, gabbro, diorite, pyroxenite and hornblendite in the Horseranch Range 225

Table A2.1: ^{40}Ar-^{39}Ar analytical data for biotite 245

Table A2.2: ^{40}Ar-^{39}Ar analytical data for muscovite 248

Table A2.3: ^{40}Ar-^{39}Ar analytical data for hornblende 250

Table A2.4: Detailed count data for fission track analyses 254

LIST OF FIGURES

Figure 1.1: Tectonic map of the northern Cordillera, British Columbia and Yukon 4

Figure 1.2: Regional geology of the northern Cordillera 5

Figure 1.3: Map units of the Horseranch Range 6

Figure 2.1: Granite compositions in the Horseranch Range 21

Figure 2.2: Map of mineral isograds in the Horseranch Range 24

Figure 3.1: Contoured stereographic plot of poles to S_2 in the schist complex 38

Figure 3.2: Stereographic scatter and contoured plots of ${}^2F_3$ fold hinge and lineation trends in the schist complex 40

Figure 3.3: Rose diagram of joint surface orientations in the schist complex 44

Figure 3.4: Scatter and contour plots of lineation trends in mylonite 70

Figure 3.5: Stereographic scatter plot of fold hinges orientatations in the mylonite zone 72

Figure 4.1: Plot of FeO^{total} versus Al_2O_3 in muscovite 79

Figure 4.2: Muscovite chemistry as a function of muscovite, paragonite and margarite 83

Figure 4.3: Garnet chemistry as a function of almandine, pyrope and spessartine + grossular end-members 83

Figure 4.4.: Normal zonation profile for garnet from staurolite-garnet schist 95

Figure 4.5.: Examples of Type I zoning in garnet from kyanite-garnet schist and sillimanite-orthoclase-muscovite schist and Type II garnet zoning in garnet from sillimanite-orthoclase-muscovite schist 96

Figure 4.6.: Type III garnet zonation profile in biotite-garnet schist 100

Figure 4.7.: Histogram of Ti^{4+} and Al^{vi} in biotite 109

Figure 4.8.: Thompson AFM plots for staurolite-garnet schist, garnet-biotite schist, biotite-garnet-kyanite schist and sillimanite-orthoclase -muscovite schist 117

Figure 4.9.: Log Mg/Fe and log Mn/Fe plots for the staurolite-garnet, biotite-garnet±kyanite and sillimanite-orthoclase-muscovite zones 119

Figure 5.1: Discontinuous phase equilibria applicable to the staurolite-garnet zone 126

Figure 5.2: Discontinuous phase equilibria applicable to the sillimanite-orthoclase-muscovite zone 129

Figure 5.3: P-T range for staurolite-garnet schist and sillimanite-orthoclase-muscovite schist 143

Figure 6.1: Concordia plots for U-Pb analyses of zircon and monazite from granite in the schist complex 154

Figure 6.2: Concordia plots for U-Pb analyses of zircon and monazite from granite mylonite 155

Figure 6.3: ^{40}Ar/^{39}Ar age spectra for biotite, muscovite and hornblende 164

Figure 6.4: Fission track length histograms for apatite 168

Figure 6.5: Time-temperature plot of isotopic data for the Horseranch Range 170

Figure 6.6: Time-temperature plots and track length histograms from track length models 1, 2 and 3 174

Figure 6.7: Time-temperature plots and track length histograms from track length models 4, 5 and 6 175

Figure 7.1: Regional Pre-mid-Cretaceous to Tertiary stress fields for the Omineca Belt 178

Figure 7.2: Riedel shear model for the mylonite zone 179

Figure 7.3: Schematic map depicting stress field for oblique-normal strike-slip in the mylonite zone 181

Figure A1.1: Locality map of samples analysed 218

Figure A2.1: J curves for irradiation canisters 243

Back Pocket

Map 1: Geologic map of and cross sections through, the Horseranch Range

Map 2: Sample locality map of all samples collected in the study

LIST OF PLATES

Plate 2.1: Compositional layering in schist complex........ 11

Plate 2.2: Pseudomorphs of chlorite, calcite and talc after dolomite in chlorite schist........ 15

Plate 2.3: Post-$^2F_3$ granite dykes in schist complex........ 19

Plate 2.4: Retrograde chlorite between boudins in staurolite........ 27

Plate 2.5: Garnet partly replaced by an intergrowth of muscovite, biotite, plagioclase and quartz........ 28

Plate 2.6: Late chlorite porphyroblasts cut S_2 in schist complex........ 29

Plate 2.7: Contact metamorphic effects by late granite in the staurolite-garnet zone........ 30

Plate 2.8: Grossular garnet in marble at granite contact in outcrop........ 32

Plate 3.1: $^1F_2$ folds defined by quartz veins in outcrop and in thin section........ 35

Plate 3.2: Syn- to post-S_2 granite in the schist complex........ 37

Plate 3.3: $^2F_3$ folds in outcrop and in thin section........ 39

Plate 3.4: Boundinaged and extended quartz vein in schist complex........ 41

Plate 3.5: Hornblende and plagioclase lineation in schist complex........ 43

Plate 3.6: Inclusion trails in garnet and staurolite porphyroblasts........ 45

Plate 3.7: Ilmenite-defined inclusion trails in staurolite........ 48

Plate 3.8: Ilmenite inclusions and partial inclusions in staurolite........ 49

Plate 3.9: Textural discontinuity in garnet porphyroblast........ 51

Plate 3.10: S_2 schistosity cut by sillimanite........ 52

Plate 3.11: Muscovite-out texture in sillimanite-garnet schist........ 53

Plate 3.12: Post-S_2 garnet in sillimanite-garnet schist........ 54

Plate 3.13: Folds in bedding and cleavage in chloritic phyllite........ 56

Plate 3.14: C-S fabric in granitic mylonite in hand sample and thin section........ 59

Plate 3.15: Strain-related myrmekite in granite mylonite........ 61

Plate 3.16: Micro-faulted plagioclase in mafic mylonite........ 62

Plate 3.17: δ-type porphyroclast systems of calcsilicate rock in a metacarbonate mylonite 64

Plate 3.18: Passive folds of the mylonitic foliation in metacarbonate mylonite 66

Plate 3.19: Diopside porphyroclasts with hornblende rims in metacarbonate mylonite 67

Plate 3.20: Fibrolite folded by folds related to mylonitization and coarse sillimanite deflected into shear-surfaces in mylonitized schist 68

Plate 3.21: σ-type biotite porphyroclast in mylonite 69

Plate 4.1: Ilmenite from staurolite-garnet schist and high-grade biotite-garnet schist 98

Plate A2.1: Zircon from quartz monzonite mylonite sample HP87-3 233

Plate A2.2: Zircon and monazite from C-S granite mylonite sample HP87-110 235

Plate A2.3: Zircon and monazite from C-S granite mylonite sample HP88-167 236

Plate A2.4: Zircon and monazite from post-S_2 granitic pegmatite sample HP87-139 in the schist complex 237

Plate A2.5: Zircon and monazite from syn- to post-S_2 granite HP87-78E in the schist complex 239

ABBREVIATIONS AND SYMBOLS

Symbols

A^*, $(A/B)^*$ = radiogenic element A, ratio of radiogenic elements A and B
T = temperature
P, P_{total} = total pressure
t = time
PH_2O = partial pressure of water
fO_2 = oxygen fugacity
ΔG = change in Gibbs free energy
ΔH = change in enthalpy
ΔS = change in entropy
ΔV = change in volume
$\bar{V}$ = partial molar volume

a = activity; e.g. a_{gro} = activity of grossular component (Ca) in garnet
$a = (X)(\gamma)$ where X = mole fraction and γ = activity coefficient.

$(X_b)^n$ = mole fraction of component "b" in a phase; n = number of moles;
e.g. X_{anor} = mole fraction of anorthite component in plagioclase

$[(X^B)_b]^n$ = mole fraction of component b in phase B; n = number of moles;
e.g. $(X^{bi})_{Al}$ = mole fraction of Al in biotite

$(\gamma^B)_b$ = activity coefficient of component "b" in phase "B"
γ_c = activity coefficient of component "c" in a phase;
e.g. γ_{alm} = activity coefficient for almandine (Fe) in garnet.

$W_{a\text{-}c}$ = Margules mixing parameter for component "a" and "c" in a phase;
e.g. $W_{gro\text{-}pyr}$ = Margules mixing parameter for grossular (Ca)
and pyrope (Mg) in garnet

R = gas constant = 1.987 cal/(mol)(K)

K_{eq} = equilibrium coefficient = $(K_D)(K\gamma)$

$(K_D{}^{B\text{-}C})_{b\text{-}c}$ = distribution coefficient for components "b" and "c" in phase "B" and "C"

$(K\gamma^{B\text{-}C})_{b\text{-}c} = (\gamma^B)_b^n/(\gamma^C)_c^n$ where n = number of moles

In the ideal case, i.e. where $K\gamma = 1.0$ and a = X,

$(K_D{}^{B\text{-}C})_{b\text{-}c} = (X^B)_b^n/(X^C)_c^n$ where n = number of moles

Rocks, Minerals, and Fabrics

act = actinolite
amp = amphibole

andl = andalusite
ann = annite
anor = anorthite (An_{10} = anorthite content of 10%)
antg = antigorite
alb = albite
alm = almandine
ap = apatite
aph = anthophyllite
bi = biotite
cc = calcite
chl = chlorite
cpx = clinopyroxene
crb = carbonate mineral
crd = cordierite
dp = diopside
dm = dolomite
ep = epidote
fsp = feldspar
gr = granite
gra = graphite
gro = grossular
gt = garnet
hb = hornblende
ilm = ilmenite
Ksp = K-feldspar
ky = kyanite
mc = microcline
mu = muscovite
mt = magnetite
mz = monazite
olv = olivine
opm = opaque minerals
opx = orthopyroxene
or = orthoclase
phl = phlogopite
pl = plagioclase
px = pyroxene
pyr = pyrope
qtz = quartz
rt = rutile
sch = schist
ser = sericite
serp = serpentine
sil = sillimanite
spe = spessartine
sph = sphene
st = staurolite
tm = tourmaline
trm = tremolite
whm = white mica
zir = zircon
zo = zoisite

Fabrics and Texture

anhd = anhedral
a.p. = axial plane
clev = cleavage
comp = compositional
cren = crenulated
D_1,D_2 = first deformation phase, second deformation phase etc.
equigran = equigranular
euhd = euhedral
frag = fragments
$^1F_2$,$^2F_3$ = first identifiable fold phase, second fold phase etc.
grano = granoblastic
hypoidiom = hypoidiomorphic
idio = idioblastic
incl = inclusion
pblast = porphyroblast
pclast = porphyroclast
poik = poikilitic
poikilo = poikiloblastic
porphyrobl = porphyroblastic
rd = rounded
recrystal = recrystallized
S_1,S_2 = first planar fabric, second planar fabric etc.
scht = schistosity
S_e = matrix foliation (external to porphyroblast)
S_i = inclusion trail in porphyroblast
skel = skeletal
subequigran = subequigranular
subid = subidioblastic
subgrano = subgranoblastic
subhd = subhedral
subrd = subrounded
xeno = xenoblastic

Grain Size

v.f.gr = very fine-grained
f.gr. = fine-grained
m.gr. = medium-grained
c.gr. = coarse-grained

Other

incl = inclusion, included, or includes
mod = moderate or moderately
tr = trace amount

CHAPTER 1

INTRODUCTION AND GEOLOGICAL SETTING

1.1. REGIONAL TECTONIC SETTING AND PURPOSE OF STUDY

The Omineca Belt is a tectonic welt, initiated in the Early to Middle Jurassic time in the zone of overlap of accreted marginal basin, ophiolitic and volcanic arc terranes onto the former North American continental margin. It consists of regionally metamorphosed and multiply deformed Middle Proterozoic to middle Paleozoic miogeoclinal strata, Paleozoic to Mesozoic volcanogenic and pelitic rocks, all intruded by Jurassic, Cretaceous and Tertiary plutons (Monger et al., 1982; Armstrong, 1988). Precambrian crystalline basement rock is locally exposed (e.g. Evenchick et al., 1984). The belt is bordered to the east by the Foreland Fold and Thrust Belt and to the west by Paleozoic and Mesozoic oceanic and island-arc terranes of the Intermontane Belt. Middle Jurassic metamorphism and west-verging back-folding and back-thrusting of the ancient continental margin over the accreted rocks are common along the western edge of the belt from southern British Columbia to approximately latitude 57°N (e.g. Archibald et al., 1983; Brown et al., 1986; Price, 1986; Bellefontaine, 1989, 1990) whereas farther north, accreted rocks are thrust over the ancient continental margin (e.g. Gabrielse, 1985 and in press; Harms, 1984, 1989). Beginning in mid-Cretaceous time, further terrane accretion formed a second tectonic welt superimposed on a magmatic arc (the Coast Plutonic Complex) along the new continental margin to the west (Monger and Price, 1979; Monger et al., 1982) and led to regional uplift of the Omineca Belt and renewed subsidence in the Western Canada foreland basin. Mid-Cretaceous convergence is thought to have been oblique because mid-Cretaceous to early Tertiary dextral strike-slip faulting along the length of the Canadian Cordillera accompanied terrane accretion (Monger, 1984; Gabrielse, 1985; Price and Carmichael, 1986). The convergence ceased abruptly in Eocene time with the onset of crustal extension in the southern Cordillera (Parrish et al., 1988), whereas dextral strike-slip faulting continued in the northern Cordillera (Price, 1986). Several models have been proposed for the cause of extension (e.g. Malavieille, 1987; Parrish et al., 1988; Ranalli et al., 1989) most of which, involve changes in oceanic plate motions coupled with a hot, thickened, weak crust as the main driving force (e.g. Sonder et al., 1987).

In the northern Omineca Belt, mid-Cretaceous (and possibly earlier) to Oligocene, strike-slip faulting resulted in up to 1000 km of dextral offset of terranes west of the TT - NRMT fault system relative to rocks east of the system (Gabrielse, 1985). The significance of dextral strike-slip faults farther west is unclear. Paleomagnetic data have been interpreted to record approximately 1300 km of northward displacement of the Stikine terrane (Intermontane Belt) (Monger and Irving, 1980) and up to 2400 km displacement of the Alexander, Wrangellia, Cascade, Cache Creek and Quesnellia terranes (Coast Plutonic Complex) since mid-Cretaceous time (Monger and Irving, 1980; Irving et al., 1985). However, the magnitude and timing of the postulated northward transport conflicts with geological data (Butler et al., 1989). This discrepancy may be due to incorrect assumptions regarding the paleohorizontal or to previous sinistral motion on existing faults (Avé Lallemant and Oldow, 1988; Butler et al., 1989).

High-grade, multiply deformed and metamorphosed continental margin and basement rocks characterized by Tertiary hornblende and mica K-Ar cooling ages are exposed in fault-bounded blocks in the Omineca Belt from southern to northern British Columbia (Wheeler and McFeely, 1987; Armstrong, 1988: Figure 16). In the southern Omineca belt, the rocks form the infrastructure of metamorphic core complexes that were rapidly cooled and uplifted during Eocene crustal extension and normal faulting (e.g. Armstrong, 1982; Parrish et al., 1988; Sevigny et al., 1990). In the northern part of the belt, the rocks are exposed in post-metamorphic, fault-bounded anticlinoria with northwest-trending hinges. The rocks are interpreted to have been uplifted and cooled in Mesozoic time and reset during Tertiary magmatism and faulting (e.g. Wanless et al., 1978; Parrish, 1979; Gabrielse, 1985; Evenchick, 1988). However, only locally is there unequivocal evidence for Mesozoic cooling and Tertiary resetting (e.g. Parrish, 1979). In addition, uplift mechanisms are known only locally (e.g. Evenchick, 1988).

With the objective of assessing the timing and nature of uplift in the northern Omineca Belt, a structural, metamorphic, and geochronometric study of the Horseranch Range in north-central British Columbia was carried out. The range is the most northerly fault-bounded anticlinoria of high-grade miogeoclinal rocks in the Omineca Belt. The area was selected for study because an Eocene K-Ar muscovite age from high-grade schist (Lowden, 1963), a sheared Eocene granite (Gabrielse, personal communication 1989) and data from reconnaissance mapping (Gabrielse, 1963), suggested that the Horseranch Range had been uplifted in Eocene time, like metamorphic core complexes of the southern Omineca Belt, rather than in Mesozoic time.

The results of this study reveal rapid Eocene cooling following the late Early Cretaceous or younger peak of regional metamorphism in the Horseranch Range.

Cooling is attributable to tectonic uplift in a dextral strike-slip fault system by northwest-directed oblique extension. Uplift by oblique extension contrasts with dip-slip extension of metamorphic core complexes and therefore, the range is not a core complex.

1.2. LOCATION, ACCESS AND EXPOSURE

The study area covers approximately 450 square kilometres in the Cassiar Mountains of north-central British Columbia, 65 km southeast of Watson Lake, Yukon Territory, in NTS 1:50,000 scale map sheets 104P/2, 104P/7 and 104P/10. It lies between latitudes 59°05' and 59°34'N and longitudes 128°59' and 128°41'W (Figure 1.1, 1.3 and Map 1 - back pocket).

Field work was carried out from tent camps positioned by helicopter, which is the most direct means of access. Bedrock exposure is good to excellent above 1500 m elevation, fair to good in creeks along the western part of the range between approximately 1000 and 1500 m elevation and almost non-existent below 1500 m elevation along the eastern flank of the range.

1.3. GENERAL GEOLOGY AND PREVIOUS WORK

The Horseranch Range lies in the Cassiar terrane (Wheeler and McFeely, 1987), part of the North American miogeocline displaced northwards along the TT - NRMT fault system (Figure 1.1 and 1.2). It is bounded to the east and west by the Deadwood and Horseranch faults, respectively, which are inferred to be steep normal faults (Gabrielse, 1963, 1985). Exposed in the range are a moderate- to high-grade schist complex, low-grade quartzite, schist, phyllite, and unmetamorphosed carbonate rocks. The schist complex includes sillimanite and staurolite-garnet schist, psammitic schist, calcareous quartzite, calcsilicate schist, marble, granitic orthogneiss and amphibolite. Discontinuous quartz veins, parallel to the schistosity, are common. The schist complex is intruded by granite (locally pegmatitic), diorite, gabbro and hornblende pyroxenite. Diorite, gabbro and pyroxenite also intrude the low-grade rocks and are cut by the Horseranch fault (Figure 1.3 and Map 1). The schist complex is correlated with the Upper Proterozoic Ingenika Group (Windermere Supergroup). The low-grade quartzite, chloritic phyllite and carbonate rocks are correlated with the Cambrian Atan, Cambrian-Ordovician Kechika and Ordovician-Silurian Sandpile groups, respectively (Gabrielse, 1963; Plint and Erdmer, 1989a; see Chapter 2). U-Pb

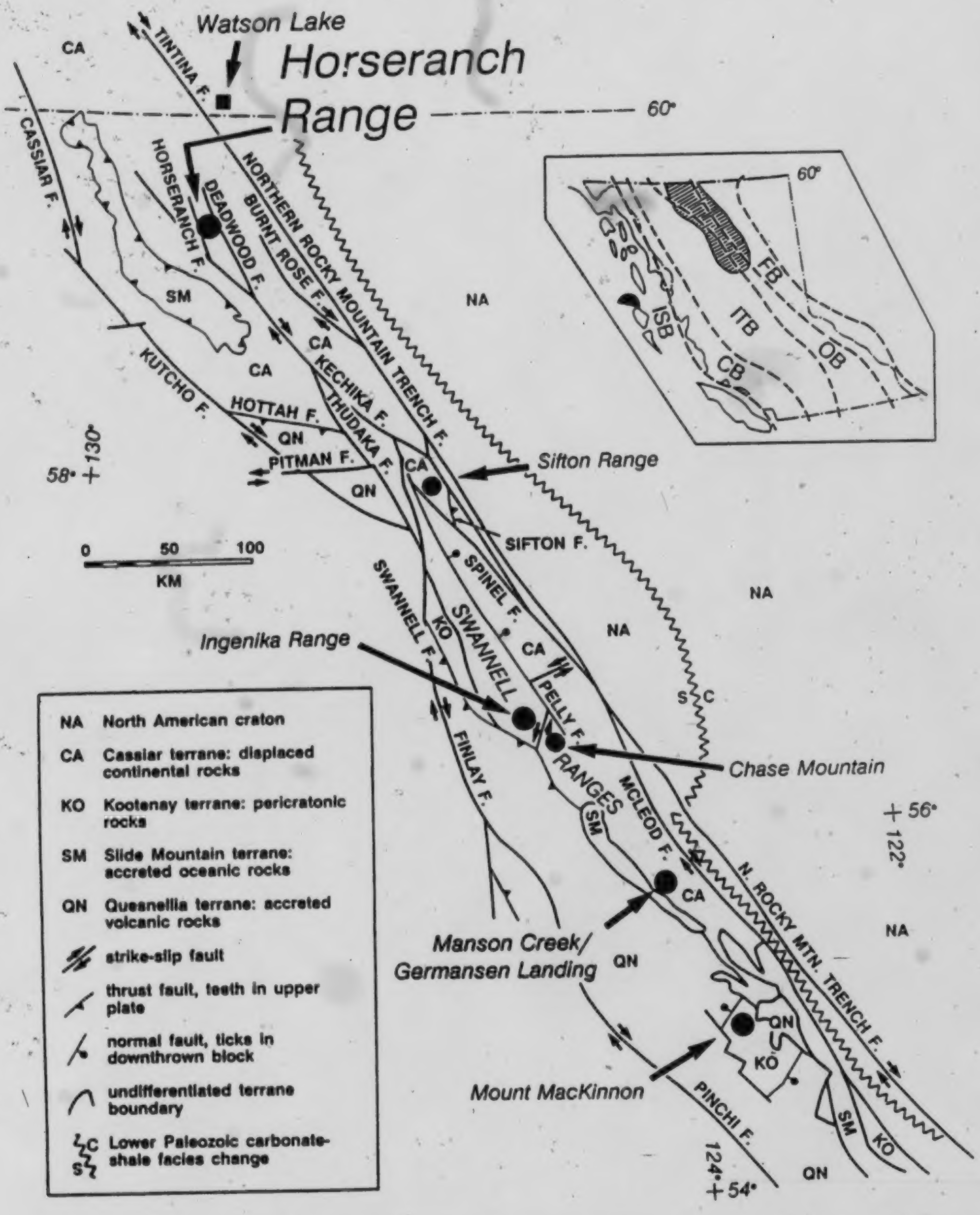
Watson Lake
Horseranch Range
60°
CA
TINTINA F.
CASSIAR F.
HORSERANCH F.
DEADWOOD F.
BURNT ROSE F.
NORTHERN ROCKY MOUNTAIN TRENCH F.
SM
NA
CA
KECHIKA F.
KUTCHO F.
HOTTAH F.
THUDAKA F.
QN
PITMAN F.
58° + 130°
Sifton Range
SIFTON F.
0 50 100
KM
SPINEL F.
SWANNELL F.
KO
SWANNELL RANGES
Ingenika Range
PELLY F.
Chase Mountain
S C
FINLAY F.
MCLEOD F.
N. ROCKY MTN. TRENCH F.
+ 56° 122°
Manson Creek/ Germansen Landing
QN
Mount MacKinnon
PINCHI F.
124° + 54°
FB
ITB
OB
ISB
CB
NA North American craton
CA Cassiar terrane: displaced continental rocks
KO Kootenay terrane: pericratonic rocks
SM Slide Mountain terrane: accreted oceanic rocks
QN Quesnellia terrane: accreted volcanic rocks
strike-slip fault
thrust fault, teeth in upper plate
normal fault, ticks in downthrown block
undifferentiated terrane boundary
C S Lower Paleozoic carbonate-shale facies change

Figure 1.1: Terranes and regional faults of east- and north-central British Columbia. The inset map shows the five-fold division of the Canadian Cordillera (FB = Fold and Thrust Belt, OB = Omineca Crystalline Belt, ITB = Intermontane Belt, CB = Coast Plutonic Belt, ISB = Insular Belt). Shaded area on inset shows region covered by the terrane map. The Wolverine Complex (see text) comprises the Kootenay terrane rocks in the vicinity of, and southeast of, Mount MacKinnon, the Cassiar terrane rocks underlying the Chase Mountain area and high-grade Cassiar-terrane rocks exposed in the Swannell Ranges southeast of Chase Mountain.

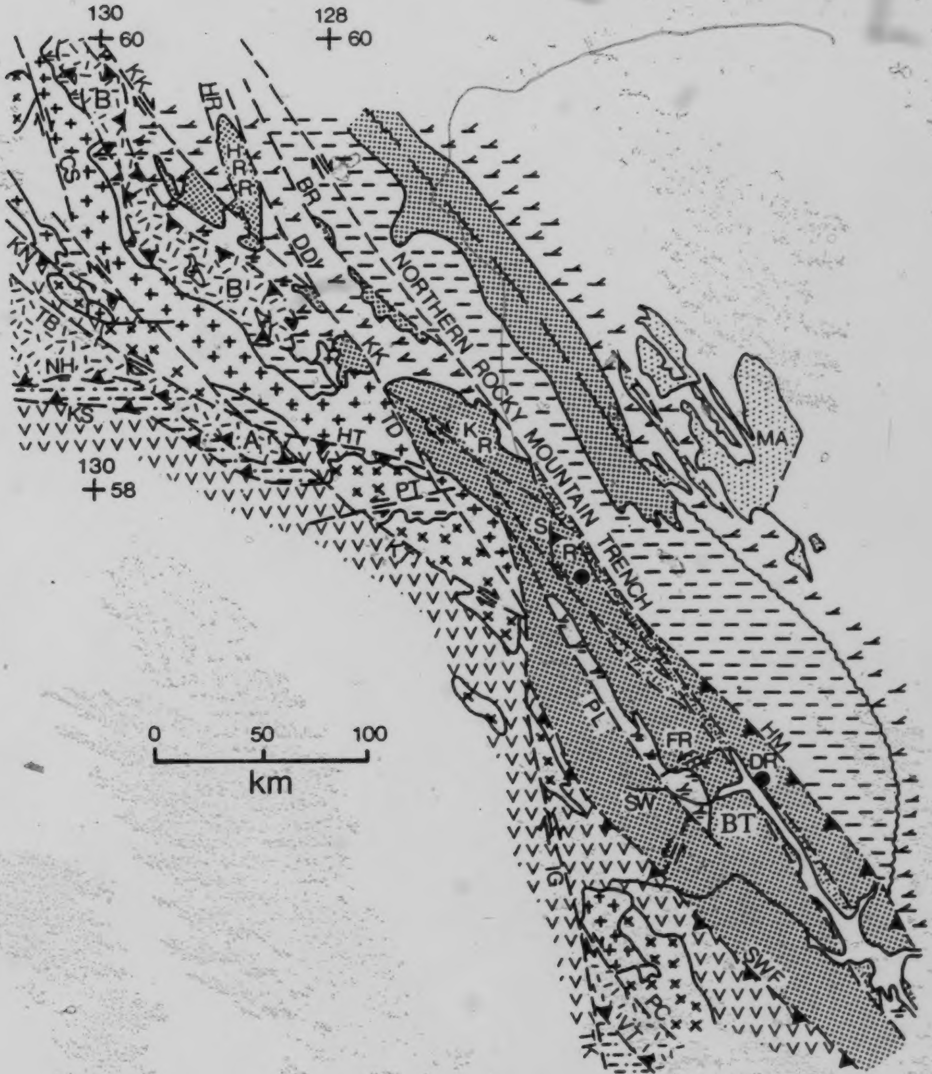
130
+60
128
+60
KK
HR
B
CS
H R R
BR
DD
NORTHERN ROCKY MOUNTAIN TRENCH
KN
TB
NH
KS
A
HT
TD
K R
PT
S R
KT
MA
PL
FR
DR
HM
SW
BT
IG
SWF
PC
VT
TK
130
+58
0
50
100
km

Figure 1.2: Regional geology of the northern Cordillera, modified from Gabrielse (1985) and Evenchick (1988). Ranges: BT = Butler, DR Deserters, FR Finlay, HR Horseranch, KR Kechika, SR Sifton, SW Swannell (WC = Wolverine Complex). MA Muskwa Anticlinorium. Faults: BR Burnt Rose, CS Cassiar, DD Deadwood, HRR Horseranch, HT Hottah, IG Ingenika, KK Kechika, KN Klinkit, KS King Salmon, KT Kutcho, NH Nahlin, PC Pinchi, PT Pitman, SWF Swannell, TD Thudaka, TB Thibert, TK Takla, VT Vital. High-grade Proterozoic rocks are exposed in the BT, HRR, SR and SW Ranges.

LEGEND

▒	Lower Cenozoic: mainly coarse clastic sediments, minor volcanics
+ + +	Mid-Cretaceous: granite
⁚ − ⁚ −	Lower Jurassic and Upper Triassic: greywacke, slate, conglomerate, andesitic volcanics
× × ×	Early Jurassic: mainly granodiorite and quartz diorite
V V V	Upper Paleozoic to Mid-Jurassic: arc facies: andesitic volcanics, sediments
⁄ ⁄ ⁄	Upper Paleozoic: oceanic facies: mafic volcanics, ultramafics, chert, limestone, shale. A, strongly deformed (Cache Creek); B, less deformed (Sylvester)
≑ ≑	Lower to Mid-Paleozoic: transitional facies: platformal Lower and Middle Devonian strata; graptolitic Ordovician and Silurian strata
− −	: offshelf facies: mainly fine-grained clastics; includes some narrow belts of carbonate
⌐ ⌐	: platformal and shelf facies: carbonate and sandstone; includes Ordovician graptolitic shale in Cassiar Mountains
▓	Upper Proterozoic: sedimentary and metamorphic rocks Windermere Supergroup)
░	Middle(?) Proterozoic: sedimentary and metamorphic rocks (Muskwa Supergroup)
●	Granitoid basement gneiss
〰	Middle Silurian facies boundary

Figure 1.2. (continued)

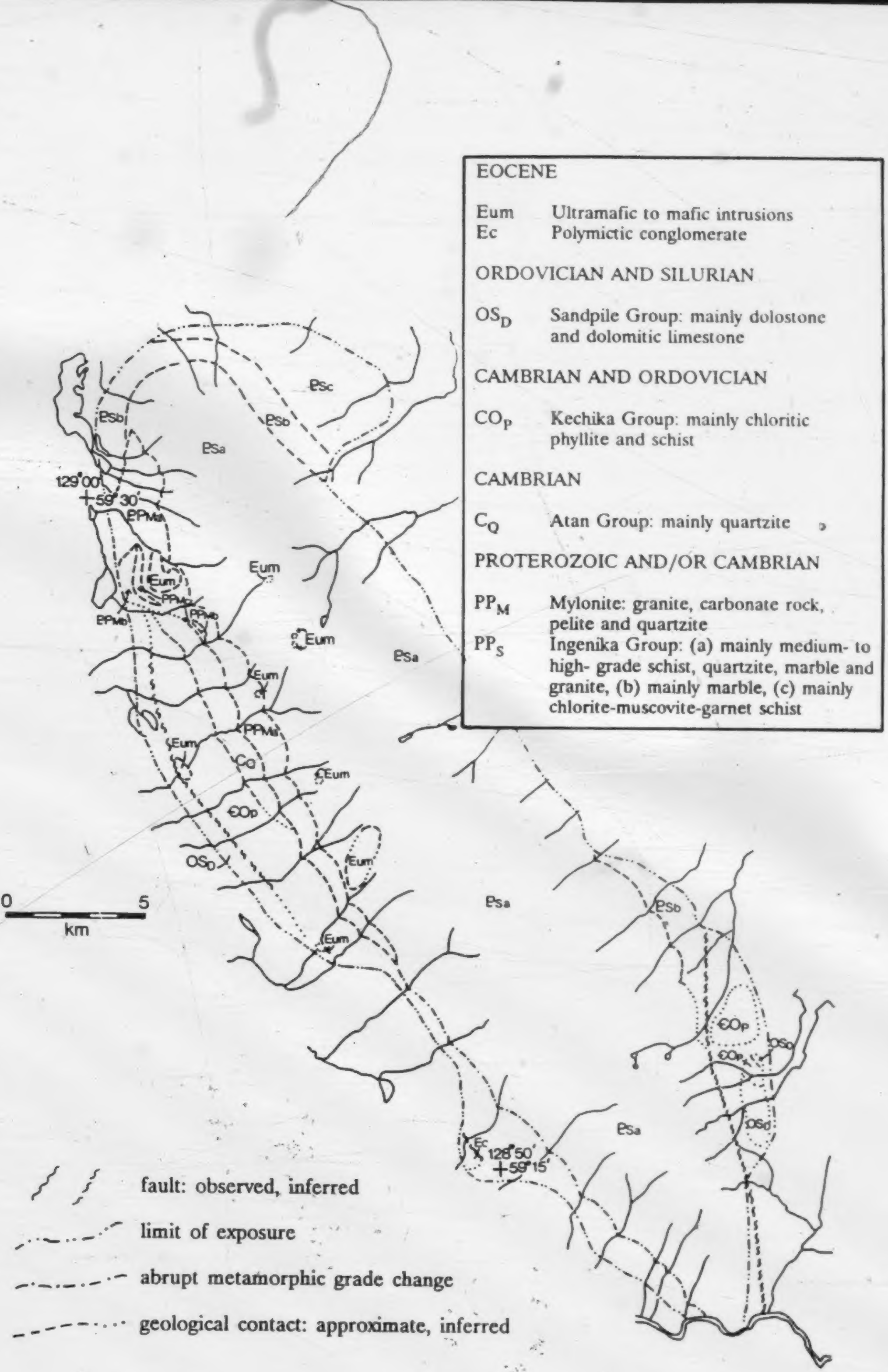
EOCENE
Eum Ultramafic to mafic intrusions
Ec Polymictic conglomerate
ORDOVICIAN AND SILURIAN
OS_D Sandpile Group: mainly dolostone and dolomitic limestone
CAMBRIAN AND ORDOVICIAN
CO_P Kechika Group: mainly chloritic phyllite and schist
CAMBRIAN
C_Q Atan Group: mainly quartzite
PROTEROZOIC AND/OR CAMBRIAN
PP_M Mylonite: granite, carbonate rock, pelite and quartzite
PP_S Ingenika Group: (a) mainly medium- to high- grade schist, quartzite, marble and granite, (b) mainly marble, (c) mainly chlorite-muscovite-garnet schist
fault: observed, inferred
limit of exposure
abrupt metamorphic grade change
geological contact: approximate, inferred
0
5
km
129°00'
59°30'
128°50'
59°15'
PSa
PSb
PSc
PPMa
PPMb
Eum
Ec
CQ
COp
OSD

Figure 1.3: Distirbution of map units in the Horseranch Range. See also Map 1 (back pocket).

ages of 2.2 Ga for detrital zircon indicate that the schists have a Proterozoic provenance, similar to source-rock ages elsewhere in the Cassiar terrane (Erdmer and Baadsgaard, 1987; Evenchick et al., 1984).

The eastern contact of the complex is not exposed. On the western side, the schist complex is juxtaposed against overlying low-grade Lower Paleozoic rocks by a north-northwesterly striking, 100 to 600 m thick, ductile mylonite zone. Mylonitic fabrics are developed in schist, quartzite, marble, calcsilicate rock, granite, quartz monzonite, gabbroic to dioritic rocks and the overlying low-grade quartzite and are cut by undeformed diorite, gabbro and hornblende pyroxenite.

Gabrielse (1963) reported crenulations, mesoscopic tight folds with axial planes forming an upward-converging fan centred on a main anticlinorial axis and a-c joints related to the major anticline in the schist complex. Plint and Erdmer (1989b) identified three fold phases in the map area: early, tight to isoclinal folds and crenulations, with axial surfaces parallel to the schistosity, later upright to steeply inclined, gently northwesterly or southwesterly plunging folds which fold the early folds and axial planar schistosity and minor, gentle, subhorizontal, upright folds with southwesterly trending hinges which are inferred to post-date all other fold phases. Passive and disharmonic folds are developed in the mylonite zone. They deform the mylonitic layering and are interpreted to have formed during mylonitization.

1.4. APPROACH

Mapping at 1:50,000 scale was carried out from 2-person tent camps during July and August, 1987 and June and July, 1988. Samples were collected for petrological and structural examination and for microprobe analysis of major mineral phases. Samples were collected for U-Pb geochronometry to establish the absolute timing of deformation events and for ^{40}Ar-^{39}Ar and fission track geochronometry to determine the time of latest metamorphic cooling. Samples analysed are described in Appendix 1 and detailed analytical procedures are given in Appendix 2.

CHAPTER 2

ROCK TYPES, FIELD RELATIONS, STRATIGRAPHIC CORRELATIONS AND METAMORPHIC MINERAL ASSEMBLAGES AND ZONES

2.1. INTRODUCTION

The spatial distribution of rocks types in the Horseranch Range is shown in Figure 1.3 and Map 1. The geology is described here according to rock type and rock units. Original stratigraphic relations are obscured due to the limited preservation of unequivocal bedding and the tectonic thickening of units. However, the overall distribution of rock units is consistent with the Upper Proterozoic and Lower Paleozoic stratigraphic sequence in the northern Cordillera (e.g. Mansy and Gabrielse, 1978; see below). Field characteristics of rock units are described from structural base to top, and hence, from high to low metamorphic grade.

General petrographic features including mineral assemblages and textures are summarized in Appendix 1. The term porphyroclast, as used here, refers to large mineral grains in a fine-grained matrix which represent deformed relicts of the pre-metamorphic and pre-deformational assemblage, such as phenocrysts or detrital grains. Foliation always wraps around porphyroclasts and they show evidence of weak to moderate grain size reduction by cataclasis or recrystallization. The term porphyroblast is used for any large metamorphic mineral in a finer grained matrix, even where it has been subsequently deformed. An exception is made for mylonitized metamorphic rocks in which the grain size of most metamorphic minerals (porphyroblasts) has been reduced by fracturing or recrystallization. These are referred to as porphyroclasts. Microstructures, including porphyroblast-matrix relations, are presented in Chapter 3 and Appendix 1.

2.2. METAMORPHIC ROCKS

2.2.1. Schist Complex

The schist complex is the most extensive and structurally lowest unit in the map area and is exposed along the entire length of the range. It is divisible into three map units: moderate- to high-grade schist, phlogopite marble and chlorite-muscovite-garnet schist.

(i) Moderate- to High-Grade Schist

This unit consists of interlayered pelitic to psammitic schist, quartzite, marble, calcsilicate rock, granitic orthogneiss and minor amphibolite. Exposed structural thickness is approximately 4 km. Compositional layering (defined by quartz-rich, carbonate-rich and mica-rich layers) approximately 5 cm to 20 m thick is parallel to the main schistosity. Contacts between schist, quartzite, marble, calcsilicate rock, orthogneiss and amphibolite are commonly sharp (Plate 2.1) except locally, where quartzite grades into calcsilicate rock.

Well foliated, fine-grained, rusty to yellowish brown-weathering to silvery grey-weathering, blueish grey, dark brown, or black and white pelitic and semipelitic schist consist mainly of muscovite, biotite, plagioclase and quartz (Table A1.1). The schist contains pale pink garnet, staurolite and sillimanite porphyroblasts ranging from 1 mm to 1 cm in their longest dimension. Kyanite porphyroblasts up to 3 cm long were observed at one locality. Average grain size is 1 to 2 mm. Schistosity is defined by biotite, muscovite, ilmenite, and elongate quartz and feldspar subgrains and the rocks exhibit a schistose to granoblastic-elongate texture (terminology of Collerson, 1974). Fine-grained, grey- to reddish grey-weathering, light grey psammitic schist consists mainly of quartz, feldspar and minor biotite and muscovite (Table A1.1). Average grain size is 1 to 2mm. Moderately sorted psammitic schist contains subangular to subrounded quartz and/or feldspar clasts (detrital "grits") up to 5 mm in the longest dimension; locally, quartz clasts are faintly blue coloured. Psammitic schist is massive relative to the pelitic and semipelitic schist; a weakly to moderately developed foliation is defined by biotite and flattened quartz or feldspar clasts forming a granoblastic-elongate texture. Contacts between pelitic, semipelitic and psammitic schist are sharp. These schists probably represent a moderately bedded succession of siltstone, argillite, shale and quartzofeldspathic to gritty sandstone (arkosic wacke).

Moderately foliated, fine-grained, rusty brown- to grey-weathering, grey to white, impure quartzite forms concordant layers up to 8 m thick in the moderate- to high-grade schist unit. It consists mainly of quartz and minor plagioclase, diopside and hornblende (Table A1.1). Quartzite adjacent to marble layers contains disseminated pyrite. Quartzite is commonly calcareous and grades into grey to greyish green-weathering, grey to greenish grey, fine-grained, diopside-garnet±hornblende calcsilicate rock. At lower metamorphic grade, calcsilicate rock contains garnet and hornblende or tremolite. Average grain size in quartzite and calcsilicate rock is 1 mm. Foliation is defined by micas and by actinolite-tremolite or hornblende and/or diopside. Quartzite and calcsilicate rock have a granoblastic-elongate texture.

Plate 2.1: Compositional layering in schist complex at north end of the range. Note granite dyke (gr) syntectonic with respect to folds. View looking northwest. Person for scale in bottom left corner of photo.

The quartzite-calcsilicate sequences probably represent a moderately bedded sequence of calcareous sandstone (calcareous quartz arenite to subarkose) grading to siliceous and dolomitic limestone.

Buff-weathering, white, cream or grey marble forms concordant layers up to 5 m thick in the schist complex. The marble is fine- to medium-grained (3 to 5 mm), massive, granoblastic to weakly foliated and composed of calcite, minor graphite(?) and locally, subrounded to subangular quartz clasts ≤ 2 mm diameter. Where in contact with late granites, marble contains large (up to 1.5 cm diameter) garnets (see Plate 2.8) and massive, granoblastic layers of intergrown garnet and diopside. Weak foliation is defined by parallel flakes of phlogopite. Marble contains 0.5 to 5 cm thick stringers or layers of rusty- or grey-weathering, grey to white quartz and greenish grey-weathering diopside-garnet calcsilicate material, oriented parallel to the foliation. These stringers and layers are deformed into tight folds with axial surfaces parallel to the foliation or are boudinaged. They are resistant relative to the marble which readily weathers to a medium-grained calcite sand. Quartz grains in marble record some detrital influx. Its protolith was likely a limestone with thin siliceous beds of dolomite and chert.

Fine- to medium-grained (≤ 5 mm), tan- to rusty yellow-weathering, well foliated, leucocratic, muscovite±biotite±garnet granite orthogneiss of unknown age locally forms 2 to 15 m wide, concordant layers and lenses within pelitic to psammitic schist, quartzite and marble. Foliation in orthogneiss is defined by muscovite and elongate quartz and feldspar subgrains; the rock has a granoblastic-elongate texture. The orthogneiss represents granite sills which have been deformed with the schist complex.

A concordant, fine-grained (≤ 2 mm), green-brown weathering, dark green to black, amphibolite layer, approximately 1 m thick (perpendicular to the schistosity), is exposed in pelitic schist in the north-central part of the range. Relict ophitic texture is preserved in its centre, and its margins are schistose, indicating that the amphibolite was originally a mafic dyke or sill intruded into the schist complex. Fine-grained (< 2 mm), well foliated, concordant amphibolite layers, 1 to 2 m thick are observed in three outcrops in the north-central part of the range. Amphibolite-schist contacts are sharp. These amphibolites may have been mafic sills, dykes or volcanic flows.

(ii) Phlogopite Marble

Exposed at the north end of the range, structurally overlying the schist complex, is a resistant, fine-grained (1-2 mm), tan-weathering, tan, grey, or white, calcareous, phlogopite marble with abundant subangular to rounded, uniformly sized, quartz clasts 0.1 to 0.2 mm in diameter. This unit forms prominent bald hills below tree-line at the north end of the map area and is structurally at least 400 m thick. Contacts with the underlying high-grade schist and overlying chlorite-muscovite-quartz schist are not exposed. Resistant, siliceous, grey, red and black weathering layers approximately 1 to 5 cm thick are commonly parallel to a weak, phlogopite-defined foliation. Minor, concordant white quartzite and pelitic schist up to 5 m thick are interlayered locally with the marble; contacts are sharp. Pelitic schist contains staurolite and garnet porphyroblasts (< 3 mm longest dimension) near its inferred contact with the moderate- to high-grade schist unit. Along the northwestern side of the range, phlogopite marble is deformed in the mylonite zone and is included in the mylonite map unit on Figure 1.3. This unit represents a succession of fine-grained limestone with a detrital component (as recorded by quartz clasts), with minor beds of siltstone, argillite, shale and sandstone.

(iii) Chlorite-Muscovite-Garnet Schist

Chlorite-muscovite-garnet phyllitic schist structurally overlies the phlogopite marble and locally contains 1 to 5 m thick layers of fine-grained ($\leq$ 2mm) actinolitic hornblende to hornblende-garnet calcsilicate schist, semipelitic to psammitic schist, grey to white quartzite and grey marble. Psammitic schist commonly contains subrounded to subangular quartz grains 1 to 2 mm in diameter. This unit is structurally at least 1000 m thick. Upper and lower contacts are not exposed. However, minor phlogopite marble is exposed in the chlorite-muscovite-garnet schist unit near the inferred contact with the underlying phlogopite marble, which implies that the contact is gradational. This unit probably represents thickly bedded siltstone with minor thinly to moderately bedded argillite, sandstone, quartzite and limestone. Quartz clasts in the psammitic schist record detrital influx.

2.2.2. Homogeneous Quartzite and Phyllite

Homogeneous, white to pink, very fine-grained to fine-grained (0.5 to 1.5 mm) quartzite structurally overlies the mylonite zone. Contacts with other units are not exposed. The quartzite is well jointed and finely rodded and commonly contains pyrite as stringers and disseminated elongate blebs which define the foliation. Minor (< 1%) rounded quartz clasts less than 1 mm in diameter are common in quartzite and interpreted to be detrital grains. Locally irregular, discordant pods of low-grade, fine-grained ($\leq$ 2 mm), buff-weathering, white actinolite marble and concordant, continuous layers of crenulated fine-grained ($\leq$ 2 mm), biotite schist are exposed within the quartzite. This quartzite unit is distinguished from quartzite layers in the schist complex by its greater thickness, homogeneity and absence of gradations into calcsilicate rock. It probably represents a thickly bedded, moderately to well sorted sandstone (quartz arenite).

Structurally overlying the quartzite is a very fine-grained (<1 mm) to aphanitic, calcareous, fissile, lustrous, silvery green-grey chloritic phyllite characteristically exposed as a rubbly scree and locally interlayered with calcareous chlorite schist. Cleavage in chloritic phyllite is defined by chlorite and white mica; minor ($<1\%$) rounded, detrital quartz grains are present in phyllite. Locally, phyllite grades into relatively more massive, calcareous, finely banded, aphanitic rock. Banding is defined by alternating, 1 to 3 mm thick chlorite-rich and carbonate-rich layers. Contacts with the homogeneous quartzite are not exposed. Phyllite contains tan-weathering, dark grey, 1 to 15 cm thick, cherty and arenaceous beds which are commonly boundinaged or tightly folded; the cleavage in phyllite is axial planar to the tight folds (see Chapter 3). Brownish-green weathering, green chlorite schist is very fine-grained ($<$ 1 mm) and contains disseminated dolomite crystals ($<$ 1 mm in their longest dimension) which are weakly to moderately elongate parallel to the chlorite-white mica defined schistosity. The crystals are locally replaced by dark material which is composed of microscopic, randomly oriented, subidioblastic, intergrown chlorite, calcite and talc (Plate 2.2).

Along the southwestern and southeastern flanks of the range, the phyllite unit also contains pink to white (weathered and fresh) siliceous, muscovitic, aphanitic phyllite, grey-weathering, dark grey, locally fossil-bearing, calcareous aphanitic meta-mudstone and black (weathered and fresh), aphanitic, calcareous slate. Rare fossils in the meta-mudstone are fragmented and unidentifiable. Contacts between phyllite, meta-mudstone and slate are sharp and concordant.

The protolith of the meta-mudstone, slate and phyllite was likely a succession of moderately bedded calcareous siltstone, argillite and shale. The protolith of the chlorite schist was likely argillaceous dolomitic limestone.

2.2.3. Regional Correlation of Metamorphic Rocks and Depositional Environment

Gabrielse (1963 and personal communication 1987) proposed a correlation of some of the rocks structurally beneath the mylonite with the lower unit of the

9

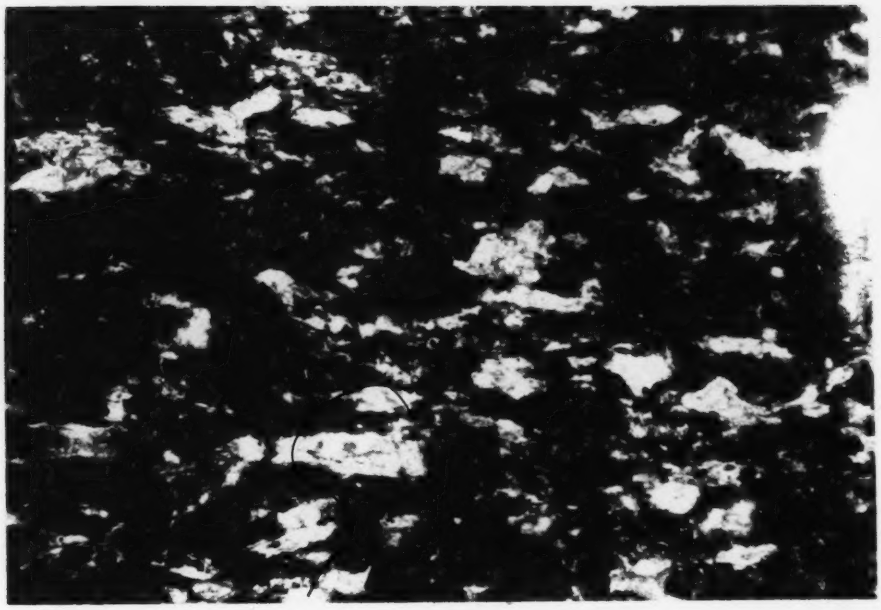

Plate 2.2: Pseudomorphs of chlorite, calcite and talc after dolomite in chlorite schist. Field of view is 4 mm.

Cambrian Atan Group (quartzite of the Boya Formation). However, homogeneous quartzite above the mylonite is lithologically more similar to the Boya Formation quartzite than the quartzite beneath the mylonite. Exposure at the contact between the homogeneous quartzite and the structurally overlying phyllite is poor and no limestone which would correlate with the upper limestone division (Rosella Formation) of the Atan Group is exposed. This makes any interpretation tentative. Assuming that the apparently condensed section results from a local hiatus, the homogeneous quartzite is correlated with the Boya Formation.

On the basis of published descriptions of the Upper Proterozoic Ingenika Group in the northern Omineca Belt (e.g. Gabrielse, 1975; Mansy and Gabrielse, 1978; Evenchick, 1985, 1988; Ferri and Melville, 1988), the tan-weathering phlogopite marble and the chlorite-muscovite-garnet schist, are correlated with the Espee and Stelkuz Formations of the Ingenika Group, respectively. The Espee Formation is characterized by a resistant, thick-bedded limestone assemblage interbedded minor calcareous shale and phyllitic shale (Mansy and Gabrielse, 1978). The Stelkuz Formation is characterized by variable relative amounts of interlayered limestone, siltstone, shale and sandstone (Mansy and Gabrielse, 1978; Fritz, 1984). The Espee and Stelkuz Formations were interpreted to record deposition in a high energy, shallow water environment and a mainly shallow marine to possibly fluvial environment, respectively (Mansy and Gabrielse, 1978). The presence of rounded, uniformly sized quartz clasts in the phlogopite marble and psammite layers in the chlorite-muscovite-garnet schist unit, and the range of rock types in the phlogopite marble unit, support this interpretation.

The moderate- to high-grade schist unit probably correlates with the Swannell and Tsaydiz Formations (Ingenika Group) which are indistinguishable in the map area. Although characteristic feldspar-quartz pebble conglomerate is absent in the schist unit, the presence of psammitic schist with feldspar and quartz grains ("grits") and of quartz grains in marble in the highest grade and structurally deepest rocks, suggest that a large part of the schist complex correlates with the middle and upper member of the Swannell Formation (cf. Mansy and Gabrielse, 1978). As the moderate- to high-grade schist, phlogopite marble and muscovite-chlorite-garnet schist are part of the same group, they are hereafter referred to collectively as the schist complex.

On the basis of poor sorting of most units, Mansy and Gabrielse (1978) interpreted the depositional environment of the Swannell and Tsaydiz Formation as deep water and below wave base. In the map area, the rocks are moderately sorted and generally fine-grained. Coarse-grained clastic rocks are absent, although detrital quartz and feldspar grains are common in psammitic schist.

Gabrielse (1963) correlated the chloritic phyllite with the Cambro-Ordovician Kechika Group and this correlation is supported by this study. The fine-grained, calcareous and argillaceous nature of these rocks and the paucity of fossils suggests deposition in deep water (Gabrielse, 1963).

2.3. SEDIMENTARY ROCKS

2.3.1. Dolostone and Dolomitic Limestone

Structurally overlying phyllite, along the west and southeast sides of the Horseranch Range is a unit of tan- to grey-weathering, grey, aphanitic dolostone (locally with chert beds 1 to 3 cm thick) dolostone breccia and dolomitic limestone. Calcite veins, 1 mm to 10 cm thick, commonly cut bedding. Fossils of rugose corals are exposed in the southwest part of the map area (Map 1) and were tentatively identified as Ordovician-Silurian Paleophyllum (B. Chatterton, personal communication, 1988).

The contact with underlying phyllite is exposed in an inaccessible cliff face in the southwestern part of the study; it is subhorizontal and sharp and assumed to be tectonic. The contact is not exposed or is faulted along the western side of the range. Gabrielse (1963) correlated this unit with the Ordovician-Silurian Sandpile Group and interpreted its depositional environment as a shallow, well-aerated, gently subsiding platform.

2.3.2. Polymictic Conglomerate

This unit was observed in one outcrop on the southwestern flank of the range. Contacts with other units are not exposed but are inferred to be faulted. The conglomerate contains locally derived, 1 to 5 cm (longest dimension), subangular to subrounded clasts of chlorite phyllite, siltstone, granitic rock and quartz. The rock exhibits a northwest-striking, steeply southwest-dipping parting (spaced cleavage?). Gabrielse (1963) suggested that the conglomerate was the result of normal faulting along the Horseranch fault.

2.4. INTRUSIVE ROCKS

Granitic and mafic to ultramafic intrusive rocks are exposed in the northern half of the range in the schist complex. Mafic to ultramafic intrusive rocks also locally intrude the Kechika Group.

2.4.1. Granite and Quartz Monzonite

Leucocratic, yellowish grey- to white-weathering, grey to white biotite-muscovite±garnet granitic dykes and sills are widespread in the northern half of schist complex (Table A1.2). They commonly cut the main foliation in all units and folds in the schist complex (Plate 2.3); injection migmatite is developed locally between late syn- to post-tectonic (with respect to the schistosity) granite dykes and sills and sillimanite schist (see Plate 3.2). Granite dykes syntectonic with respect to upright folds with northwest-trending hinges are exposed locally at the northern end of the range (see Plate 2.1). Contacts oblique to mylonitic foliation are locally preserved between mylonitic schist and granitic mylonite which may indicate that some granite intrusion predated mylonitization. However, the widespread development of C-S fabric and geochronometry data indicate that most granites are synkinematic (see Chapters 3 and 6).

The granitic rocks range from two-mica granodiorite to granite (Figure 2.1). As the granodiorite composition was determined for a pegmatitic rock, it may be incorrect. Transitional granite to quartz monzonite (Figure 2.1) (hereafter referred to as quartz monzonite) is deformed in the mylonite zone. All compositions reported by Gabrielse (1963) for granitic orthogneiss and pegmatite in the Horseranch Range are granite, except one sample which lies on the granite-granodiorite boundary.

Grain size in the granitic rocks is variable and commonly less than 1 cm. Large alkali or perthitic feldspar phenocrysts are common in medium- to coarse-grained granitic rocks. Tourmaline, developed locally as radiating sprays up to 4 cm long and euhedral garnets 1 to 5 mm in diameter are common accessory phases. Tourmaline-rich zones up to 2 cm wide are developed locally along schist-granite contacts. At one locality at the north end of the study area, subidioblastic andalusite porphyroblasts, up to 0.5 cm in diameter, are developed in staurolite-garnet pelite in contact with a late granite intrusion. Quartz veins cut and are cut by the granitoid intrusions.

a

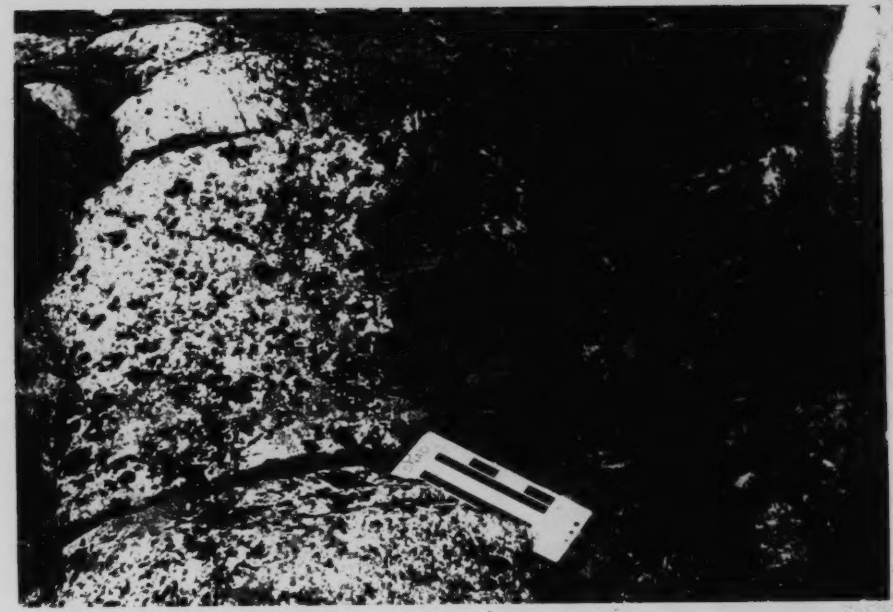

Plate 2.3: (a) Granite dyke cuts upright folds with northwesterly trending hinges which fold the schistosity in the schist complex. These are ${}^2F_3$ folds (see Chapter 3). View looking northwest.

b

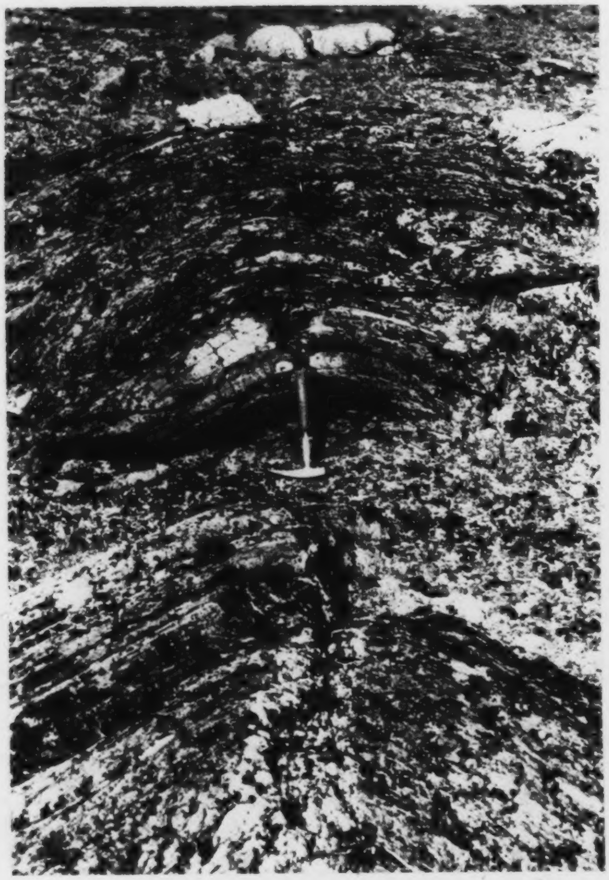

Plate 2.3 (continued): (b) Granite dyke has intruded schist along axial surface of upright fold with northwesterly trending hinge. This is an $^2F_3$ fold (see Chapter 3). View looking northwest.

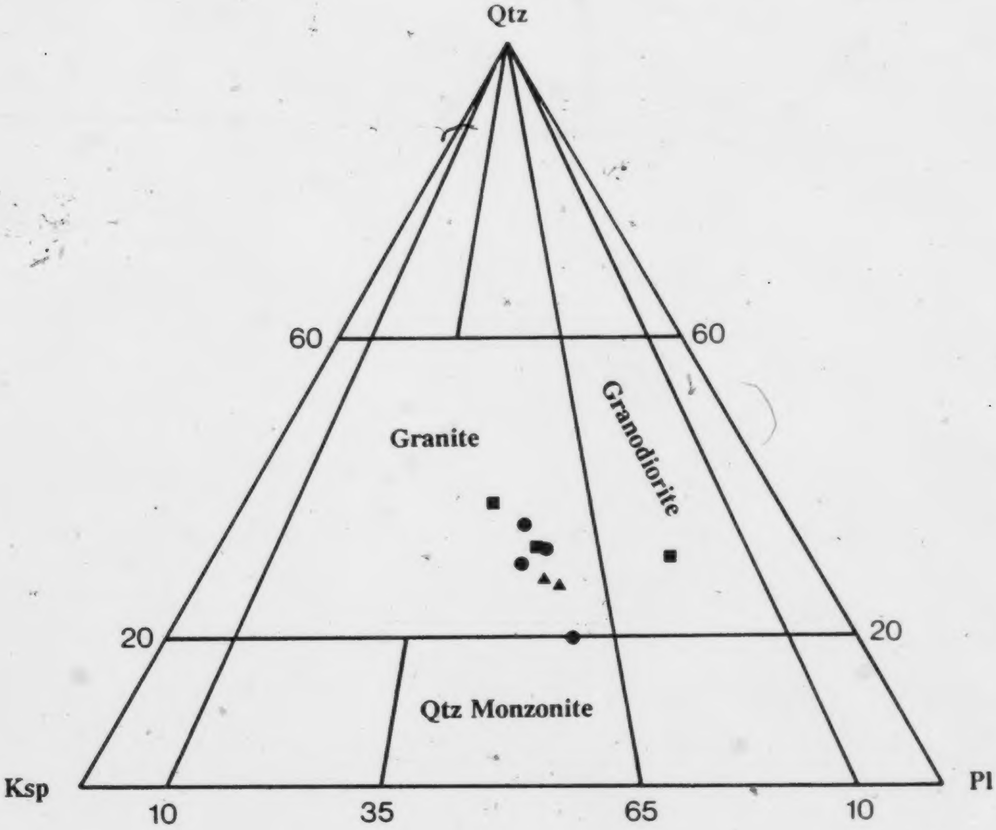

Figure 2.1: Classification of granitic rocks in the Horseranch Range, following Streckeisen (1976). Squares = syn- to post-tectonic granite in the schist complex; circles = C-S granite mylonite; triangles = orthogneiss in the schist complex. Data from point counting of stained slabs using a 1 mm grid.

2.4.2. Mafic and Ultramafic Rocks

Dark green to black, medium- to coarse-grained (3 mm to 1 cm), equigranular, massive hornblende and pyroxene diorite, pyroxene gabbro, hornblende pyroxenite and hornblendite intrude the schist complex, mylonite and chloritic phyllite (Figure 1.3; Table A1.2). They commonly form bodies 6-10 m across. Contacts with host rocks are exposed locally and are sharp. A large, irregularly shaped body of medium- to coarse-grained, massive hornblende pyroxenite, diorite and gabbro approximately 1.5 km^2 in area crops out in the northeastern part of the map area (Figure 1.3 and Map 1). This body contains inclusions of fine-grained quartzite and tourmaline- and garnet-bearing felsic rocks. In the west-central part of the schist complex is exposed a large body of coarse- to medium-grained hornblende pyroxenite, pyroxenitic gabbro and diorite. Contacts with granite, which crops out within this body, are sharp but temporal relations are ambiguous. Pyroxenitic diorite is fractured and chloritized in the Horseranch fault zone (Figure 1.3 and Map 1). No contact metamorphic effects associated with the mafic to ultramafic intrusions were observed.

2.5. MYLONITE ZONE

Rocks in the mylonite zone are distinguished from L-S tectonites in the schist complex by abundant evidence of non-coaxial deformation, such as ubiquitous C-S fabric (terminology of Berthé et al, 1979) in granite, σ- and δ-porphyroclast systems (terminology of Passchier and Simpson, 1986) in metacarbonate rock, quartzite and granite, rotated boudins and asymmetric folds of originally continuous quartz veins and of 1 to 5 mm thick compositional layering in metacarbonate rock. The rocks range from protomylonite to ultramylonite and are predominantly mylonite (Higgins, 1971); initial grain size was estimated from similar rocks types outside the mylonite zone.

Mylonite is developed in a zone 400 m to 1 km thick and at least 20 km long between the schist complex and overlying quartzite along the western margin of the Horseranch Range (Figure 1.3 and Map 1). It is inferred to extend to the southwestern end of the range (see section 3.4).

The mylonite zone includes part of the moderate- to high-grade schist unit (mainly diopside marble or calcsilicate schist and sillimanite schist), dioritic to gabbroic rocks of unknown affinity, fine-grained white, homogeneous white quartzite, leucocratic granite and quartz monzonite. Mylonitic foliation is parallel to schistosity in the underlying schist complex and overlying quartzite and phyllite. Contacts are not exposed. The lower boundary of the mylonite zone is delineated on the basis of widespread mylonitic textures. This generally occurs through 6 to 10 m of section. Locally, mylonitic textures are developed in granite sills 2 to 5 m thick in the schist complex up to approximately 50 m (horizontal distance) from the delineated lower boundary and therefore, the mylonite-schist complex contact is interpreted to be gradational. Mylonites are described in detail in Chapter 3.

Mylonite is cut by undeformed mafic to ultramafic intrusions (Figure 1.3 and Map 1) and by minor granite dykes. No widespread retrogression is associated with the zone.

2.6. METAMORPHIC MINERAL ASSEMBLAGES

Prograde mineral assemblages for the main rock types are reported in Appendix 1 (Table A1.1). Prograde pelitic mineral assemblages were used to define isograds and mineral zones (Figure 2.2) and are described below along with retrograde and contact metamorphic mineral assemblages.

2.6.1. Prograde Mineral Assemblages and Mineral Zones

Six metamorphic mineral zones are defined by pelitic mineral assemblages: chlorite, chlorite-biotite, biotite, staurolite-garnet, biotite-garnet±kyanite and sillimanite-orthoclase-muscovite (Figure 2.2). The mylonite zone lies predominantly in the sillimanite-orthoclase-muscovite zone at the north end of the range. It separates the biotite and sillimanite-orthoclase-muscovite zones in the northwestern part of the study area and is inferred to separate the biotite and staurolite-garnet zones in the southwestern part. The nature of isograds between these mineral zones can be determined from porphyroblast-matrix relations, mineral chemistry and phase equilibria. Therefore, the significance of the isograd pattern and phase equilibria applicable to isograds are discussed in Chapters 3 and 5, respectively.

Metapelite in the chlorite zone consists mainly of chlorite, white mica, plagioclase and quartz. Minor biotite is present locally. The biotite zone is defined by the first appearance of biotite porphyroblasts, coincident with a decrease in chlorite in the pelitic assemblage bi-mu-qtz-pl ± chl ± gt along the western flank of the range. Biotite forms subidioblastic to xenoblastic porphyroblasts; garnet forms idioblastic to xenoblastic porphyroblasts. Inclusion trails are absent. In the southwestern part of the

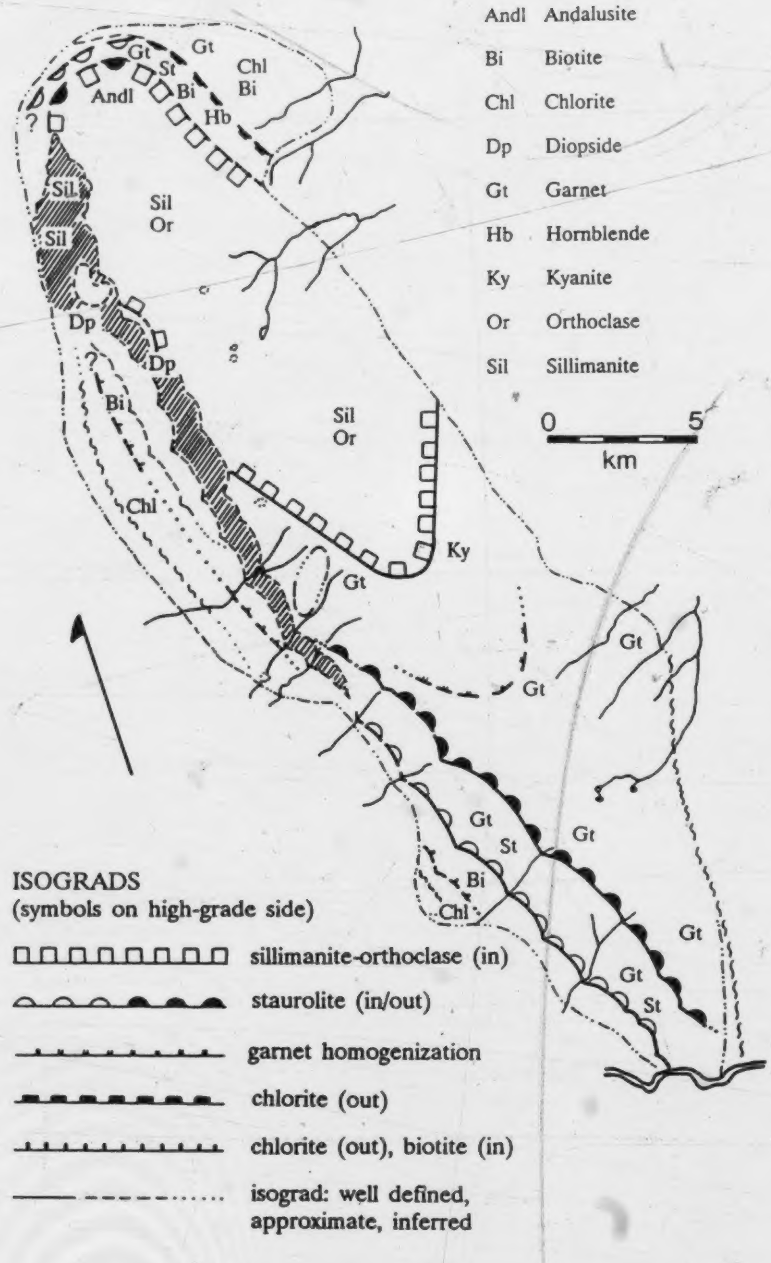
Andl Andalusite
Bi Biotite
Chl Chlorite
Dp Diopside
Gt Garnet
Hb Hornblende
Ky Kyanite
Or Orthoclase
Sil Sillimanite
0
5
km
Gt
St
Andl
Bi
Hb
Chl
Sil
Or
Dp
?
Ky
ISOGRADS
(symbols on high-grade side)
sillimanite-orthoclase (in)
staurolite (in/out)
garnet homogenization
chlorite (out)
chlorite (out), biotite (in)
isograd: well defined, approximate, inferred

Figure 2.2: Traces of regional metamorphic isograds in the Horseranch Range (symbols on high-grade side of isograd). Dip of isograds is assumed to be parallel to compositional layering and hence, to main schistosity (see text). The nature of the isograds (i.e mineral reactions, compositional control) is discussed in chapters 4 and 5. Note that deepest rocks (highest grade) are exposed in the north. Other symbols as for Figure 1.3.

range, the transition from biotite zone to staurolite-garnet zone is abrupt. At the northern end of the range, biotite and chlorite coexist in equal abundance up to the staurolite-in isograd and a chlorite-biotite zone is defined in this area (Figure 2.2). Chlorite in some samples is intergrown with biotite and may be retrograde, but textures are equivocal.

The staurolite-garnet zone, marked by the appearance of staurolite in the major mineral assemblage st-bi-mu-pl-qtz-ilm±gt±sil, is mappable around the northern end and along the southwestern flank of the Horseranch Range. Staurolite, garnet, biotite, plagioclase, ilmenite and locally, muscovite form subidioblastic porphyroblasts. Plagioclase is present as a matrix phase in the lower staurolite-garnet zone and forms porphyroblasts in the middle to upper staurolite zone, coincident with an overall increase in grain size of the schist. Minor optical zoning occurs locally in plagioclase. Chlorite is absent except as minor inclusions in garnet and as a retrograde phase after staurolite, biotite or garnet (section 2.6.2). One exception is observed in the northeastern part of the map area where garnet, staurolite and biotite porphyroblasts are developed in a chlorite-muscovite-rich layer in chlorite-muscovite-quartz schist. Minor fibrolite locally overprints biotite in staurolite-garnet schist (see below).

The biotite-garnet±kyanite zone is restricted to the southern part of the range. It is bounded by the staurolite-out isograd to the west, the sillimanite-orthoclase-in isograd to the north and by inferred faults and limit of exposure to the south and east. The major mineral assemblage is bi-gt-mu-pl±ilm. Kyanite is developed in one locality. Garnet and plagioclase form subidioblastic to xenoblastic porphyroblasts. Biotite, muscovite and kyanite form subidioblastic porphyroblasts. Fibrolite overprints biotite in kyanite-garnet schist.

The sillimanite-orthoclase-muscovite zone is restricted to the northern half of the range and is defined by the first appearance of sillimanite (commonly fibrolite), with or without orthoclase, in the assemblage sil-bi-pl-gt±or±mu. No sillimanite, sillimanite-muscovite, or sillimanite-orthoclase zone is mappable although locally orthoclase and muscovite are absent or present only in trace amounts. Subidioblastic to idioblastic porphyroblasts of muscovite, biotite, garnet, plagioclase, orthoclase and sillimanite are developed in this zone. Sillimanite overprints biotite, muscovite, plagioclase and quartz.

2.6.2. Retrograde Metamorphic Mineral Assemblages

Retrogression is negligible throughout the area except in the biotite-garnet±kyanite and staurolite-garnet zones, where it is moderate to extensive. Retrograde chlorite after biotite, staurolite, garnet or plagioclase is common in the southern staurolite-garnet zone; chlorite commonly occupies fractures or space between boudins in staurolite and garnet (Plate 2.4). Plagioclase is weakly to moderately sericitized or saussuritized. Locally, staurolite and garnet are partly replaced or pseudomorphed by chlorite, plagioclase, muscovite or an intergrowth of the three.

In the biotite-garnet±kyanite zone, garnet is partly to entirely pseudomorphed by an intergrowth of biotite, chlorite, quartz, plagioclase, fine-grained muscovite, opaque minerals (ilmenite?) and locally epidote (Plate 2.5). These pseudomorphs commonly show iron oxide staining. Biotite is moderately to strongly chloritized. Late chlorite porphyroblasts cut the schistosity (Plate 2.6) and are apparently unaffected by northwest-trending upright folds. Chlorite porphyroblasts are absent in the rest of the map area. Plagioclase is moderately sericitized or saussuritized.

Retrogression in the sillimanite-orthoclase-muscovite zone (including the mylonite zone) consists of minor hornblende after diopside, minor chlorite after biotite, hornblende and garnet and weak to moderate sericitization or saussuritization of plagioclase. The absence of significant retrogression in the mylonite zone implies that mylonitization took place at high temperatures, under low water-rock ratios (i.e. "dry" conditions) or that the fluid was well equilibrated with the rock.

2.6.3. Contact Metamorphic Mineral Assemblages

Evidence of contact metamorphism by granite intrusions is found locally in the schist complex. At the north end of the range, andalusite porphyroblasts are developed in staurolite-garnet schist in contact with post-S_2 (see Chapter 3) two-mica±garnet granite. Andalusite forms coarse, subidioblastic, optically continuous poikiloblasts that include coarse grains of plagioclase, biotite, muscovite, staurolite and garnet and that partly replace staurolite. Coarse biotite porphyroblasts partly replace garnet. In some cases, biotite has preferentially replaced garnet cores, forming atoll garnets (Plate 2.7). The absence of late andalusite and biotite porphyroblasts in staurolite-garnet schist on the southwest flank of the range, where post-tectonic granite is absent, supports the interpretation that late andalusite and biotite at the north end of the range result from contact metamorphism.

At all metamorphic grades, large (up to 1 cm in the longest dimension), idioblastic to subidioblastic, tourmaline porphyroblasts commonly overgrow S_2 in

Plate 2.4: Retrograde chlorite occupies space between boudins and in fractures in staurolite. Field of view is 4 mm.

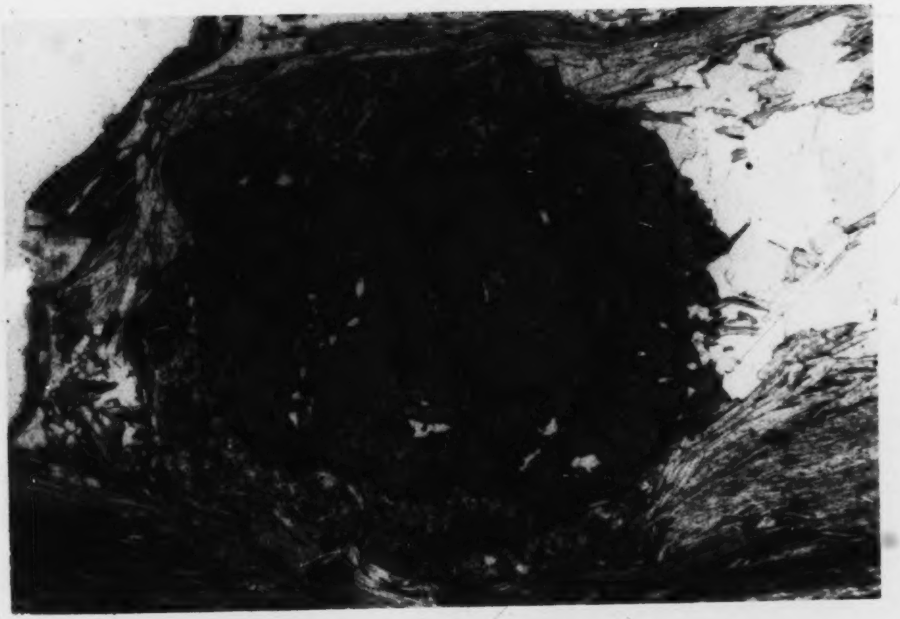

Plate 2.5: Garnet in pelitic schist in the biotite-garnet ± kyanite zone is partly replaced by an intergrowth of muscovite, biotite, plagioclase, and quartz. The significance of the textural discontinuity is discussed in chapters 4 and 5. Field of view is 4 mm.

Plate 2.6: Late chlorite porphyroblasts cut the matrix schistosity in pelitic schist in the biotite-garnet ± kyanite zone. Field of view is 4 mm.

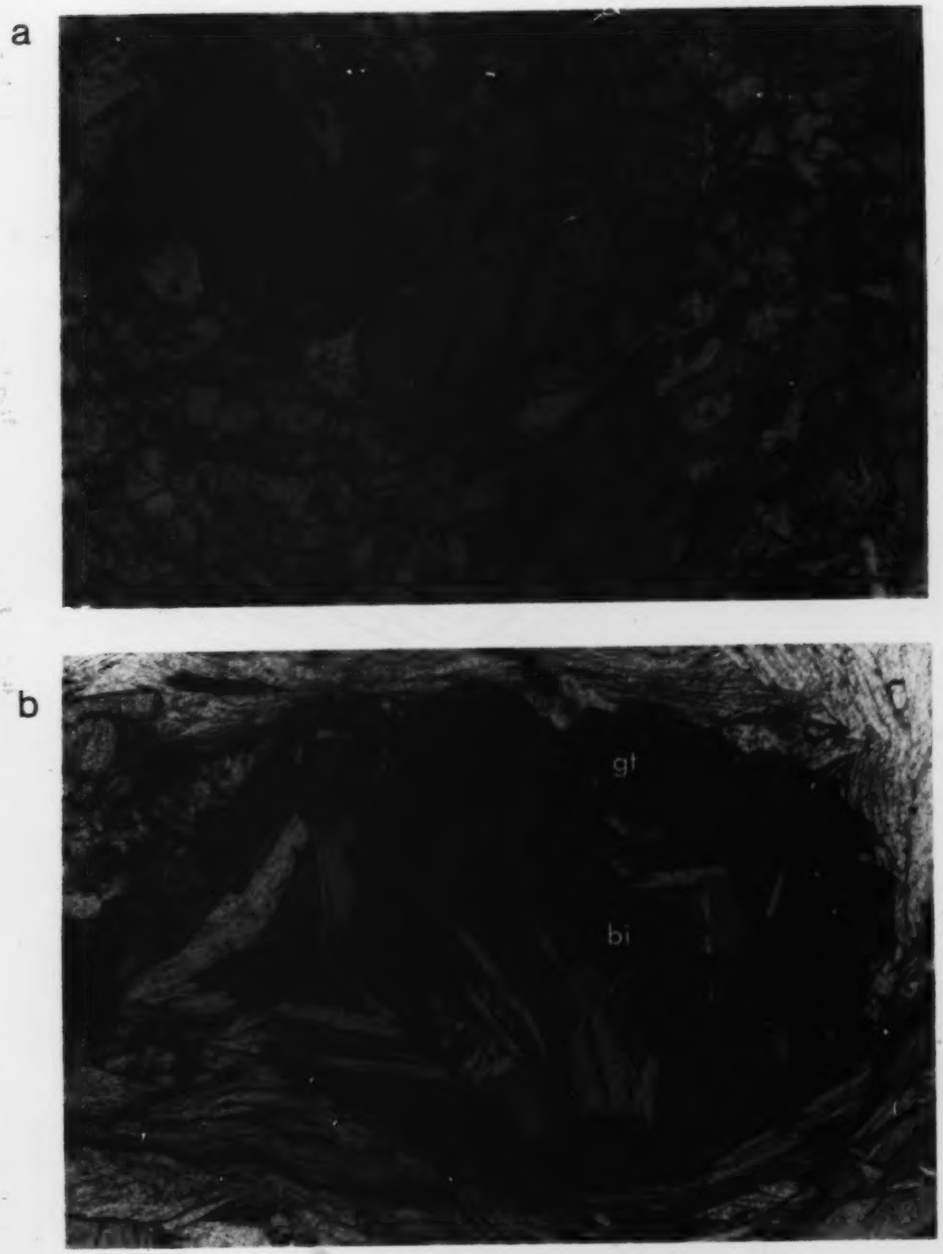

Plate 2.7: Contact metamorphic effects by late two-mica ± garnet granite in staurolite-garnet schist at the north end of the range. (a) Andalusite partly replaces staurolite. Field of view is 4 mm. (b) Biotite partly replaces garnet core, forming an atoll garnet. Field of view is 2 mm.

schist at schist-granite contacts and locally, form zones up to 1 cm wide at the contacts. Tourmaline porphyroblasts contain straight inclusion trails of quartz, plagioclase and fine-grained opaque minerals that are continuous with the matrix foliation. Although tourmaline is present in schists at all grades, post-S_2 tourmaline porphyroblasts are only developed at schist-granite contacts.

Marble in the schist complex contains large (up to 1.5 cm diameter), idioblastic to subidioblastic garnets at granite contacts (Plate 2.8). Garnet is optically zoned; zoning is emphasized by calcite, zoisite and quartz which form crystallographically controlled inclusion trails with hexagonal traces.

Granite intrusions are confined to the northern half of the range, largely within the sillimanite-orthoclase-muscovite zone. Together with evidence of late crystallization of sillimanite (see section 3.2), this suggests that sillimanite could be contact-metamorphic. However, minor sillimanite is present in the southwestern exposure of the staurolite-garnet zone where granite is absent. Therefore, all sillimanite is interpreted to result from regional metamorphism.

Plate 2.8: Large grossular garnet (resistant-weathering mass below scale bar) developed in center of a marble layer which is in contact with granite sill (lichen-covered at base of photo).

CHAPTER 3
STRUCTURE

3.1. INTRODUCTION

A study of macroscopic and microscopic fabric elements was carried out to determine the macroscopic geometry of the map units, the nature and number of phases of deformation and the relative timing of metamorphism and deformation. At least 5 phases of deformation have occurred. Pre-, syn- and post-metamorphic structures are observed. Microscopic structures correlate directly with macroscopic structures.

Conventional notation for deformation phases in polydeformed rocks operates on the assumption that S_1 formed by folding (F_1) of bedding (S_o) (that is, S_1 is an axial planar fabric), so that folds deforming S_1 must be at least F_2. This notation is used here. However, in this study the F_2 fold phase by this notation is the earliest identifiable phase and whether S_1 formed by folding of S_o in the schist complex is unclear. Therefore, to denote the relative age amongst fold phases, that is, whether a fold phase is the earliest identifiable phase or the second identifiable phase, superscripts are used. Thus, ${}^1F_2$ is the earliest fold phase identified, which following conventional notation would be denoted as F_2. This notation is similar to that proposed by Bell and Duncan (1978).

In the following descriptions, the terms porphyroblast and porphyroclast are applied as defined in Chapter 2. Inclusion trails in porphyroblasts and the matrix foliation (or external foliation with respect to porphyroblasts) are referred to as S_i and S_e, respectively. Relationships between metamorphism and deformation are summarized in Table 3.1. All stereographic projection plots were created using the computer program ORIENT written by H. Charlesworth at The University of Alberta.

3.2. STRUCTURE OF THE SCHIST COMPLEX

3.2.1. Macroscopic Folds and Planar Fabrics

The earliest folds (${}^1F_2$) in the schist complex are minor, tight to isoclinal, and deform a pre-existing, muscovite-quartz-defined schistosity (S_1) and locally, S_1-parallel quartz veins (Plate 3.1). These folds are commonly only detected in thin section. They are typically rootless and transposed along the main schistosity in the schist complex

Table 3.1.: Relative timing of deformation, metamorphism and granite intrusion in the Horseranch Range, based on field relations and microstructures. Granite intrusions are syn- to post-tectonic with respect to ${}^2F_3$ folds in the region where contact metamorphic andalusite is developed, and thus, andalusite is shown as post-${}^2F_3$. Late chlorite porphyroblasts (*) cut S_2 and are not affected by ${}^2F_3$ and thus, shown as later than ${}^2F_3$ folds.

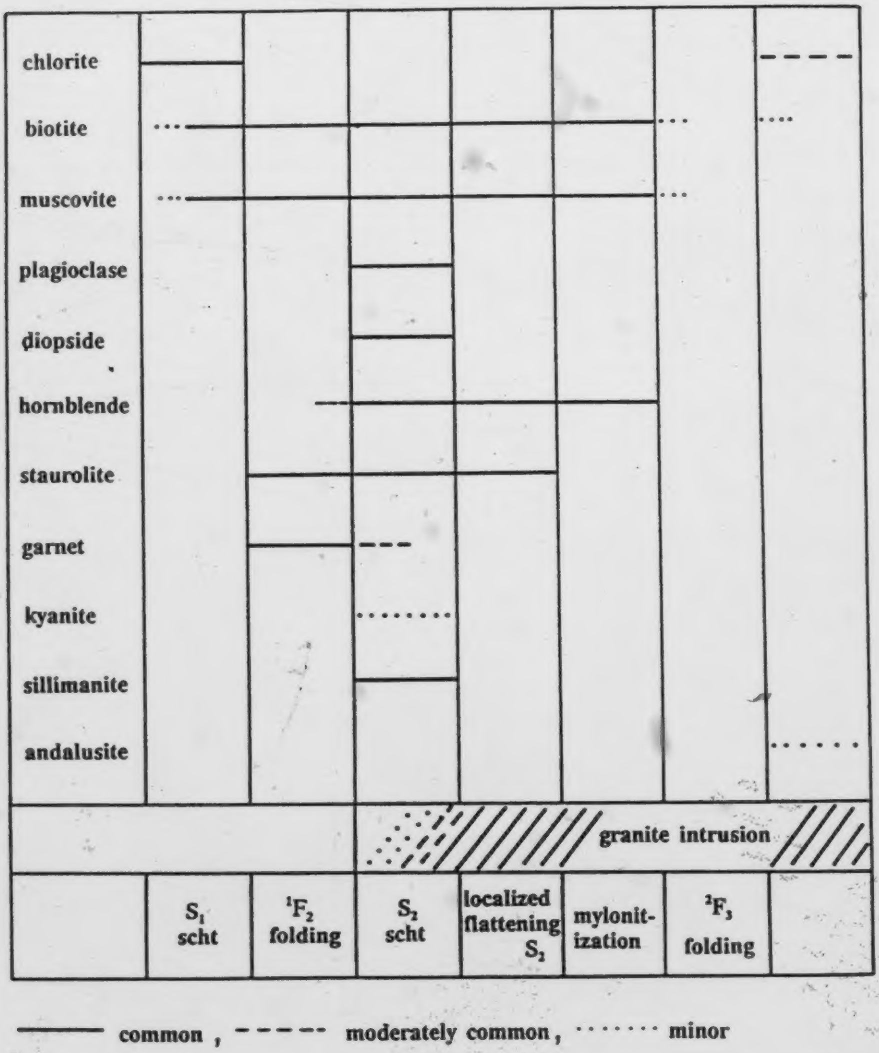
chlorite
biotite
muscovite
plagioclase
diopside
hornblende
staurolite
garnet
kyanite
sillimanite
andalusite
granite intrusion
S1 scht
1F2 folding
S2 scht
localized flattening S2
mylonitization
2F3 folding
common , moderately common , minor

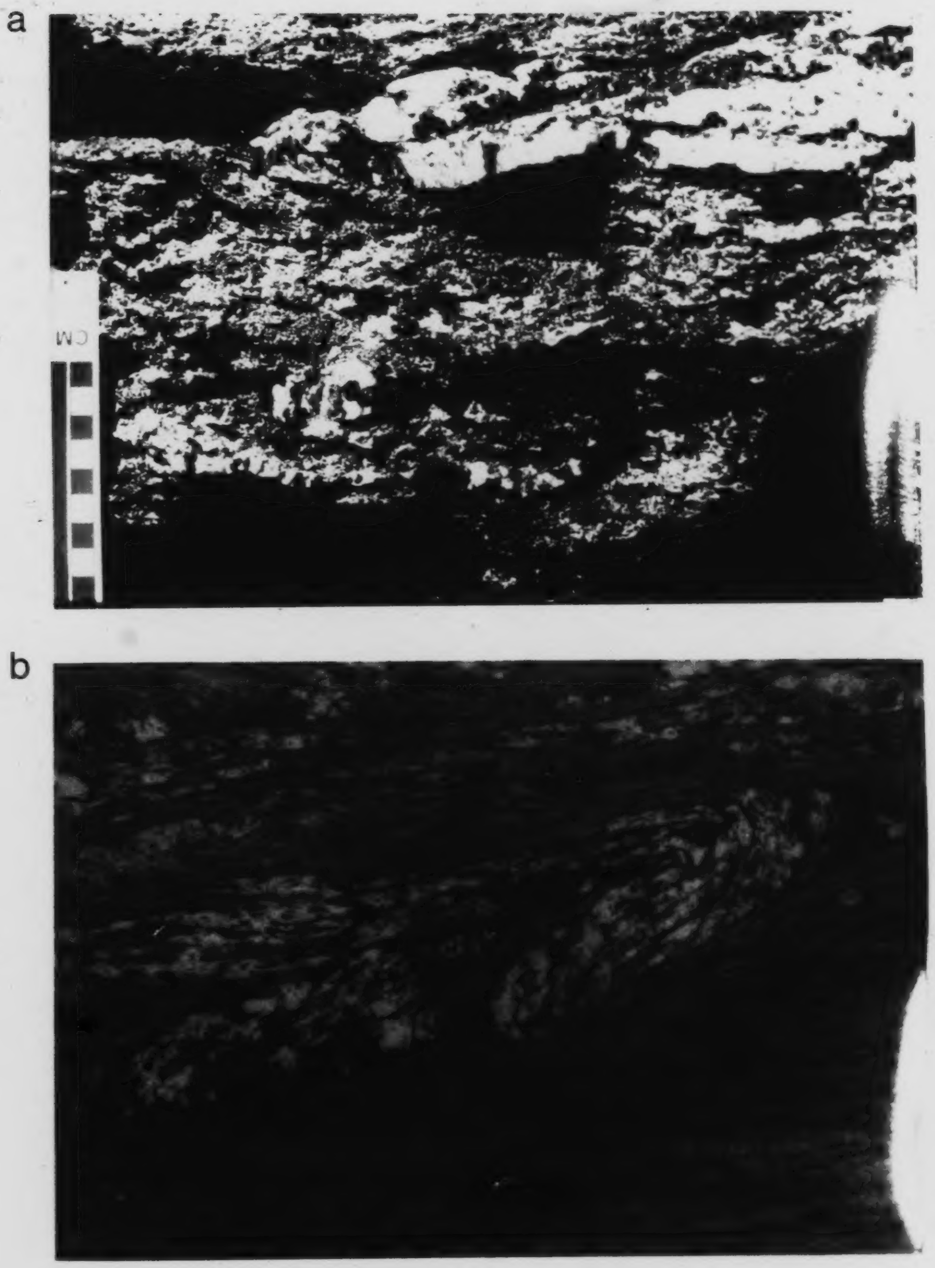

Plate 3.1: (a) Early isoclinal fold defined by quartz vein with axial surface parallel to the schistosity, refolded by northwesterly trending upright crenulations. View looking north-northwest. (b) Early $^1F_2$ crenulation of a mica-defined schistosity in staurolite-garnet schist with axial planes parallel to the pervasive matrix foliation (S_2). Field of view is 4 mm.

(S_2) which is defined by muscovite, biotite and flattened quartz and plagioclase. Sparse data suggest that $^1F_2$ hinges are subhorizontal and have north-northwest trends. S_2 schistosity is axial planar to $^1F_2$ and parallel to compositional layering (interpreted to be transposed bedding). Because S_1 and $^1F_2$ are preserved only locally, the schistosity measured in outcrop in the schist complex is interpreted to be S_2 (see section 3.2.3). Locally, non-foliated granite forms sills along S_2 which are pinched-and-swelled or folded and transposed along the schistosity and in some cases, traceable into large bodies which truncate S_2. These granites are interpreted to have intruded syn- to post-S_2 development (Plate 3.2).

S_2 is deformed by open to tight folds ($^2F_3$) with northwest-trending hinges and axial surfaces that are upright or steeply inclined towards the centre of the range (Figure 3.1; Plate 3.3). Granite dykes commonly cut, and locally are deformed by, $^2F_3$ folds (see Plates 2.1 and 2.3).

$^2F_3$ hinges typically plunge 10° to 30° northwest in the northern part of the range, 10° to 30° southeast in the south and are subhorizontal, northwest- or southeast-plunging in the central part of the range (Figure 3.2a and Map 1). Acceptions to this trend are presently locally in the schist complex (see Map 1). Minor subhorizontal folds with northeast-trending hinges are present locally but not clearly associated with the change in plunge of $^2F_3$ hinges. Therefore, the change in plunge direction is interpreted to indicate that the $^2F_3$ folds are non-cylindrical.

At several localities near the centre of the range, where the northwest-trending S_2 schistosity is vertical, asymmetric pull-aparts (i.e. boudins) in S_2-parallel quartz veins and granite sills indicate shear along the foliation (Plate 3.4). The significance of this localized shear is unclear.

3.2.2. Lineations

The mineral lineation in the schist complex is defined by elongate quartz and feldspar grains in psammitic schist and marble and locally, in post-S_2 granite at the northern end of the range. The lineation is parallel to $^2F_3$ hinges, i.e. trends northwest and plunges 10° to 30° northwest or southeast (Figure 3.2b). Rodding is well developed in quartzite and in folded, S_2-parallel quartz veins in $^2F_3$ hinges. Boudins in S_2-parallel quartz veins are locally elongate parallel to the rodding. The absence of a sillimanite-defined mineral lineation in the schist complex indicates that the northwest-trending, quartz-feldspar mineral lineation developed before sillimanite growth and hence, before the peak of regional metamorphism. Locally in calcareous

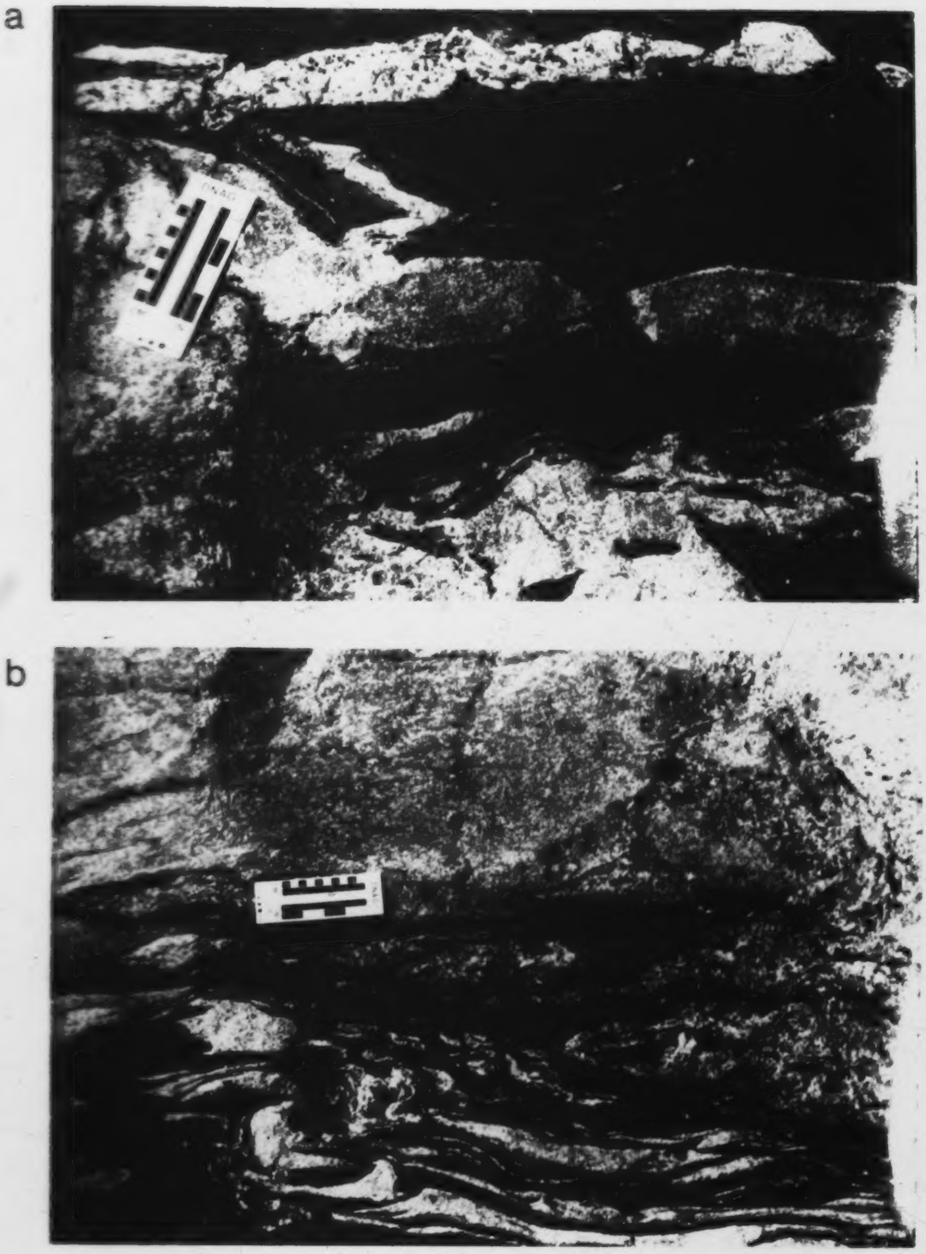

Plate 3.2: (a) and (b) Syn- to post-S_2 granite (HP87-78E) in the schist complex. Folded and boudinaged sills grade into undeformed granite which cuts S_2.

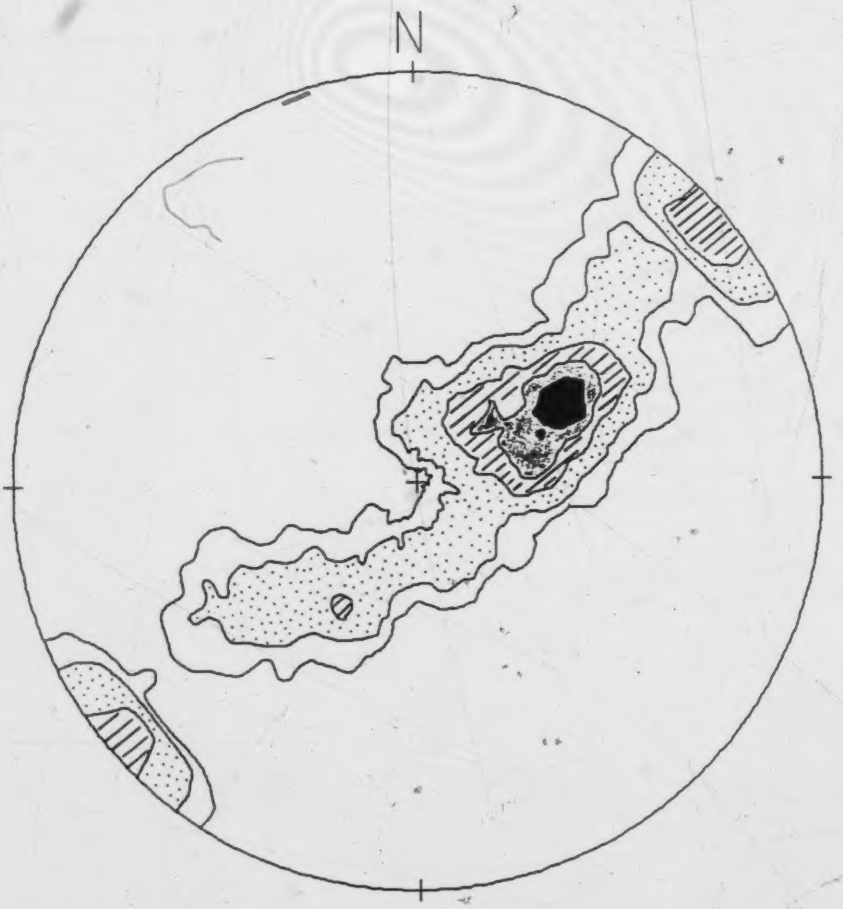

Figure 3.1: Contoured stereographic plot of poles to schistosity (S_2) in the schist complex, showing the folding about northwest trending hinges which predominates in the range. Contour densities at 1% (white), 2% (stippled), 4% (diagonal lines), 6% (shaded) and 8% (black) of 1% of the area. Number of data points = 529.

a

b

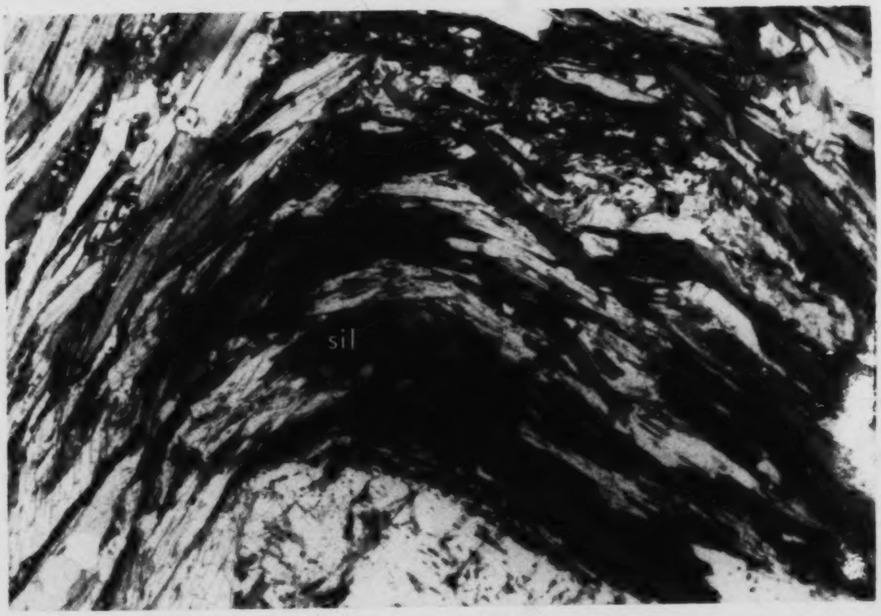

Plate 3.3: (a) Outcrop of mesoscopic, gently northwest-plunging ${}^2F_3$ folds in the schist complex viewed looking southeast. (b) Fibrolitic sillimanite folded by ${}^2F_3$ crenulations. Note the absence of new mineral growth in the axial planar region. These textures indicate that ${}^2F_3$ folds developed after the peak of metamorphism. Field of view is 4 mm.

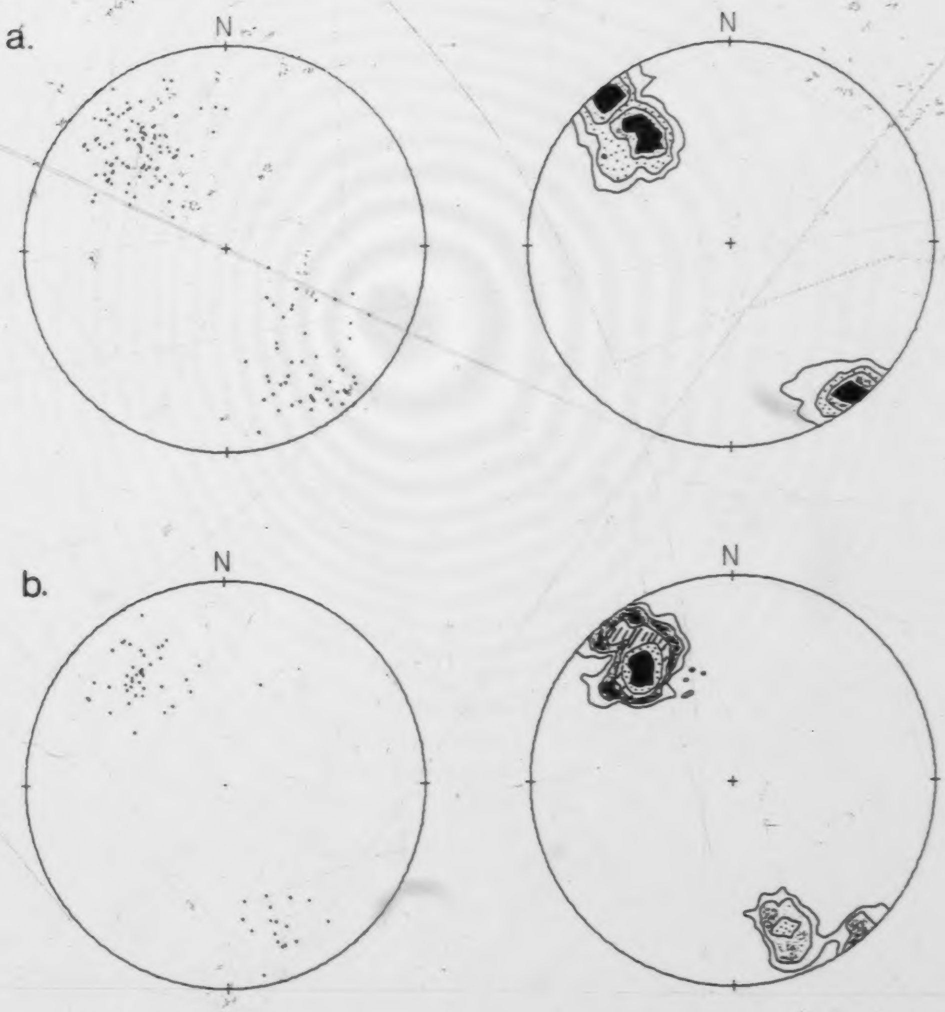

Figure 3.2: (a) Stereographic scatter and contour plots of $^2F_3$ fold hinges in the schist complex. Contours at 4% (white), 7% (stippled), 10% (shaded) and 13% (black) per 1% of the area. Number of data points = 192. (b) Stereographic scatter and contour plots of mineral stretching lineations and quartz rodding in the schist complex. Contour densities at 4% (white), 6% (shaded), 10% (diagonal lines), 15% (stippled) and 22% (black) per 1% of the area. Number of data points = 68

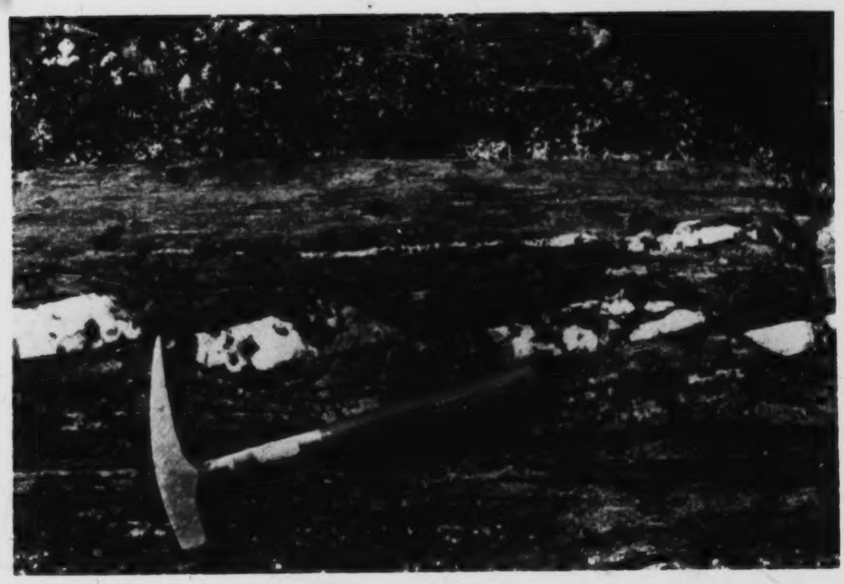

Plate 3.4: Boundinaged and extended quartz vein which is parallel to the northwest-striking, subvertical schistosity in schist complex. View looking down on traces of subvertical schistosity surfaces.

psammitic schist, hornblende and minor garnet have nucleated on plagioclase grains which define the lineation. Hornblende and garnet have also grown parallel to the lineation both on the ends of plagioclase grains (Plate 3.5) and in the matrix. This texture indicates that some of the lineation formed during regional metamorphism or that mimetic hornblende and garnet growth took place along a pre-existing, plagioclase-defined lineation. In addition, a north-trending horizontal hornblende-defined lineation is developed in schist at one locality. This anomalous mineral lineation may be relict, because ${}^1F_2$ hinges have a similar orientation and are syn-metamorphic (see below). Alternatively, it may be cogenetic with the quartz-feldspar lineation. The quartz-feldspar lineation in the schist complex is interpreted to be a stretching lineation which developed before or during regional metamorphism, but before metamorphic peak. Ubiquitous cross or "a-c" joints associated with ${}^2F_3$ folds (which postdate the peak of metamorphism - see below) record continued northwest-directed extension (Figure 3.3).

3.2.3. Microstructures and Porphyroblast-Matrix Relations

S_1 schistosity and ${}^1F_2$ folds are well preserved in thin section, but were not detected in outcrop, in the staurolite-garnet zone in the schist complex (see Plate 3.1b). Subidioblastic plagioclase porphyroblasts in the middle to upper staurolite-garnet zone have grown along S_2, and locally contain S_i trails defined by a fine-grained opaque mineral (graphite?) that are parallel to S_2. Similarly, subidioblastic biotite porphyroblasts locally contain a graphite(?)-defined S_i continuous with S_e. Subidioblastic ilmenite porphyroblasts commonly grow along, but locally cut, S_2. Garnet is subidioblastic to xenoblastic, locally skeletal and locally contains straight to sigmoidal inclusion trails defined mainly by quartz and ilmenite and less commonly by muscovite, biotite, tourmaline, apatite and chlorite. Straight S_i traces in garnet are oriented at a high angle to the matrix foliation, whereas axial surface traces of sigmoidal trails are commonly parallel to the matrix foliation (Plate 3.6a). Sigmoidal S_i traces are locally continuous with matrix foliation. Idioblastic to xenoblastic, locally skeletal staurolite includes idioblastic to subidioblastic garnet porphyroblasts, quartz, ilmenite, biotite, tourmaline and fine-grained, opaque material (graphite?). Commonly, staurolite has preferentially grown in muscovite-rich folia. Garnet partly enclosed by staurolite is typically idioblastic where in contact with staurolite and subidioblastic where in contact with the matrix. Straight S_i traces at a high angle to S_e and sigmoidal S_i traces at moderate to low angles to S_e are present in staurolite. Most

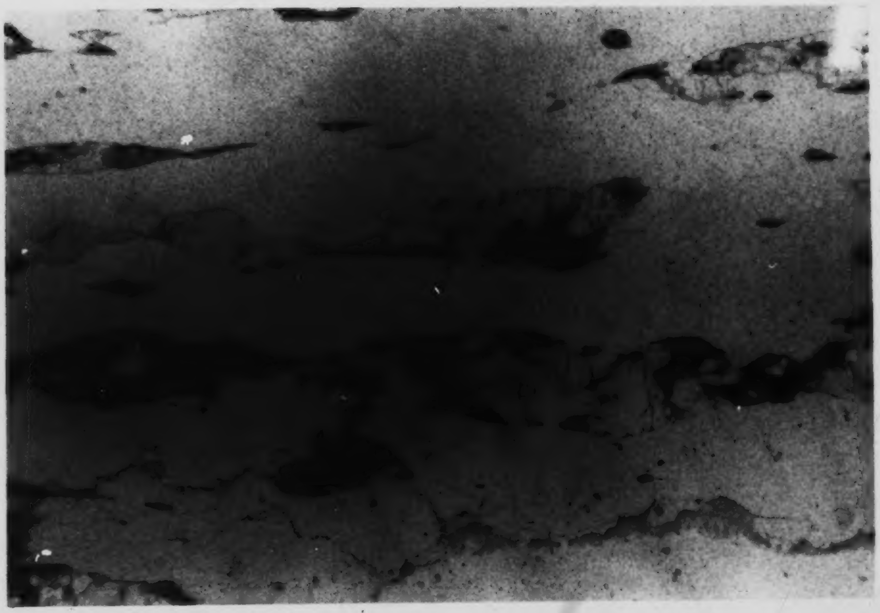

Plate 3.5: Hornblende and garnet that have nucleated on plagioclase grains define a stretching lineation in calcareous psammite of the schist complex. Hornblende and garnet have grown along the lineation direction, indicating that metamorphism accompanied or postdated the development of the plagioclase lineation. Field of view is 4 mm.

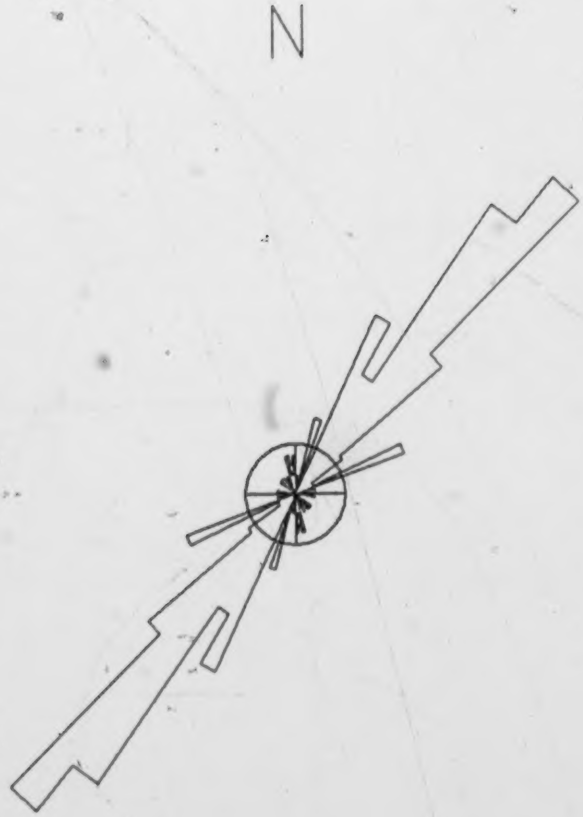

Figure 3.3: Rose diagram of joint surface strikes (at 5° intervals) in the schist complex. Joints are steeply dipping (≥ 80°) to vertical, have a strong preferred northeast-southwest strike and are interpreted to be cross (i.e. A-C) joints associated with ${}^2F_3$ folds. Number of data points = 93

a

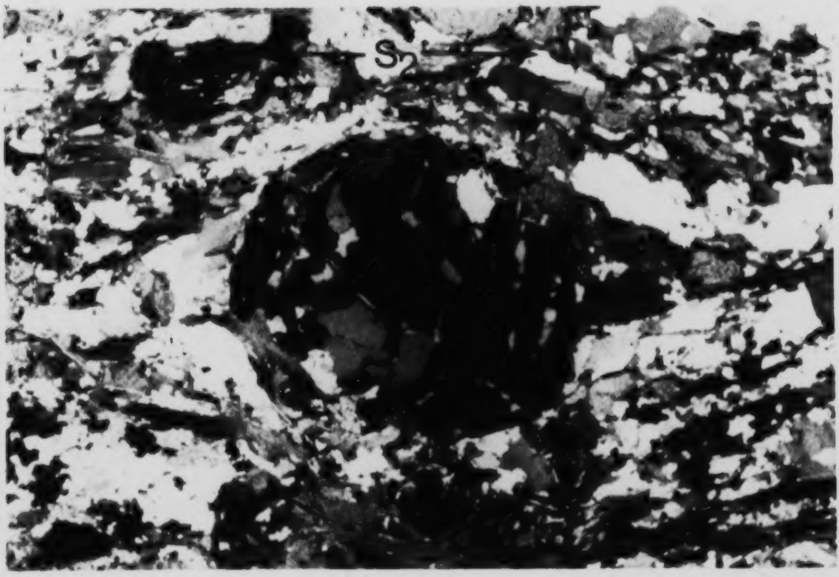

Plate 3.6:(a) Large garnet with stage 2 S_i in staurolite-garnet schist indicating that garnet growth was syntectonic with respect to ${}^1F_2$ folds and S_2 development. Garnet is 4 mm in diameter.

commonly staurolite overgrows matrix schistosity (Plate 3.6b). Sigmoidal S_i traces in garnet and staurolite are interpreted to be equivalent to $^1F_2$ crenulations observed in the matrix (cf. Bell, 1985; Bell and Rubenach, 1983).

According to the stages of crenulation cleavage development defined by Bell and Rubenach (1983), garnet has overgrown stage 1 to 3 and staurolite has overgrown stages 1 to 6, although most commonly stages 4 to 6. Determination of the relative timing of staurolite and garnet growth is hindered by the paucity of inclusion trails in garnet coexisting with staurolite that contains well developed inclusion trails and by retrogression. Only one sample contains both garnet and staurolite with well developed S_i. In this case, garnet contains stage 1-2 inclusion trails and staurolite contains stage 6 inclusion trails. On the basis of idioblastic to subidioblastic garnet inclusions in staurolite and the apparently stable coexistence of garnet and staurolite throughout the staurolite-garnet zone, staurolite and garnet growth are inferred to have been contemporaneous. However, at least locally, inclusion trail patterns indicate that staurolite growth outlasted garnet growth.

Porphyroblast-matrix relations reflect flattening normal to S_2 pre-, syn- and post-staurolite growth. Pre-staurolite flattening is indicated by straight S_i traces in staurolite continuous with the matrix foliation (S_2) that does not bend around staurolite. Syn- to post- staurolite flattening is reflected by: (1) boudinaged staurolite with chlorite-filled fractures normal to S_2 in thin section (see Plate 2.4), (2) staurolite porphyroblasts with a graphite-defined S_i in their rims, that bends around inclusion-free or inclusion-poor cores and is continuous with the matrix schistosity (S_2) that wraps around staurolite (Plate 3.7), and (3) staurolite porphyroblasts with straight, ilmenite-defined inclusion trails that are parallel to S_2 and bend as they passes from porphyroblast to matrix; S_2 wraps around staurolite (Plate 3.8).

Idioblastic garnet partly included in staurolite and truncated by the matrix indicates that porphyroblast dissolution (cf. Bell and Rubenach, 1983) has occurred along S_2. Dissolution may have occurred during S_2 formation or subsequent flattening. The latter is most probable, considering evidence cited above for flattening syn- to post-staurolite growth.

In summary, porphyroblast-matrix relations in staurolite-garnet schist indicate that metamorphism began during S_1 and $^1F_2$ folding of S_1 and continued after S_2 development. Garnet, staurolite, biotite, plagioclase and ilmenite growth was contemporaneous. Staurolite outlasted garnet growth locally. Flattening associated with the formation of S_2 locally postdated staurolite, garnet and ilmenite growth.

Porphyroblast inclusion trails are uncommon in the biotite-garnet±kyanite zone.

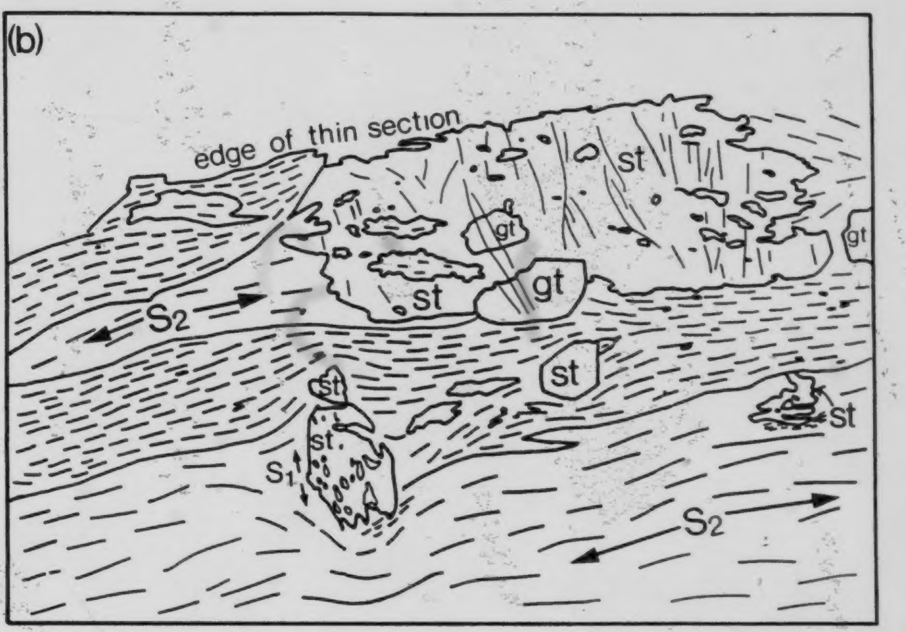

Plate 3.6 (continued):(b) Tracing from composite photograph of a staurolite-garnet schist. Staurolite porphyroblasts contain straight, quartz- and ilmenite-defined inclusion trails. The staurolite porphyroblast near the bottom of diagram contains a stage 1 inclusion trails (terminology of Bell and Rubenach, 1983). The large staurolite porphyroblast at the top includes garnet and contains stage 6 inclusion trails continuous with S_2. These textures indicate that staurolite growth postdates S_1, began prior to, and continued after, S_2 development, and was rapid relative to deformation rate. The small, skeletal staurolite at the right of the diagram has grown preferentially along narrow, muscovite-rich zones. Garnet lacks inclusion trails in this sample. Closely spaced dashed lines depict muscovite- and biotite-rich zones. Widely spaced dashed lines depict quartz- and feldspar-rich zones with minor muscovite and biotite. Field of view is 1.15 cm.

Plate 3.7: Inclusion trails in staurolite rim bend around its core, and S_e wraps around the porphyroblast recording rim growth during and after flattening. Field of view is 4 mm.

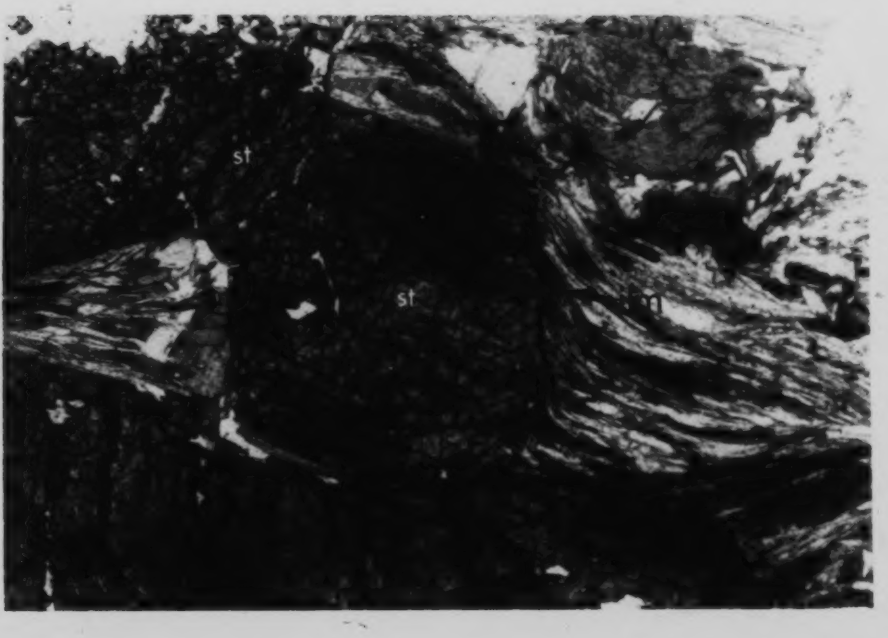

Plate 3.8; Ilmenite grains bend as they pass from staurolite porphyroblast to matrix and the matrix foliation wraps around staurolite indicating that flattening perpendicular to S_2 followed staurolite growth. Field of view is 4 mm.

Plagioclase locally exhibits weak, quartz-defined, straight S_i parallel to S_e. S_e is defined by micas, elongate quartz subgrains and ilmenite. Plagioclase porphyroblasts also grow across the schistosity. Garnet locally exhibits inclusion-free or -poor, subidioblastic to idioblastic cores surrounded by subidioblastic to xenoblastic, relatively inclusion-rich rims (Plate 3.9). In one sample, the idioblastic garnet core contains straight S_i defined by fine-grained ilmenite (?) oriented at a high angle to the matrix foliation. Fine-grained ilmenite and rutile inclusions and coarse biotite, plagioclase and quartz inclusions are concentrated in the rim near the discontinuity, suggesting that the garnet rim overgrew an already coarsened matrix. This may reflect two-stage garnet growth or a change in garnet-producing reaction (see Chapters 4 and 5). Biotite partly replaces garnet along the discontinuity and grain boundaries. Kyanite porphyroblasts include quartz and opaque minerals and have grown along the schistosity and locally, across it. In some sections, kyanite overprints or is rimmed by muscovite. It is unclear whether kyanite is relict or prograde after muscovite. Minor fibrolite overprints plagioclase, biotite and muscovite in kyanite-garnet schist.

$^1F_2$ folds were not observed in the biotite-garnet±kyanite zone. However, minor straight S_i traces at a high angle to S_e are present in garnet cores, recording the presence of a pre-existing schistosity. In addition, the transition from staurolite-garnet zone to biotite-garnet±kyanite zone is well exposed, and no structural discontinuity or change in fabric orientation was observed. Therefore, schistosity in the biotite-garnet±kyanite zone is interpreted to be S_2. Microstructures indicate that plagioclase and kyanite and probably garnet rims, postdate matrix schistosity.

Crenulations of S_1 are not observed in thin section in the sillimanite-orthoclase-muscovite zone although $^1F_2$ folds are preserved locally in outcrop (see Plate 3.1a). Sillimanite has grown along and across S_2 indicating that regional metamorphism outlasted S_2 development (Plate 3.10). Breakdown of muscovite, quartz and plagioclase to orthoclase and sillimanite (commonly fibrolite), is reflected by (a) wormy intergrowth between muscovite, quartz and orthoclase, (b) sillimanite overprinting muscovite, biotite, plagioclase and quartz and (c) development of xenoblastic to subidioblastic, orthoclase porphyroblasts (Plate 3.11). Xenoblastic to subidioblastic garnet porphyroblasts include quartz, micas and ilmenite. Inclusion trails are uncommon in garnet and absent in other porphyroblasts. Locally, subidioblastic garnet is elongate parallel to S_2 and contains biotite inclusions with (001) cleavage parallel to biotite defining S_2. (Plate 3.12). This indicates that garnet growth in this zone postdates S_2.

Sillimanite is folded by upright $^2F_3$ crenulations and shows undulose extinction

Plate 3.9: Garnet with idioblastic, inclusion-poor core rimmed by xenoblastic, relatively inclusion-rich rim in pelitic schist of the biotite-garnet ± kyanite zone which likely reflects two stage garnet growth. Field of view is 4 mm.

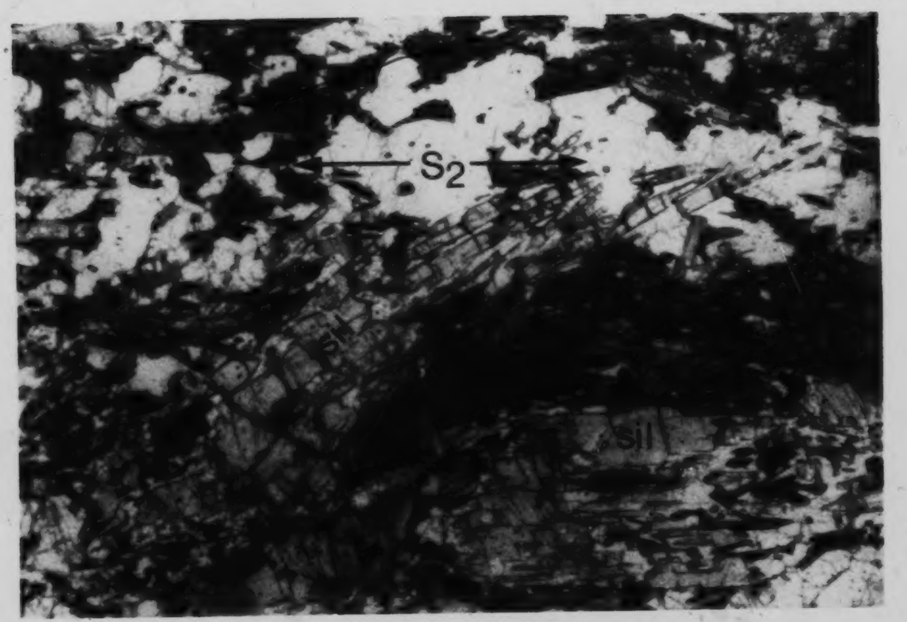

Plate 3.10: Coarse sillimanite has grown across and along S_2 foliation indicating that metamorphism outlasted deformation in the sillimanite-orthoclase-muscovite zone. Field of view is 4 mm.

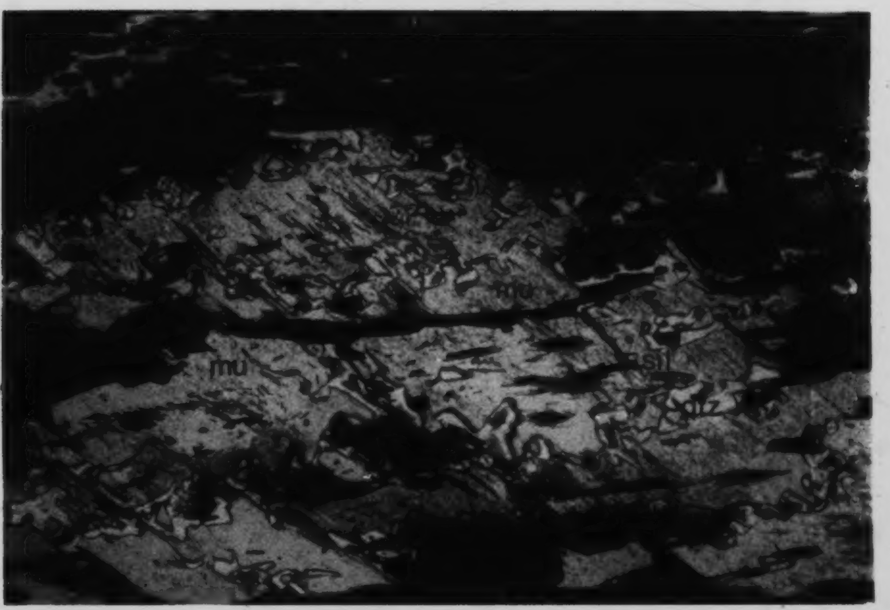

Plate 3.11: Arrested muscovite-out reaction texture in sillimanite-garnet schist. Wormy intergrowth of muscovite and quartz is overprinted by fibrolitic sillimanite (acicular masses) and elsewhere in the thin section, overprints plagioclase. Orthoclase porphyroblasts (not shown) are developed also in this section. Field of view is 4 mm.

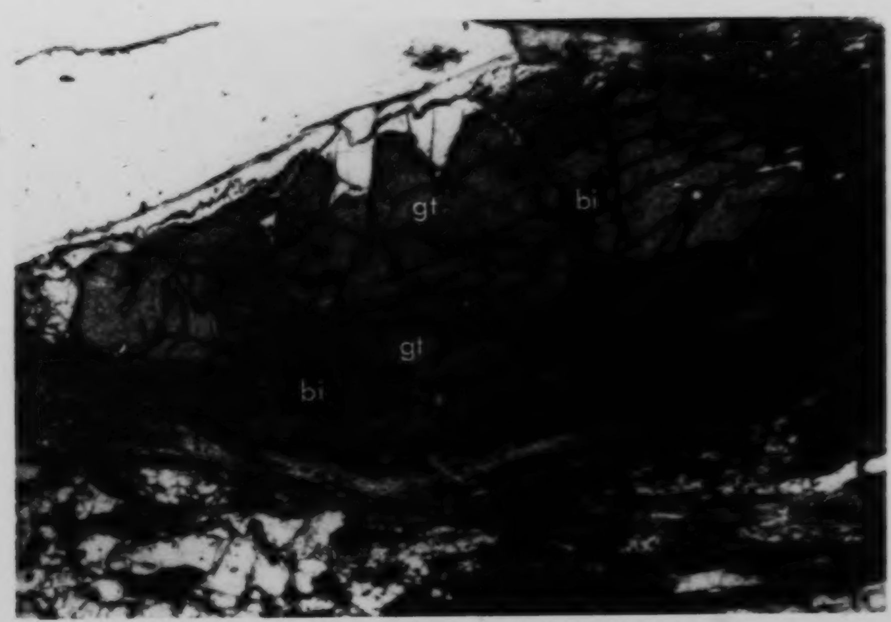

Plate 3.12: Subidioblastic garnet is elongated parallel to S_2 and contains biotite inclusions with (001) cleavage parallel to that in biotite in the matrix. This texture suggests that garnet overgrew S_2. Field of view is 4 mm.

5

around the fold hinges, precluding the possibility of post-${}^2F_3$ mimetic sillimanite growth. There is little or no new mineral growth along ${}^2F_3$ axial surfaces (see Plate 3.3.b). ${}^2F_3$ folds therefore, developed after the peak of regional metamorphism.

3.3. STRUCTURE OF LOW-GRADE ROCKS

3.3.1. Macroscopic Planar Fabrics and Folds

In the low-grade rocks overlying the mylonite zone, bedding is folded into tight-to-isoclinal folds with northwest-trending subhorizontal hinges and an axial planar, generally 10° to 40° southwest-dipping, phyllitic cleavage. In an arenaceous bed at one locality, a shallowly dipping, axial planar cleavage associated with recumbent folds is cut by a more steeply dipping cleavage associated with steeply inclined folds of the same layer (Plate 3.13a) recording progressive refolding of bedding and cleavage. Locally, folds with upright to moderately southwest-dipping (30° - 40°) axial surfaces and north-northwest-trending hinges deform the phyllitic cleavage. Kinks and chevron folds with gently southwest-plunging hinges also deform cleavage (Plate 3.13b).

Because the low-grade rocks and schist complex are separated by the mylonite zone, direct correlation of fold phases across this discontinuity is uncertain. Folds with north-northwest-trending hinges in the low-grade rocks deform bedding and an early phyllitic cleavage whereas those in the schist complex (${}^2F_3$) deform S_2. Therefore, folds with north-northwest-trending hinges in the low-grade rocks can not be unequivocally correlated with those in the schist complex.

3.3.2. Microstructure

In the chlorite zone, cleavage in chloritic phyllite is defined by chlorite and white mica. Compositional layering is defined by the concentration of quartz with or without calcite and of muscovite and chlorite. It is folded into tight to isoclinal folds with axial planes parallel to cleavage in chloritic phyllite, as is observed between bedding and axial planar cleavage in outcrop. Therefore, the compositional layering observed in thin section is inferred to be transposed bedding and the cleavage is interpreted as S_1.

Cleavage and schistosity in the chlorite-biotite and biotite zones are interpreted to be S_1 and are defined by muscovite plus chlorite and/or biotite. Whether S_1 in the chlorite and biotite zones is of the same generation as S_1 in the staurolite-garnet zone

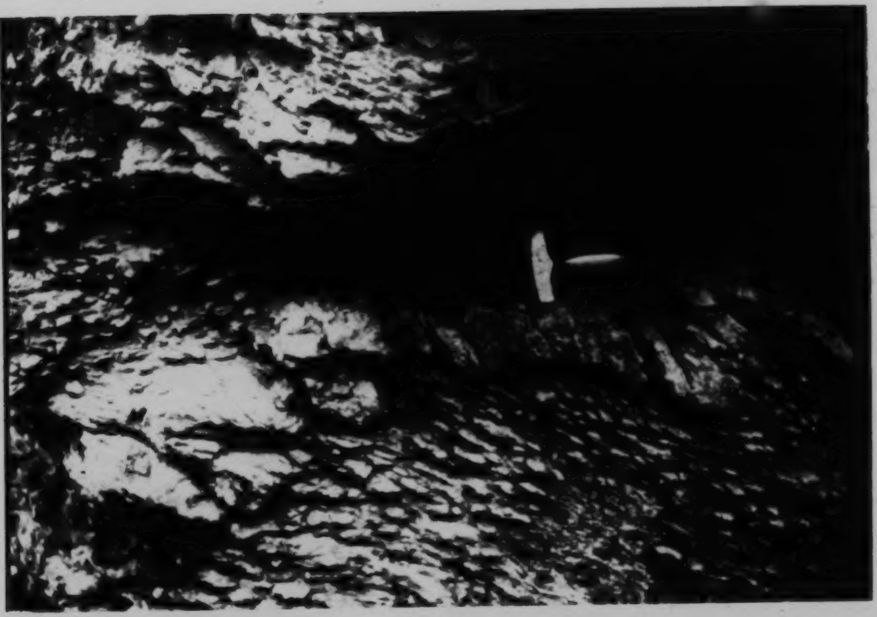

Plate 3.13: (a) Tight to isoclinal, east-verging folds with northwest-trending hinges and recumbent to subvertical axial surfaces, in psammitic bed in phyllite cut by an axial planar cleavage. Note that the gently dipping cleavage associated with the recumbent folds is cut by that of the subvertical folds. View looking southeast.

b

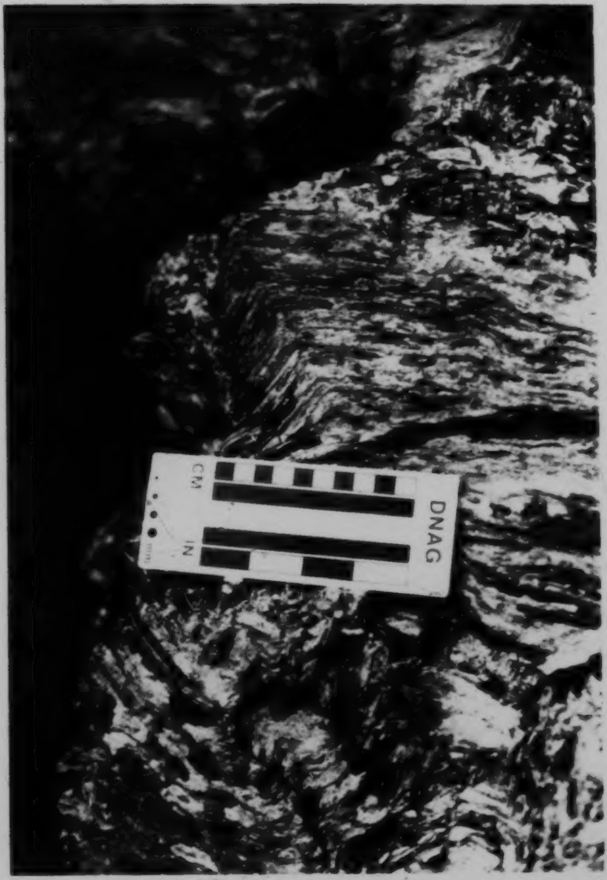

Plate 3.13 (continued): (b) Southwest-plunging kink folds in cleavage in phyllite. View looking southwest.

is unclear.

3.4. STRUCTURE AND KINEMATICS IN THE MYLONITE ZONE

In the northern part of the range, the mylonite zone lies mainly within the sillimanite-orthoclase-muscovite metamorphic zone. An abrupt grade change from amphibolite facies (sillimanite-orthoclase-muscovite zone) in the hanging wall to greenschist facies (biotite zone) in the footwall occurs across the mylonite zone. The zone is inferred to extend to the southern end of the range where exposure is poor, because an abrupt change in metamorphic grade occurs along the southwestern flank of the range. Here, phyllite and fine-grained biotite schist are juxtaposed against staurolite-garnet schist through 150 to 200 m of section. No change in foliation attitude or rock type accompanies the abrupt metamorphic transition. To the north the mylonite zone apparently pinches out; this may be real or may be an artifact of limited exposure in that part of the map area.

Macroscopic and microscopic fabric elements are described below for each rock type in the mylonite zone. The foliation in mylonite, including the C-plane in C-S mylonite, strikes northwest and dips moderately (ca. 30°) to steeply (ca. 60°) southwest. It is parallel to S_2 in the schist complex and to cleavage in the low-grade rocks (see Map 1).

3.4.1. Folds, Planar Fabrics and Microstructures

(i) Granitic Protomylonite to Mylonite

C-S fabric is nearly ubiquitous in granitic mylonite, from outcrop to thin section scale (Plate 3.14). S-planes are defined by muscovite and/or biotite, by quartz subgrains and by feldspar (plagioclase and orthoclase or microcline) σ-type porphyroclast systems. The spacing of S-surfaces is governed by the size of feldspar porphyroclasts. C-surfaces are parallel to the foliation in surrounding mylonitic schist and are defined by quartz subgrains and strongly recrystallized biotite and muscovite.

In all samples, quartz is strongly recrystallized and has lobate subgrain boundaries. Feldspar porphyroclasts with undulose extinction are abundant and locally, contain lobate subgrains. Recrystallized feldspar or quartz is common in the "tail" region of feldspar porphyroclasts. Fractures are uncommon in feldspar but where developed they are restricted to the grain, are typically wedge-shaped, narrowing towards the centre of the grain, and are occupied by quartz and/or micas.

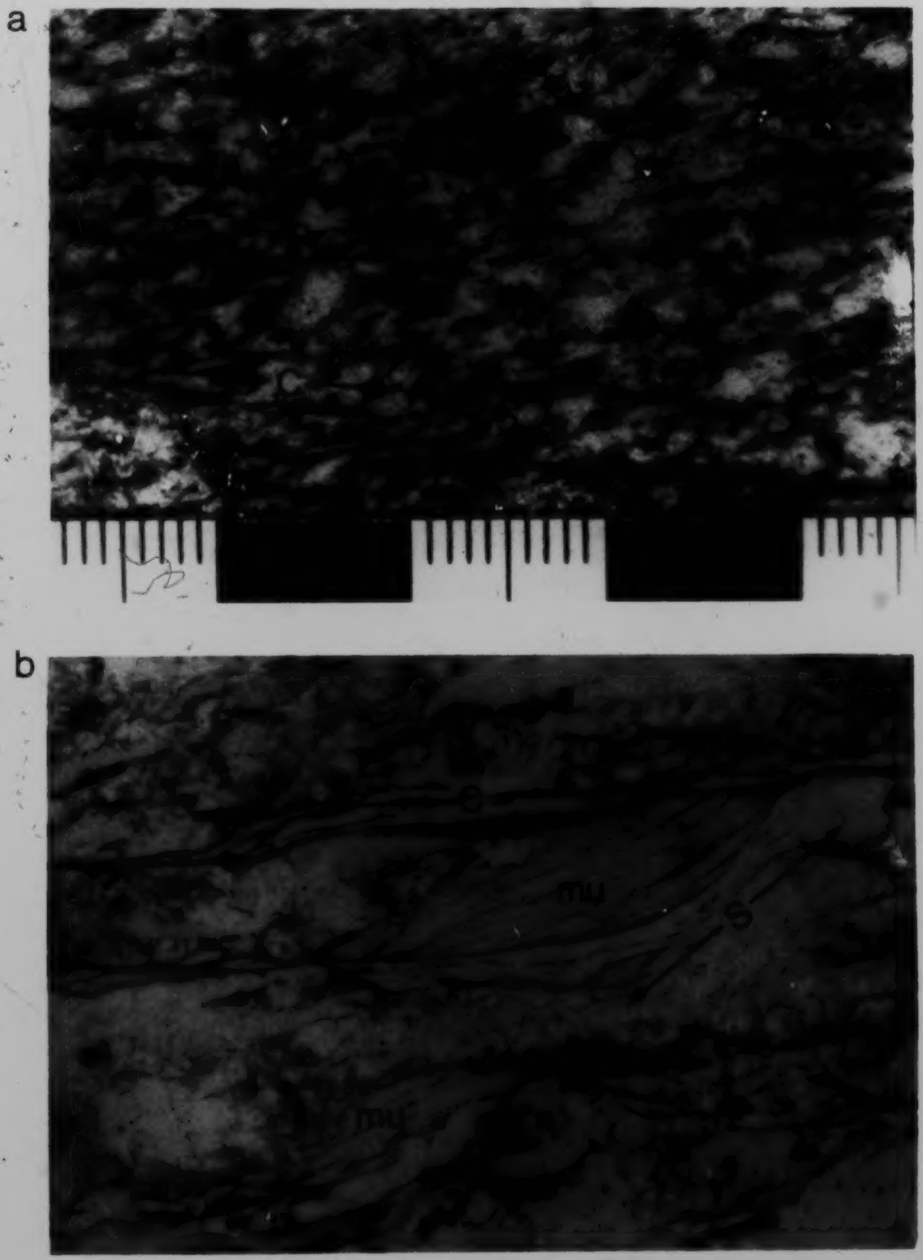

Plate 3.14: (a) C-S fabric in hand sample of granite mylonite. Surface cut parallel to the lineation and perpendicular to the foliation. Fine graduations on scale bar are 1 mm (b) C-S fabric in thin section. Note muscovite "fish". Field of view is 2 mm.

Partial replacement of orthoclase by quartz and strain-related myrmekite along S-planes is common (Plate 3.15). These textures are characteristic of mylonitization at or above the brittle-ductile transition at epidote-amphibolite facies conditions or greater (Simpson, 1985; Simpson and Wintsch, 1989). Plastic deformation in quartz requires temperatures of at least 300°C (Sibson, 1977).

On the basis of textural observations, Gapais (1989) found that pervasive grain scale shear bands (C-S fabric) are characteristic of syntectonic granites deformed during substantial and rapid cooling, that is, granites with a retrograde thermal history and strain which begins to accumulate above the brittle-ductile transition. Therefore, pervasive C-S fabric in granitic mylonite in the Horseranch Range suggests that the granites are syn-kinematic and cooled rapidly following emplacement.

Gapais (1989) observed a rapid decrease of the relict feldspar fraction in granite mylonite above the brittle-ductile transition. As microtextures indicate an overall ductile behaviour for feldspar, the abundance of relict feldspar in granitic mylonite in the Horseranch Range may reflect insufficient time for extensive feldspar grain size reduction due to rapid cooling below the brittle-ductile transition.

(ii) Dioritic to Gabbroic Protomylonite to Mylonite

Dioritic to gabbroic protomylonite to mylonite near the base of the mylonite zone contains partly recrystallized hornblende (locally to acicular needles) and plagioclase and recrystallized quartz. Near the top of the mylonite zone, dioritic mylonite to ultramylonite contains recrystallized quartz, fine-grained recrystallized biotite, large kinked biotite crystals and ubiquitous micro-faulting in plagioclase, reflected by the offset of albite twins (Plate 3.16). Deformation twins, kink bands and microshears are common in hornblende. Discrete ultramylonite zones, generally ≤ 2 mm across, are common. Boundaries of these ultramylonite zones are gradational to sharp. Locally, late fractures < 1 mm across and commonly filled by chlorite or carbonate cut the mylonitic fabric.

Microstructures in deformed hornblende are not well documented and factors controlling their development are poorly understood (e.g. Cumbest et al., 1989; Biermann, 1981). However, recrystallization to acicular hornblende has been reported in an amphibolite facies mylonite zone (Cumbest et al., 1989) and suggests that dioritic to gabbroic mylonites near the base of the mylonite zone may have been deformed under amphibolite facies conditions. Microtextures in nearby granitic mylonite record deformation under epidote-amphibolite facies or higher conditions (cf. Simpson, 1985).

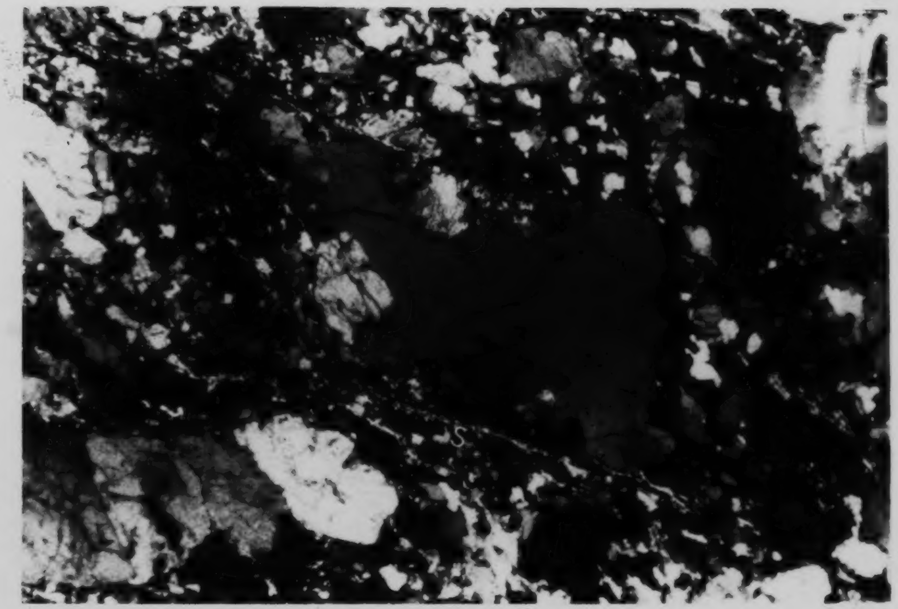

Plate 3.15: Strain-related myrmekite in orthoclase between two S-planes in C-S granite mylonite indicates that mylonitization took place at epidote-amphibolite or higher P-T conditions. Field of view is 2 mm.

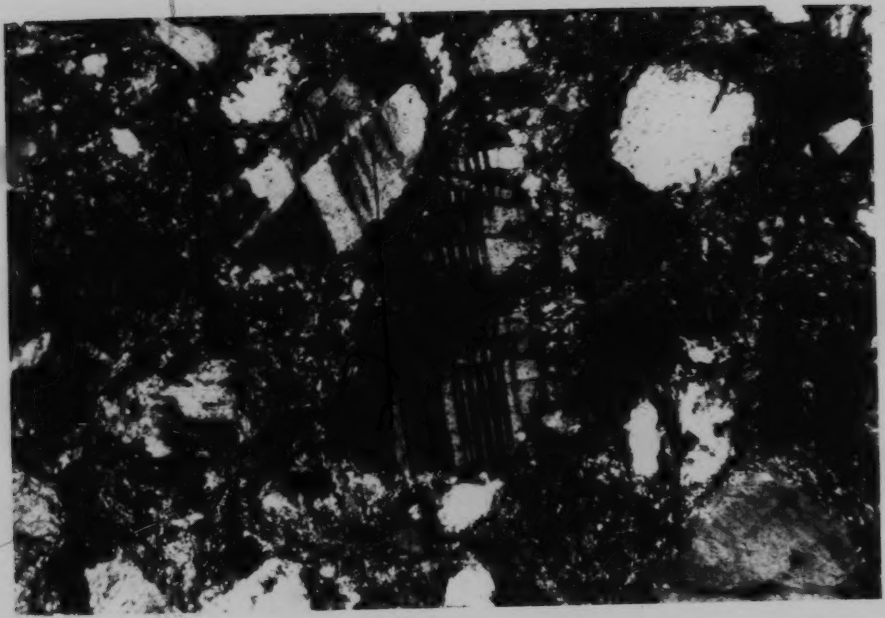

Plate 3.16: "Micro-faulting" in plagioclase in dioritic/gabbroic mylonite reflecting semibrittle deformation. Field of view is 2 mm.

Twinning in hornblende is not diagnostic of P-T conditions during deformation. It occurs in greenschist and amphibolite facies amphibolitic mylonites and in shocked amphibolite (Biermann, 1981; Cumbest et al., 1989). In granitic rocks, micro-faulting of plagioclase and discrete deformation zones are characteristic of deformation at lower greenschist facies conditions (Simpson, 1985) near, but below, the brittle-ductile transition. Therefore, dioritic to gabbroic rocks near the top of the mylonite zone may have been mylonitized under greenschist facies conditions, near or slightly below the brittle-ductile transition. However, quartz monzonite mylonite in contact with gabbroic to dioritic mylonite exhibits textures characteristic of epidote-amphibolite facies or higher conditions (cf. Simpson, 1985). This difference could reflect (1) slightly later intrusion by the dioritic to gabbroic rocks during mylonitization relative to granitic rocks (assuming intrusion of the mafic rocks during mylonitization), when conditions had dropped near or below the brittle-ductile transition, (2) overall higher competency of the mafic rocks or (3) localized brittle deformation related to the Horseranch fault (see below).

The bulk of the deformation in the dioritic and gabbroic mylonite zones is semibrittle (or semiductile) and not cataclastic and therefore, it can not be attributed to the Horseranch fault (third hypothesis). The first hypothesis is supported by the presence of numerous, dioritic and gabbroic intrusions which cut mylonitic fabrics and a dioritic dyke near the top of the mylonite zone with an incipient foliation, bent hornblende and micro-faulted plagioclase. The absence of semibrittle fabrics overprinting ductile fabrics in other mylonite may indicate that strain was localized by the time of diorite and gabbro displacement. The second hypothesis is also viable. It is probable that late intrusion and a higher overall competency of the mafic rocks contributed to the semi-brittle behaviour of these rocks.

(iii) Metacarbonate Mylonite to Ultramylonite

Foliation in metacarbonate mylonite is defined by elongate quartz grains, muscovite, biotite, hornblende and alignment of inequant plagioclase grains. Planar, 1 to 5 mm thick compositional layers are developed parallel to the foliation and reflect varying concentrations of diopside, hornblende, quartz, plagioclase, muscovite and biotite. Calcsilicate-rich layers weather resistantly relative to carbonate-rich layers and locally, the calcsilicate-rich layers are boudinaged and rotated to form σ- and δ-type porphyroclast systems with tails of the same material (Plate 3.17). Commonly, the foliation and layering are deformed into tight to isoclinal folds which are transposed along the foliation indicating progressive refolding of the mylonitic foliation.

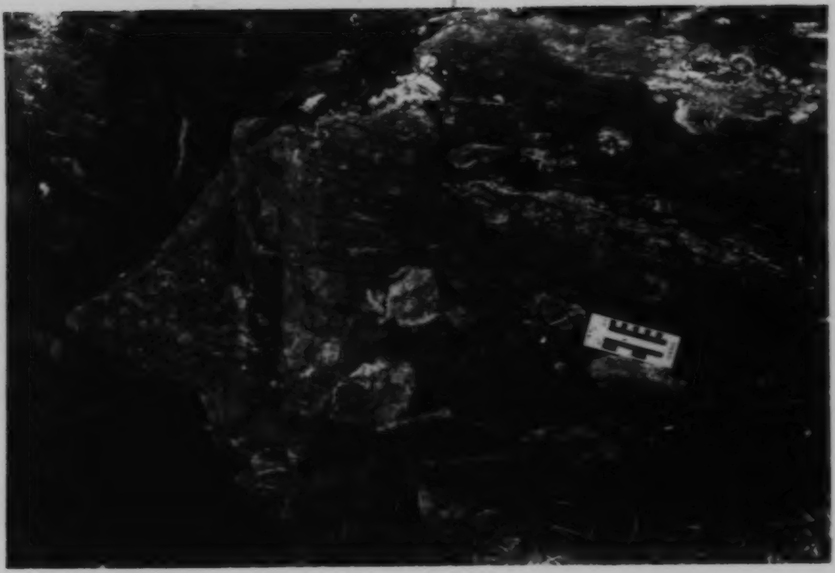

Plate 3.17: δ-type porphyroclast systems in a metacarbonate mylonite record top-to-the-northwest shear. The porphyroclasts and tails are composed of calcsilicate rock; the matrix is dominantly carbonate. View looking southwest.

Disharmonic folding is also common (Plate 3.18). Diopside shows a moderate degree of grain size reduction by fracturing, but no dynamic recrystallization. Hornblende forms rims and asymmetric tails on diopside or has grown in strain shadows (Plate 3.19). Hornblende also forms σ-type porphyroclast systems with tails of recrystallized hornblende. The absence of dynamically recrystallized diopside and presence of synkinematic hornblende indicate that mylonitization took place after diopside growth, at a temperature high enough to permit hornblende growth.

(iv) Quartzite Mylonite and Mylonitic Schist

Foliation in white quartzite mylonite is defined by fine-grained recrystallized biotite and the elongate quartz subgrains. In mylonitized schist, the schistosity is defined by biotite and muscovite with or without sillimanite. It is commonly deformed by tight to isoclinal, disharmonic folds transposed along the schistosity (Plate 3.20a) recording progressive refolding of the mylonitic schistosity. These folds are distinguished from ${}^1F_2$ folds in the schist complex because they fold sillimanite and are developed in schist interleaved with C-S granite mylonite.

Mylonitized schist locally has C-S fabrics in which muscovite (as "fish") and sillimanite are deflected into C-surfaces (Plate 3.20b). Sillimanite is not recrystallized. Biotite has grown in strain shadows of muscovite fish and forms discrete σ-type porphyroclast systems (Plate 3.21). The muscovite fish are partly replaced by quartz and fibrolite. Therefore, mylonitization took place after sillimanite growth at temperatures high enough to permit biotite and muscovite growth.

3.4.2. Lineations and Kinematic Indicators

The lineation in the mylonite zone is defined by fine rodding in quartzite and by elongate quartz, feldspar, or quartz-feldspar aggregates and the alignment of long axes of inequant feldspar grains in granitic mylonite. It lies in the motion plane (C-surface of C-S mylonite) and plunges up to 30° northwest, except near the southern limit of exposure of the mylonite zone where it is horizontal (Map 1). The lineation in mylonite is parallel to the lineation in the schist complex (Figure 3.4).

Kinematic indicators are C-S fabric in granitic mylonite and locally in schist, σ-type and δ-type porphyroclast systems in metacarbonate mylonite, quartzite mylonite, granitic mylonite and mylonitic schist, granitic pull-apart "fish" and quartz boudins derived from originally continuous veins, sills, or dykes and minor asymmetric folds. In general, asymmetric pull-aparts indicate non-coaxial deformation but do not

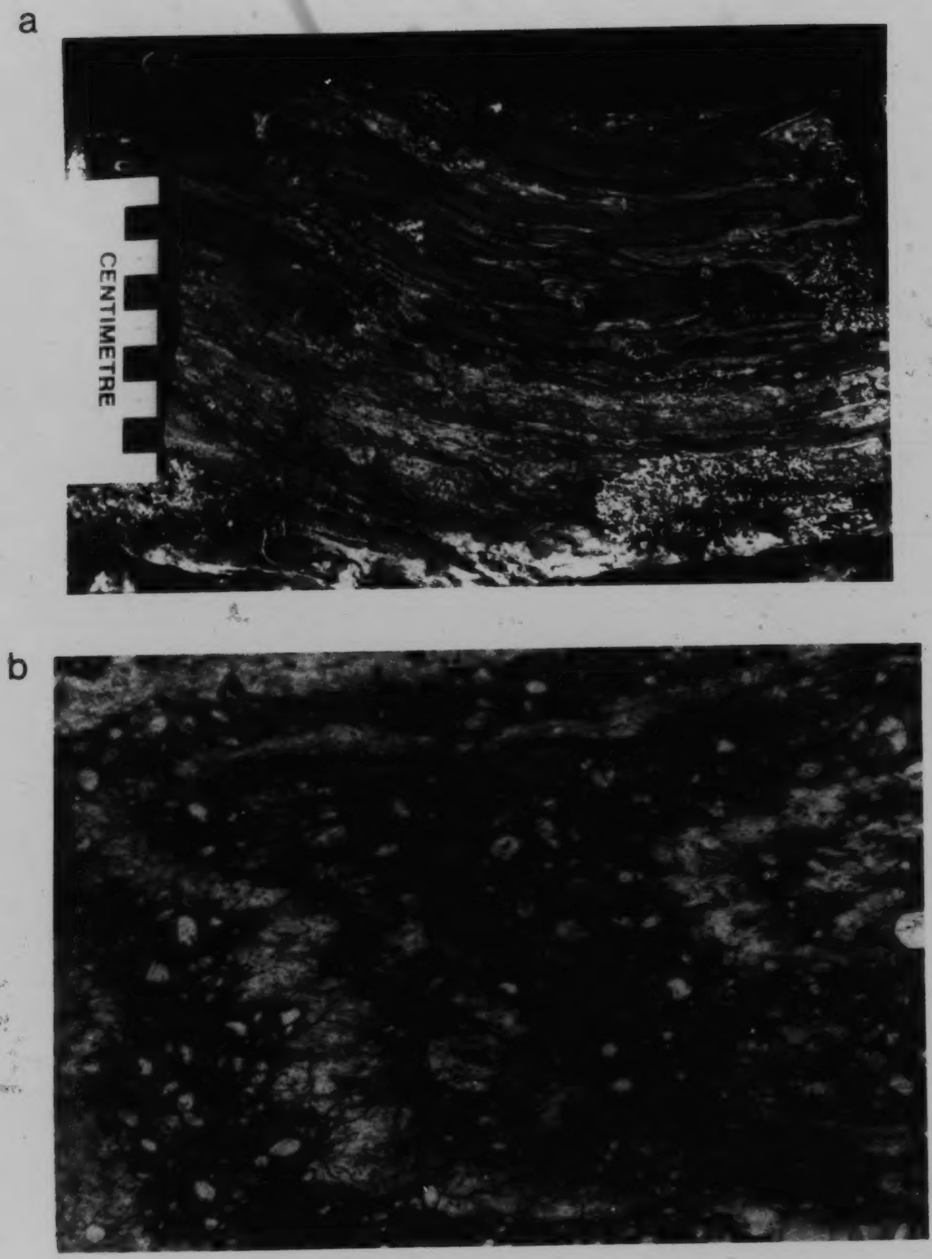

Plate 3.18:(a) Outcrop of disharmonic, transposed, tight to isoclinal folds of the mylonitic foliation in mylonitic metacarbonate. (b) Thin section of disharmonically folded compositional layering in mylonitic metacarbonate. Field of view is 4 mm.

dp
hb
dp
hb
dp
hb

Plate 3.19: Diopside porphyroclasts with hornblende rims and tails in metacarbonate mylonite. Field of view is 4 mm.

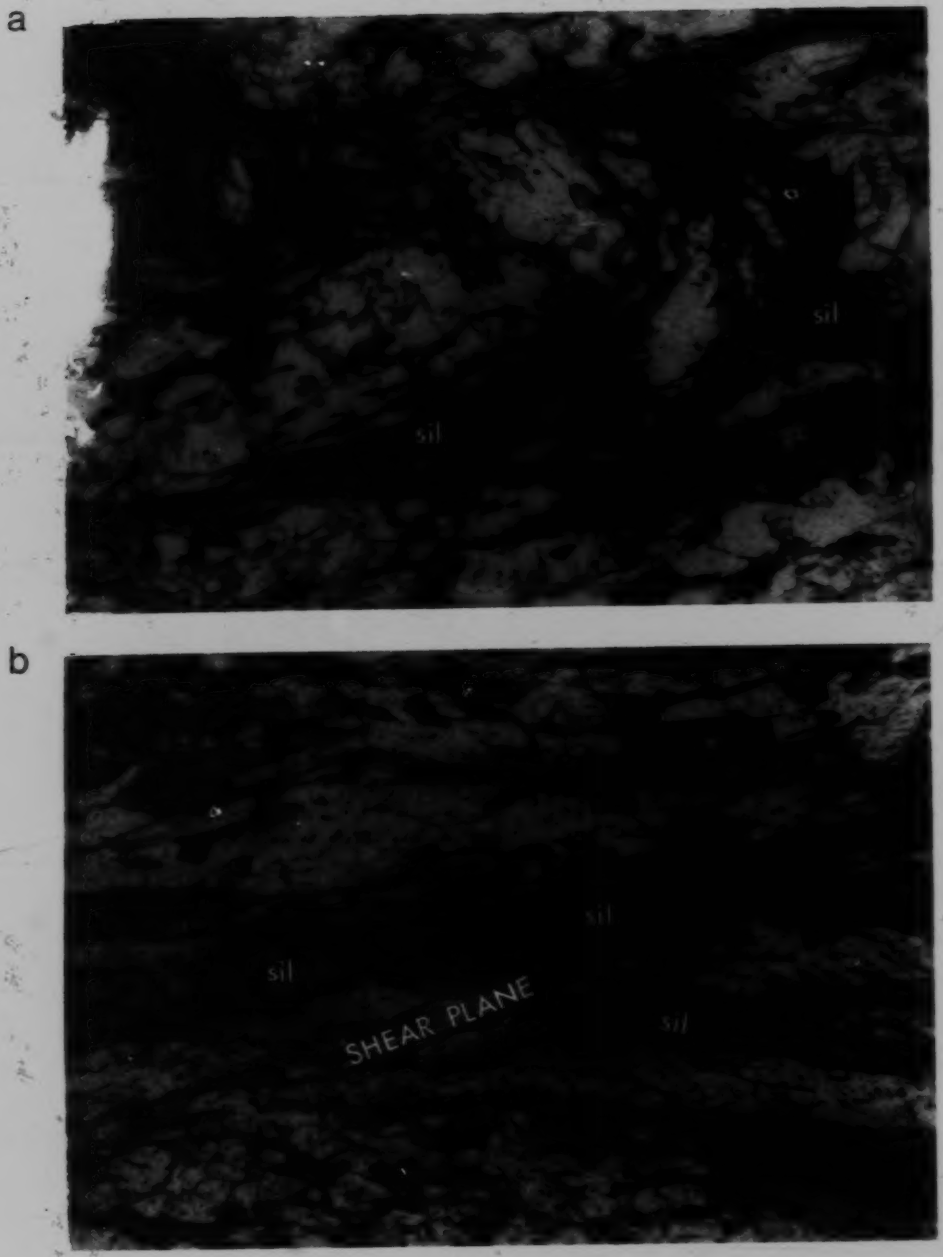
a
sil
sil
b
sil
sil
SHEAR PLANE
sil

Plate 3.20:(a) Fibrolite folded by folds related to mylonitization in mylonitic sillimanite schist. Field of view is 4 mm. (b) Coarse sillimanite deflected into shear-planes in mylonitized sillimanite schist. Note lack of retrogression. Field of view is 4 mm.

Plate 3.21: σ-type biotite porphyroclast recording dextral shear in mylonitic schist. View parallel to lineation and perpendicular to foliation. Field of view is 2 mm.

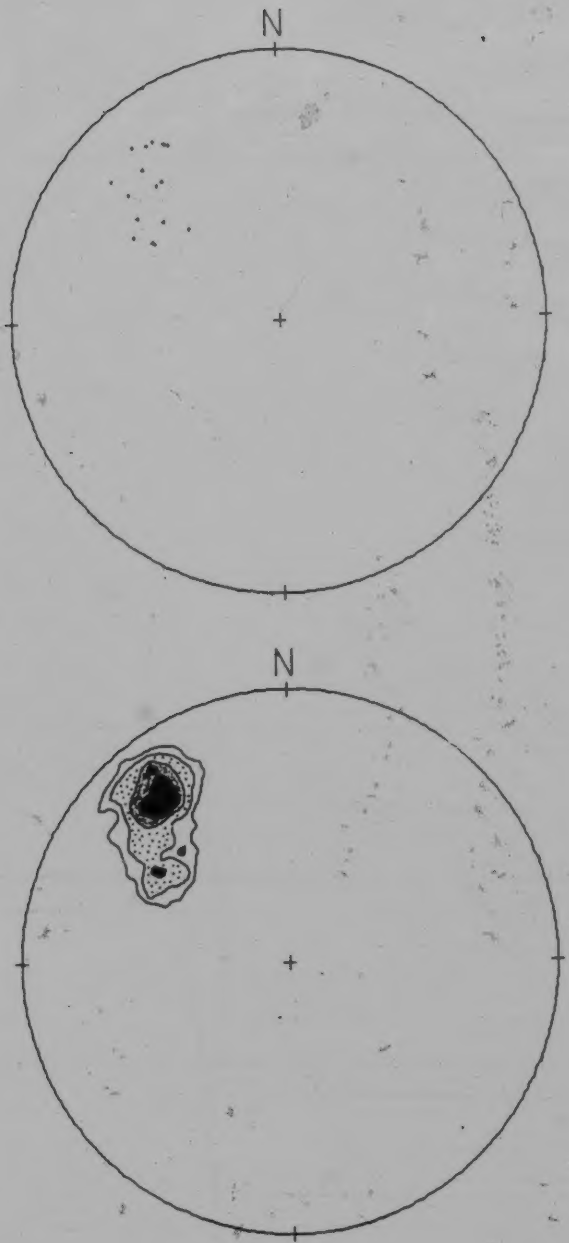

Figure 3.4: Stereographic scatter and contour plots of mineral stretching lineations and quartz rodding in mylonite. Contour densities at 8% (white), 14% (stippled), 23% (shaded) and 30% (black) per 1% of the area. Number of data points = 20.

provide unequivocal shear sense (Hanmer, 1986; Goldstein, 1988) and they are not considered here for kinematic interpretation. Hinge lines of asymmetric folds show variable orientations (Figure 3.5) and data are too few to assess their kinematic significance. Both C-S fabrics and porphyroclast systems record displacement of the upper member of the shear couple to the northwest along the lineation in its present orientation. As kinematic indicators show consistent shear sense in the plane parallel to the lineation and perpendicular to the mylonitic foliation, the lineation is interpreted to be a stretching lineation which developed during mylonitization, subparallel to the extension direction. The lineation and kinematic indicators record dextral oblique-normal strike-slip displacement, and locally near the southern limit of exposure of the mylonite zone, dextral strike-slip displacement.

3.5. BRITTLE FAULTS

The Horseranch Range lies between the Kechika and Burnt Rose dextral strike-slip faults (Figures 1.1. and 1.2). The range is bounded to the west and east by the north-striking Horseranch and Deadwood faults, respectively and by an inferred north-northeast-striking fault here referred to as the Southeastern fault, all of which are interpreted to merge with the Kechika fault (Figure 1.1 and 1.2)(Gabrielse, 1963, 1985; Plint and Erdmer, 1988, 1989a). The Horseranch and Deadwood faults cut low-grade rocks whereas the Southeastern fault is inferred to juxtapose the schist complex and the low-grade phyllite.

The only brittle fault exposed is the Horseranch fault in the northwest part of the map area. It is marked by an approximately 100 metre-wide zone of brecciated and chloritized rock and vertical north-south and east-west-striking fractures and juxtaposes dolomitic limestone against chloritic phyllite and pyroxenitic diorite. Minor polymictic conglomerate containing locally derived, subangular to subrounded clasts of chloritic phyllite, siltstone, granitic rock and quartz is exposed in the southwestern part of the map area along the trace of the fault (Gabrielse, 1963).

There are little data regarding the dip of these faults and the nature, timing and amount of displacement along them. Gabrielse (1985) interpreted the Horseranch and Deadwood faults as steep, brittle faults with up to 2 km of normal displacement along them. Interpretation of these faults as steep normal faults is compatible with their relative orientation to the northwest-trending Kechika and Burnt Rose strike-slip faults, as theory and clay- and sand-box experiments predict steep, north-striking normal faults in panels between steep, northwest-striking strike-slip faults (e.g. Wilcox

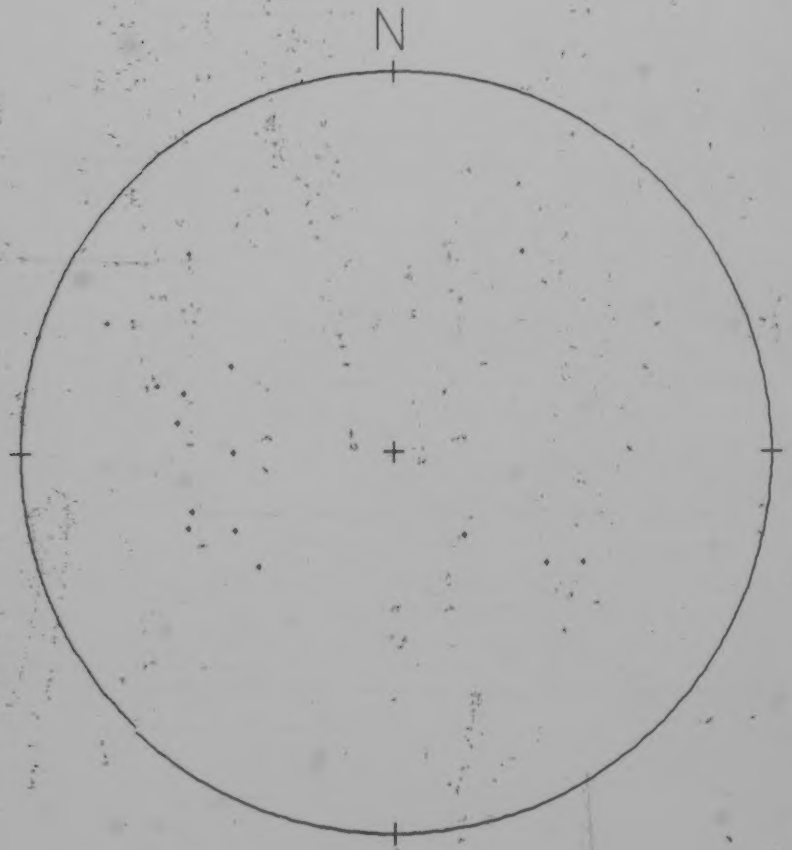

Figure 3.5: Stereographic scatter plot of fold hinges in the mylonite zone. Number of data points = 16

and others, 1973; Naylor et al., 1986).

3.6. RELATIVE TIMING OF METAMORPHISM AND DEFORMATION

The relative timing of porphyroblast growth, folding and schistosity development, mylonitization and granite intrusion is summarized in Table 3.1. The timing of fold and cleavage development in the low-grade rocks relative to structures in the schist complex is unclear and is not included in Table 3.1.

Staurolite and garnet growth were mainly synchronous; staurolite growth locally outlasted garnet growth. Chlorite, muscovite and biotite nucleated early during metamorphism. Chlorite growth ceased with the development of staurolite. Muscovite growth ceased with the onset of sillimanite and orthoclase, whereas biotite growth continued throughout metamorphism. Preservation of several crenulation stages in porphyroblasts of the same mineral in a single thin section indicates that syndeformational porphyroblast growth was rapid relative to strain rate.

Microstructures indicate that: (1) regional metamorphism was synchronous with ${}^1F_2$ folding, outlasted S_2 formation and was followed by ${}^2F_3$ folding, (2) quartz-feldspar mineral lineation in the schist complex developed before or during, but prior to the peak of, regional metamorphism and (3) mylonite developed after the peak of regional metamorphism under epidote-amphibolite to amphibolite facies conditions at temperature of at least 300°C.

The staurolite-in and sillimanite-orthoclase-in isograds form a northwest-trending elliptical map pattern in the northern part of the range (Figure 2.2). This pattern is consistent with post-metamorphic ${}^2F_3$ folding. The three-dimensional definition of isograds is hindered by lack of exposure. Although the folding of isograds about ${}^2F_3$ folds can not be demonstrated directly in the field, ${}^2F_3$ folds in sillimanite schist postdate the peak of regional metamorphism in thin section. Thus, folding of isograds about ${}^2F_3$ hinges is inferred.

From the map pattern, isograds are truncated by the mylonite zone, although the lack of pelitic rock types in key areas makes this observation equivocal. However, microstructures clearly demonstrate that mylonitization postdates the peak of regional metamorphism and therefore, it is likely that the mylonite zone cuts metamorphic isograds. Mylonite is not folded around the northern part of the range, around which units of the schist complex can be traced, which indicates that mylonitization postdates ${}^2F_3$ folds. The amount of time between ${}^2F_3$ folding and mylonitization is unconstrained.

3.7. COMPARISON WITH OTHER HIGH-GRADE ANTICLINORIA IN NORTHERN BRITISH COLUMBIA

Detailed studies in the Sifton Range (Evenchick, 1985, 1988), Swannell Ranges (Chase Mountain area, Parrish, 1976, 1979; Ingenika Range, Bellefontaine, 1989, 1990) and Mount MacKinnon area, McLeod Lake map sheet (Struik, 1989; Deville and Struik, 1990) provide a basis for comparison with the Horseranch Range. The Chase Mountain and Mount MacKinnon areas are part of the Wolverine Complex which occupies a large area of central and north-central British Columbia (see Figure 1.1). In general, the structural and thermal histories and relative timing of deformation, metamorphism and granite intrusion are similar in the Horseranch, Swannell and Sifton Ranges and the Mount MacKinnon area. However, differences in the timing and mechanisms of uplift are evident between the northern Swannell Ranges (Chase Mountain area and Ingenika Range) and the Horseranch Range, Sifton Range and Mount MacKinnon area. Uplift is discussed in Chapter 7.

3.7.1. Regional Metamorphism and Folds

Regional metamorphism to sillimanite or kyanite grade accompanied and outlasted one or more phases of tight to isoclinal, recumbent to gently inclined, locally northeast vergent folding and was followed by upright regional-scale folding about northwest-trending hinges in the Swannell, Sifton and Horseranch ranges (Parrish, 1976, 1979; Evenchick, 1985, 1988; this study). In the Swannell and Sifton ranges, the early syn-metamorphic folds are interpreted to have formed during mid-Cretaceous or older crustal shortening and thickening (Parrish, 1976, 1979; Evenchick, 1988). As geochronometric evidence constrains syn-metamorphic $^1F_2$ folds in the Horseranch Range to late Early Cretaceous or older (Chapter 6), the folds are interpreted also to have developed during crustal shortening and thickening. No upright folding is observed in the Mount MacKinnon area but northwest-striking thrust faults which bring Triassic to Middle Devonian limestone over Upper Proterozoic and Lower Paleozoic rocks are interpreted to be related to Cretaceous and older crustal shortening and thickening (Struik, 1989; Deville and Struik, 1990). Two phases of early folding, distinguishable in kyanite-staurolite grade rocks near Chase Mountain are more difficult to separate at sillimanite-staurolite grade (Parrish, 1976). Higher regional metamorphic grade in the Horseranch and Sifton Ranges (sillimanite-K-feldspar) and Mount MacKinnon area (sillimanite grade) may account for the identification of only one early, syn-metamorphic fold phase in these areas (this study; Evenchick, 1985, 1988). Alternatively, only one fold phase may have developed.

Post-metamorphic, upright to steeply inclined, locally doubly plunging folds with northwest-trending hinges are characteristic of exposures of high-grade Upper Proterozoic strata in northern British Columbia (Parrish, 1976; Gabrielse, 1975; Evenchick, 1985, 1988; Bellefontaine, 1989, 1990; this study). Most of these antiforms are interpreted to have developed during pre-mid Cretaceous, northeast-directed shortening (Gabrielse, personal communication 1990). In the Ingenika Range of the northern Swannell Ranges, regional post-metamorphic folding about a northwest-trending hinge (Swannell Antiform) is interpreted to have developed during west-directed, Middle Jurassic (?) thrusting of the Ingenika Group (Omineca Belt) over accreted rocks of the Quesnellia (Intermontane Belt) along the Swannell fault (Bellefontaine, 1989, 1990). Regional antiforms with northwest-trending hinges in the Chase Mountain area, Horseranch Range and Sifton Range are not genetically related to thrust faults.

3.7.2. Granitic Basement and Intrusive Rocks

Precambrian granitic basement rock (1.85 Ga) has been reported in the Sifton Range (Evenchick, 1988). Granitic rocks (granodiorite to quartz monzonite) syn-tectonic with respect to early, syn-metamorphic folds, are present in the Swannell Ranges (Parrish, 1976). On the basis of Late Cretaceous and older metamorphic cooling ages for the host schists in the Swannell Range (Parrish, 1976), the granites are older than Late Cretaceous. This is consistent with structural and geochronometric data from this study which indicate that syn- to post-$^1F_2$ granite is late Early Cretaceous (Chapter 6). Eocene granitic rocks cut schists and locally caused contact metamorphism (andalusite grade) in the Swannell and Sifton Ranges (Parrish, 1976; Evenchick, 1988). Similar contact metamorphic effects near an undated, post-S_2 granite are observed at the north end of the Horseranch Range. Leucogranites, similar to Eocene granite in the Chase Mountain area, cut syn-metamorphic tight folds in the Mount MacKinnon area (Deville and Struik, 1990). In the Swannell Range, as in the Horseranch Range (section 2.6.3.), granites are abundant in the highest (sillimanite-staurolite) grade rocks and minor in lower grade rocks.

Post-tectonic lamprophyre dykes with Eocene cooling ages are documented only in the Sifton Range (Evenchick, 1985, 1988). Post-tectonic ultramafic to mafic intrusions with Eocene cooling ages (see Chapter 7) are documented only in the Horseranch Range.

3.8. SUMMARY

Five deformation phases have been identified: (1) S_1 development, (2) ${}^1F_2$ folding of S_1 to form S_2, (3) ${}^2F_3$ folding of S_2 about northwest-trending hinges, (4) mylonitization along the western side of the range and (5) brittle faulting along the Horseranch fault. The relative timing of fold and schistosity development, regional metamorphism and granite intrusion in the Horseranch Range is similar to that reported for the Swannell Ranges, Sifton Range and Mount MacKinnon area. P-T and geochronometric data are required to synthesize these deformation phases into a model consistent with regional tectonic constraints. A tectonic synthesis is presented in Chapter 7.

CHAPTER 4

MINERAL CHEMISTRY AND EQUILIBRIUM ASSESSMENT

4.1. INTRODUCTION

Mineral chemistry of major mineral phases and an assessment of equilibrium amongst coexisting phases are presented here and subsequently used in conjunction with porphyroblast-matrix relations (Chapter 3) to constrain the P-T conditions of metamorphism (Chapter 5).

4.2. MINERAL CHEMISTRY

Electron microprobe analyses of major mineral phases in pelite were carried out to assess chemical equilibrium and for geothermobarometry (Table 4.1). Data are presented in Tables 4.2 through 4.8. Statistical error at the 95% confidence level is ± 1% for major elements and ± 10% for minor elements. Values below instrument detection limit are reported as zero. Analytical operating conditions are given in Appendix 2.

4.2.1. Muscovite

Muscovite was analysed in pelitic schist in the staurolite-garnet, biotite-garnet ± kyanite and sillimanite-orthoclase-muscovite zones. Muscovite is unzoned and homogeneous on the thin section scale in all samples.

Muscovite compositions are typical of staurolite and sillimanite zone pelites (Figure 4.1). Muscovite shows minor Tschermak substitution ((Mg, $Fe^{2+})^{vi}$ for Al^{vi}), moderate to minor paragonite substitution (Na^+ for K^+) (Table 4.2, Figure 4.2) and approaches ideal muscovite with increasing metamorphic grade (cf. Miyashiro, 1975).

Muscovite composition is partly a function of bulk rock composition (cf. Guidotti, 1973; Guidotti and Sassi, 1976). In the three-component system Al-K-Na, a three-phase limiting assemblage (i.e. number of phases = number of components) of muscovite-plagioclase-Al_2SiO_5 polymorph is required to eliminate bulk compositional effects. Despite the absence of the required limiting assemblage in pelite in this study, there is an increase in Ti^{4+} and decrease in Na/(Na+K) with increasing metamorphic grade, as is commonly observed in Barrovian metamorphic terranes (Table 4.2). Increasing Al^{iv} and (Mg + Fe^{tot}) and decreasing Si and Al^{vi} in muscovite with

Table 4.1: Mineral phases analysed by microprobe. "X" = analysed phases. "--" = phases not analysed. Blanks = absent or undetected phases.

SAMPLE	gt	mu	bi	st	Ksp	pl	sil	ky	and	ilm	rtl
HP151									X		
HP171	X	X	X	X	--	X	--	--	--		--
HP272	X	X	X	X	--	X	--	--	--	X	--
HP297	X	X	X	X	--	X	--	--	--		--
HP255	X	X	X	--	--	X	--	--	--	X	X
HP308	X	X	X	--	--	X	--	--	--	X	--
HP324	X		X	--	--	X	--	X	--	X	--
HP325	X	X	X	--		X		--	--	X	--
HP5	X	X	X	--		X		--	--		--
HP65	X		X	--	X		X	--	--		--

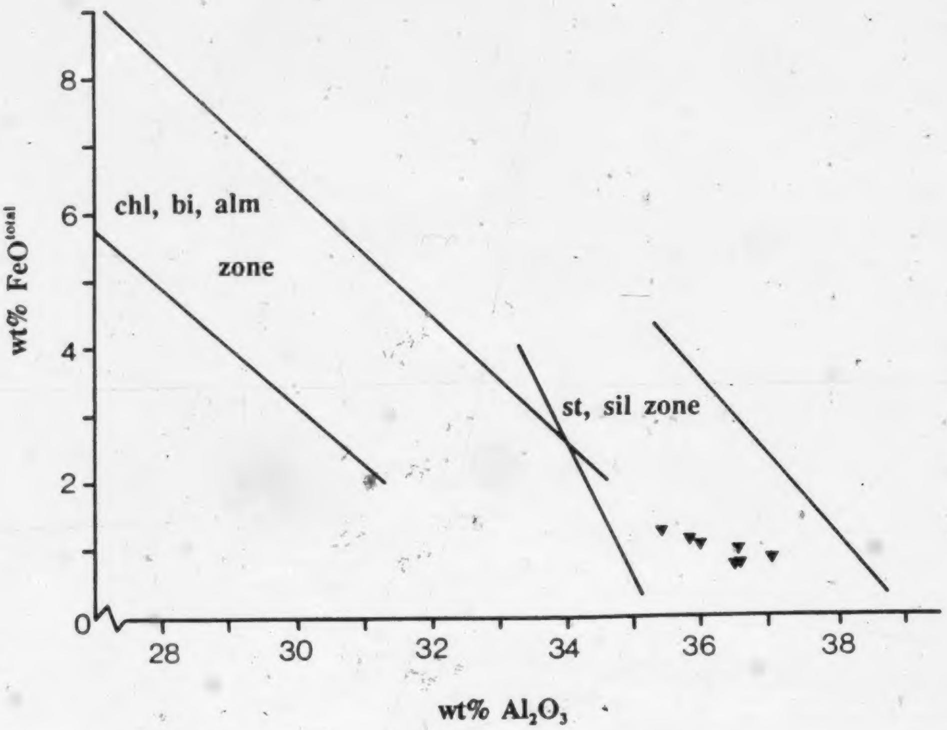

Figure 4.1: Plot of FeO^{total} versus Al_2O_3 in muscovite. Fields delineated by Miyashiro (1973). Muscovite compositions in the study area are typical of regional staurolite and sillimanite zones.

Table 4.2.: Average muscovite microprobe analyses. n = number of analyses. All Fe as Fe^{2+}. Samples are arranged in order of increasing metamorphic grade. Sample numbers are abbreviated. Metamorphic mineral zone for each sample is indicated.

	HP171	HP171	HP272	HP272	HP297	HP255
	rim	core	rim	core	core	rim
	st-gt	st-gt	st-gt	st-gt	st-gt	bi-gt-ky
SiO_2	46.40	47.15	45.41	46.53	46.11	46.41
TiO_2	0.40	0.39	0.28	0.33	0.43	0.45
Al_2O_3	36.81	36.47	36.76	36.23	36.54	37.14
FeO	0.96	1.04	0.71	0.83	1.04	0.87
MnO	0.00	0.00	0.00	0.00	0.00	0.00
MgO	0.47	0.67	0.45	0.62	0.56	0.58
CaO	0.03	0.02	0.03	0.01	0.00	0.02
BaO	0.25	0.24	0.25	0.19	0.32	0.15
Na_2O	1.36	1.25	1.81	1.81	1.51	1.81
K_2O	9.31	9.21	8.80	8.80	9.11	8.79
F	0.04	0.09	0.08	0.07	0.05	0.05
H_2O	3.74	3.27	5.26	4.37	4.13	3.53
	-----	-----	-----	-----	-----	-----
Total	99.77	99.80	99.84	99.79	99.80	99.80
	-----	-----	-----	-----	-----	-----
n	2	4	2	3	5	1
Si	6.009	6.159	6.005	6.142	6.090	6.071
Al^{iv}	1.901	1.841	1.945	1.858	1.910	1.929
Al^{vi}	3.802	3.773	3.832	3.778	3.778	3.796
Ti	0.040	0.038	0.028	0.033	0.043	0.044
Fe^{2+}	0.106	0.144	0.079	0.092	0.115	0.095
Mn	0.000	0.000	0.000	0.000	0.000	0.000
Mg	0.092	0.130	0.089	0.122	0.110	0.113
Ca	0.004	0.003	0.004	0.001	0.000	0.003
Ba	0.013	0.012	0.013	0.010	0.017	0.008
Na	0.347	0.317	0.468	0.463	0.387	0.459
K	1.561	1.535	1.497	1.482	1.535	1.467
O	24	24	24	24	24	24
F	0.017	0.037	0.034	0.029	0.021	0.021
OH	3.983	3.963	3.966	3.971	3.979	3.979
Mg+Fe	0.20	0.27	0.17	0.21	0.23	0.21
$\frac{Na}{(Na+K)}$	0.18	0.17	0.24	0.24	0.20	0.24
PARA	18%	17%	24%	24%	20%	24%
MUSC	82%	83%	76%	76%	80%	76%

Table 4.2. (continued): Average muscovite microprobe analyses.

	HP255	HP308	HP308	HP325	HP325	HP5
	core	rim	core	rim	core	rim
	bi-gt-ky	bi-gt-ky	si-or-mu	sil-or-mu	sil-mu-or	sil-or-mu
SiO_2	46.95	45.38	45.60	45.75	45.95	45.45
TiO_2	0.46	0.80	0.82	0.79	0.94	0.66
Al_2O_3	36.97	35.85	34.97	35.78	35.87	35.86
FeO	0.82	1.24	1.29	1.15	1.14	1.13
MnO	0.00	0.00	0.00	0.00	0.00	0.00
MgO	0.63	0.67	0.64	0.71	0.71	0.57
CaO	0.01	0.00	0.00	0.00	0.00	0.01
BaO	0.18	0.30	0.19	0.26	0.27	0.17
Na_2O	1.64	0.94	0.97	0.93	0.95	1.12
K_2O	8.84	9.82	9.92	9.98	10.08	10.01
F	0.09	0.08	0.04	0.08	0.07	0.07
H_2O	3.20	4.72	5.40	4.38	3.77	4.74
	-----	-----	-----	-----	-----	-----
Total	99.79	99.80	99.84	99.81	99.75	99.79
	-----	-----	-----	-----	-----	-----
n	3	2	2	3	3	5
Si	6.116	6.063	6.131	6.088	6.083	6.074
Al^{iv}	1.884	1.937	1.869	1.912	1.917	1.926
Al^{vi}	3.792	3.708	3.672	3.699	3.679	3.721
Ti	0.045	0.080	0.083	0.079	0.094	0.066
Fe^{2+}	0.089	0.139	0.145	0.128	0.126	0.126
Mn	0.000	0.000	0.000	0.000	0.000	0.000
Mg	0.122	0.133	0.128	0.141	0.140	0.114
Ca	0.001	0.000	0.000	0.000	0.000	0.001
Ba	0.009	0.016	0.010	0.014	0.014	0.009
Na	0.414	0.243	0.253	0.240	0.244	0.290
K	1.469	1.674	1.701	1.694	1.702	1.706
O	24	24	24	24	24	24
F	0.037	0.034	0.017	0.034	0.029	0.030
OH	3.963	3.966	3.983	3.966	3.971	3.970
Mg+Fe	0.21	0.27	0.27	0.27	0.27	0.24
$\frac{Na}{(Na+K)}$	0.22	0.13	0.13	0.12	0.13	0.15
PARA	22%	13%	13%	12%	13%	15%
MUSC	78%	87%	87%	88%	87%	85%

Table 4.2. (continued): Average muscovite microprobe analyses.

	HP5 core sil-or-mu
SiO_2	45.60
TiO_2	0.63
Al_2O_3	36.03
FeO	0.99
MnO	0.00
MgO	0.55
CaO	0.02
BaO	0.00
Na_2O	1.11
K_2O	9.97
F	0.08
H_2O	4.70

Total	99.68
	-----
n	4
Si	6.082
Al^{iv}	1.918
Al^{vi}	3.746
Ti	0.063
Fe	0.110
Mn	0.000
Mg	0.109
Ca	0.003
Ba	0.000
Na	0.287
K	1.696
O	24
F	0.034
OH	3.966
Mg+Fe	0.22
$\frac{Na}{(Na+K)}$	0.14
PARA	15%
MUSC	85%

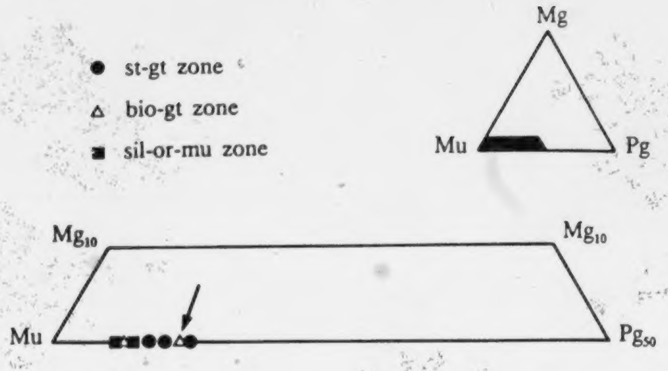

Figure 4.2: Muscovite composition as a function of muscovite (Mu), paragonite (Pg) and margarite (Mg) end-members. Inset gives location of figure in the Mu-Pg-Mg ternary system. Arrow indicates muscovite composition for a sample of biotite-garnet schist (HP88-255) that has the same composition as muscovite in staurolite-garnet schist.

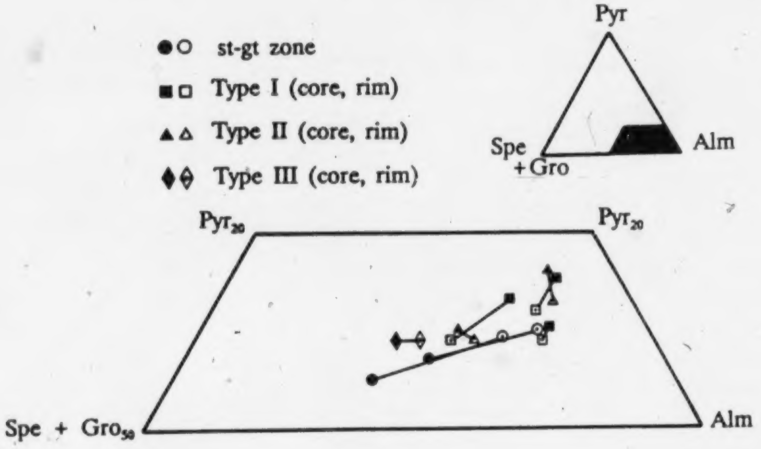

Figure 4.3: Garnet composition as a function of almandine (Alm), pyrope (Pyr), and spessartine (Spe) + grossular (Gro) end-members. Inset gives location of figure in the Pyr-Alm-Spe+Gro ternary system. Garnet rim and core compositions are joined by solid lines. Compositions for the inner zone of Type III garnet is plotted for HP88-255. Garnet from sample HP88-297 is not plotted (see text).

increasing metamorphic grade has been reported in some Barrovian metamorphic terranes (e.g. Miyashiro, 1975). A slight increase in Al^{iv} and ($Mg + Fe^{total}$) and decrease in Al^{vi} with increasing metamorphic grade is observed here. There is no consistent trend in silica.

Due to the absence of the required limiting assemblage, the effect of anorthite content in coexisting plagioclase and a_{H2O} on muscovite composition (cf. Guidotti and Sassi, 1976) cannot be assessed.

4.2.2. Plagioclase and Orthoclase

Anorthite content (An) commonly increases with metamorphic grade by the substitution Al,Ca = Si,Na (e.g. Miyashiro, 1975), but this trend is not observed here. In almost all cases, matrix plagioclase is oligoclase-andesine (An_{22} to An_{31}) in the staurolite-garnet, biotite-garnet ± kyanite and sillimanite-orthoclase-muscovite zones (Table 4.3), typical of the amphibolite facies. Zoning is uncommon. One sample of staurolite-garnet schist (HP88-272) shows a slight increase in Ca towards the rim. Albite (An_8) is present in one sample of staurolite-garnet schist (sample HP88-297, Table 4.3). No textural evidence exists to support retrograde albite after oligoclase in this sample (cf. Ashworth and Evirgen, 1984). Na-content of muscovite in sample HP88-297 is the same as other staurolite-garnet schist samples, which negates a bulk rock compositional control on plagioclase composition. Therefore, it may be that the peristerite gap affects the staurolite-garnet zone although coexisting albite and oligoclase were not detected.

Albite is also present in a sample of sillimanite-orthoclase-garnet schist where the muscovite-out reaction is well advanced and in kyanite-garnet schist. More sodic plagioclase in these samples may be due to Al consumption by the Al_2SiO_5 phase. Possible reactions are discussed in Chapter 5. Andesine is included in garnet in one sample of staurolite-garnet schist (sample HP88-177, Table 4.3) which may reflect more available Ca at the onset of garnet and plagioclase growth or consumption of plagioclase during garnet growth (cf. Spear et al., 1991). However, zoisite inclusions in garnet (see below) record the presence of Ca phases other than plagioclase, precluding the latter hypothesis (cf. Spear et al., 1991).

Orthoclase analysed in a sample of sillimanite-orthoclase-garnet schist (HP87-65, Table 4.3) contains 17% albite. This likely reflects solid solution common at temperatures above ca. 600°C (e.g. Hurlbut and Klein, 1971, p. 423). Temperature of 650°C, indicated by mineral assemblage and geothermometry calculations for this

Table 4.3.: Average plagioclase and orthoclase microprobe analyses. n = number of analyses. All Fe as Fe^{2+}. "oligo" and "andes" are oligoclase and andesine. Samples are arranged in order of increasing metamorphic grade. Sample numbers are abbreviated. Metamorphic mineral zone for each sample is indicated.

	HP171 rim st-gt	HP171 core st-gt	HP171 incl st-gt	HP272 rim st-gt	HP272 core st-gt	HP297 rim st-gt
SiO_2	61.57	61.83	56.91	61.83	61.79	65.73
Al_2O_3	23.72	23.89	27.71	24.03	23.10	21.89
FeO	0.12	0.08	0.29	0.09	0.06	0.16
MgO	0.00	0.00	0.00	0.00	0.00	0.00
CaO	5.21	5.35	9.33	5.26	4.98	1.63
BaO	0.00	0.00	0.00	0.00	0.00	0.00
Na_2O	8.79	8.71	6.42	8.59	8.81	10.66
K_2O	0.09	0.09	0.11	0.08	0.09	0.12
	-----	-----	-----	-----	-----	-----
Total	99.50	99.95	100.77	99.88	98.83	100.19
	-----	-----	-----	-----	-----	-----
n	6	3	3	3	1	4
Si	2.747	2.745	2.539	2.744	2.771	2.882
Al	1.247	1.250	1.457	1.257	1.221	1.131
Fe	0.004	0.003	0.011	0.003	0.002	0.006
Mg	0.000	0.000	0.000	0.000	0.000	0.000
Ca	0.249	0.254	0.446	0.250	0.239	0.077
Ba	0.000	0.000	0.000	0.000	0.000	0.000
Na	0.760	0.750	0.555	0.739	0.766	0.906
K	0.005	0.005	0.006	0.005	0.005	0.007
O	8	8	8	8	8	8
An	25%	25%	44%	25%	24%	8%
Ab	75%	74%	55%	74%	76%	91%
Or	0%	1%	1%	1%	1%	1%
	oligo	oligo	andes	oligo	oligo	albite

Table 4.3. (continued): Average plagioclase and orthoclase microprobe analyses.

	HP297 core st-gt	HP255 rim bi-gt±ky	HP255 core bi-gt±ky	HP255 incl bi-gt±ky	HP308 rim bi-gt±ky	HP308 core bi-gt±ky
SiO_2	66.26	60.88	60.79	60.94	62.74	62.38
Al_2O_3	21.45	24.84	24.70	24.96	23.57	23.40
FeO	0.06	0.11	0.07	0.24	0.11	0.08
MgO	0.00	0.00	0.00	0.00	0.00	0.00
CaO	1.61	6.14	6.24	6.51	4.93	4.81
BaO	0.00	0.00	0.00	0.00	0.00	0.00
Na_2O	10.59	8.21	8.10	8.06	8.82	8.87
K_2O	0.09	0.10	0.09	0.08	0.13	0.15
	-----	-----	-----	-----	-----	-----
Total	100.06	100.28	99.99	100.79	100.30	99.69
	-----	-----	-----	-----	-----	-----
n	3	6	8	2	3	2
Si	2.904	2.700	2.703	2.693	2.771	2.772
Al	1.108	1.299	1.295	1.300	1.227	1.225
Fe	0.002	0.004	0.003	0.009	0.004	0.003
Mg	0.000	0.000	0.000	0.000	0.000	0.000
Ca	0.076	0.292	0.297	0.308	0.233	0.229
Ba	0.000	0.000	0.000	0.000	0.000	0.000
Na	0.900	0.706	0.698	0.691	0.755	0.764
K	0.005	0.006	0.005	0.005	0.007	0.009
O	8	8	8	8	8	8
An	8%	29%	30%	31%	23%	23%
Ab	92%	70%	70%	69%	76%	76%
Or	1%	1%	1%	1%	1%	1%
	albite	oligo	oligo	andes	oligo	oligo

Table 4.3. (continued): Average plagioclase and orthoclase microprobe analyses.

	HP324 rim bi-gt±ky	HP324 core bi-gt±ky	HP325 rim bi-gt±ky	HP325 core bi-gt±ky	HP5 rim sil-or-mu	HP5 core sil-or-mu
SiO_2	66.38	66.00	62.45	63.19	65.63	64.87
Al_2O_3	20.81	20.80	23.45	23.10	21.53	21.68
FeO	0.11	0.06	0.07	0.06	0.19	0.12
MgO	0.00	0.00	0.00	0.00	0.00	0.00
CaO	1.76	1.73	4.69	4.75	1.99	2.27
BaO	0.00	0.00	0.00	0.00	0.00	0.00
Na_2O	10.54	10.52	9.01	9.11	10.67	10.55
K_2O	0.09	0.12	0.19	0.14	0.10	0.08
	-----	-----	-----	-----	-----	-----
Total	99.69	99.23	99.86	100.35	100.11	99.57
	-----	-----	-----	-----	-----	-----
n	8	5	6	1	7	3
Si	2.921	2.918	2.771	2.789	2.885	2.869
Al	1.079	1.084	1.226	1.201	1.115	1.130
Fe	0.004	0.002	0.003	0.002	0.007	0.004
Mg	0.000	0.000	0.000	0.000	0.000	0.000
Ca	0.083	0.082	0.223	0.225	0.094	0.108
Ba	0.000	0.000	0.000	0.000	0.000	0.000
Na	0.899	0.902	0.775	0.779	0.909	0.905
K	0.005	0.007	0.011	0.008	0.006	0.005
O	8	8	8	8	8	8
An	8%	8%	22%	22%	9%	11%
Ab	91%	91%	77%	77%	90%	89%
Or	1%	1%	1%	1%	1%	0%
	albite	albite	oligo	oligo	albite	oligo

Table 4.3. (continued): Average plagioclase and orthoclase microprobe analyses.

	HP65 rim sil-or-mu	HP65 core sil-or-mu
SiO_2	63.03	64.09
Al_2O_3	18.69	18.57
FeO	0.09	0.09
MgO	0.02	0.01
CaO	0.03	0.05
BaO	1.47	1.51
Na_2O	1.44	1.81
K_2O	14.10	13.48
	-----	-----
Total	98.87	99.61
	-----	-----
n	1	2
Si	2.963	2.979
Al	1.035	1.021
Fe	0.004	0.004
Mg	0.001	0.001
Ca	0.002	0.002
Ba	0.027	0.028
Na	0.131	0.163
K	0.845	0.799
O	8	8
An	0%	0%
Ab	13%	16%
Or	84%	81%
Cel	3%	3%

orthoclase

sample (Chapter 5) and similar orthoclase compositions in sillimanite-orthoclase ± muscovite schist reported by Evans and Guidotti (1966) and Tracy (1978) support this interpretation.

4.2.3. Garnet

Garnet was analysed in pelitic schist in the staurolite-garnet, biotite-garnet ± kyanite and sillimanite-muscovite-orthoclase zones. Garnet is dominantly an almandine-pyrope solid solution (Figure 4.3) and no chemical evidence for retrograde Fe-Mg exchange between garnet and biotite was found (Table 4.4).

Analyses of garnet chemistry are partly affected by the "cut effect". In concentrically zoned garnets, a traverse that passes close to the true garnet core will yield a profile different from that across a garnet whose core is not in the thin section. To avoid this problem, the largest garnets in each section were analysed where possible. Minor variation in chemical analyses suggest that this method is effective. In most cases where different-sized coexisting garnets were analysed, the zonation profile, but not the absolute values, are consistent.

Garnet in staurolite-garnet schist shows continuous, normal compositional zoning with high Mn and Ca cores, high Fe and Mg rims and a core-to-rim decrease in Fe/Mg ratio (Figure 4.4). This is typical of prograde (ie. increasing temperature), medium-grade almandine garnets (e.g. Hollister, 1966, 1969; Woodsworth, 1977; Tracy, 1982; Spear et al., 1991) and is further supported by inclusions of minor zoisite and chlorite, which are absent from the matrix except as clearly retrograde phases. The lack of zoning in sample HP88-297 is attributed to the "cut effect", as only one small garnet was analysed.

Garnet zoning in the biotite-garnet ± kyanite and sillimanite-orthoclase-muscovite zones differs significantly from that in the staurolite-garnet zone. Three types of zoning have been identified:

(i) Type I Garnet Zoning

Type I zoning (Figure 4.5) is observed in several samples from the biotite-garnet ± kyanite zone and sillimanite-orthoclase-muscovite zone and shows the following characteristics.

(1) Zoning is continuous.

(2) More than 80% of the zonation profile is flat or weakly oscillatory.

(3) Garnet rims (outer 0.15 to 0.20 mm) show a sharp increase in Mn coincident with

Table 4.4.: Average garnet microprobe analyses. n = number of analyses. All Fe as Fe^{2+}. "i.z." and "o.z." refer to inner and outer zones in Type III zoned garnets. Samples are arranged in order of increasing metamorphic grade. Sample numbers are abbreviated. Metamorphic mineral zones for each sample are indicated.

	HP171 rim st-gt	HP171 mid st-gt	HP171 core st-gt	HP272 rim st-gt	HP272 mid st-gt	HP272 core st-gt
SiO_2	37.31	37.17	37.37	37.41	37.30	37.11
TiO_2	0.03	0.00	0.06	0.00	0.02	0.00
Al_2O_3	20.72	20.37	20.82	20.97	21.04	20.74
FeO	34.49	34.16	30.63	35.58	32.76	32.09
MnO	3.73	3.45	3.45	2.35	6.07	6.18
MgO	2.36	2.36	1.25	2.44	1.73	1.64
CaO	1.64	2.51	6.78	1.89	2.11	2.57
	-----	-----	-----	-----	-----	-----
Total	100.28	100.02	100.36	100.64	101.03	100.33
	-----	-----	-----	-----	-----	-----
n	9	2	3	8	2	2
Si	3.013	3.013	3.004	3.007	3.000	3.006
Al^{iv}	0.000	0.000	0.000	0.000	0.000	0.000
Al^{vi}	1.972	1.946	1.972	1.986	1.994	1.980
Ti	0.002	0.000	0.004	0.000	0.001	0.000
Fe^{2+}	2.330	2.316	2.059	2.392	2.203	2.174
Mn	0.255	0.237	0.235	0.160	0.414	0.424
Mg	0.284	0.285	0.150	0.292	0.207	0.198
Ca	0.142	0.218	0.584	0.163	0.182	0.223
O	12	12	12	12	12	12
ALM	77%	76%	68%	80%	73%	72%
PYR	9%	9%	5%	10%	7%	7%
SPE	8%	8%	8%	5%	14%	14%
GRO	5%	7%	19%	5%	6%	7%

Table 4.4. (continued): Average garnet microprobe analyses.

	HP297	HP297	HP297	HP255	HP255	HP255
	rim	mid	core	rim	mid	core
				i.z.	i.z.	i.z.
	st-gt	st-gt	st-gt	bi-gt±ky	bi-gt±ky	bi-gt±ky
SiO_2	36.70	36.89	36.82	37.73	37.23	37.42
TiO_2	0.02	0.00	0.02	0.03	0.05	0.07
Al_2O_3	20.37	20.61	20.67	20.52	21.09	20.51
FeO	36.12	36.77	36.61	32.39	31.09	30.67
MnO	2.97	2.46	2.47	4.79	6.43	6.51
MgO	2.60	2.87	2.78	2.40	2.14	2.18
CaO	1.01	0.40	0.82	2.60	2.68	3.00
	-----	-----	-----	-----	-----	-----
Total	99.79	100.00	100.19	100.46	100.71	100.36
	-----	-----	-----	-----	-----	-----
n	4	3	3	2	2	2
Si	2.984	2.990	2.978	3.036	2.990	3.016
Al^{iv}	0.016	0.010	0.022	0.000	0.010	0.000
Al^{vi}	1.936	1.958	1.948	1.945	1.986	1.948
Ti	0.001	0.000	0.001	0.002	0.003	0.004
Fe^{2+}	2.456	2.492	2.476	2.179	2.087	2.067
Mn	0.204	0.169	0.169	0.326	0.437	0.444
Mg	0.315	0.347	0.335	0.288	0.256	0.262
Ca	0.088	0.035	0.071	0.224	0.231	0.259
O	12	12	12	12	12	12
ALM	80%	82%	81%	72%	69%	68%
PYR	10%	11%	11%	10%	9%	9%
SPE	7%	6%	6%	11%	15%	15%
GRO	3%	1%	2%	7%	8%	9%

Table 4.4. (continued): Average garnet microprobe analyses.

	HP255 rim o.z. bi-gt±ky	HP255 mid o.z. bi-gt±ky	HP255 core o.z. bi-gt±ky	HP308 rim bi-gt±ky	HP308 mid bi-gt±ky	HP308 core bi-gt±ky
SiO_2	37.58	38.58	37.41	37.35	37.81	37.45
TiO_2	0.07	0.02	0.11	0.00	0.00	0.00
Al_2O_3	21.12	21.55	21.13	21.05	21.11	21.27
FeO	31.75	31.48	30.67	36.18	37.17	36.39
MnO	1.05	2.51	3.86	2.43	1.33	1.57
MgO	2.19	2.37	2.09	2.39	2.82	2.61
CaO	6.77	5.36	5.48	1.52	1.36	1.81
Total	100.53	101.87	100.75	100.92	101.60	101.10
n	2	1	2	7	2	3
Si	2.992	3.026	2.989	3.000	3.009	2.994
Al^{iv}	0.008	0.000	0.012	0.000	0.000	0.006
Al^{vi}	1.974	1.992	1.978	1.992	1.980	1.998
Ti	0.004	0.001	0.006	0.000	0.000	0.000
Fe^{2+}	2.114	2.065	2.049	2.430	2.473	2.433
Mn	0.071	0.167	0.261	0.165	0.090	0.106
Mg	0.260	0.277	0.248	0.286	0.334	0.311
Ca	0.577	0.450	0.469	0.131	0.116	0.155
O	12	12	12	12	12	12
ALM	70%	70%	68%	81%	82%	81%
PYR	9%	9%	8%	9%	11%	10%
SPE	2%	6%	9%	6%	3%	4%
GRO	19%	15%	16%	4%	4%	5%

Table 4.4. (continued): Average garnet microprobe analyses.

	HP324 rim bi-gt±ky	HP324 mid bi-gt±ky	HP324 core bi-gt±ky	HP325 rim sil-or-mu	HP325 mid sil-or-mu	HP325 core sil-or-mu
SiO_2	37.33	37.46	37.61	37.27	37.67	37.55
TiO_2	0.00	0.00	0.00	0.00	0.00	0.01
Al_2O_3	20.59	20.86	21.11	20.66	20.77	21.08
FeO	35.36	35.64	35.69	32.60	34.38	34.42
MnO	3.18	2.41	1.83	6.12	2.94	2.91
MgO	3.03	3.46	3.78	2.28	3.29	3.23
CaO	0.71	0.77	0.79	1.38	1.58	1.49
	-----	-----	-----	-----	-----	-----
Total	100.20	100.60	100.81	100.31	100.63	100.69
	-----	-----	-----	-----	-----	-----
n	6	7	3	8	6	6
Si	3.014	3.004	3.000	3.014	3.014	3.003
Al^{iv}	0.000	0.000	0.000	0.000	0.000	0.000
Al^{vi}	1.960	1.972	1.985	1.969	1.958	1.986
Ti	0.000	0.000	0.000	0.000	0.000	0.001
Fe^{2+}	2.388	2.390	2.381	2.205	2.300	2.301
Mn	0.218	0.164	0.124	0.419	0.199	0.197
Mg	0.365	0.414	0.449	0.275	0.392	0.385
Ca	0.061	0.066	0.068	0.120	0.135	0.128
O	12	12	12	12	12	12
ALM	79%	79%	79%	73%	76%	76%
PYR	12%	14%	15%	9%	13%	13%
SPE	7%	5%	4%	14%	7%	7%
GRO	2%	2%	2%	4%	5%	4%

Table 4.4. (continued): Average garnet microprobe analyses.

	HP5 rim sil-or-mu	HP5 mid sil-or-mu	HP5 core sil-or-mu	HP65 rim sil-or-mu	HP65 mid sil-or-mu	HP65 core sil-or-mu
SiO_2	36.80	36.61	36.97	37.40	37.44	37.43
TiO_2	0.02	0.00	0.00	0.02	0.02	0.00
Al_2O_3	20.25	20.27	20.53	21.17	20.91	21.05
FeO	33.26	33.21	32.75	36.12	35.70	35.45
MnO	6.23	6.00	6.05	1.43	1.10	1.01
MgO	2.14	2.34	2.38	3.30	3.91	4.01
CaO	0.78	0.81	1.17	1.27	1.25	1.27
	-----	-----	-----	-----	-----	-----
Total	99.48	99.24	99.85	100.71	100.33	100.22
	-----	-----	-----	-----	-----	-----
n	7	2	2	8	4	4
Si	3.013	3.004	3.007	2.993	2.999	2.996
Al^{iv}	0.000	0.000	0.000	0.007	0.001	0.004
Al^{vi}	1.954	1.960	1.968	1.990	1.972	1.982
Ti	0.001	0.000	0.000	0.001	0.001	0.000
Fe^{2+}	2.278	2.279	2.227	2.417	2.391	2.373
Mn	0.432	0.417	0.417	0.097	0.075	0.068
Mg	0.261	0.286	0.289	0.394	0.467	0.478
Ca	0.068	0.071	0.102	0.109	0.107	0.109
O	12	12	12	12	12	12
ALM	75%	75%	73%	80%	79%	78%
PYR	9%	9%	10%	13%	15%	16%
SPE	14%	14%	14%	3%	2%	2%
GRO	2%	2%	3%	4%	4%	4%

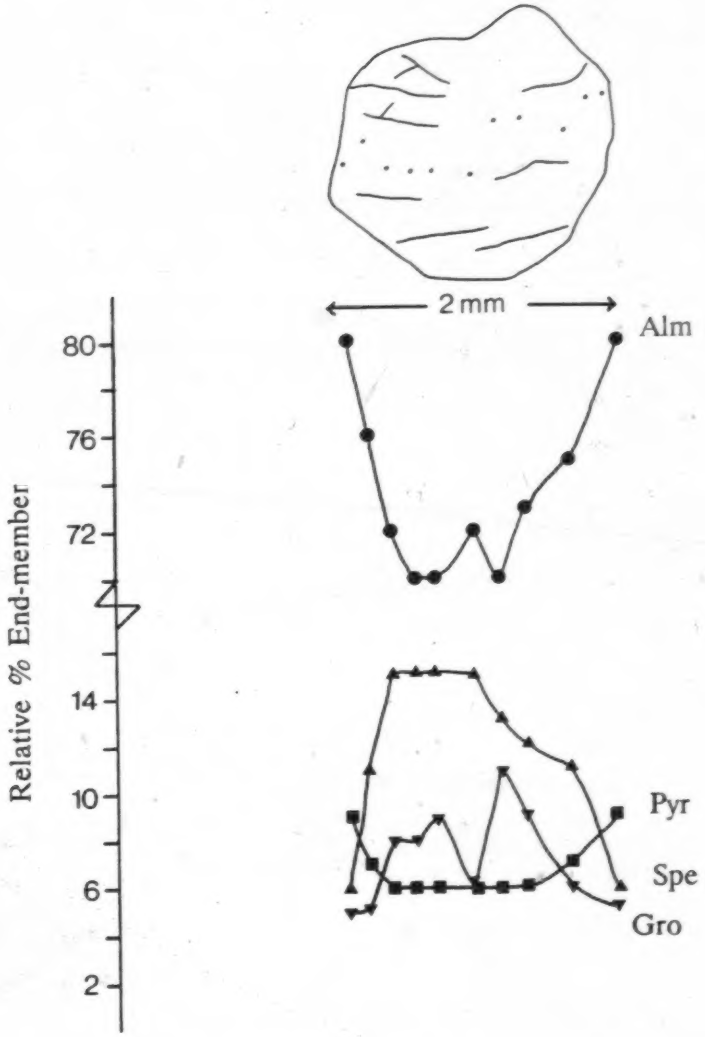

Figure 4.4: Zoning profile for garnet from staurolite-garnet schist. Bell-shaped, normal zoning profile is typical of medium-grade, prograde garnet growth.

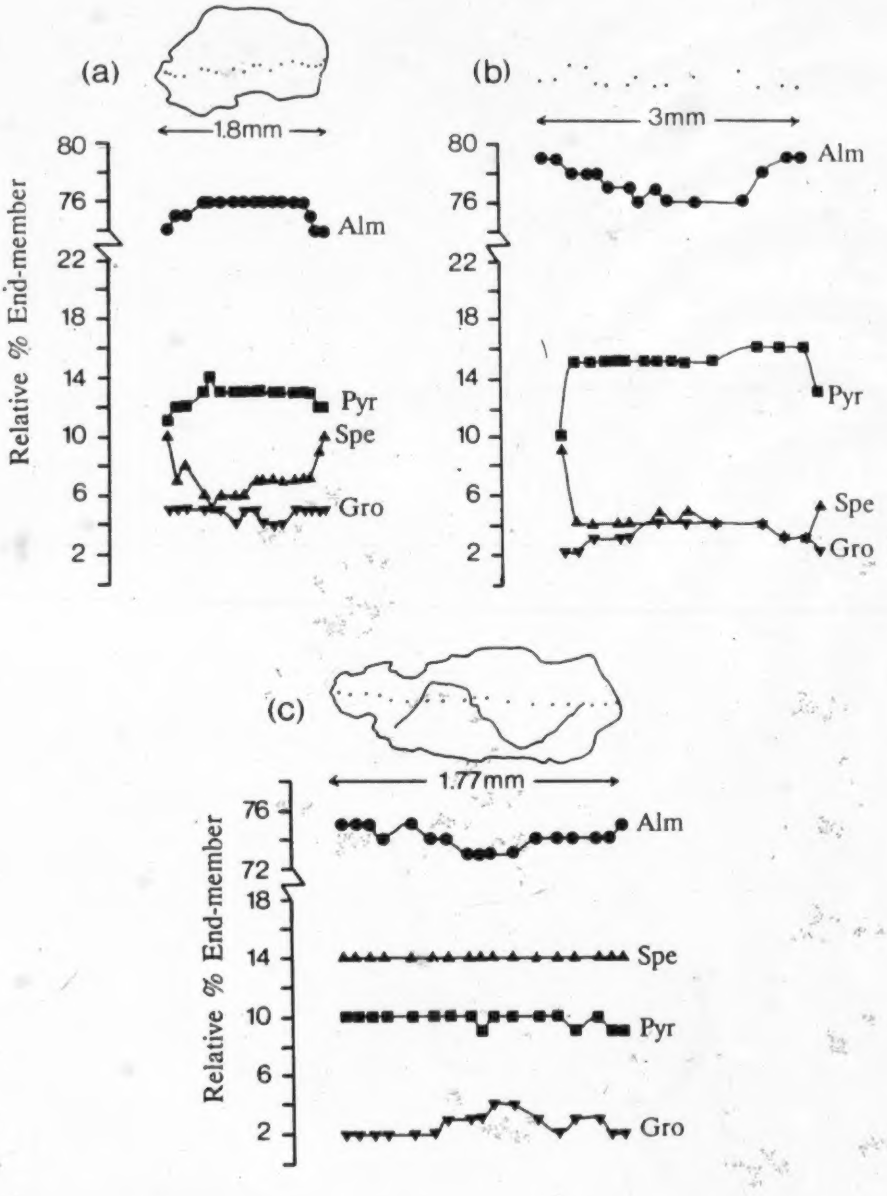

Figure 4.5: Examples of Type I zoning profiles in garnet from (a) sillimanite-orthoclase-muscovite-garnet schist and (b) kyanite-garnet schist. Note increase in Mn near garnet rims. (c) Type II garnet zoning profile for garnet from sillimanite-orthoclase-muscovite schist.

an increase in Fe/Mg ratio and a decrease or no change in Fe, Mg and Ca. One exception is sample HP88-324 where Fe increases.

Homogeneous garnet zoning profiles are typical of high-grade garnet and probably reflect zonation elimination by volume diffusion at approximately 600 to 700°C (e.g. Woodsworth, 1977; Yardley, 1977; Tracy, 1982); this temperature range is consistent with garnet-biotite geothermometry results (Chapter 5).

Mn-rich garnet rims have been attributed to (a) preferential retention of Mn in garnet during resorption under prograde (e.g. Hollister, 1977) or high-temperature retrograde reactions (e.g. Grant and Weiblen, 1971; Petrakakis, 1986), (b) high oxygen fugacity (fO_2) (e.g. Chinner, 1960) and (c) an increase in available Mn during prograde garnet growth by Mn-release during breakdown of a suitable phase (e.g. Evans and Guidotti, 1966; Hollister, 1969).

Hypothesis (a) requires temperature high enough for volume diffusion in garnet to occur (i.e. close to and above the sillimanite-orthoclase isograd) and that prograde or retrograde products after garnet do not readily accept Mn (e.g. Grant and Weiblen, 1971). Garnets showing Type II zoning are close to or above the sillimanite-orthoclase isograd but show no textural evidence of resorption. Where garnet grain boundaries are irregular, they are occupied by quartz and coarse biotite. Chemistry of the biotite is inconsistent with retrograde growth. Therefore, hypothesis (a) can not account for the Mn-rich rims on garnet.

Hypothesis (b) is also improbable. Oxygen fugacity (fO_2) is interpreted to be low in samples with Type I garnet zoning, on the basis of low Fe_2O_3 in sillimanite and kyanite (section 4.2.6), absence of hematite and presence of ilmenite (see Chapter 5).

Hypothesis (c) requires proof that garnet growth took place during prograde metamorphism. Weak core-to-rim decrease in Ca and corresponding increase in Fe, preserved in several Type III garnets is consistent with prograde garnet growth in the sillimanite-orthoclase-muscovite and biotite-garnet ± kyanite zones.

Samples containing homogenous garnet with Mn-rich rims contain xenoblastic ilmenite with highly irregular grain boundaries. This ilmenite appears unstable and contrasts strongly with large, locally poikiloblastic, subidioblastic ilmenite in staurolite-garnet schist and in biotite-garnet schist with zoned garnet (Type III, see below) (Plate 4.1). Modal proportions of ilmenite also decrease from staurolite-garnet zone to sillimanite-orthoclase-muscovite zone (cf. Evans and Guidotti, 1966). The coincidence of texturally unstable ilmenite with the development of Mn-rich rims on garnet suggests that ilmenite is a Mn-source for garnet and supports hypothesis (a) for these samples. This is further supported by observed unsystematic Fe-Mn

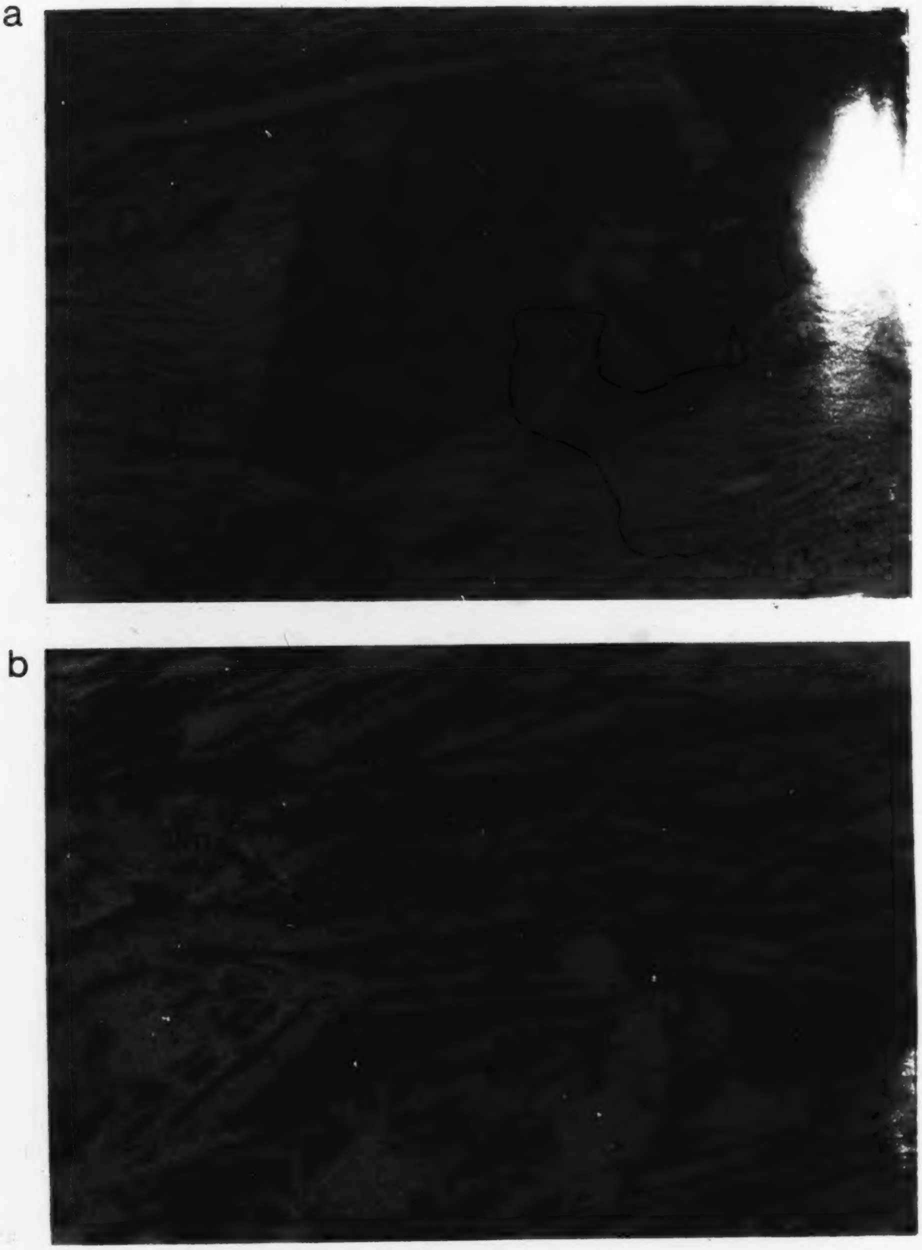

Plate 4.1: (a) Ilmenite from staurolite-garnet schist. Field of view is 4 mm. (b) Ilmenite from biotite-garnet schist with homogeneous garnet, that is, a high-grade schist as defined in section 4.3.2. Field of view is 4 mm. Note that ilmenite is large and has smooth grain boundaries relative to that in biotite-garnet schist.

distribution between garnet rims and ilmenite in these samples (see section 4.3.2). Possible reactions are discussed in Chapter 5.

(ii) Type II Garnet Zoning

Type II garnet zoning is similar to Type I but shows little or no increase in Mn at garnet rims (samples HP87-5, HP87-65, Table 4.4). This zoning is displayed in two samples of sillimanite-orthoclase-garnet schist. It is characterized by a continuous, homogeneous zonation profile with or without a weak core-to-rim decrease in Ca and Mg and a corresponding increase in Fe (Figure 4.5). Zonation elimination by volume diffusion is the probable cause for the homogenous zonation profile.

Ilmenite is texturally similar in samples with Type I and Type II garnets. Garnets in sample HP87-5 are small and uniformly Mn-rich. They likely nucleated and grew at the onset of ilmenite breakdown. Garnet in sample HP87-65 lacks a Mn-rich rim and has a low Mn-content. The reason for the lack of a Mn-rich rim is unclear. Biotite in this sample is also low in Mn and the absence of a Mn-rich garnet rim may be the effect of bulk composition.

(iii) Type III Garnet Zoning

Type III zoning is developed in the southern part of the biotite-garnet ± kyanite zone. It is characterized by idioblastic, inclusion-poor, normally zoned cores (cf. Hollister, 1966) (referred to here as the inner zone) surrounded by xenoblastic, inclusion-rich rims (referred to as the outer zone - Plate 3.9). The garnet core of the inner zone is significantly more magnesian than those of the staurolite-garnet schist. A sharp chemical discontinuity coincides with the textural discontinuity where Fe, Mg and Mn decrease and Ca increases abruptly. Outwards from the discontinuity, Fe and Ca increase, Mn decreases and Mg remains approximately constant (Figure 4.6).

The preservation of zoning in Type III garnet indicates maximum temperature ca. 600°C for this sample (cf. Tracy, 1982; Woodsworth, 1977, Yardley, 1977). Chemical discontinuities in garnet have been attributed to renewed growth on an earlier, metastable garnet (e.g. Foster, 1986), a decrease in garnet growth rate (e.g. Rast and Sturt, 1957) or a combination of the two, such as a change in garnet producing reaction that produces a change in growth rate (e.g. Thompson et al., 1977).

Interpretation of Type III garnet zoning is hindered by the paucity of data. Well-preserved type III zoning was found in one sample. Moderately to poorly preserved garnets showing similar textural zonation patterns are observed in a sample

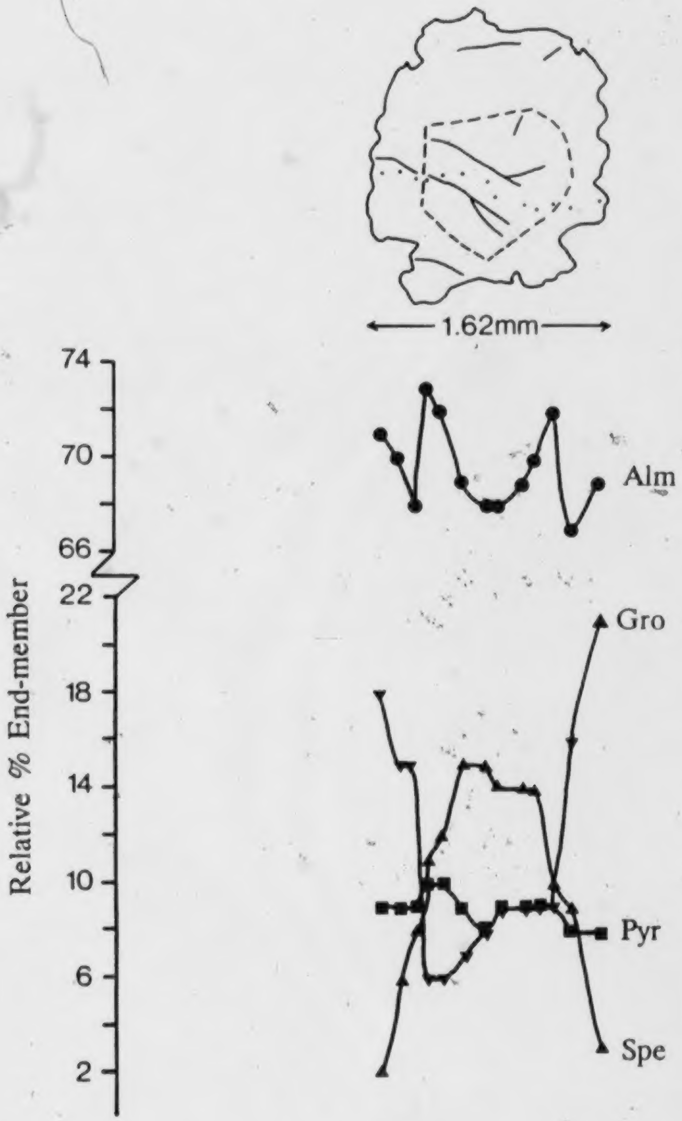

Figure 4.6: Type III garnet zoning profile from sample HP88-255 in the biotite-garnet±kyanite zone. Note the coincidence of textural and chemical discontinuity.

ca. 5 km to the north. Chlorite, biotite, quartz, fine-grained muscovite, plagioclase and locally, epidote partly replace garnet along grain boundaries and the textural discontinuity. In many samples, relict garnets are surrounded by xenoblastic masses or pseudomorphs of chlorite, biotite, quartz, plagioclase and locally, epidote. Therefore, the paucity of Type III zoning in the southern part of the range results from widespread garnet retrogression.

Several observations indicate that Type III zonation reflects a 2 stage, prograde garnet growth. (1) Garnet core is idioblastic, shows no signs of resorption and is normally zoned (cf. Hollister, 1966), which is characteristic of prograde garnets. (2) Chemistry trends in the garnet outer zone, excluding Ca, are entirely consistent with normal, prograde garnet zonation (cf. Hollister, 1966). (3) Chemistry of ilmenite inclusions suggests an increase in metamorphic grade during outer zone garnet growth (see section 4.2.7).

Because only one well-preserved example of Type III garnet zonation has been found, determination of a reaction for garnet rim formation is difficult. In addition, Ca zoning in garnet is typically complex (e.g. Crawford, 1977). In general, high Ca in garnet is attributed to the resorption of garnet by a phase unable to accept Ca, so the Ca is effectively concentrated in garnet and to the breakdown of a Ca-bearing phase during garnet growth and absence of any product phase other than garnet to readily accept Ca (e.g. DeBethune et al., 1975; Olimpio and Anderson, 1978; Crawford, 1977). Entry of Ca into garnet is favoured by high pressure (e.g. Ghent and Stout, 1981; Råheim and Green, 1974) and/or by decreasing temperature (e.g. Crawford, 1977).

Ca enrichment by garnet resorption can be eliminated because Ca increase occurs at the textural discontinuity where the inner garnet zone has an idioblastic outline and shows no evidence of resorption. In addition, the resorption hypothesis requires temperatures high enough to permit volume diffusion to occur in garnet (i.e. > 600°C). The preservation of normal zoning in the inner and outer zones of the Type III garnet indicates that volume diffusion did not occur.

Outer zone garnet growth under decreasing temperature can be eliminated on the basis of evidence cited above for garnet growth during prograde metamorphism.

Therefore, it is likely the high Ca in the outer zone reflects breakdown of a Ca-bearing phase and garnet growth under increasing pressure. The garnet-forming reaction is unclear. Crawford (1977) reported garnet zoning similar to that of Type III garnets in this study. She observed an increase in Ca and a flattening of Mg profiles coincident with a change in inclusions from ilmenite to rutile; coexisting plagioclase was sparse and corroded. She suggested that the reaction: muscovite + chlorite + Ca-plagioclase + ilmenite = staurolite + biotite + Ca-garnet + rutile + quartz + Na-plagioclase + H_2O could account for the observed phases. In sample HP88-255, both garnet and plagioclase are calcic relative to those in the staurolite-garnet zone and ilmenite coexists with rutile in the garnet rim. Staurolite is absent. Therefore, the reaction above can not account for Type III garnet zoning. There is no textural evidence to support the breakdown of epidote to produce Ca-rich garnet. Tourmaline is present in only trace amounts in the sample with Type III garnet zoning and comprises approximately 0.5 to 1.0 modal percent in the staurolite-garnet pelites. Therefore, tourmaline may be a source of calcium (e.g. Henry and Guidotti, 1985).

4.2.4. Biotite

Matrix biotite is unzoned and homogeneous on thin section scale (Table 4.5). The commonly reported biotite compositional trends of increasing Ti^{4+} (e.g. Atherton, 1968; Yardley et al., 1980; Frank, 1983; Ghent and Stout, 1984) and decreasing Al^{vi} (Guidotti, 1984) with increasing metamorphic grade are observed in this study (Figure 4.7). Biotite in HP88-255 from the garnet-biotite zone is clearly more magnesian than others in the biotite-garnet and staurolite-garnet zone (Table 4.5) which may reflect a more magnesian bulk rock composition relative to the other samples. Mg and Fe content in biotite overlaps between samples from the staurolite-garnet zone and from the biotite-garnet ± kyanite and sillimanite-orthoclase-muscovite zones. However, overall Fe is higher in biotite from the biotite-garnet ± kyanite and sillimanite-orthoclase-muscovite zones (2.5 to 2.9 cations) relative to biotite in the staurolite-garnet zone (2.4 to 2.7 cations). Similarly, Mg is lower in the higher grade zones (1.6 to 2.0 cations) relative to the staurolite-garnet zone (1.9 to 2.2 cations). These trends are opposite to an increase in Mg/Fe in biotite commonly reported in pelite up to kyanite grade (e.g. Atherton, 1968; Miyashiro, 1975). This discrepancy could be due to bulk rock composition or variation in fO_2 (e.g. Wones and Eugster, 1965; Guidotti, 1970). However, Fe-rich biotite, along with an increase in Mn in garnet, is predicted by Evans and Guidotti (1966) in sillimanite-grade rocks where ilmenite has become unstable.

Biotite in sillimanite-orthoclase-muscovite zone samples shows significantly higher Ti^{4+} (0.249 - 0.354 cations) than in the staurolite-garnet zone (0.152 - 0.204 cations) (Figure 4.7). Bulk rock compositional control is precluded by the presence of ilmenite, which indicates Ti saturation; an abrupt increase in Ti^{4+} is reported by

Table 4.5.: Average biotite microprobe analyses. "mtx" refers to matrix biotite not in contact with garnet. "nmtx" refers to biotite in contact with garnet. n = number of analyses. "incl" refers to biotite included in garnet. All Fe as Fe^{2+}. Samples arranged in order of increasing metamorphic grade. Sample numbers are abbreviated. Metamorphic mineral zone for each sample is indicated.

	HP171	HP171	HP171	HP272	HP272	HP272
	rim	core	rim	rim	core	rim
	mtx	mtx	nmtx	mtx	mtx	nmtx
	st-gt	st-gt	st-gt	st-gt	st-gt	st-gt
SiO_2	35.90	35.54	35.18	35.86	35.78	34.45
TiO_2	1.72	1.65	1.63	1.58	1.52	1.33
Al_2O_3	20.10	19.88	20.46	19.77	19.48	20.57
FeO	20.09	20.04	20.61	19.46	19.79	21.01
MnO	0.09	0.07	0.10	0.00	0.00	0.07
MgO	9.25	9.41	8.35	9.96	9.98	9.45
CaO	0.02	0.01	0.04	0.00	0.01	0.02
BaO	0.00	0.00	0.00	0.00	0.00	0.00
Na_2O	0.18	0.21	0.13	0.39	0.41	0.44
K_2O	8.97	8.77	9.12	8.68	8.55	8.52
F	0.34	0.37	0.33	0.28	0.35	0.34
H_2O	3.05	3.75	3.77	3.72	3.78	3.52
	-----	-----	-----	-----	-----	-----
Total	99.71	99.70	99.72	99.70	99.65	99.72
	-----	-----	-----	-----	-----	-----
n	4	3	9	2	3	5
Si	5.391	5.379	5.347	5.401	5.407	5.232
Al^{iv}	2.609	2.621	2.653	2.599	2.593	2.768
Al^{vi}	0.948	0.925	1.013	0.910	0.887	0.914
Ti	0.194	0.188	0.186	0.179	0.173	0.152
Fe^{2+}	2.523	2.537	2.620	2.451	2.501	2.668
Mn	0.011	0.009	0.013	0.000	0.000	0.009
Mg	2.070	2.123	1.892	2.236	2.248	2.139
Ca	0.003	0.002	0.007	0.000	0.002	0.003
Ba	0.000	0.000	0.000	0.000	0.000	0.000
Na	0.052	0.062	0.038	0.114	0.120	0.130
K	1.718	1.693	1.768	1.668	1.648	1.651
O	24	24	24	24	24	24
F	0.161	0.177	0.159	0.133	0.167	0.163
OH	3.839	3.823	3.841	3.867	3.833	3.837
Mg+Fe	4.59	4.66	4.51	4.69	4.75	4.81
ANN	55%	54%	58%	52%	53%	55%
PHLOG	45%	46%	42%	48%	47%	44%

Table 4.5. (continued): Average biotite microprobe analyses.

	HP272	HP297	HP297	HP297	HP297	HP255
	core	rim	core	rim	core	rim
	nmtx	mtx	mtx	nmtx	nmtx	mtx
	st-gt	st-gt	st-gt	st-gt	st-gt	bi-gt±ky
SiO_2	35.18	35.08	35.62	35.07	35.17	36.61
TiO_2	1.60	1.74	1.80	1.78	1.12	1.39
Al_2O_3	19.95	20.38	20.05	20.45	20.22	20.13
FeO	20.62	20.61	20.69	20.63	20.84	18.75
MnO	0.07	0.11	0.08	0.11	0.09	0.09
MgO	9.40	8.88	8.76	8.71	9.02	10.89
CaO	0.01	0.06	0.03	0.07	0.04	0.01
BaO	0.00	0.00	0.00	0.04	0.00	0.00
Na_2O	0.37	0.57	0.43	0.36	0.45	0.29
K_2O	8.61	8.49	8.47	8.47	8.46	8.31
F	0.34	0.20	0.21	0.20	0.17	0.35
H_2O	3.58	3.58	3.56	3.91	4.20	4.05
	-----	-----	-----	-----	-----	-----
Total	99.73	99.70	99.70	99.80	99.78	100.87
	-----	-----	-----	-----	-----	-----
n	2	3	2	4	1	2
Si	5.330	5.308	5.379	5.317	5.351	5.424
Al^{iv}	2.670	2.692	2.621	2.683	2.649	2.576
Al^{vi}	0.892	0.942	0.948	0.969	0.977	0.940
Ti	0.182	0.198	0.204	0.203	0.128	0.155
Fe^{2+}	2.613	2.608	2.613	2.615	2.652	2.323
Mn	0.009	0.014	0.010	0.014	0.012	0.011
Mg	2.123	2.003	1.972	1.968	2.046	2.405
Ca	0.002	0.010	0.005	0.011	0.007	0.002
Ba	0.000	0.000	0.000	0.000	0.000	0.000
Na	0.109	0.167	0.126	0.110	0.133	0.083
K	1.664	1.639	1.632	1.637	1.642	1.571
O	24	24	24	24	24	24
F	0.163	0.096	0.100	0.097	0.082	0.164
OH	3.837	3.904	3.900	3.903	3.918	3.836
Mg+Fe	4.74	4.61	4.59	4.58	4.70	4.73
ANN	55%	56%	57%	57%	56%	49%
PHLOG	45%	43%	43%	43%	43%	51%

Table 4.5. (continued): Average biotite microprobe analyses.

	HP255	HP255	HP308	HP308	HP308	HP308
	core	rim	rim	core	rim	core
	mtx	nmtx	mtx	mtx	nmtx	nmtx
	bi-gt±ky	bi-gt±ky	bi-gt±ky	bi-gt±ky	bi-gt±ky	bi-gt±ky
SiO_2	37.10	36.29	34.62	34.18	34.76	34.67
TiO_2	1.56	1.33	2.21	2.18	1.83	2.08
Al_2O_3	20.72	20.24	19.68	18.88	20.65	19.47
FeO	18.61	18.81	22.22	22.09	21.90	22.74
MnO	0.09	0.25	0.12	0.11	0.12	0.13
MgO	10.92	10.92	7.44	7.37	7.01	7.54
CaO	0.01	0.02	0.01	0.01	0.03	0.00
BaO	0.00	0.00	0.00	0.13	0.00	0.13
Na_2O	0.29	0.27	0.30	0.30	0.29	0.29
K_2O	8.51	8.10	8.60	8.89	8.87	8.73
F	0.45	0.37	0.27	0.24	0.23	0.27
H_2O	1.56	3.31	4.23	5.42	4.08	3.67
	-----	-----	-----	-----	-----	-----
Total	99.82	99.91	99.70	99.80	99.77	99.72
	-----	-----	-----	-----	-----	-----
n	1	4	2	5	6	2
Si	5.412	5.398	5.329	5.349	5.325	5.328
Al^{iv}	2.588	2.602	2.671	2.651	2.675	2.672
Al^{vi}	0.974	0.946	0.900	0.831	1.053	0.855
Ti	0.171	0.167	0.256	0.257	0.211	0.240
Fe^{2+}	2.270	2.340	2.861	2.891	2.806	2.923
Mn	0.011	0.013	0.016	0.015	0.016	0.017
Mg	2.374	2.422	1.707	1.719	1.601	1.727
Ca	0.002	0.004	0.002	0.002	0.005	0.000
Ba	0.000	0.000	0.000	0.008	0.000	0.008
Na	0.082	0.079	0.090	0.091	0.086	0.086
K	1.584	1.533	1.689	1.775	1.733	1.711
O	24	24	24	24	24	24
F	0.208	0.174	0.131	0.119	0.111	0.131
OH	3.792	3.826	3.869	3.881	3.889	3.869
Mg+Fe	4.644	4.762	4.568	4.610	4.407	4.650
ANN	49%	49%	62%	63%	63%	63%
PHLOG	51%	51%	37%	37%	36%	37%

Table 4.5. (continued): Average biotite microprobe analyses.

	HP324	HP324	HP324	HP324	HP325	HP325
	rim	core	rim	core	rim	core
	mtx	mtx	nmtx	nmtx	mtx	mtx
	bi-gt±ky	bi-gt±ky	bi-gt±ky	bi-gt±ky	sil-or-mu	sil-or-mu
SiO_2	35.50	35.54	35.17	35.61	34.85	35.58
TiO_2	2.10	2.32	1.82	1.95	2.51	2.19
Al_2O_3	19.63	19.83	20.63	20.20	19.49	20.53
FeO	19.01	19.44	19.30	19.75	20.45	20.38
MnO	0.07	0.08	0.10	0.14	0.16	0.21
MgO	9.15	9.24	9.03	8.91	7.67	7.90
CaO	0.02	0.01	0.03	0.01	0.04	0.01
BaO	0.23	0.21	0.25	0.21	0.16	0.00
Na_2O	0.27	0.31	0.28	0.28	0.27	0.27
K_2O	8.91	8.88	8.80	8.87	8.86	8.76
F	0.31	0.31	0.26	0.24	0.31	0.33
H_2O	4.59	3.56	4.11	3.57	5.06	3.50
Total	99.79	99.73	99.78	99.74	99.83	99.66
n	5	3	9	2	6	1
Si	5.404	5.363	5.327	5.373	5.376	5.376
Al^{iv}	2.596	2.637	2.673	2.627	2.624	2.624
Al^{vi}	0.926	0.890	1.010	0.965	0.919	1.032
Ti	0.240	0.263	0.207	0.221	0.291	0.249
Fe^{2+}	2.420	2.453	2.445	2.492	2.638	2.575
Mn	0.009	0.010	0.013	0.018	0.021	0.027
Mg	2.076	2.078	2.039	2.004	1.764	1.779
Ca	0.003	0.002	0.005	0.002	0.007	0.002
Ba	0.014	0.012	0.015	0.012	0.010	0.000
Na	0.080	0.091	0.082	0.082	0.081	0.079
K	1.730	1.709	1.700	1.707	1.743	1.688
O	24	24	24	24	24	24
F	0.149	0.148	0.125	0.115	0.151	0.158
OH	3.851	3.852	3.875	3.885	3.849	3.842
Mg+Fe	4.496	4.531	4.484	4.496	4.402	4.354
ANN	54%	54%	54%	55%	60%	59%
PHLOG	46%	46%	45%	44%	40%	41%

Table 4.5. (continued): Average biotite microprobe analyses.

	HP325	HP325	HP325	HP5	HP5	HP5
	rim	core	core	rim	core	rim
	nmtx	nmtx	incl	mtx	mtx	nmtx
	sil-or-mu	sil-or-mu	sil-or-mu	sil-or-mu	sil-or-mu	sil-or-mu
SiO_2	34.86	35.10	36.06	34.27	34.18	34.51
TiO_2	2.74	2.73	2.59	2.45	2.41	2.67
Al_2O_3	20.26	20.40	20.78	19.40	19.53	19.83
FeO	20.56	20.65	16.93	22.07	22.18	21.85
MnO	0.23	0.19	0.09	0.24	0.17	0.26
MgO	7.70	7.84	9.61	7.03	6.87	6.97
CaO	0.02	0.01	0.11	0.03	0.01	0.01
BaO	0.12	0.21	0.10	0.00	0.00	0.10
Na_2O	0.27	0.28	0.33	0.20	0.19	0.18
K_2O	8.89	9.04	8.72	9.33	9.39	9.38
F	0.32	0.33	0.37	0.68	0.55	0.61
H_2O	3.81	3.03	4.09	4.12	4.22	3.43
	-----	-----	-----	-----	-----	-----
Total	99.78	99.81	99.78	99.82	99.70	99.80
	-----	-----	-----	-----	-----	-----
n	9	2	2	3	3	9
Si	5.307	5.303	5.384	5.316	5.309	5.302
Al^{iv}	2.693	2.697	2.616	2.684	2.691	2.698
Al^{vi}	0.941	0.935	1.041	0.862	0.885	0.893
Ti	0.314	0.310	0.291	0.286	0.282	0.309
Fe^{2+}	2.617	2.609	2.114	2.863	2.881	2.808
Mn	0.030	0.024	0.011	0.032	0.022	0.034
Mg	1.747	1.765	2.139	1.625	1.591	1.596
Ca	0.003	0.002	0.018	0.005	0.002	0.002
Ba	0.007	0.012	0.006	0.000	0.000	0.006
Na	0.080	0.082	0.096	0.060	0.057	0.054
K	1.726	1.742	1.661	1.846	1.861	1.839
O	24	24	24	24	24	24
F	0.154	0.158	0.175	0.334	0.270	0.296
OH	3.846	3.842	3.825	3.666	3.730	3.704
Mg+Fe	4.364	4.374	4.253	4.488	4.472	4.404
ANN	60%	59%	50%	63%	64%	63%
PHLOG	40%	40%	50%	36%	35%	36%

Table 4.5. (continued): Average biotite microprobe analyses.

	HP5 core nmtx sil-or-mu	HP65 rim nmtx sil-or-mu	HP65 core nmtx sil-or-mu
SiO_2	34.89	34.57	34.66
TiO_2	2.63	2.82	3.08
Al_2O_3	20.27	19.45	19.27
FeO	21.59	20.00	19.97
MnO	0.22	0.00	0.00
MgO	6.95	8.41	8.55
CaO	0.01	0.04	0.01
BaO	0.00	0.16	0.20
Na_2O	0.23	0.17	0.16
K_2O	9.36	9.36	9.51
F	0.53	0.31	0.33
H_2O	3.04	4.48	4.01
	-----	-----	-----
Total	99.72	99.77	99.75
	-----	-----	-----
n	2	8	3
Si	5.317	5.309	5.304
Al^{iv}	2.683	2.691	2.696
Al^{vi}	0.957	0.829	0.779
Ti	0.301	0.326	0.354
Fe^{2+}	2.751	2.568	2.556
Mn	0.028	0.000	0.000
Mg	1.579	1.925	1.950
Ca	0.002	0.007	0.002
Ba	0.000	0.010	0.012
Na	0.068	0.051	0.047
K	1.819	1.833	1.856
O	24	24	24
F	0.255	0.151	0.160
OH	3.745	3.849	3.840
Mg+Fe	4.330	4.493	4.506
ANN	63%	57%	57%
PHLOG	36%	43%	43%

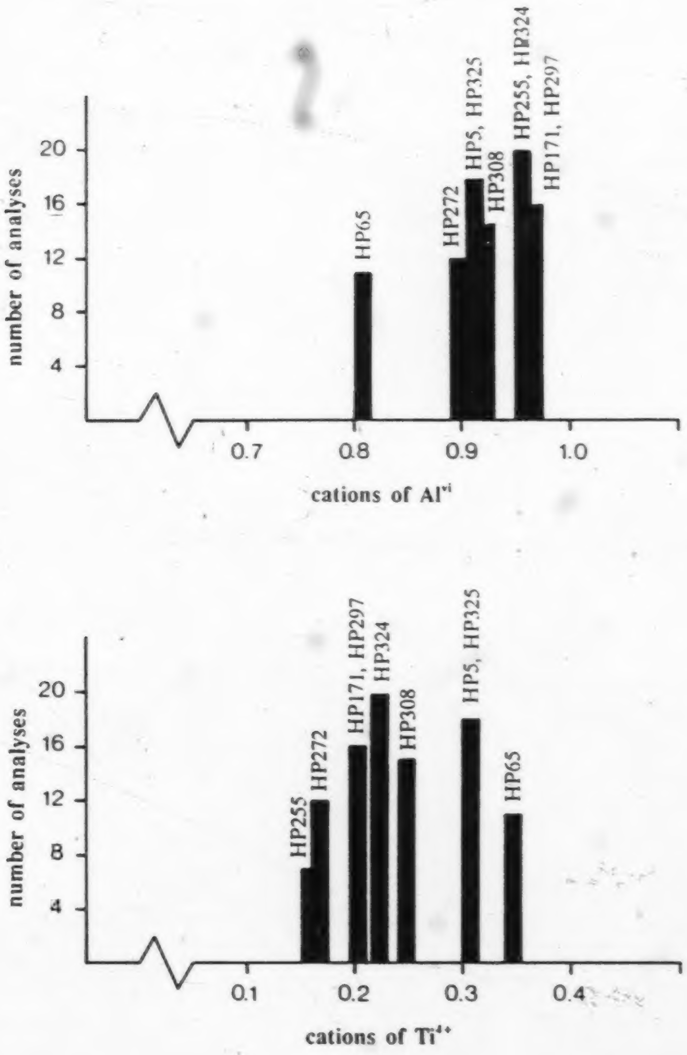

Figure 4.7: Histogram showing overall Ti^{4+} increase and Al^{vi} decrease in biotite with increasing metamorphic grade. Sample numbers abbreviated for clarity.

Guidotti (1984) to coincide with muscovite + quartz breakdown.

Biotite included in garnet in sample HP88-325 has significantly higher Mg and Mg/(Mg + Fe), significantly lower Fe and slightly higher Al^{vi} and lower Ti relative to matrix biotite. High Mg/(Mg + Fe) and low Fe relative to matrix biotite suggest formation at higher metamorphic grade, whereas higher Al and lower Ti suggest formation at lower grade relative to matrix biotite (cf. Yardley et al., 1980; Frank, 1983; Guidotti, 1984). As discussed above, higher Fe in biotite reflects higher metamorphic grade in pelite, due to ilmenite breakdown. Therefore, low Fe compared to the matrix indicates formation at lower temperature. However, the chemistry of the enclosing garnet has been affected by volume diffusion and as biotite has higher diffusivity than garnet (Freer, 1981), biotite inclusion composition has likely been modified by volume diffusion also.

4.2.5. Staurolite

Staurolite is iron-rich (ΣFe = 83.3 to 85.6, Table 4.6), unzoned and homogeneous on thin section scale. The average composition approximates common ferroan staurolite (Deer et al., 1978) indicating that Zn, if present, is a minor component.

4.2.6. AL_2SiO_5 Polymorphs

The stability fields of Al_2SiO_5 polymorphs are partly affected by minor element substitution (e.g. Althaus, 1969; Grambling and Williams, 1985; Kerrick and Speer, 1988). Andalusite, coarse sillimanite and kyanite were analysed for MgO, MnO and Fe_2O_3. In all cases, Fe_2O_3 is the most significant minor element at 0.20 to 0.31 wt% (Table 4.7). Grambling and Williams (1985) observed that Fe_2O_3 in Al_2SiO_5 polymorphs increases with increasing fO_2 and is lowest in Al_2SiO_5 polymorphs coexisting with ilmenite or rutile and highest with hematite. Compared with published values (e.g. Grambling and Williams, 1985), Al_2SiO_5 polymorphs in this study have a low iron content. Fe^{3+} contents overlap within analytical error in kyanite and sillimanite. These observations are consistent with Al_2SiO_5 polymorph coexistence with ilmenite (e.g. Grambling and Williams, 1985) and suggest that fO_2 (oxygen fugacity) was low in both kyanite and sillimanite schists. Low fO_2 is also indicated by the absence of hematite and magnetite. Fe^{3+} content in andalusite, although slightly higher than sillimanite and kyanite, is also low.

Table 4.6.: Average staurolite microprobe analyses. n = number of analyses. All Fe as Fe^{2+}. Σ Fe = $((Fe^{tot} + Mn)/(Mg + Mn + Fe^{tot})) \times 100$. All samples from the staurolite-garnet zone along the southwestern flank of the range. Sample numbers are abbreviated.

	HP171 rim	HP171 mid	HP171 core	HP272 rim	HP272 core
SiO_2	26.38	26.69	27.07	27.31	26.82
TiO_2	0.66	0.44	0.46	0.53	0.50
Al_2O_3	54.41	54.50	53.36	52.97	51.58
FeO	14.31	14.24	14.21	14.17	14.34
MnO	0.23	0.20	0.22	0.16	0.14
MgO	1.37	1.40	1.41	1.60	1.53
CaO	0.00	0.00	0.00	0.00	0.00
F	0.00	0.00	0.00	0.00	0.00
H_20	2.32	2.24	3.02	3.04	4.92
	-----	-----	-----	-----	-----
Total	99.68	99.71	99.75	99.81	99.83
	-----	-----	-----	-----	-----
n	2	1	2	1	1
Si	7.713	7.778	7.953	8.021	8.045
Al^{iv}	0.287	0.222	0.047	0.000	0.000
Al^{vi}	18.478	18.523	18.434	18.333	18.250
Ti	0.141	0.105	0.106	0.124	0.108
Fe	3.496	3.469	3.492	3.473	3.592
Mn	0.052	0.035	0.053	0.035	0.036
Mg	0.597	0.613	0.617	0.705	0.684
Ca	0.000	0.000	0.000	0.000	0.000
O	48	48	48	48	48
F	0	0	0	0	0
OH	2	2	2	2	2
ΣFe	85.6	85.1	85.2	83.3	84.1

Table 4.7.: Average microprobe analyses of Al_2SiO_5 polymorphs. n = number of analyses. Sample numbers are abbreviated.

	HP151 avg and	HP324 avg ky	HP65 avg sil
SiO_2	36.24	37.00	35.44
TiO_2	0.04	0.01	0.00
Al_2O_3	63.55	62.54	63.64
Fe_2O_3	0.31	0.21	0.20
MnO	0.00	0.00	0.00
MgO	0.05	0.04	0.02
	------	------	------
Total	100.19	99.81	99.30
	------	------	------
n	6	3	4
Si	3.916	4.003	3.859
Al	8.084	7.976	8.168
Ti	0.001	0.000	0.000
Fe	0.028	0.016	0.020
Mn	0.000	0.000	0.000
Mg	0.025	0.008	0.006
O	20	20	20

4.2.7. Opaque Minerals

Opaque minerals analysed, with the exception of rutile in one sample, are ilmenite; the main substitution is Mn for Fe (Table 4.8). Guidotti (1974) reports that Mn/Fe in ilmenite increases with increasing metamorphic grade. Data is limited and interpretation hindered by the large analytical error on trace amounts of Mn. However, Mn/Fe in ilmenite increases from the staurolite-garnet zone to the biotite-garnet zone and decreases in the sillimanite-orthoclase-muscovite zone. This trend supports the interpretation that ilmenite becomes unstable with increasing metamorphic grade (see above).

In Type III garnet, ilmenite inclusions show a slight increase in Mn/Fe from the discontinuity outward and matrix ilmenite has the highest Mn/Fe. This trend suggests that the inclusion-rich rims on garnet in sample HP88-255 are prograde.

4.3. ASSESSMENT OF EQUILIBRIUM

The application of phase equilibria and geothermobarometry to P-T determination in the study area requires an assessment of textural and chemical equilibrium.

4.3.1. Textural Disequilibrium

Evidence of textural disequilibrium in the staurolite-garnet zone is the sequence of porphyroblast growth and minor optical zoning of plagioclase. In the staurolite-garnet and biotite-garnet ± kyanite zones, chlorite replaces staurolite and garnet. In the sillimanite-orthoclase-muscovite zone, sillimanite overprints muscovite and muscovite shows a wormy intergrowth with quartz, coincident with sillimanite and orthoclase development. These textures reflect disequilibrium amongst coexisting phases.

4.3.2. Chemical Disequilibrium

Several criteria are commonly used to test the assumption of chemical equilibrium. These are the presence or absence of: (a) divariant mineral assemblages, (b) chemical zonation, (c) consistent element partitioning between coexisting phases in a thin section and within a suite of samples and (d) consistent and plausible

Table 4.8.: Average ilmenite and rutile microprobe analyses. n = number of analyses. All Fe as Fe^{2+}. All analyses for matrix phases unless otherwise indicated. "core o.z." and "rim o.z." refer to core and rim of outer zone of Type III zoned garnet in sample HP88-255. Samples are arranged in order of increasing metamorphic grade. Sample numbers are abbreviated. Metamorphic mineral zone for each sample is indicated.

	HP272	HP255	HP255	HP255	HP308	HP324
		rim	core			
		o.z.	o.z.			
	st-gt	bi-gt±ky	bi-gt±ky	bi-gt±ky	bi-gt±ky	bi-gt±ky
SiO_2	0.26	0.29	0.40	0.29	0.20	0.49
TiO_2	52.20	53.65	50.27	53.41	52.32	52.69
Al_2O_3	0.16	0.25	0.25	0.29	0.20	0.24
FeO	45.82	42.28	45.89	43.22	43.49	42.16
MnO	0.62	0.84	0.26	1.42	2.12	2.32
MgO	0.13	0.64	0.42	0.06	0.05	0.09
	-----	-----	-----	-----	-----	-----
Total	99.19	97.95	97.49	98.69	98.38	97.99
	-----	-----	-----	-----	-----	-----
n	4	1	2	2	4	4
Si	0.013	0.015	0.011	0.015	0.010	0.025
Ti	1.990	2.039	1.954	2.028	2.007	2.015
Al	0.001	0.015	0.015	0.017	0.012	0.014
Fe^{2+}	1.943	1.787	1.984	1.825	1.850	1.793
Mn	0.027	0.036	0.012	0.061	0.092	0.100
Mg	0.009	0.048	0.032	0.005	0.004	0.007
O	6	6	6	6	6	6
Mn/Fe	0.014	0.020	0.006	0.033	0.050	0.056

Table 4.8. (continued): Average ilmenite and rutile microprobe analyses.

	HP325
SiO_2	0.32
TiO_2	52.00
Al_2O_3	0.18
FeO	44.02
MnO	0.91
MgO	0.25

Total	97.68
	-----
n	3
Si	0.016
Ti	2.004
Al	0.011
Fe^{2+}	1.886
Mn	0.040
Mg	0.019
O	6
Mn/Fe	0.021

temperature and pressure calculated using geothermobarometry (e.g. Spear, 1989). The first three criteria are applied here. The fourth criteria is applied in Chapter 5.

Most pelites in the map area approximate the K_2O-Na_2O-FeO-MgO-Al_2O_3-SiO_2-H_2O (KNFMASH) system with MnO, CaO and TiO_2 as the common "impurity" components. The mineral assemblages for staurolite-garnet and kyanite-garnet schists are divariant in the KNFMASH system, which suggests equilibrium. The mineral assemblage for sillimanite-orthoclase-garnet schist is univariant in the KNFMASH system, suggesting that the assemblage lies on a univariant (discontinuous) reaction boundary, or reflects disequilibrium. In sillimanite-orthoclase-garnet schist, textural evidence suggests that the assemblage reflects the arrested reaction of muscovite, quartz and plagioclase breakdown to sillimanite, orthoclase and water (see section 5.2.3). The mineral assemblage for biotite-garnet schist has a variance of 3 in the KNFMASH system. This could indicate that these samples contain fewer components than KNFMASH. Mineral chemistry in sample HP88-308 indicates bulk rock composition similar to the staurolite-garnet schist. Mineral chemistry in HP88-255 indicates that, although CaO is a more significant component relative than in staurolite-garnet schists, FeO is a less significant component. Therefore, a variance of 3 in these samples more likely reflects variation in Al_2O_3 or in water activity (a_{H2O}).

Garnet zoning in all pelites analysed indicates chemical disequilibrium. It is generally assumed that the rim of zoned garnet is in chemical equilibrium with matrix phases (e.g. Ghent et al., 1979). However, where retrograde Mn enrichment or re-equilibration in homogeneous high-grade garnets is detected, this assumption is invalid (e.g. Indares and Martignole, 1985). To assess the degree of chemical disequilibrium between coexisting mineral phases and within a suite of samples, AFM diagrams (Thompson, 1957) and log Mg/Fe and log Mn/Fe plots (Albee, 1965) were constructed.

Interpretation of AFM diagrams is hindered by the similarity of garnet and biotite compositions on thin section scale, which itself suggests an approach to chemical equilibrium on that scale. Tielines are commonly subparallel. In most cases, tieline intersection is insignificant because variation in mineral chemistry is within statistical error. In addition, Mn is a significant component in high-grade garnet rims and is not accounted for by these plots. AFM plots for samples of staurolite-garnet schist (HP88-171), biotite-garnet schist (HP88-308), kyanite-garnet schist (HP88-324) and sillimanite-orthoclase schist (HP87-5) are shown in Figure 4.8. Garnet and biotite rims both adjacent to and isolated from one another show no difference within statistical error in Mg/(Mg+Fe), indicating no retrograde Mg-Fe exchange between

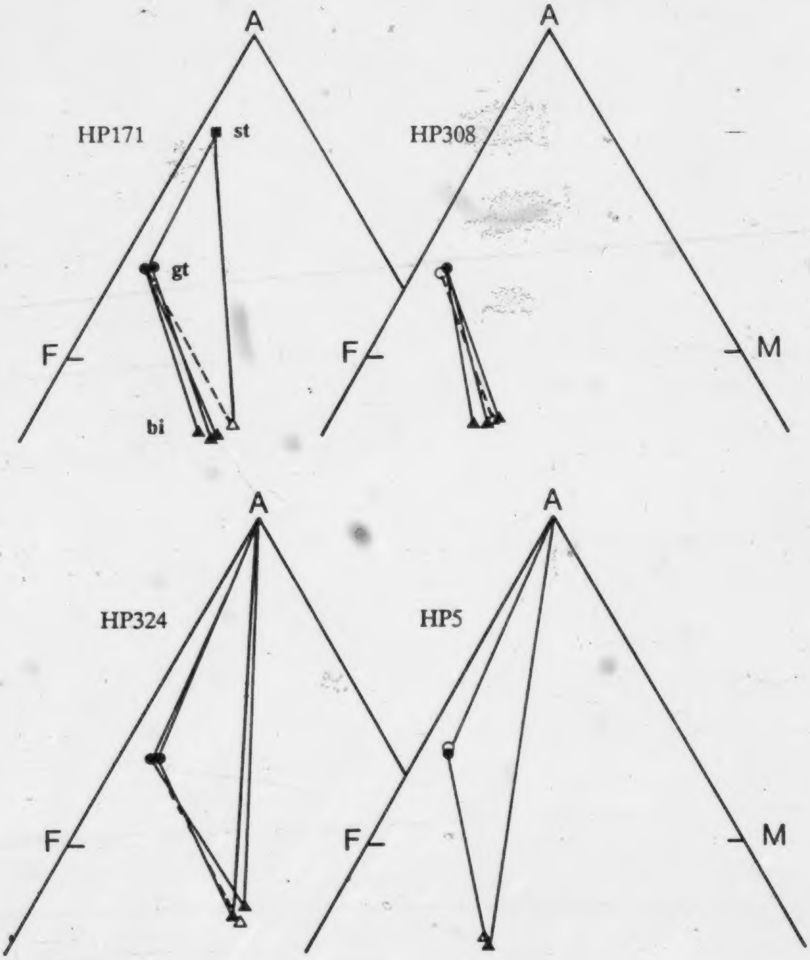

Figure 4.8: Thompson AFM plots for staurolite-garnet schist (HP88-171), garnet-biotite schist (HP88-308), biotite-garnet-kyanite schist (HP88-324) and sillimanite-orthoclase-muscovite schist (HP87-5). Garnet rim and adjacent biotite rim compositions are joined by solid tielines. Average garnet rim and biotite rim compositions isolated from each other are joined by dashed lines for reference. These tielines are parallel or intersect at a low angle. However, chemical variation is generally within error suggesting that chemical equilibrium was attained. The similarity of garnet rim composition where in contact with and where isolated from biotite, indicates that retrograde Fe-Mg exchange between garnet and biotite has not occurred. The variation in biotite rim compositions in contact and isolated from garnet is within statistical error, but may indicate that equilibrium was obtained only at the micron scale.

garnet and biotite (cf. Thompson, 1976; Indares and Martignole, 1985).

Log Mg/Fe and log Mn/Fe plots are useful because equal distribution coefficients (K_D) are represented by equal line segments between points for coexisting phases a and b:

$$\log (K_D{}^{a\text{-}b})_{Mg\text{-}Fe} = \log [(Mg/Fe)a/(Mg/Fe)b] \quad = \log (Mg/Fe)a - \log (Mg/Fe)b$$

(Albee, 1965).

In order to decipher trends and anomalies in cation distribution, data for numerous pelites (on the order of 10 samples) from the same metamorphic zone are required (e.g. Albee, 1968; Guidotti, 1974). In this study, data is available for two staurolite-garnet zone pelites, three biotite-garnet ± kyanite zone pelites and three sillimanite-orthoclase-muscovite zone pelites. Interpretation of this small database is hindered by the temperature range in the biotite-garnet ± kyanite zone as recorded by garnet zoning. To facilitate discussion, staurolite-garnet schist and biotite-garnet schist with Type III garnet zoning (sample HP88-255) are referred to as medium-grade schist ($T < 600°C$) and biotite-garnet ± kyanite and sillimanite-orthoclase-garnet schist with Type I or II garnet zoning are referred to as high-grade schist ($T > 600°C$).

Figure 4.9 shows log Mg/Fe and log Mn/Fe plots for samples from the staurolite-garnet, biotite-garnet ± kyanite and sillimanite-orthoclase-muscovite zones. As there is no significant compositional variation of a given phase within a sample, excluding garnet cores and rims, average values are plotted.

At staurolite grade, typical relative Mg/Fe ratios are ilmenite < garnet core < garnet rim < staurolite < biotite ≤ muscovite and the relative Mn/Fe ratios are biotite < staurolite < ilmenite < garnet rim < garnet core (Albee, 1972; Ghent, 1975). The plots of Figure 4.9 show that these trends are present in staurolite-garnet schist in this study and indicate uniform $(K_D)_{Mg\text{-}Fe}$ (see Appendix 3) between garnet rim, biotite, muscovite and staurolite and uniform $(K_D)_{Mn\text{-}Fe}$ between garnet rim, biotite and staurolite. As well, values of $(K_D{}^{gnt\ rim\text{-}bio})_{Mg\text{-}Fe}$ for staurolite-garnet schist (Table 4.9) are typical for staurolite-grade pelites (e.g. Albee, 1965). Thus despite the small database, Mg, Fe and Mn distribution is systematic which, in addition to phase rule considerations and AFM plots, indicates equilibrium between garnet rims, biotite, muscovite and staurolite in staurolite-garnet schist. Ilmenite was analysed in one sample of staurolite-garnet schist and is consistent with the general trend; therefore, ilmenite is assumed to be in chemical equilibrium with coexisting garnet rims, biotite, muscovite and staurolite, in staurolite-garnet schist.

Log Mg/Fe ratios for inner and outer zone garnet rims of Type III garnet in

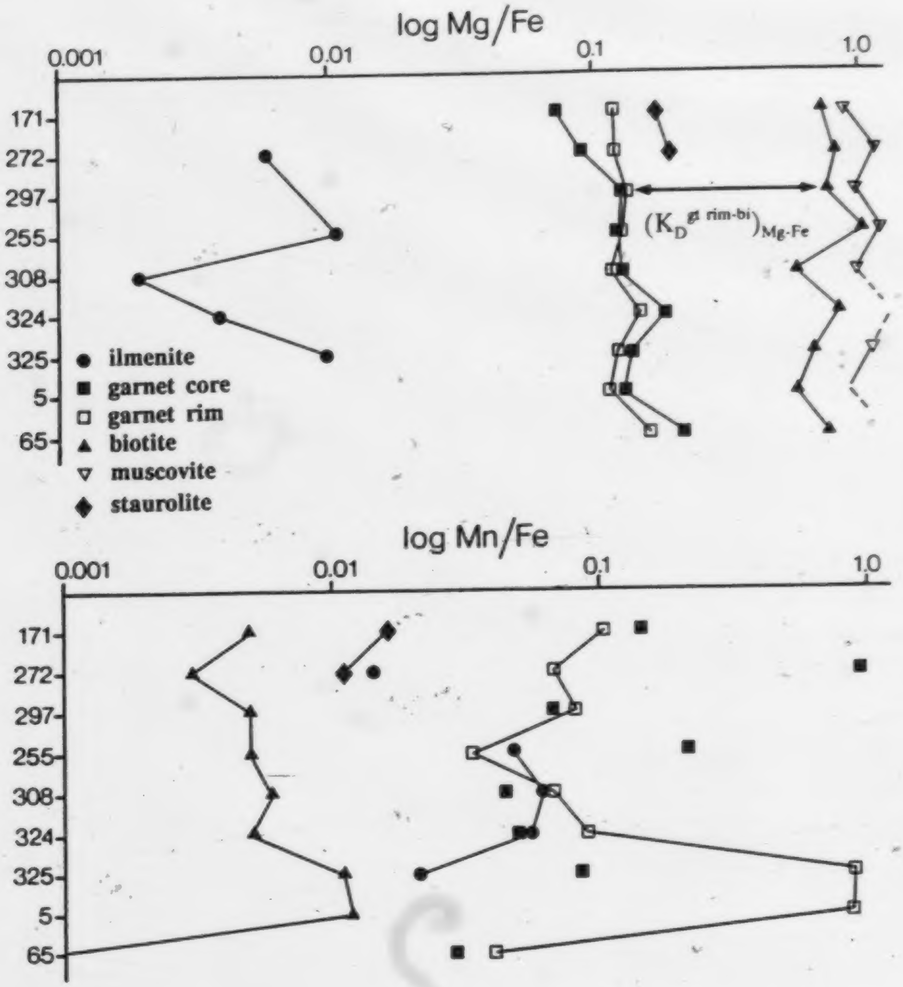

Figure 4.9: Log Mg/Fe and log Mn/Fe plots for the staurolite-garnet, biotite-garnet±kyanite and sillimanite-orthoclase-muscovite zones. Equal distribution coefficients (K_D) are represented by equal line segments between coexisting phases. Sample numbers abbreviated for clarity.

sample HP88-255 are the same within error, whereas log Mn/Fe values are different (Figure 4.9), due to stronger zoning in the inner garnet zone relative to the outer zone (see Figure 4.6). Log Mg/Fe and Mn/Fe for Type III garnet in sample HP88-255 is consistent with the general trend of staurolite-garnet schist. This is not surprising, considering that the preservation of normal zoning in the inner zone of Type III garnet indicates temperature (< 600°C) similar to those in staurolite-garnet schist. However, $(K_D^{gnt\ rim\text{-}bio})_{Mg\text{-}Fe}$ for the inner and outer zones Type III garnet rims is less than that for the staurolite-garnet schist. Similarly, $(K_D^{gnt\ rim\text{-}bio})_{Mn\text{-}Fe}$ values for the inner and outer zone garnet rims differ from those in staurolite-garnet schist (Figure 4.9). These differences may be a function of bulk composition, as mineral chemistry and assemblages in HP88-255 suggest that it is more magnesian relative to staurolite-garnet schist. Alternatively, garnet and biotite in HP88-255 may be in disequilibrium as suggested by the partial replacement of garnet by biotite. Therefore, temperature calculated using garnet-biotite geothermometry for this sample should be interpreted with caution.

Ilmenite shows systematic log Mg/Fe and log Mn/Fe partitioning with coexisting biotite, muscovite and inner and outer zone garnet rim in sample HP88-255. Therefore, equilibrium between ilmenite and these phases is assumed for this sample.

Overall, the log Mg/Fe ratio distribution in high-grade schist is systematic between garnet rims, biotite and muscovite, which suggests chemical equilibrium between these phases. However, these samples show a reversal in Mg/Fe ratio for garnet rims and cores such that log Mg/Fe ratio in garnet rim is less than in garnet core relative to medium-grade schist. This reversal has also been reported for garnet in other sillimanite-zone pelites (Guidotti, 1974). Similarly, garnet cores and rims show a reversal in log Mn/Fe such that garnet rim is greater than garnet core. Partitioning of log Mn/Fe between biotite and garnet rims is systematic in the high-grade samples, except sample HP88-308. The latter is interpreted to reflect disequilibrium partitioning of Mn/Fe between garnet and biotite.

In high-grade schist, ilmenite shows systematic Mg/Fe partitioning with biotite, muscovite and garnet rims, except in sample HP88-325. Ilmenite shows systematic partitioning of Mn/Fe with biotite but not with garnet rims or garnet cores, except in sample HP88-325 where it also shows unsystematic partitioning with biotite. Excluding HP88-325, these trends suggest equilibrium distribution of Mg/Fe between ilmenite and coexisting biotite, muscovite and garnet rims, equilibrium distribution of Mn/Fe between ilmenite and biotite (except sample HP88-325) and disequilibrium distribution of Mn/Fe between ilmenite and garnet rims. Disequilibrium Mn/Fe distribution between garnet rims and ilmenite in high-grade schist supports the interpretation that Type I garnet zoning is due to ilmenite breakdown (see above). Possible reactions are discussed in Chapter 5.

Figure 4.9 shows a negative correlation between log Mg/Fe and log Mn/Fe in each phase within a sample. This interdependence has been reported by Albee (1968). Ghent (1975) observed a decrease in $(K_D^{gnt\text{-}bio})_{Fe\text{-}Mg}$ values with increasing Mn/Fe in garnet. This trend is not observed in the study area (Table 4.9).

4.4. SUMMARY

Mineral assemblages and mineral chemistry of major phases in pelite is consistent with commonly observed trends in other Barrovian terranes and with an increase in metamorphic grade towards the north-central part of the schist complex. Analysis of K_D for Fe-Mg and Fe-Mn in coexisting phases suggests that equilibrium compositions were attained for coexisting ilmenite, biotite, muscovite, staurolite and garnet rims in staurolite-garnet schist. In medium-grade biotite-garnet schist (HP88-255), K_D values for Fe-Mg and Fe-Mn for biotite and garnet rims are inconsistent with those commonly reported for staurolite-garnet schist, which may reflect a bulk compositional difference or garnet rim-biotite disequilibrium.

Excluding ilmenite in HP88-325, Fe/Mg distribution among coexisting phases in high-grade schist is systematic and suggests chemical equilibrium. Similarly, excluding sample HP88-325, Fe/Mn distribution is systematic between ilmenite and biotite, which implies equilibrium. However, Fe-Mn distribution is unsystematic between garnet and ilmenite in high-grade schist, suggesting disequilibrium between these phases. This is further supported by textural evidence of ilmenite instability in samples containing garnet with Type I zoning.

Table 4.9.: Log Mn/Fe ratios for garnet rims and $(K_D^{gnt\ rim\text{-}bio})_{Fe\text{-}Mg}$ for pelites. Note the lack of correlation between log Mn/Fe and $(K_D^{gnt\ rim\text{-}bio})_{Fe\text{-}Mg}$.

Sample	log Mn/Fe	$(K_D^{gnt\ rim\text{-}bio})_{Fe\text{-}Mg}$
Medium-grade schists		
HP171	0.110	0.169
HP297	0.083	0.173
HP272	0.067	0.152
HP255	0.033	0.119
High-grade schists		
HP5	0.190	0.202
HP325	0.190	0.187
HP324	0.091	0.184
HP65	0.040	0.218

CHAPTER 5

P-T CONDITIONS OF METAMORPHISM AND MYLONITIZATION

5.1. INTRODUCTION

P-T conditions of metamorphism are determined using mineral assemblages, mineral chemistry, phase equilibria and geothermobarometry. The sequence of porphyroblast growth and interpretation of equilibrium mineral assemblages are used to infer discontinuous phase equilibria applicable to each mineral zone and isograd. Most metamorphic reactions take place initially by continuous reactions (Yardley et al., 1980). Discontinuous reactions proposed here are used only to place some restriction on the P-T conditions of metamorphism. Mineral chemistry is used to refine the isograd map and for geothermobarometry. Isograds are assumed to be parallel to S_2.

Sulphides are absent in pelite which precludes a significant S component in the fluid phase. Graphite, which acts as an fO_2 buffer (e.g. Miyashiro, 1964; French and Eugster, 1965), is present locally in staurolite-garnet schist, indicating low fO_2. Although graphite was not optically detected in high-grade pelite, the presence of ilmenite, the absence of hematite and low Fe_2O_3 in kyanite and sillimanite suggest that fO_2 was low also in high-grade pelite. In any case, fO_2 variation is important only where major minerals, such as biotite, have significant amounts of Fe^{3+}, which is unlikely at high-grades such as in the staurolite-garnet and sillimanite-orthoclase-muscovite zones. For pressures of 2 to 10 kb, the temperature of some reactions involving staurolite vary by only 20°C for fO_2 between the C-buffer and the FMQ buffer (Hoschek, 1969). Therefore, the effects of fO_2 variation on phase equilibria for these rocks are assumed to be negligible.

The fugacity of CO_2 is partly a function of fO_2 (Miyashiro, 1964). Thus, in graphite-bearing rocks where fO_2 is low, fCO_2 is also likely to be low. As well, CO_2 is unlikely to be significant in the fluid phase in pelite except near marble. Thus, it is assumed initially that $PH_2O = P_{total}$ ($XH_2O = 1.0$). This assumption is further supported in staurolite-garnet schist by the agreement between temperatures estimated using experimentally determined discontinuous reactions for $XH_2O = 1.0$ and those from mineral chemistry and geothermobarometry. However, in sillimanite-orthoclase-muscovite pelites, the lack of partial melting indicates that $P_{H20} < P_{total}$ (see below).

5.2. [illegible]ASE EQUILIBRIA AND MINERAL ISOGRADS

5.2.1. Biotite Zone

A large number of biotite-forming reactions have been proposed for pelitic rocks although generally, they are not well understood (Winkler, 1979; Ferry, 1984)). The appearance of abundant biotite coincident with a decrease in chlorite suggests biotite formation at the expense of chlorite in the study area. However, chlorite persists into the biotite zone in the south and into the staurolite-garnet zone in the north, indicating that the biotite-forming reaction is continuous and probably involves chlorite and quartz breakdown.

5.2.2. Staurolite-Garnet Zone and Biotite-Garnet ± Kyanite Zone

Garnet-forming reactions have apparently gone to completion in the staurolite-garnet zone. The abundance of chlorite and muscovite at lower grades and the inclusion of quartz, minor muscovite and minor chlorite in garnet in the staurolite-garnet zone suggests that garnet may have formed by a reaction such as:

(1) $\mathrm{chl + mu + qtz \rightleftharpoons gt + bi + H_2O}$

However, in some staurolite-garnet schists in the southern staurolite-garnet zone, garnet includes zoisite, which is absent in the matrix. This suggests that zoisite was a reactant in garnet formation in some samples, by a reaction such as:

(2) $\mathrm{zo + qtz \rightleftharpoons Ca\text{-}pl + Ca\text{-}gt + H_2O}$ (Richardson, 1968).

The absence of chloritoid at lower grade and in the staurolite-garnet zone indicates that staurolite did not form by breakdown of chloritoid (cf. Hoschek, 1969; Ganguly, 1972). The following chloritoid-independent discontinuous reactions for staurolite formation at moderate pressure have been reported:

(3) $\mathrm{chl + mu \rightleftharpoons st + bi + qtz + H_2O}$ (Hoschek, 1969)
(4) $\mathrm{bi + Al2SiO5 \rightleftharpoons st + mu + qtz}$ (Rao and Johannes, 1979)
(5) $\mathrm{mu + gt + chl \rightleftharpoons st + bi + qtz + H_2O}$ (e.g. Yardley et al., 1980; Bell and Rubenach, 1983).

The decrease in chlorite coincident with staurolite development, the preferential growth of staurolite, locally with garnet and biotite, in muscovite ± chlorite-rich layers in pelite and the stable coexistence of staurolite, garnet and biotite suggest that reaction (3) best approximates the staurolite-in isograd. The reaction limits metamorphic temperature to 500 to 600°C for pressures of 3 to 10 kb (Hoschek, 1969) (Figure 5.1). Reaction (4) is precluded by the absence of an Al_2SiO_5 phase and reaction (5) by the contemporaneous development of garnet and staurolite. However, as staurolite outlasted garnet growth, reaction (5) may have operated after the initiation of reaction (3). Reaction (5) has not been experimentally determined. Therefore, minimum temperature for the staurolite-garnet zone is approximately 500°C. The preservation of garnet zoning in staurolite-garnet schist (Chapter 4) limits the maximum temperature for this zone to ≤ 600°C (cf. Woodsworth, 1977; Yardley, 1977).

Commonly cited discontinuous staurolite-out reactions include:

(6) $st + qtz \rightleftharpoons Al_2SiO_5 + crd + H_2O$ (Richardson, 1968)
(7) $st + chl + mu \rightleftharpoons Al_2SiO_5 + bi + qtz + H_2O$ (Hoschek, 1969; Thompson, 1976)
(8) $st + bi + qtz \rightleftharpoons Al_2SiO_5 + gt + mu + H_2O$ (Ganguly, 1972)
(9) $st + qtz \rightleftharpoons Al_2SiO_5 + alm + H_20$ (Richardson, 1968; Hoschek, 1969; Ganguly, 1972; Rao and Johannes, 1979; Bickle and Archibald, 1984; Dutrow and Holdaway, 1989)
(10) $st + mu + qtz \rightleftharpoons Al_2SiO_5 + bi + H_2O$ (Hoschek, 1969; Ganguly, 1972; Thompson and Bard, 1982; Dempster, 1985)
(11) $st + mu + qtz \rightleftharpoons Al_2SiO_5 + bi + gt + H_2O$ (Hoschek, 1969; Tracy et al., 1976)

These reactions all produce an Al_2SiO_5 polymorph. In the northern part of the range, the staurolite-out isograd is placed where there is a sudden decrease in the abundance of staurolite from approximately 15-20% to trace amount, coincident with an increase in sillimanite from trace amount to approximately 15-20%. Staurolite and sillimanite coexist for approximately 80 m (measured normal to the isograd) beyond the staurolite-out/sillimanite-orthoclase-in isograd (see Figure 2.2). Both sillimanite and garnet overgrow S_2 and biotite is stable in the sillimanite-orthoclase-muscovite zone. This suggests that the staurolite-out isograd in this region is continuous and that discontinuous reaction (11) best fits the observed changes in mineral assemblage. Reaction (11) has not been experimentally calibrated but Hoschek (1969) suggests that it is probably intermediate between the experimentally determined reactions (9)

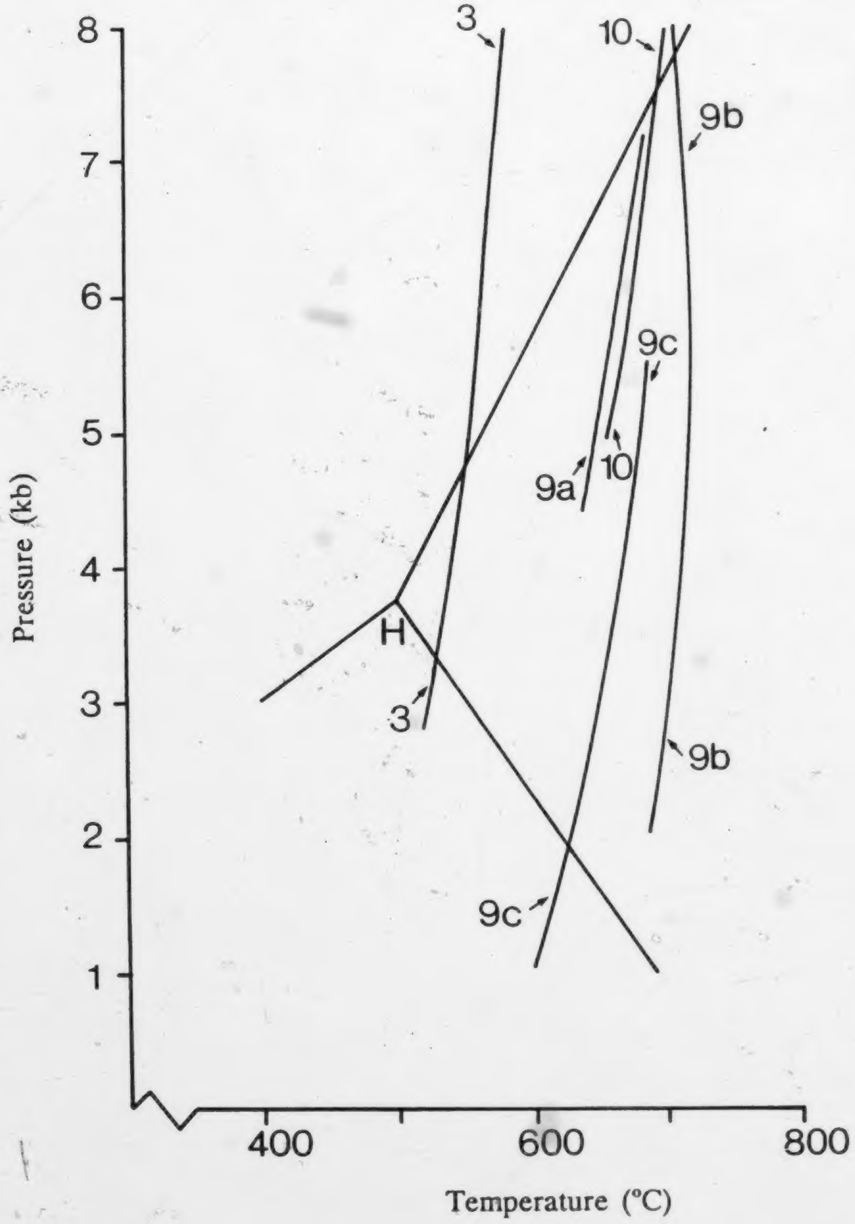

Figure 5.1: Discontinuous phase equilibria applicable to staurolite-in, staurolite-out and sillimanite-orthoclase-in isograds in this study. Al_2SiO_5 phase diagram modified after Holdaway (1971) denoted by H. Data for reactions (9A) from Bickle and Archibald (1984), (9B) from Hoschek (1969), (9C) from Dutrow and Holdaway (1989). References for other equilibria given in text.

and (10). Therefore, the reaction would take place between 600 and 750°C, at 3 to 10 kb, depending on the calibration used for reaction (9) (Figure 5.1). This temperature range is consistent with homogeneous garnet in the sillimanite-orthoclase-muscovite zone and the northern part of the biotite-garnet ± kyanite zone.

Within 150 m of the northern staurolite-out isograd (measured normal to the isograd), the assemblage muscovite-plagioclase-quartz is partly replaced by sillimanite and orthoclase (see below), indicating that the muscovite-out or second sillimanite isograd has been reached (reaction (13) below). The muscovite-quartz-out reaction has been experimentally calibrated in the same temperature range (650 to 750°C at 4 to 7 kb) as reaction (11) (e.g. Turner, 1981). Therefore, it is probable that reaction (12) was overstepped by the muscovite-out reaction.

The discontinuous reactions cited above are inconsistent with the lack of the appearance of a new mineral phase coincident with the disappearance of staurolite across the staurolite-out boundary in the southwestern part of the range. Although trace amounts of fibrolite are present in the upper staurolite-garnet zone, no widespread Al_2SiO_5 phase is present to the east, up-grade and structurally down section from the staurolite-out boundary. Kyanite is present at one locality in the biotite-garnet ± kyanite zone. Excluding rims on Type III garnets, there is no change in mineral assemblage coincident with staurolite disappearance. Therefore, the staurolite-"out" isograd in the southwestern part of the range is compositionally controlled. Mineral chemistry reflects more magnesian compositions in medium-grade biotite-garnet schist (HP88-255) relative to staurolite-garnet schist. Major mineral phases in high-grade biotite-garnet schist (HP88-308) have Fe-content similar to those in staurolite-garnet schist; the absence of staurolite in these rocks is probably due to higher temperature. The absence of sillimanite or kyanite probably reflects less aluminous bulk rock compositions relative to staurolite-garnet schist and sillimanite-orthoclase-muscovite schist.

Equivocal microtextures in the kyanite-garnet schist hinder determination of a kyanite-forming reaction. There is no evidence to support kyanite formation by staurolite breakdown. Kyanite includes quartz and opaque minerals and overprints muscovite and biotite. Plagioclase in this sample is albite (Chapter 4). Therefore, it is probable that kyanite formed by a reaction such as

(12) $\text{mu} + \text{qtz} + Na^+ \rightleftharpoons \text{alb} + Al_2SiO_5 + K^+ + H_2O$ (Chinner, 1967),

which explains the presence of albite in kyanite-garnet schist. Fibrolite partly replaces biotite and kyanite. This may indicate polymorphic inversion of kyanite to sillimanite via one of Carmichael's (1969) cyclic reactions, as there is no textural evidence for fibrolite formation by the muscovite + quartz-out reaction or by staurolite-breakdown.

5.2.3. Sillimanite-Orthoclase-Muscovite Zone and Partial Melting

Both fibrolite and coarse sillimanite are developed in the sillimanite-orthoclase-muscovite zone, commonly in the same sample. Fibrolite has been interpreted as a rapidly and metastably crystallized protosillimanite (e.g. Holdaway, 1971; Woodsworth, 1979; Grambling, 1981) and as late, retrograde, probably metastable phase (e.g. Vernon, 1979; Kerrick, 1987). In the study area, coarse sillimanite is developed most commonly where the muscovite-out reaction is highly advanced (i.e. muscovite is present in trace amounts or absent). This would suggest that fibrolite is a precursor to coarse sillimanite. However, coarse sillimanite is typically rimmed by fibrolite and thus, microtextures are equivocal. On the basis of its abundance, fibrolite is interpreted to be stable (cf. Grambling, 1981).

The effect of fibrolitic sillimanite versus coarse sillimanite on the P-T stability range of Al_2SiO_5 polymorphs is unclear. Heat capacity measurements by Salje (1986) indicate that the slope of the andalusite-sillimanite phase boundary becomes steeper with increasing fibrolitization, whereas experimental work by Kerrick and Heninger (1984) revealed that the P-T conditions of the andalusite-sillimanite equilibrium are identical regardless of whether fibrolite or coarse sillimanite is used as a starting material. In light of this uncertainty, it is assumed in subsequent discussion that fibrolite and coarse sillimanite have the same P-T range of stability.

The reaction:

(13) $mu + qtz \rightleftharpoons sil + or + H_2O$

is commonly cited for the development of sillimanite and orthoclase coincident with the breakdown of muscovite in pelite. Reaction (13) is discontinuous in the KASH system and has been experimentally determined to take place between 600 and 750°C at 2 to 7 kb and $XH_2O = 1.0$ (e.g. Evans and Guidotti, 1966; Kerrick, 1972; Chatterjee and Johannes, 1974) (Figure 5.2). Reaction (13) does not account for the involvement of plagioclase or the phengite component of muscovite and production of a ferromagnesian phase upon phengitic muscovite and quartz breakdown (e.g. Tracy,

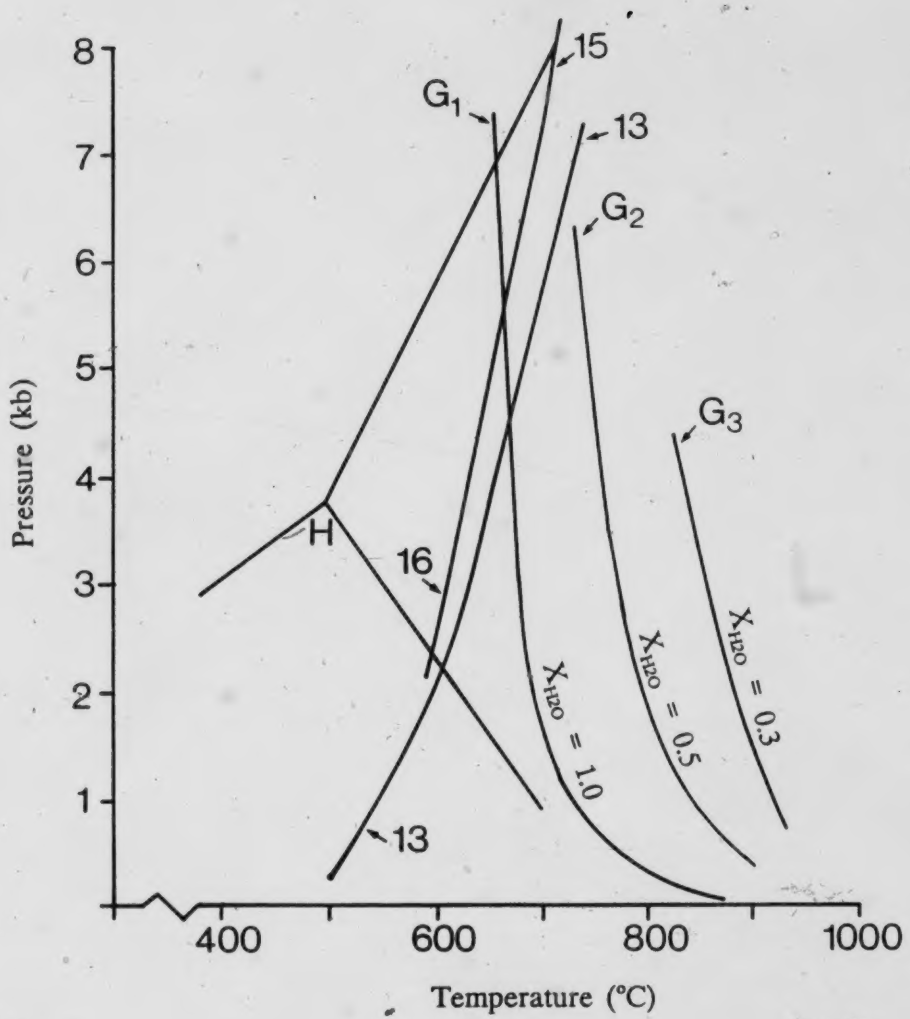

Figure 5.2: P-T conditions for muscovite-out reactions (13) and (15) (see text) modified after Turner (1981) and Thompson (1982). Granite melting reactions (G1, G2, G3) for X_{H2O} = 1.0, 0.5 and 0.3 modified after Binns (1969). The absence of partial melting in the Horseranch Range pelites indicates that $X_{H2O} < 1.0$. Al_2SiO_5 phase diagram modified after Holdaway (1971) is denoted by H.

1978; Thompson, 1982). However, the phengite component in muscovite is minor in this study and not a problem.

Microtextures in the sillimanite-orthoclase-muscovite zone indicate that muscovite, quartz and plagioclase have reacted to form sillimanite and orthoclase, suggesting the reaction:

(14) mu + alb component in pl + qtz $\rightleftharpoons$ sil + or (with high alb component) + H_2O (e.g. Evans and Guidotti, 1966).

This reaction does not account for albite in one sample of sillimanite-orthoclase-muscovite schist (HP87-5), as it should progressively enrich plagioclase in the anorthite (An) component. However, the resultant increase in %An depends on the initial relative proportions of muscovite and plagioclase. If these are present in equal amounts, an increase of only 2% An is expected (Evans and Guidotti, 1966). In sample HP87-5, muscovite is much more abundant than plagioclase and therefore, plagioclase composition may not have changed significantly by reaction (14).

On the basis of experimental data and a Schreinemaker analysis, Tracy (1978) determined that reaction (14) takes place between 650 and 700°C at 3.5 to 7 kb and $PH_2O = P_{total}$ ($XH_2O = 1$). Under these conditions reaction (15) intersects the granite minimum melting curve and pelites will show evidence of partial melting. Granite which is interpreted to be syn-metamorphic is exposed locally in the Horseranch Range (see below), however, little field evidence is found for partial melting (i.e. migmatization) of pelites. This suggests that $PH_2O < P_{total}$. Thompson (1982) determined that for $PH_2O < P_{total}$, widespread partial melting in pelites at depths of 15 to 40 km (3 to 13 kb) requires temperature of 650 to 750°C. The absence of widespread partial melting in the Horseranch Range limits peak temperatures to a maximum of ca. 650°C. Thompson (1982) determined the reaction:

(15) mu + alb + qtz $\rightleftharpoons$ sil + or + H_2O

(i.e. the equivalent of reaction (14) in the KNASH system) to take place at 660 to 720°C at 5 to 8 kb (Figure 5.2). As reaction (14) should take place at temperature slightly lower than that of (15), this is consistent with the interpretation that maximum temperature in the sillimanite-orthoclase-muscovite zone was ca. 650°C.

In the system NCKASH, reaction (14) is divariant. However, Evans and Guidotti (1966) have argued that, in the subsolidus case, Ca and Na in plagioclase are insufficient to produce notable divariance. Consequently, the commonly reported coexistence of muscovite, quartz, plagioclase, sillimanite and orthoclase in pelites has been attributed to (a) buffering of X_{H2O} in an impure gas with increasing temperature, such that P_{H2O} approaches P_{total} and counteracts reaction (14) (Evans and Guidotti, 1966), (b) thermal buffering by syn-metamorphic granite (e.g. Guidotti et al., 1983) and (c) kinetic control exerted by slow-forming sillimanite (e.g. Evans and Guidotti, 1966).

In the study area, reaction (14) is well advanced up to 3 km (normal to the isograd) away from the sillimanite-orthoclase-in isograd. Thus, kinetic controls are an unlikely cause for divariance. It is probable that permeability in high-grade schist was low by the time reaction (14) was initiated, which would favour buffering of X_{H2O} by the mineral assemblage. However, PH_2O was likely less than P_{total}, as discussed above.

Abundant granite bodies are present in the sillimanite-orthoclase-muscovite zone. Some are syn-tectonic and many are post-tectonic with respect to S_2, as is the peak of regional metamorphism (Table 3.1). At least some of the granites were intruded after staurolite-garnet schist began to cool (i.e. after the peak of regional metamorphism), because the schist is locally contact metamorphosed (Chapter 2). Several granites in the sillimanite-orthoclase-muscovite zone contain fibrolitic sillimanite and muscovite which shows the same partial replacement texture as in adjacent schist. Although this could be an igneous rather than metamorphic effect, a syn- to post-S_2 and a post-S_2 granite which show this texture have yielded late Early Cretaceous U-Pb zircon or monazite crystallization ages (see Chapter 6). Eocene granites (see Chapter 6) do not show the muscovite-out texture. The syn- and post-S_2, late Early Cretaceous granites fall within the interpreted late Jurassic to mid-Cretaceous time of regional metamorphism in the Swannell Range further south (Parrish, 1976, 1979; see Chapters 6 and 7). As regional metamorphism in the Horseranch Range is syn-to post-S_2 (Table 3.1), late Early Cretaceous syn- to post-S_2 granites are syn-metamorphic and may have caused divariance in the sillimanite-orthoclase-muscovite zone.

Biotite and garnet are overprinted by sillimanite in sillimanite-orthoclase-muscovite zone pelite, but are stable where reaction (14) is well advanced. Biotite shows an increase in Ti and Fe relative to medium-grade schist. Garnet shows an increase in Mn in its rims or is Mn-rich, in all but one high-grade schist and garnet rims show unsystematic Mn/Fe distribution relative to ilmenite. Modal proportions of ilmenite decrease from the staurolite-garnet and lower biotite-garnet zones into the upper garnet-biotite and sillimanite-orthoclase-muscovite zones. These observations suggest that a continuous reaction such as:

(16) mu + qtz + MnFe ilmenite $\rightleftharpoons$ FeTi biotite + Mn garnet + sillimanite

(cf. Evans and Guidotti, 1966) is responsible for Mn-rich garnet rims in high-grade schist. This reaction may have begun prior to the onset of reaction (14) and continued to operate with reaction (14) (cf. Evans and Guidotti, 1966).

5.3. ISOGRAD MAP PATTERN

Staurolite-garnet-in and sillimanite-orthoclase-in isograds form an elliptical map pattern, implying either post-isograd deformation or thermal doming. Structural analysis (Chapter 3) indicates that folding is responsible for the isograd map pattern.

The presence of kyanite indicates that the biotite-garnet ± kyanite zone, at least in its northern part, represents a higher metamorphic grade than the staurolite-garnet zone. Garnet zonation trends allow a temperature subdivision of this zone into moderate (< 600°C) and high temperature (> 600°C) zones (Figure 2.2). Although more detailed sampling is required to confirm the garnet homogenization pattern, it is consistent apparently with the elliptical map pattern.

5.4. CONTACT METAMORPHISM

Partial replacement of staurolite and garnet by andalusite and biotite in contact metamorphosed staurolite-garnet schist suggests a reaction such as (11) at a pressure low enough for andalusite formation. Assuming that reaction (11) takes place at a temperature intermediate to reactions (9) and (10), comparison with Holdaway's (1971) Al_2SiO_5 phase diagram indicates that maximum pressure for contact metamorphism was 2 to 3 kb.

5.5. GEOTHERMOBAROMETRY

5.5.1. Introduction

Temperatures can be calculated in the Horseranch Range using the garnet-biotite geothermometer which is based on temperature-dependent Fe^{2+}-Mg^{2+} exchange between garnet and biotite according to the reaction:

(17) pyrope + annite ⇄ phlogopite + almandine (e.g. Ferry and Spear, 1978).

Mineral assemblages in sillimanite-orthoclase-muscovite zone pelite permit pressure calculation using the pressure-dependent reaction:

(18) 3 anorthite ⇄ grossular + 2 Al_2SiO_5 + quartz (e.g. Ghent, 1976).

The lack of an Al_2SiO_5 phase in staurolite-garnet schist and in nearly all schist in the biotite-garnet ± kyanite zone precludes the wide application of this geobarometer. However, the plagioclase-biotite-garnet-muscovite geobarometer (Ghent and Stout, 1981) can be applied to the staurolite-garnet schist and biotite-garnet schist. This geobarometer is based on the reaction (17) and the reactions:

(19) pyrope + grossular + muscovite ⇄ 3 anorthite + phlogopite

(20) almandine + grossular + muscovite ⇄ 3 anorthite + annite

Reactions (19) and (20) are pressure-sensitive (Ghent and Stout, 1981). Numerical expressions for the geothermometer and geobarometers are given in Appendix 3. Definitions of mole fractions used in P and T calculations are given in Table 5.1. A key to abbreviations used in text and tables is given at the beginning of the thesis.

An estimate of pressure is required in most calibrations of the garnet-biotite geothermometer. A comparison of garnet-biotite temperature calculated using Thompson's (1976) empirical, pressure-independent garnet-biotite geothermometer (see below) and Holdaway's (1971) Al_2SiO_5 phase diagram yields a minimum pressure for the kyanite-garnet schist of ca. 5 kb and maximum of ca. 6.5 kb for sillimanite-orthoclase-muscovite schist. Comparison of the maximum temperature (ca. 650°C) estimate based on phase equilibria for sillimanite-orthoclase-muscovite schist and Holdaway's Al_2SiO_5 phase diagram yields a maximum pressure of ca. 7 kb for these rocks. These estimates are subject to error in microprobe data, in Thompson's (1976) calibration and in Holdaway's (1971) phase diagram. However, garnet-biotite geothermometry is relatively insensitive to the pressure used. For example, a change of 2 kb yields only an 8°C temperature change using the Ferry and Spear (1978) calibration. Therefore, a pressure range of 5 to 7 kb was used for all garnet-biotite

Table 5.1.: Definitions of mole fractions used in geothermobarometry calculations (see Tables 5.2 and 5.3 and Appendix 3).

Garnet

$X_{alm} = Fe/(Fe + Mg + Ca + Mn)$
$X_{gro} = Ca/(Fe + Mg + Ca + Mn)$
$X_{pyr} = Mg/(Fe + Mg + Ca + Mn)$
$X_{spe} = Mn/(Fe + Mg + Ca + Mn)$

Biotite

$X_{ann} = Fe/(Fe + Mg + Ti + Al^{vi})$
$X_{phl} = Mg/(Fe + Mg + Ti + Al^{vi})$

$(X^{bi})_{Al^{vi}} = Al^{vi}/(Al^{vi} + Ti + Fe + Mn + Mg)$
$(X^{bi})_{Ti} = Ti/(Al^{vi} + Ti + Fe + Mn + Mg)$

Muscovite

$(X^{mu})_{K} = K/(Ca + Na + K)$
$(X^{mu})_{Al^{vi}} = Al^{vi}/(Al^{vi} + Ti + Fe + Mn + Mg)$

Plagioclase

$X_{alb} = Na/(Ca + Na + K)$
$X_{anor} = Ca/(Ca + Na + K)$

For Ferry and Spear (1978) garnet-biotite geothermometer:

$(X^{bi})_{Ti+Al} = (Ti + Al^{vi})/(Ti + Al^{vi} + Fe + Mg)$
$X_{gro+spe} = X_{gro} + X_{spe}$

geothermometry calculations for Al_2SiO_5-bearing schists. Pressure for staurolite-garnet and biotite-garnet schists is difficult to estimate due to the absence of Al_2SiO_5 polymorphs. Minor fibrolite is present locally in staurolite-garnet schist. Comparison of the temperature range of 500 to 600°C determined for staurolite-garnet schist using garnet zoning, phase equilibria and Thompson's (1976) garnet-biotite geothermometry (see below), yields pressures of approximately 3.8 to 5.5 kb, assuming sillimanite stability. This estimate is subject to the same error as that for sillimanite-orthoclase-muscovite schist. As garnet-biotite temperature calculations are insensitive to pressure inputs, pressures of 5 to 7 kb are used in all geothermometry calculations for staurolite-garnet and biotite-garnet schist.

As part of another study, $\delta^{18}O$ exchange temperatures were calculated for quartz-hornblende, quartz-muscovite and quartz-biotite pairs (R. Rushton, personal communication 1988). The results are summarized in Table 5.5 and discussed in section 5.6.

5.5.2. Garnet-Biotite Geothermometry

Application of the garnet-biotite geothermometer is hindered by the effects of Ca and Mn in garnet and Al and Ti in biotite and the tendency of reaction (18) to re-equilibrate during retrograde metamorphism. High Ca and Mn in garnet leads to preferential Fe^{2+} substitution in garnet (relative to biotite) and a corresponding increase in calculated temperature. Conversely, an increase in octahedral Ti, Al and Fe^{3+} in biotite causes preferential Fe^{2+} substitution in biotite and corresponding decrease in calculated temperature (Dallmeyer, 1974).

Chemical equilibrium assessment indicates that garnet rims and adjacent biotite have retained equilibrium Fe-Mg distribution. Two to six garnet-biotite pairs (that is, garnet rims and adjacent biotite rims) were analysed in each sample. Garnet and biotite were in contact in all cases. Compositional variation is insignificant and thus, average compositions were used in the temperature calculations.

Three calibrations were used: Thompson (1976), Ferry and Spear (1978) and Perchuk and Lavrent'eva (1983). Modifications to the Ferry and Spear (1978) calibration by Newton and Haselton (1981) for Ca in garnet, Ganguly and Saxena (1984) for Ca and Mn in garnet and Indares and Martignole (1985) for Ca in garnet and Ti and Al in biotite were also applied to assess the effects of Ca and Mn in garnet and Al and Ti in biotite. The Goldman and Albee (1977) expression was not used because it is calibrated against the $^{18}O/^{16}O$ geothermometer, which may have reequilibrated during cooling (Ghent et al., 1979).

Thompson's (1976) expression (T_{TH}) is an empirical calibration based on a compilation of natural compositions with temperatures determined from independent sources. Ferry and Spear (1978) experimentally calibrated the geothermometer using synthetic, pure Fe-Mg end-members. They stated that their calibration is probably unsuitable for garnet with $X_{gro+spe} > 0.2$ and biotite $X_{Ti+Al} > 0.15$. Perchuk and Lavrent'eva (1983) (T_{PL}) experimentally calibrated the geothermometer using natural minerals, from 575 to 950°C, at 6 kb. They predicted that $\ln K_D$ is dependent on $(X_{bio})^{Al}$ and observed a dependence of $\triangle V$ on $(X_{bio})^{Al}$ at low pressures. The latter was kept constant during their experiments.

Newton and Haselton (1981) proposed a correction for Ca in garnet and Ganguly and Saxena (1984) proposed a correction for Ca and Mn in garnet. Indares and Martignole (1985) proposed a correction for Al and Ti in biotite in conjunction with Newton and Haselton's (1981) correction for Ca in garnet to the Ferry and Spear (1978) calibration (Appendix 3).

The Newton and Haselton (1981) (T_{NH}), Ganguly and Saxena (1984) (T_{GS}) and Indares and Martignole (1985) ($T_{IM}{}^{A\text{ or }B}$) corrections require an initial pressure and temperature to calculate the temperatures reported in Table 5.2 (see Appendix 3). The corrections are insensitive to the initial T and P input. For example, a change in initial T of 100 Kelvin translates into a calculated temperature difference in the Newton and Haselton (1981) correction of 1 Kelvin and in the Indares and Martignole (1985) correction, a difference of approximately 2 Kelvin. Therefore, the temperature calculated using Ferry and Spear's (1978) calibration (T_{FS}) was used in calculation of T_{NH}, T_{GS} and T_{IM}.

Table 5.2 lists $(K_D{}^{gnt\text{-}bio})_{Fe\text{-}Mg}$, calculated garnet-biotite temperatures and relevant mineral chemistry data. Generally, $T_{NH} \geq T_{IM}{}^{B} > T_{PL} > T_{GS} \geq T_{FS} > T_{TH} > T_{IM}{}^{A}$. Ferry and Spear (1978) reported an experimental error of ± 50°C for their calibration. This error is likely to be greater when error on microprobe analysis is considered and 50°C is taken here as the minimum. Garnet-biotite temperatures calculated with different calibrations for a given sample overlap within error and in most cases fall within the temperature range determined by phase equilibria. This consistency confirms chemical equilibrium between garnet and biotite. Temperatures for sample HP88-255 are low relative to staurolite-garnet schist. However, microtextures and Fe-Mg distribution suggest that garnet and biotite are in disequilibrium. Therefore, temperatures calculated for HP88-255 do not reflect peak metamorphic temperatures.

Although they overlap within error, biotite inclusion - garnet core temperature

Table 5.2.: Temperatures (°C) calculated using garnet-biotite geothermometry; T_{TH}, T_{FS}, $T_{PL}{}^{1}$, $T_{PL}{}^{2}$, T_{NH}, T_{GS}, $T_{IM}{}^{A}$, $T_{IM}{}^{B}$ are temperatures calculated using calibrations or corrections of (respectively) Thompson (1976), Ferry and Spear (1978), Perchuk and Lavrent'eva (1983) for $\Delta V = 0.0246$, and $\Delta V = 0.0577$, Newton and Haselton (1981), Ganguly and Saxena (1984), and Indares and Martignole (1985) models A and B. Values listed are the averages from the range calculated using $P = 5$ to 7 kb. Average T_{FS} are used in calculation of T_{NH} (see Appendix 1). Sample numbers are abbreviated.

SAMPLE	K_D	T_{TH}	T_{FS}	$T_{PL}{}^{1}$	$T_{PL}{}^{2}$	$T_{IM}{}^{A}$	$T_{IM}{}^{B}$	T_{NH}	T_{GS}	$X_{spe+gro}$	$(X^{bi})_{Ti+Al}$
HP171	0.169	550	566	577	577	526	584	585	572	0.13	0.21
HP272	0.152	526	534	558	558	473	540	554	541	0.11	0.18
HP297	0.170	552	568	578	578	518	564	580	576	0.10	0.20
HP255	0.119	471	465	518	522	438	522	537	468	0.21	0.19
HP308	0.206	603	637	614	615	587	630	654	646	0.10	0.22
HP324	0.183	571	594	592	592	535	579	601	602	0.09	0.21
HP325m	0.187	576	601	596	596	523	640	677	605	0.18	0.22
HP325i	0.165	545	558	569	568	489	550	566	565	0.11	0.24
HP5	0.202	596	629	611	611	544	664	637	634	0.16	0.21
HP65	0.218	617	658	627	626	579	639	678	672	0.29	0.21

is 27 to 111°C lower than that for garnet rims and adjacent biotite (sample HP88-325, Table 5.2). Although biotite inclusion chemistry may have been affected partly by volume diffusion, these data suggest that garnet grew under increasing temperature and that biotite adjacent to garnet rims has retained its high-temperature composition. In all samples (excluding HP88-255 and HP88-325), the temperature range from different calibrations is 50°C or less (i.e. within minimum error). Temperature ranges of 72°C and 81°C from different calibrations in samples HP88-255 and HP88-325 may reflect disequilibrium between garnet and biotite as suggested by unsystematic Mg/Fe partitioning (see section 4.3.2).

Temperature calculated using Indares and Martignole's (1985) model A is commonly below the lower temperature limit determined from phase equilibria. Indares and Martignole (1985) based their correction for Ti and Al^{vi} in biotite on biotite that contain less Al and Ti than that in this study and thus, the correction may be inapplicable. Temperature calculated using model B of Indares and Martignole (1985) is 43 to 177°C higher than that calculated using model A. Model B does not account for non-ideality of Fe-Mg solution, which may be important in garnets in this study where alm/pyr is > 3 (cf. Ganguly and Saxena, 1984; Indares and Martignole, 1985). This, together with "insufficient" correction for Ti and Al^{vi} in biotite, makes temperature calculated using Indares and Martignole's (1985) model B expression suspect. Temperatures calculated using Indares and Martignole (1985) models A and B are not considered further.

Temperature calculated using Perchuk and Lavrent'eva's (1983) calibration is insensitive to the value of $\triangle V$ used (Table 5.2; Appendix 3). Although biotite compositions here are similar to those of Perchuk and Lavrent'eva (1983), garnets in this study are more Mn-rich and, excluding sample HP88-255, less magnesian. Therefore, the Perchuk and Lavrent'eva (1983) calibration may not be applicable to samples in this study.

As garnets in high-grade schist contain significant Mn, Ganguly and Saxena's (1984) correction for Ca and Mn is more applicable to this study than Newton and Haselton's (1981) correction for Ca. However, Ganguly and Saxena's (1984) correction has little effect on the calculated temperature relative to the Ferry and Spear calibration which assumes ideality, as T_{GS} differs from T_{FS} by only 3 to 8°C. Ganguly and Saxena's (1984) correction may be invalid for garnets in this study and T_{FS} is used for all pressure calculations and subsequent discussions.

5.5.3. Garnet-Plagioclase-Al_2SiO_5-Quartz Geobarometry

Application of the garnet-plagioclase-Al_2SiO_5-quartz geobarometer (hereafter referred to as garnet-plagioclase geobarometer) is hindered by paucity of data for a_{gro} and a_{anor}. Four calibrations of the geobarometer were used: Ghent (1976), Ghent et al. (1979), Newton and Haselton (1981) and Koziol and Newton (1988). Numerical expressions are given in Appendix 3.

Table 5.3 gives calculated pressures and relevant activities, mole fractions, partial molar volume change at one bar and partial molar volumes and volume changes for the end-member reactions. Partial molar volume of grossular ($\overline{V}_{gro}$) was determined graphically (see Appendix 3).

Ghent et al. (1979) report a resolution of 1.6 kb for the garnet-plagioclase-geobarometer. Error in microprobe analysis will increase this. In subsequent discussion, a minimum error of 2 to 3 kb on this geobarometer is used. In general, $P_{GHideal} > P_{KN} > P_{NH} > P_{GHnon\text{-}ideal}$. Pressure calculated using Newton and Haselton's (1981) original expressions for P^o_{sil} are 400 bars higher than those calculated using the corrected expression for P^o_{sil} determined by Froese (in Ganguly and Saxena, 1984). Pressure for the kyanite-garnet schist ranges from 6 to 7 kb. Pressures for two samples of sillimanite-orthoclase-muscovite schist range from 5 to 8 kb. Sillimanite-orthoclase-muscovite schist in which reaction (14) is not well advanced yields pressures of 5 to 6 kb and sillimanite-orthoclase-muscovite schist in which reaction (14) is nearly complete yields pressures of 6.5 to 8 kb. These results overlap within the estimated error.

All calibrations, excluding Ghent's (1976) which was calculated assuming ideality, are subject to uncertainty of the value for $K\gamma$. In addition, extrapolation of experimental data to natural metamorphic P-T ranges and low Ca in plagioclase and garnet are sources of error. As sillimanite-orthoclase-muscovite schist shows no textural evidence of straddling the kyanite-sillimanite isograd, the empirical correction of Ghent et al. (1979) is probably not applicable to these samples. Variation in pressure using the calibrations of Newton and Haselton (1981) and Koziol and Newton (1988) is within error. As it is unclear which calibration is best applicable to this study, the pressure range determined using all calibrations is used in subsequent discussions. Pressure for the kyanite-garnet schist is taken as 6 to 7 kb and for sillimanite-muscovite-garnet schist as 5 to 7 kb. If the error of ± 2 kb is included, results of this geobarometer provide such a broad range of metamorphic pressure that they are of little use in tectonic reconstructions.

Table 5.3.: (a) Values of parameters used in garnet-plagioclase-Al_2SiO_5-quartz geobarometry. See Table 5.1, Appendix 3, and front of thesis for definitions of parameters. P^o_{NH} and $P^o_{NH^\bullet}$ refer to pressures of the end-member reaction calculated using the expression for P^o_{sil} of Newton and Haselton (1981) and Froese (1984, in Ganguly and Saxena, 1984), respectively. (b) Calculated activities (method of Newton and Haselton, 1981; see Appendix 3) and pressures (in kb) for sillimanite-orthoclase-muscovite schist (HP87-5, HP87-65) and kyanite-garnet schist (HP88-324). Sample numbers are abbreviated.

Table 5.3.a:

Sample	T_{FS} •C	X_{anor}	X_{gro}	V^o_{sil} cal/bar	V^o_{ky} cal/bar	$\bar{V}_{gro}$ cal/bar	$\Delta\bar{V}$ cal/bar	P^o_{NH} bar	$P^o_{NH^\bullet}$ bar	P^o_{KN} bar
HP324	594	.084	.02	---	-1.5815	2.92	-1.6550	11,681	---	12,450
HP325	601	.221	.04	-1.3044	---	2.94	-1.3553	13,585	13,134	13,909
HP5	629	.093	.02	-1.3044	---	2.82	-1.4765	14,244	13,800	14,649

Table 5.3.b:

SAMPLE	a_{anor}	a_{gro}	P_{GH} kb	P_{GH} nid kb	P_{NH} kb	$P_{NH^\bullet}$ kb	P_{KN} kb
HP324	0.023	0.099	6.9	5.9	6.6	---	7.3
HP325	0.044	0.349	6.2	5.0	5.1	4.7	5.4
HP5	0.024	0.106	7.8	6.5	7.2	6.8	7.5

5.5.4. Plagioclase-Biotite-Garnet-Muscovite Geobarometry

Pressures calculated using the plagioclase-biotite-garnet-muscovite geobarometer are given in Table 5.4. This geobarometer is subject to the same error as the garnet-plagioclase geobarometer and to propagation of errors from each equilibrium constant equation. Thus, the error on this geobarometer is greater than for the garnet-plagioclase geobarometer. In addition, this geobarometer is affected by bulk compositional effects where an Al-rich phase (e.g. staurolite) is absent. Ghent and Stout (1981) suggested that even relative pressures may be useful for samples lacking an Al-rich phase. However, this requires that the samples have similar bulk rock compositions. Mineral chemistry indicates that the two samples of biotite-garnet schist analysed in this study (HP88-255, HP88-308) have significantly different bulk compositions and pressures calculated for the biotite-garnet schists are not considered meaningful.

Pressures for staurolite-garnet schist are 4 to 6.5 kb, consistent with 3.8 to 5.5 kb estimated from comparison of temperature estimates with Holdaway's (1971) Al_2SiO_5 phase diagram. The absence of kyanite in staurolite-garnet schist limits pressure to approximately 5 kb at 600°C. A pressure range of 4 to 5 kb is used in subsequent discussions. Ghent and Stout (1981) suggest a standard deviation on calculated pressures of ± 0.8. As error on this geobarometer is greater than that of the garnet-plagioclase geobarometer, a minimum error of ± 3 kb is probable.

5.6. SUMMARY OF METAMORPHIC P-T CONDITIONS

Figure 5.3 shows the peak P-T range determined for the staurolite-garnet and sillimanite-orthoclase-muscovite zones from geothermobarometry and the Al_2SiO_5 phase diagram. The temperature range of 530 to 570°C is consistent with temperature estimated from staurolite-in equilibria and the preservation of normal garnet zonation. An upper temperature limit greater than 600°C indicated by some experimental determinations of staurolite-out reactions is precluded by the preservation of zoning in garnet. Pressures and temperatures calculated for kyanite-garnet schist and sillimanite-orthoclase-muscovite schist are consistent with temperatures estimated from homogeneous garnet zonation profiles and phase equilibria and with pressures indicated by Al_2SiO_5 polymorphs. Peak temperature for kyanite-garnet schist and sillimanite-orthoclase-muscovite schist was ≤ 650°C.

Oxygen isotope temperatures for quartz-biotite, quartz-muscovite and quartz-

Table 5.4.:Pressures calculated for staurolite-garnet and biotite-garnet schists using the plagioclase-biotite-garnet-muscovite geothermometer of Ghent and Stout (1981). See Appendix 1 for definitions of $K_D(1)$ and $K_D(2)$. Sample numbers are abbreviated.

SAMPLE	$K_D(1)$	$K_D(2)$	T_{FS} °C	P_1 kb	P_2 kb
HP171	8,249.96	34.90	566	4.5	4.7
HP272	11,303.08	34.27	534	4.3	4.5
HP297	1,007.81	4.63	568	6.5	6.6
HP255	503.18	0.94	465	6.8	7.0
HP308	6,849.09	53.04	637	4.7	4.8

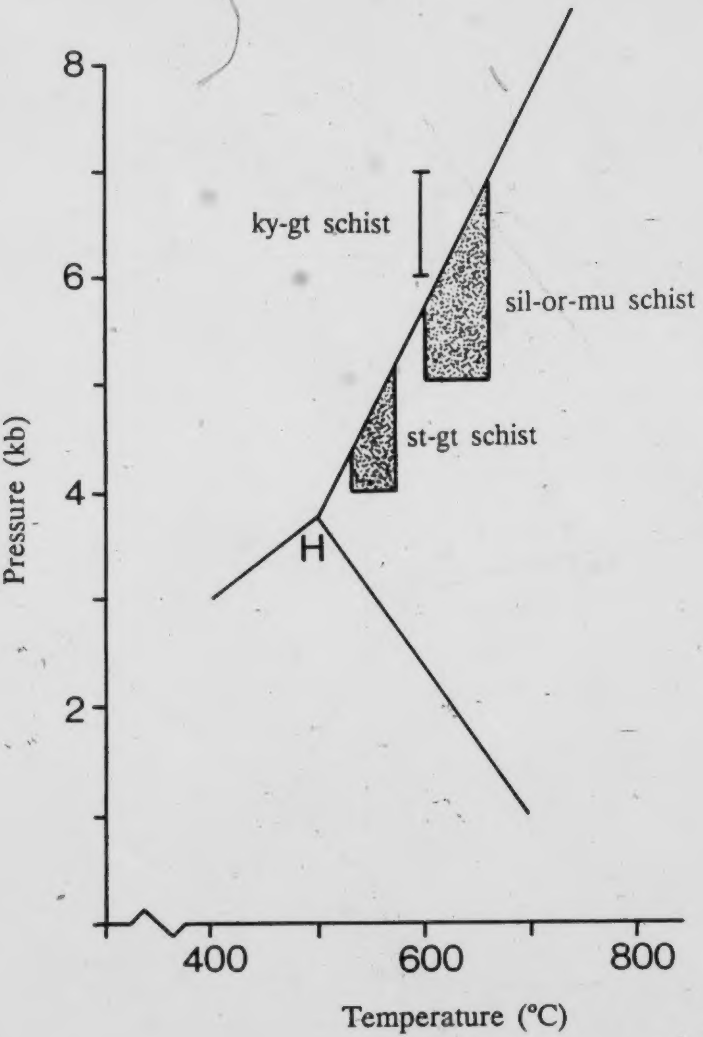

Figure 5.3: P-T conditions for staurolite-garnet, kyanite-garnet and sillimanite-orthoclase-muscovite schist determined using geothermobarometry and stable Al_2SiO_5. For clarity, minimum errors of ± 50 °C and 2-3 kb (see text) are omitted. Al_2SiO_5 diagram modified from Holdaway (1971) denoted by H.

hornblende calculated by R. Rushton (personal communication 1988) for schist, amphibolite and dioritic mylonite in the Horseranch Range are summarized in Table 5.5. Some quartz-biotite temperatures agree within error with garnet-biotite temperatures but most are inconsistent. The quartz-hornblende temperature (HP87-78) is anomalously high and the quartz-biotite temperature for sillimanite-orthoclase-muscovite schist (HP87-5) is anomalously low, which may reflect disequilibrium. The slightly low quartz-muscovite temperature for staurolite-garnet schist (HP88-272) relative to garnet-biotite temperature is attributed to unexplicably large quartz-muscovite fractionation (R. Rushton, personal communication 1988). The quartz-biotite temperature for a dioritic mylonite (sample HP87-28) is consistent with the inferred mylonitization temperature of 300° to 350°C (see Chapters 3 and 6). The quartz-hornblende temperature of 555°C may reflect regional metamorphic conditions.

Temperature increases towards the north-central part of the range. Pressure increases from the staurolite-garnet zone to the sillimanite-orthoclase-muscovite zone and from south to north within the sillimanite-orthoclase-muscovite zone. Pressure for biotite-garnet schist is indeterminate due to the absence of suitable mineral assemblages. In general, pressure increases with temperature, although because all the calculated pressures overlap within error (± 2 to 3 kb), the pressure values are only broadly constrained in the study area. On the basis of phase equilibria and geothermobarometry calculations, pressures of 4 to 5 kb, 6 to 7 kb and 5 to 7 kb are used for the staurolite-garnet schist, kyanite-garnet schist and sillimanite-orthoclase-muscovite schist, respectively, in subsequent discussions. Assuming an average rock density of 2.85 g/cm^3, these pressures correspond to depths of 12 to 15 km, 18 to 21 km and 15 to 21 km, respectively.

As metamorphic P-T conditions for the biotite zone were likely less than those of the staurolite-garnet zone, pressure of 2 to 4 kb and temperature of ca. 300°C to 400°C are assumed for biotite zone rocks.

5.7. P-T CONDITIONS OF MYLONITIZATION AND MAGNITUDE OF DISPLACEMENT

The microstructures described in Chapter 3 and the absence of widespread retrogression in mylonite indicate that mylonitization took place under epidote-amphibolite to lower amphibolite facies conditions with temperature ≥ 300°C. An ^{40}Ar-^{39}Ar cooling age for muscovite "fish" from granite mylonite indicates that

Table 5.5: Oxygen isotope temperatures (°C) for mineral pairs in the Horseranch Range calculated by Rushton (1988, unpublished) using the calibration of Bottinga and Javoy (1973, 1975) and Matsuhisa et al. (1979). Error at ± 3 %

SAMPLE	Qtz-Bi	Qtz-Mu	Qtz-Hb
HP87-5	161 ± 4	----	----
HP87-28A	392 ± 16	----	555 ± 49
HP87-78D	694 ± 50	----	827 ± 124
HP87-105	677 ± 47	----	----
HP88-272	587 ± 29	439 ± 25	----

mylonitization took place at temperature greater than ca. 350°C (see Chapter 6). Assuming a steady state geotherm of 25 to 40°C/km, this implies a depth of 9 to 14 km. The temperature of 658°C (garnet-biotite) calculated for mylonitized sillimanite-garnet schist (HP87-65) agrees with that calculated for sillimanite-orthoclase schist in the schist complex and likely reflects regional metamorphic temperature.

Displacement across the mylonite zone is uncertain due to the absence of a hanging wall - footwall cutoff. The juxtaposition of greenschist facies (upper plate) rocks over amphibolite facies (lower plate) rocks along the northwestern side of the range suggests large vertical displacement. On the basis of data presented in this chapter, the metamorphic temperature change across the mylonite zone is ca. 650°C to 300 - 400°C (avg. difference 300°C) in the north and 500 - 600°C to 300 - 400°C (avg. 200°C) in the south. Assuming a steady-state geothermal gradient of 25 to 40°C/km for both plates and an average motion plane dip of 25° along the stretching lineation, displacement was 18 to 28 km along the northern part of the mylonite zone and 12 to 19 km along the southern part. If an error of ± 50°C on the average temperature difference is included, displacement may be as small as 12 to 19 km in the north and 6 to 9 km in the south. However, if lateral heat conduction from the upper to lower plate was significant (e.g. Buck et al., 1988), these estimates are minimums.

CHAPTER 6
GEOCHRONOMETRY

6.1. INTRODUCTION

To place the thermal and structural history of the Horseranch Range in a regional context and to shed light on the "direct Eocene cooling" versus "Eocene resetting" quaestion in the northern Omineca Belt (see Chapter 1), constraints on the timing of deformation and timing and rate of metamorphic cooling and uplift are required. Therefore, U-Pb dates on zircon and monazite, $^{40}Ar/^{39}Ar$ dates on hornblende, muscovite and biotite and fission track dates and track length measurements on apatite were determined (Table 6.1). Closure temperatures for these systems cover a sufficient temperature range (ca. 425°C) to provide a cooling rate and constraints on the uplift rate. In most cases, U-Pb zircon and monazite dates provide crystallization ages of granitic rocks. Fission track dates give information about the low temperature ($\leq$ ca. 100 - 120°C) history of the schist complex and mylonite. As closure temperatures for $^{40}Ar/^{39}Ar$ in hornblende, muscovite and biotite are higher than the annealing temperature of fission tracks in apatite, the $^{40}Ar/^{39}Ar$ dates provide an independent check on the fission track dates which should be the youngest. Errors quoted throughout are at the 2σ level.

Previous isotopic age data for the Horseranch Range consist of a U-Pb age of 49.0 ± 0.6 Ma for three concordant zircon fractions from a granite mylonite (R. Armstrong, written communication 1990; H. Gabrielse, personal communication 1988) and a 53 Ma ± ca. 10 Ma muscovite K-Ar age from the northern end of the schist complex (Lowden, 1963).

6.2. ANALYTICAL METHODS AND CLOSURE/ANNEALING TEMPERATURES

Samples analysed represent a widely distributed, diverse suite of rock types. Sample locations, numbers and rock types are given in Figure A1.1 and Appendix 1. Minerals were separated from approximately 2 to 35 kg of rock using conventional crushing, grinding, Wilfley table, heavy liquid and magnetic separation techniques.

Table 6.1: Summary of methods and mineral phases used and rock types from which mineral separates were derived for geochronometry study. ^ indicates that only track length measurements were done, i.e. no age was calculated.

SAMPLE	METHOD	MINERAL	ROCK TYPE
HP87-3	U-Pb	zircon	gtz monzonite protomylonite
	F.T.	apatite	
HP87-5	^{40}Ar-^{39}Ar	biotite	sil-or schist
HP87-28A	^{40}Ar-^{39}Ar	biotite	hb-bi protomylonite
HP87-75	F.T.	apatite	granitic orthogneiss (sil-or zone)
HP87-78D	^{40}Ar-^{39}Ar	biotite, hornblende	amphibolite (sil-or zone)
HP87-78E	U-Pb	zircon, monazite	syn- to post-S_2 granite (sil-or zone)
HP87-79	^{40}Ar-^{39}Ar	biotite muscovite	post-S_2 granitic pegmatite (sil-or zone)
HP87-92	^{40}Ar-^{39}Ar	biotite	post-S_2 px diorite (sil-or zone)
HP87-105	^{40}Ar-^{39}Ar	biotite	hb-bi schist (sil-or zone)
HP87-110B	U-Pb	zircon monazite	granite mylonite
	^{40}Ar-^{39}Ar	muscovite	
	F.T.	apatite	
HP-87-139	U-Pb	zircon monazite	post-S_2 granitic pegmatite (sil-or zone)
HP88-159	F.T.	apatite	granite mylonite
HP88-167	U-Pb	zircon, monzonite	granite mylonite
HP88-272	^{40}Ar-^{39}Ar	muscovite	st-gt schist
HP88-296	^{40}Ar-^{39}Ar	muscovite	granitic orthogneiss (st-gt zone)
	F.T.^	apatite	

6.2.1. U-Pb Method

Of the 8 samples processed for U-Pb dating, 5 yielded sufficient amounts of zircon and/or monazite for analysis. Zircon and monazite were analysed from a syn- to post-S_2 granite (sample HP87-78E) and a post-S_2 granite (HP87-139) in the schist complex (Table 6.1). Zircon was analysed from three samples of granitic mylonite (HP87-3; HP87-110; HP88-167); monazite was analysed from two of these samples (HP87-110; HP88-167) (Table 6.1). Zircons and monazites were hand picked from mineral separates at the Geological Survey of Canada (G.S.C.) geochronometry laboratory in Ottawa by R. Parrish on the basis of size, morphology and clarity and are described in Table 6.2. Photographs of mineral separates are included in Appendix 2. Where possible, mineral grains with abundant inclusions were avoided. Overall, morphologies are typical of igneous zircon and monazite (e.g. Parrish, 1990; Pupin, 1980). Zircon and monazite U-Pb analyses were carried out by R. Parrish at the G.S.C., Ottawa. Analytical techniques are described by Parrish et al. (1987) and summarized in Appendix 2.

Closure temperatures published for U-Pb in zircon (Tc_{zir}) are > 800°C for nonmetamict zircon (Mattinson, 1982). Monazite U-Pb closure temperature (Tc_{mz}) range from 530 to 730°C (Köppel and Grünenfelder, 1975; Copeland et al., 1988; Parrish and Roddick, 1985; Parrish, 1988). Parrish (1990) reviewed the constraints on monazite U-Pb closure temperature and noted that Tc will depend in part on composition and grain size. On the basis of available data, $Tc_{mz} = 725 \pm 25$°C is reasonable (Parrish 1990) and is used here.

6.2.2. $^{40}Ar/^{39}Ar$ Method

Hornblende, biotite and muscovite were analysed by the $^{40}Ar/^{39}Ar$ method by the author at Dalhousie University in Halifax. Analytical procedures used are described by Reynolds et al. (1987) and Muecke et al. (1988) and are summarized in Appendix 2. All analysed minerals formed or recrystallized during regional metamorphism (Chapters 3 and 5), except in samples HP87-79, HP87-110 and HP87-92. HP87-79 consists of muscovite and biotite books from a post-S_2 pegmatitic, muscovite-biotite-garnet granite. Sample HP87-110 comprises igneous muscovite from a two-mica, C-S granite mylonite. Sample HP87-92 consists of biotite from a post-S_2, coarse-grained, pyroxenitic diorite (Table 6.1).

$^{40}Ar/^{39}Ar$ closure temperature varies with cooling rate and in biotite, with

Table 6.2: Zircon and monazite descriptions. See Appendix 2 for photographs of minerals.

SAMPLE	FRACTION	DESCRIPTION	ABRADED	n
HP87-3	zircon-A	clear, long, euhd to suhd, acicular incl, no cores	mod	7
	zircon-B	clear, flatish, subhd, acicular incl, no cores	mod	7
	zircon-C	clear, subhd to euhd, acicular incl, no cores	mod	15
HP87-78E	zircon-A	cloudy, very long, subhd, abundant incl, no cores	none	7
	monazite-A	clear, large, subhd, minor incl	none	5
	monazite-B	clear, small, subhd, minor incl	none	7
HP87-110B	zircon-A	all very cloudy, subhd to euhd, some frag & cores; large greenish, clear subhd frag. was analysed	none	1
	monazite-A	clear, small, euhd, high quality, very minor incl	none	7
	monazite-B	clear, rhombic, subhd, larger than A	none	3
HP87-139	zircon-A	all very cloudy, subhd, some frag., large frag. analysed, no cores	none	2
	monazite-A	fairly clear, subhd, some incl	none	3
	monazite-B	clear, small, euhd, some incl	none	6
HP-167	zircon-A	clear, long, subhd, some frag., no cores	none	8
	monazite-A	clear, small, euhd	none	8
	monazite-B	clear, large, euhd, some incl	none	4

composition. Tc may also be affected by grain size and strain state (e.g. Maluski, 1978; Harrison, 1983). Grain size is interpreted to have had little effect in this study because grain size is greater than commonly cited diffusion radii of < 200 μm (e.g. Harrison et al., 1985). The effect of strain state in this study, if any, is unknown. With the exception of muscovite and biotite from mylonite, the minerals analysed from pelitic schist and amphibolite contain no subgrains which indicates that the minerals were entirely recrystallized during regional metamorphism. Microtextures in mylonite indicate that strain is partitioned mainly into the matrix resulting in relatively undeformed mica "fish" (excluding the recrystallized tails).

The effect of composition on Tc in muscovite has not been studied, and in hornblende is unclear (e.g. Harrison, 1981; Onstott and Peacock, 1987; Berry and McDougall, 1986). For a moderate cooling rate of 100°C/Ma, Tc_{hb} is ca. 500 to 550°C. Therefore, Tc_{hb} of 525 ± 25°C is used here. For Tc_{mu}, the value of 350°C suggested by McDougall and Harrison (1988) for unspecified "moderate" (= 100°C/Ma?) cooling rates is used here. Biotite closure temperature is commonly between 300 and 350°C for moderate cooling rates (McDougall and Harrison, 1988). Annite content in biotite analysed in this study are: HP87-5 = 64% annite, HP87-28 = 56%, HP87-78D = 34%, HP87-92 = 47% and HP87-105 = 34%. Assuming a diffusional radius of 150 microns, Harrison et al. (1985) calculated closure temperatures of 340°C, 310°C and 280°C at cooling rates of 100°C/Ma, 10°C/Ma and 1°C/Ma for a biotite with 56 % annite. Therefore, 350°C is a reasonable upper limit on Tc_{bi} for biotite samples with annite-contents of 56 and 64% whereas Tc_{bi} will be lower (likely ca. 300°C) for biotite with 47% and 34% annite. An intermediate value of 325 ± 25°C is used here for Tc_{bi}; this has no effect on the conclusions drawn from the $^{40}Ar/^{39}Ar$ data.

6.2.3. Fission Track Method

Apatite from two samples of C-S granitic mylonite (samples HP87-3, HP87-110) and from two samples of granitic orthogneiss in the schist complex (HP87-75, HP87-296) was analysed by the fission track method by A. Grist at Dalhousie University in Halifax (Table 6.1). Theory of the method and analytical procedures are described in Appendix 2.

Annealing temperature in apatite is dependent on the duration of heating and mineral composition (Naeser et al., 1990). Annealing experiments and empirical observations in drill holes show that complete annealing of fission tracks in F-apatite, Sr-F apatite and OH-apatite takes place at 100 to 120°C (T_a) for heating durations of 1 to 100 Ma (e.g. Green et al., 1989a; Naeser et al., 1990). T_a in Cl-apatite may be up to 30°C higher than in other apatite (Naeser et al., 1990). Partial annealing of fission tracks in F-, Sr-F- and OH- apatite takes place between T_a and the complete retention temperature (T_r) for heating durations of 1 to 100 Ma. T_r for F-, F-Sr-, OH-apatite is ca. 50°C (e.g. Naeser, 1981; Green et al., 1989b; Naeser et al., 1990). The composition of apatite in this study is unknown. It is assumed that T_a is 110 ± 10°C, corresponding to non-Cl-apatite. This assumption has little effect on the calculated cooling rates and does not alter the basic conclusions drawn from the data.

6.3. RESULTS

6.3.1. U-Pb

U-Pb data are given in Table 6.3 and shown on concordia plots in Figures 6.1 and 6.2. All zircons, excluding those from quartz monzonite mylonite (HP87-3) are slightly to strongly discordant. All monazites are reversely discordant, plotting above concordia. Reverse discordance is a common characteristic of igneous monazite (e.g. Schärer, 1984; Schärer et al., 1986; Copeland et al., 1988; Parrish et al., 1988; Sevigny et al., 1989). It is attributed to U-Th fractionation between the crystallizing monazite and the magma (which is assumed to be in secular equilibrium) which results in the incorporation of an initial excess of ^{230}Th in monazite. The excess ^{230}Th decays to ^{206}Pb resulting in excess or unsupported ^{206}Pb (Schärer, 1984). Consequently, ^{238}U/^{206}Pb dates are high, ^{207}Pb/^{206}Pb dates are low and only the ^{235}U/^{207}Pb dates can be interpreted to have any geologic significance (Schärer, 1984; Parrish, 1990). Similarly, Th-poor minerals such as zircon will show a deficit in ^{206}Pb due to an initial deficiency in ^{230}Th and U-Pb dates will have opposite trends to that of monazite (i.e. ^{238}U/^{206}Pb ages will be low and ^{207}Pb/^{206}Pb ages will be high) (Schärer, 1984). The effect of ^{230}Th disequilibrium is important for monazite ≤ 500 Ma as the excess ^{206}Pb/^{238}U age is large relative to analytical uncertainties on measured U/Pb ratios (Parrish, 1990). Corrections for ^{230}Th disequilibrium in monazite and zircon can be made assuming that (1) the magma is in secular equilibrium, (2) the Th/U of the whole rock is equal to that of the magma from which monazite crystallized, (3) the mineral behaved as a system closed to U and Th and (4) the ^{207}Pb/^{235}U age approximates the crystallization age of the mineral (Schärer, 1984). Implicit in the

Table 6.3: U-Pb analytical data for the Horseranch Range. Z= zircon, M = monazite.

Mineral	Wt. mg	U ppm	Pb* ppm	$^{206}\text{Pb}^{\bullet}/^{204}\text{Pb}$	Pb_c● pg	^{208}Pb** %	$^{206}\text{Pb}/^{238}\text{U}$^	$^{207}\text{Pb}/^{235}\text{U}$^	Corr. Coeff.	$^{207}\text{Pb}/^{206}\text{Pb}$^
HP87-3										
Z-A	0.079	243	2.24	160	71	20.3	0.008166 ± 0.43%	0.052909 ± 1.20%	0.66	0.04699 ± 1.00%
Z-B	0.064	241	2.29	554	15	22.1	0.008200 ± 0.18%	0.052871 ± 0.25%	0.65	0.04676 ± 0.19%
Z-C	0.085	272	2.31	628	20	12.7	0.008229 ± 0.34%	0.053643 ± 0.55%	0.54	0.04728 ± 0.46%
HP87-78E										
Z-A	0.035	5650	83.9	1202	174	0.6	0.016385 ± 0.09%	0.109296 ± 0.17%	0.76	0.04838 ± 0.12%
M-A	0.079	4789	341	3099	138	77.3	0.017789 ± 0.12%	0.117971 ± 0.14%	0.92	0.04810 ± 0.05%
M-B	0.054	4697	364	2573	113	79.1	0.017801 ± 0.11%	0.118002 ± 0.13%	0.87	0.04808 ± 0.07%
HP87-110										
Z-A	0.084	15853	109	2138	305	0.2	0.007659 ± 0.13%	0.049842 ± 0.16%	0.89	0.04720 ± 0.07%
M-A	0.063	15557	234	3703	135	52.3	0.007945 ± 0.10%	0.049968 ± 0.12%	0.91	0.04562 ± 0.05%
M-B	0.064	15141	230	[illegible]432	144	52.7	0.007969 ± 0.31%	0.049831 ± 0.32%	0.98	0.04535 ± 0.06%
HP87-139										
Z-A	0.094	4506	69.2	655	717	0.4	0.016979 ± 0.17%	0.113250 ± 0.31%	0.73	0.04838 ± 0.22%
M-A	0.035	22694	351	3688	126	46.6	0.009155 ± 0.10%	0.058755 ± 0.12%	0.92	0.04654 ± 0.05%
M-B	0.045	18672	344	2658	211	48.3	0.001526 ± 0.13%	0.068394 ± 0.16%	0.88	0.04713 ± 0.07%
HP88-167										
Z-A	0.008	4239	39.4	703	31	3.3	0.009825 ± 0.10%	0.087623 ± 0.15%	0.77	0.06468 ± 0.09%
M-A	0.047	7065	151	1756	94	67.7	0.007646 ± 0.14%	0.048837 ± 0.18%	0.80	0.04633 ± 0.11%
M-B	0.063	7858	161	2235	109	66.1	0.007678 ± 0.22%	0.048869 ± 0.24%	0.94	0.04616 ± 0.08%

* Radiogenic Pb, corrected for spike, fractionation, blank and common Pb
• Measured ratio, corrected only for spike and fractionation
● Total common Pb in analysis
** Radiogenic ^{208}Pb, expressed as % of total radiogenic Pb
^ Uncertainties are 1 sigma %

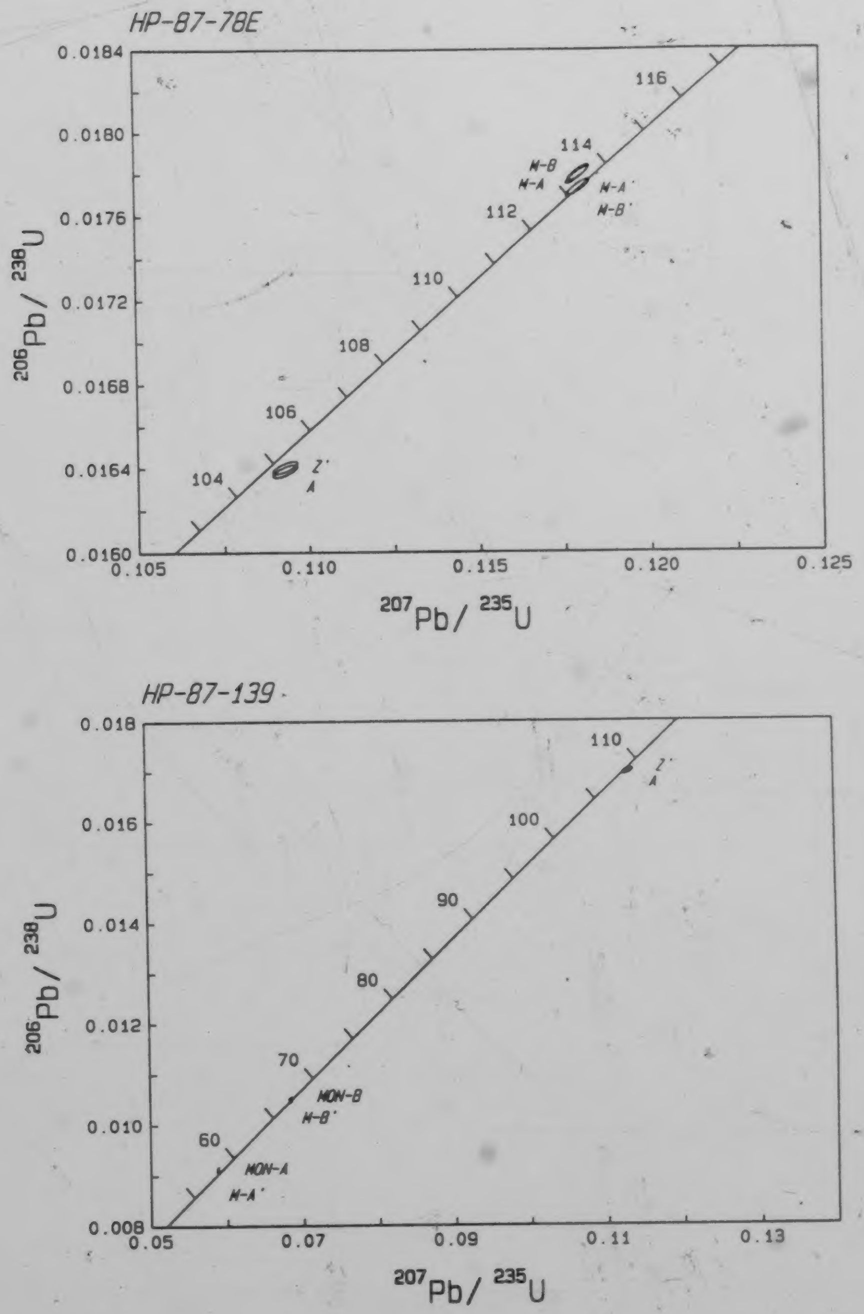

Figure 6.1: Concordia diagram showing the results of U-Pb analyses of zircon (Z) and monazite (M) from syn- to post-S_2 granite and post-S_2 granitic pegmatite in the schist complex. M-A', M-B', and Z-A' indicate analyses corrected for 230Th disequilibrium.

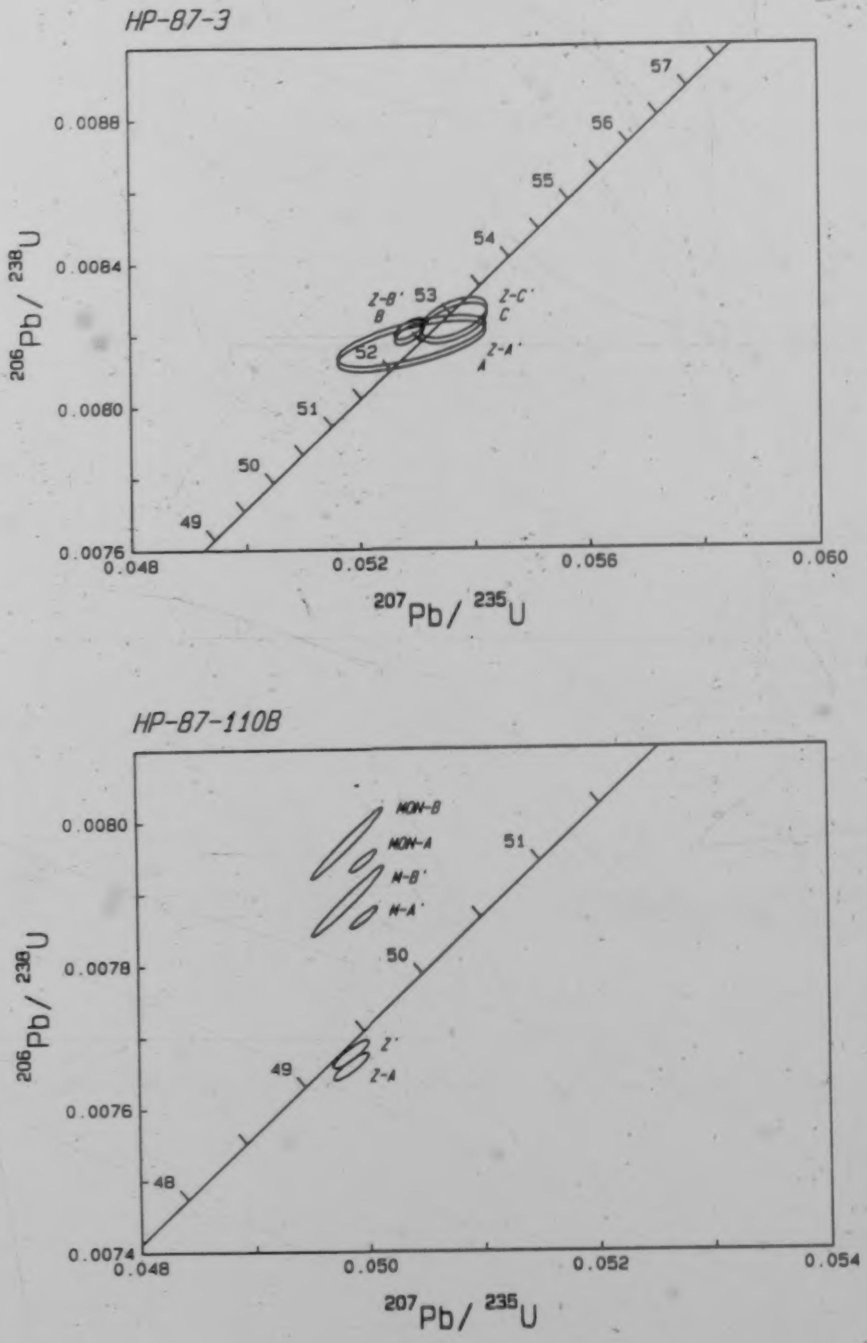

Figure 6.2: Concordia plot showing the results of U-Pb analyses of zircon (Z) and monazite (M) from granitic mylonites in the Horseranch Range. M-A', M-B', and Z' indicate analyses corrected for ^{230}Th disequilibrium.

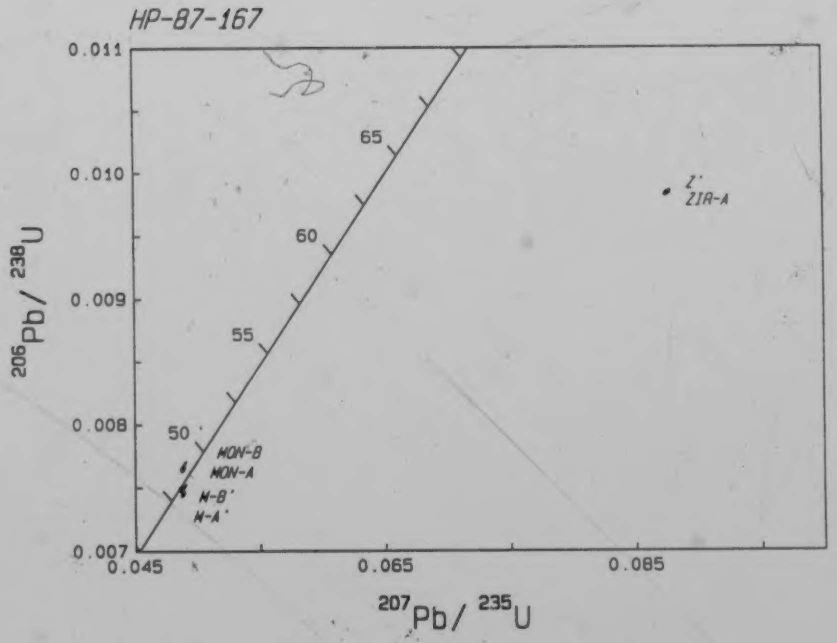

Figure 6.2: (continued).

fourth assumption is that the mineral has no inheritance and has not lost Pb. These corrections (Schärer,1984; Parrish,1990) are applied to this study and are summarized in Appendix 2.

Schärer (1984) noted that ^{231}Pa could produce a slight excess of ^{207}Pb in monazite, assuming that Pa has a similar geochemical behaviour to Th. However, the validity of this assumption is unknown (Parrish, 1990) and Pa/U is difficult to measure due to the lack of a stable Pa isotope. Therefore, in the following discussion, the ^{207}Pb/^{235}U date is considered to be unaffected by ^{231}Pa disequilibrium (cf. Parrish, 1990).

Most of the U-Pb dates obtained for this study are ≤ 120 Ma (see below). Interpretation of U-Pb systematics in such young samples is complicated by the coincidence of linear Pb loss trajectories and the concordia curve which is nearly linear between 0 and 100 Ma. As a result, highly disturbed minerals may yield apparently concordant ages and determination of upper and lower intercept ages is precluded. To interpret U-Pb systematics in such samples, several fractions of the same mineral must be analyzed (Schärer et al., 1986). In this study, zircon from all but sample HP87-3 was too sparse and of too poor quality to permit analysis of more than one fraction. However, two monazite fractions were analysed for every sample.

(i) Granite in the Schist Complex

Figure 6.1 shows concordia plots for zircon and monazite from a syn- to post-S_2 granite (HP87-78E) and a post-S_2 granitic pegmatite (HP87-139) in the schist complex. Zircon shows slight Pb loss in both samples consistent with its high uranium content and cloudy (metamict?) appearance (Tables 6.2 and 6.3; Plates A2.4 and A2.5). The uncorrected ^{206}Pb/^{238}U and ^{207}Pb/^{235}U zircon ages in both samples HP87-78E and HP87-139 are ca. 105 Ma and 109 Ma, respectively (Table 6.4). Correction for ^{230}Th disequilibrium in zircon increase the ^{206}Pb/^{238}U date by 0.1 Ma in both samples and decreases the ^{207}Pb/^{206}Pb date by 2.3 Ma in sample HP87-139 and 2.5 Ma in sample HP87-78E. The corrected ^{207}Pb/^{206}Pb date is 115 Ma in both samples, suggesting that they have the same crystallization age. Zircon remains weakly discordant despite the correction, which may reflect the effect of inheritance which is a common phenomenon in zircon from leucogranites (e.g. Parrish, 1990). The 115 Ma date therefore, is a maximum estimate of the crystallization age for these samples.

Monazite ^{207}Pb/^{235}U ages for two fractions from HP87-78E overlap within error at 114 Ma. Correction for disequilibrium moves the monazite fractions in sample

HP87-78E to concordia and yields an age of 113 Ma (Table 6.4, Figure 6.1). This age is the preferred crystallization age of the granite because: (1) the U-Pb zircon age of 115 Ma is likely a maximum estimate of the crystallization age, (2) $^{207}Pb/^{235}U$ dates for both monazite fractions in HP87-78E agree within error, suggesting closed system behaviour of U and Pb and an absence of inheritance in this mineral and (3) monazite has a high closure temperature (ca. 725°C) with respect to U and Pb and thus, begins to accumulate radiogenic Pb (Pb^*) early in the cooling history of the granite. Therefore, the crystallization age of the syn- to post-S_2 granite (sample HP87-78E) and the post-S_2 pegmatitic granite (HP87-139) is taken as 113 Ma.

Correction for ^{230}Th disequilibrium in monazite in the pegmatitic granite moves monazite fraction A towards concordia, decreasing the $^{206}Pb/^{238}U$ date to 58 Ma and increasing the $^{207}Pb/^{206}Pb$ date to 42 Ma. These data indicate that there is under-correction for ^{230}Th disequilibrium in fraction A (see below). Correction for ^{230}Th disequilibrium moves monazite fraction B to concordia, decreasing the $^{206}Pb/^{238}U$ date to 67 Ma and increasing the $^{207}Pb/^{206}Pb$ date to 71 Ma (Table 6.4, Figure 6.1). The $^{207}Pb/^{235}U$ ages for fractions A and B are 58 and 67 Ma, respectively. Analysis of more monazite fractions is required to assess whether the post-correction concordancy of fraction B is coincidence or real.

Under-correction for ^{230}Th disequilibrium as observed in monazite fraction A of HP87-139 indicates that f is too low and, assuming that monazite has remained closed to Th and U, indicates that the Th/U of the whole rock is higher than Th/U of the magma from which monazite crystallized. Parrish (1990) postulated several explanations for low f values including post-crystallization U-leaching, monazite inheritance, and early fractionation of Th-rich phase. The U-content in monazite in HP87-139 is anomalously high (18,672 to 22,694 ppm: Table 6.3) compared to average U-contents of 1,000 to 4,000 ppm observed in monazite in leucogranites (cf. Parrish, 1990), but is characteristic of monazite in pegmatites (e.g. Murata et al., 1958; Fleischer, 1965; Parrish, 1990: Table 1; van Breemen et al., 1990: Table 1). As most of the U, Th and rare earth elements are contained in accessory phases in granitic rocks (e.g. Gromet and Silver, 1983; Fourcade and Allègre, 1981; Miller and Mittlefehldt, 1982; Yeliseyeva, 1977), U (and Th) will probably be inhomogeneously distributed in the sample, particularly where the accessory mineral is U- or Th-rich. Therefore the measured Th/U of the whole rock powder may mis-represent the true Th/U of the whole rock causing over- or under-correction for ^{230}Th disequilibrium. This problem will be magnified if the sample is coarse-grained or pegmatitic. Therefore, under-correction in HP87-139 is attributed to analysis of whole rock powder that mis-

Table 6.4: ^{230}Th disequilibrium correction data and age data. Z = zircon, M = monazite, w.r. = whole rock

Mineral	Th/U	f	$\frac{^{206}Pb}{^{238}U}$	$\frac{^{207}Pb}{^{206}Pb}$	uncorrected ages^			corrected ages^	
					$\frac{^{206}Pb}{^{238}U}$	$\frac{^{207}Pb}{^{235}U}$	$\frac{^{207}Pb}{^{206}Pb}$	$\frac{^{206}Pb}{^{238}U}$	$\frac{^{207}Pb}{^{206}Pb}$
HP87-3									
Z-A	0.8304	0.1150	0.008181	0.046905	52.4 ± 0.4	52.3 ± 1.3	48.8 ± 47.7	52.5 ± 0.4	44.4 ± 47.7
Z-B	0.9275	0.1284	0.008215	0.046678	52.6 ± 0.2	52.3 ± 0.3	37.2 ± 9.0	52.7 ± 0.2	32.8 ± 9.0
Z-C	0.4768	0.0660	0.008245	0.047187	52.8 ± 0.4	53.1 ± 0.6	63.2 ± 22.1	52.9 ± 0.4	58.7 ± 22.1
w.r.	7.222 (Th = 13 ppm, U = 2.1 ppm)								
HP87-78E									
Z-A	0.0201	0.0083	0.016402	0.048329	104.8 ± 0.2	105.3 ± 0.3	117.9 ± 5.5	104.9 ± 0.2	115.4 ± 5.5
M-A	11.2	4.634	0.017728	0.048263	113.7 ± 0.3	113.2 ± 0.3	104.0 ± 2.5	113.3 ± 0.3	112.2 ± 2.5
M-B	12.45	5.151	0.017731	0.048268	113.7 ± 0.2	113.3 ± 0.3	103.2 ± 3.1	113.3 ± 0.2	112.4 ± 3.1
w.r.	2.417 (Th = 2.9 ppm, U = 1.2 ppm)								
HP87-110									
Z-A	0.007059	0.0112	0.007676	0.047093	49.2 ± 0.1	49.4 ± 0.2	59.3 ± 3.5	49.3 ± 0.1	53.9 ± 3.5
M-A	3.5765	5.6806	0.007866	0.046072	51.0 ± 0.1	49.5 ± 0.1	-22.7 ± 2.4	50.5 ± 0.1	1.4 ± 2.4
M-B	3.6307	5.7667	0.007889	0.045812	51.2 ± 0.3	49.4 ± 0.3	-36.8 ± 2.7	50.7 ± 0.3	-12.3 ± 2.7
w.r.	0.6296 (Th = 3.4 ppm, U = 5.4 ppm)								
HP87-139									
Z-A	0.01263	0.0204	0.016995	0.048330	108.5 ± 0.4	108.9 ± 0.6	117.7 ± 10.4	108.6 ± 0.4	115.4 ± 10.4
M-A	2.846	4.5977	0.009095	0.046853	58.8 ± 0.1	58.0 ± 0.1	25.9 ± 2.3	58.4 ± 0.1	41.7 ± 2.3
M-B	3.055	4.9354	0.010460	0.047423	67.5 ± 0.2	67.2 ± 0.2	55.6 ± 3.6	67.1 ± 0.2	70.6 ± 3.6
w.r.	0.619 (Th = 1.3 ppm, U = 2.1 ppm)								
HP88-167									
Z-A	0.1179	0.2183	0.009838	0.064597	63.0 ± 0.1	85.3 ± 0.2	763.9 ± 3.9	63.1 ± 0.1	761.2 ± 3.9
M-A	6.831	12.65	0.007450	0.047544	49.1 ± 0.1	48.4 ± 0.2	14.6 ± 5.0	47.9 ± 0.1	76.6 ± 5.0
M-B	6.347	11.75	0.007497	0.047276	49.3 ± 0.2	48.4 ± 0.2	6.1 ± 3.7	48.2 ± 0.2	63.2 ± 3.7
w.r.	0.5400 (Th = 2.7 ppm, U = 5.0 ppm)								

^ errors at 1 sigma

represents the true composition of the whole rock.

The monazite U-Pb ages in HP87-139 are significantly younger than those for monazite in HP87-78E which was collected only 400 m away and which is interpreted to have the same crystallization age. The discrepancy in monazite ages between these samples could reflect a difference in U-Pb systematics between samples and/or a difference in their thermal history. The igneous morphology of the monazites in HP87-139 precludes the possibility that they are metamorphic (Table 6.2; Plate A2.4). Monazites in HP87-139 are slightly cloudier, contain more inclusions and approximately four times more U than monazites in HP87-78E. The high uranium content may have caused sufficient radiation damage to increase its susceptibility to Pb loss (effectively lowering its closure temperature). As samples HP87-78E and HP87-139 were collected at localities only 400 m apart, any difference in thermal history between the samples must have been localized, such as later granite emplacement. Fine-grained biotite granite of unknown age is exposed ca. 80 m (horizontal distance) from sample locality HP87-139. Although granites with crystallization ages younger than 113 Ma were not detected in the schist complex by isotopic study, field relations indicate that younger granite (post-$^2F_3$ and hence post-S_2 and post-regional metamorphism) is present in the schist complex; granitic pegmatite with Eocene $^{40}Ar/^{39}Ar$ muscovite and biotite cooling ages (section 6.3.2) is also present. Eocene granite is widespread in the mylonite zone (see below). In addition, Eocene granite intrusive into mid-Cretaceous granite is a well documented phenomenon in the northern Omineca Belt (e.g. Wanless et al., 1969; Hunt and Roddick, 1987, p.12). Therefore, the monazite dates for sample HP87-139 are interpreted to reflect strong partial resetting by the thermal effect of later (probably Eocene) granite emplacement, facilitated by very high U-content in monazite. The absence of monazite resetting in sample HP87-78E indicates that it was not affected by the effects of later granite and/or that monazite was less susceptible to resetting due to lower U-content.

(ii) Granitic Mylonites

Mylonitization can disturb U-Pb systematics in zircon if temperature or fluid pressure is high and commonly results in Pb-loss and U-gain. In these cases, zircon is typically fragmented, in some cases along weak, radiation- damaged zones, and has pitted surfaces or porous zircon overgrowths (e.g. Sinha and Glover, 1978; Lindh and Schöberg, 1988; Wayne and Sinha, 1988). Mylonitization in the Horseranch Range took place under moderate temperature (≥ 350°C) and apparently low fluid-rock ratios (Chapter 2). The samples analysed in this study contained only a small percentage of zircon fragments, most of which could result from sample preparation (Plates A2.1, A2.2 and A2.3). Therefore, the effects of mylonitization on U-Pb systematics in samples of this study are assumed to be negligible. This assumption is supported by the small range of U-Pb crystallization ages (ca. 2 Ma) determined for C-S granitic mylonites (see below).

Figure 6.2 shows concordia plots for zircon and monazite from granitic mylonites. Two of the three zircon fractions from quartz monzonite mylonite (HP87-3) are concordant and yield an average, corrected U-Pb date of 53 Ma which is inferred to be the crystallization age of this sample. The reason for the slight reverse discordance in fraction B is unclear and may be an analytical artifact. As the U-Pb ages overlap within error with those of the other fractions, this discrepancy is considered geologically insignificant.

Zircon from granite mylonite sample HP87-110 shows slight discordance which may record some Pb loss. The zircon contains visible cores which may reflect inheritance, such that the corrected $^{207}Pb/^{206}Pb$ age of 54 Ma is a maximum limit on the crystallization age, despite possible Pb loss. The $^{207}Pb/^{235}U$ ages for both monazite fractions in HP87-110 agree within error at 49.5 ± 0.1 Ma and 49.4 ± 0.3 Ma (ca. 50 Ma). The corrected $^{206}Pb/^{238}U$ dates for both monazite fractions agree within error and average 51 Ma, approximately 1 Ma older than the $^{207}Pb/^{235}U$ dates. The corrected $^{207}Pb/^{206}Pb$ dates remain anomalously low or negative (Table 6.4). This discrepancy is attributed to an under-correction for ^{230}Th disequilibrium.

As both monazite and zircon are U-rich, the under-correction likely indicates that the measured Th/U of the whole rock powder mis-represents the true Th/U of the whole rock as discussed with reference to HP87-139. This may be further complicated by an *increase* in the f-value by inheritance in zircon which results in the Th/U whole rock value being less than that of the magma from which the monazite (and zircon) crystallized. Whatever the cause for under-correction in monazite, the $^{207}Pb/^{235}U$ ages for both fractions are consistent with the inferred maximum crystallization age of coexisting zircon and with crystallization ages of other granitic mylonites in the zone. Therefore, 50 Ma is taken as the crystallization age of this sample.

Zircon from granite mylonite sample HP88-167 is strongly discordant, reflecting a strong inherited component despite the absence of visible cores (cf. Pidgeon and Aftalion, 1978; Schärer and Allègre, 1983). The corrected $^{207}Pb/^{206}Pb$ age is 761 Ma which indicates that the inherited component is at least Proterozoic (Table 6.4).

Assuming a simple system in which (1) zircon contains only two U-Pb components, i.e. an inherited component and a component the same age as the crystallization of the granite (= monazite age, ca. 50 Ma), (2) the inherited component in zircon has not experienced Pb loss, and (3) neither monazite or zircon have lost Pb since the granite crystallized, that is, since ca. 50 Ma, a regression line through monazite fractions A and B and zircon may approximate the age of the inherited component. Regression yields an upper intercept of 1917 ± 12 Ma (M.S.W.D. = 2.2872). This age is consistent with 1.9 to 2.1 Ga ages reported for basement rock along the western margin of ancient North America (see Evenchick et al., 1984; Aleinikoff et al., 1986) and is slightly younger than the 2.2 Ga zircon provenance age determined for psammitic schist in the schist complex of the Horseranch Range (Erdmer and Baadsgaard, 1987). Although preliminary, this result suggests that the source area of some Horseranch granites was Precambrian basement. Alternatively, if the inherited component had undergone Pb-loss prior to incorporation into zircon, i.e. the inherited component is older than assumed above, the granite could have been derived from partial melting of the schist complex containing 2.2 Ga detrital zircon.

The corrected $^{206}Pb/^{238}U$ and $^{207}Pb/^{235}U$ dates for monazite fraction A are ca. 48 Ma and the corrected $^{207}Pb/^{206}Pb$ date is ca. 77 Ma,. The corrected $^{206}Pb/^{238}U$ and $^{207}Pb/^{235}U$ dates for monazite fraction B are ca. 48 Ma and $^{207}Pb/^{206}Pb$ dates is ca. 63 Ma (Table 6.4). The high $^{207}Pb/^{206}Pb$ ages relative to the U/Pb ages may reflect Pb loss or over-correction for ^{230}Th disequilibrium due to an erroneously high f-value. Significant Pb loss is unlikely as the $^{207}Pb/^{235}U$ ages for fractions A and B agree and because the ages are only 1 to 2 Ma less than crystallization ages determined for other granitic mylonites. Therefore, the over-correction is attributed to an erroneously high f-value due to zircon inheritance which caused the measured U-content of the whole rock to be greater, and the measured Th/U of the whole rock to be less, than that of the magma from which monazite crystallized. Therefore, the $^{207}Pb/^{235}U$ monazite age of ca. 48 Ma (i.e. 47.9 ± 0.1 Ma and 48.2 ± 0.2 Ma: Table 6.4) is taken to be the crystallization age of this sample.

(iii) Usefulness of the ^{230}Th Disequilibrium Correction

The complexities encountered in application of the ^{230}Th disequilibrium correction in this study indicate that it is of limited use and that the corrected ages must be interpreted with caution. The assumption that the measured Th/U in the whole rock is equal to that of the magma from which monazite crystallized is interpreted to be invalid in this study due to inheritance in zircon in one sample and to high U in monazite in two other samples. Common geological processes such as crystal fractionation and alteration (U-leaching) increase the probability that the assumption will be invalid in many cases. As the $^{207}Pb/^{235}U$ ages are unaffected by ^{230}Th disequilibrium, the correction is not required to gain information regarding the crystallization and thermal history of the sample. However, analysis of two or more mineral phases and at least two monazite fractions is crucial to assessing the geological significance of the $^{207}Pb/^{235}U$ monazite ages. Although where sufficient, the correction adds strength to the interpretation of the crystallization age based on $^{207}Pb/^{235}U$ monazite ages and on other mineral phases (e.g. HP87-78E), it adds no new information and therefore, is not very useful.

6.3.2. $^{40}Ar/^{39}Ar$

$^{40}Ar/^{39}Ar$ age spectra (6 biotite, 4 muscovite and 1 hornblende) are shown in Figure 6.3. The quoted errors (2σ) include the uncertainty in the measurement of the parameter J but do not include error in the assumed age (519 Ma) of the hornblende standard (Appendix 2). Exclusion of the latter decreases the error of all dates by the same amount and does not affect the conclusions drawn from the data.

An age plateau is one where at least two successive heating steps which represent more than 50% of the total gas released have apparent ages that are identical within experimental uncertainty at the 2σ level (Fleck et al., 1977). Accordingly, the spectrum for hornblende HP87-78D has a 43.5 ± 2.2 Ma plateau (5 steps representing 83% of the total ^{39}Ar released). Three of the four muscovite spectra have plateau ages (HP87-110: 43.8 ± 1.2 Ma, 3 steps, 67% of the gas; HP88-272: 44.7 ± 1.0 Ma, 4 steps, 66 %; HP88-296: 44.4 ± 0.4 Ma, 7 steps, 84%). The fourth muscovite, HP87-79, did not yield a plateau; its total gas age (excluding the final small step) is 43.5 ± 0.6 Ma. These dates agree within error with the hornblende plateau age. Two of the six biotite spectra have age plateaus (HP87-92: 45.7 ± 0.4 Ma, 7 steps, 84% of the gas; HP87-105: 43.2 ± 1.2 Ma, 6 steps, 78%). The remaining four spectra (HP87-5; HP87-28A; HP87-78D, HP87-79) have low apparent age "saddles" over the middle portion of the gas release (Figure 6.3).

Saddles in biotite spectra are common but not well understood and have been attributed to gas released from two distinct phases of biotite (York and Lopez-Martinez, 1986), to ^{39}Ar recoil during irradiation from biotite into an intergrown potassium-poor phase such as chlorite (e.g. Muecke et al., 1988; Lo and Onstott,

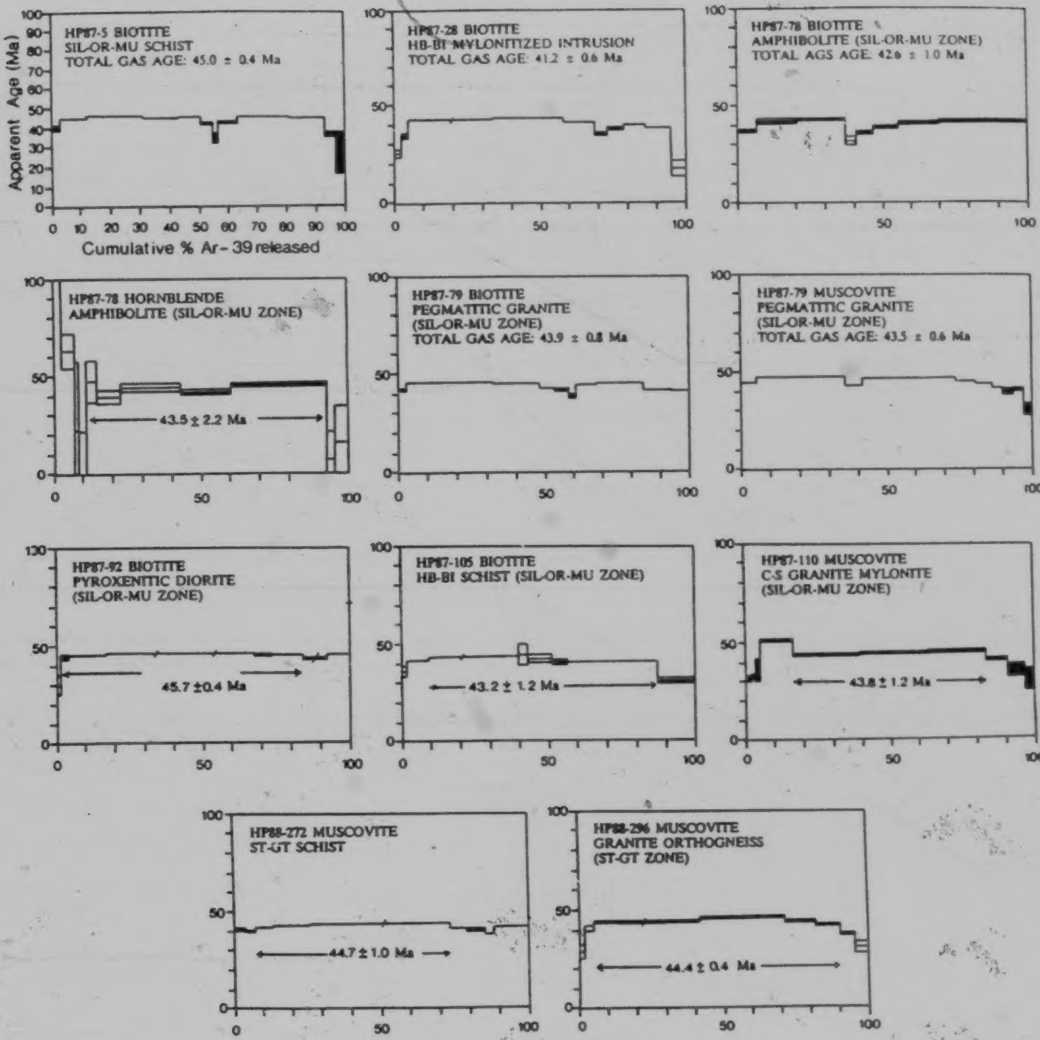

Figure 6.3: ^{40}Ar-^{39}Ar age spectra for muscovite and biotite in the schist complex and mylonite zone, for hornblende from amphibolite in the sillimanite-orthoclase-muscovite zone and for biotite from a post-S_2 pyroxenitic diorite intrusion in the schist complex. The reduction in apparent age in the highest temperature steps of the extraction is interpreted to be an analytical artifact and has no geological significance. Width of bars represents 2σ between-step (relative) uncertainties. Abbreviations given at front of thesis.

1988), or to excess argon (i.e. trapped argon with $^{40}Ar/^{36}Ar > 295.5$) such that the apparent age of the saddle is greater than the known age of the sample (e.g. Lanphere and Dalrymple, 1976). In addition, highly disturbed biotite spectra have been attributed to one or more trapped argon components with different $^{40}Ar/^{36}Ar$ values (e.g. Heizler and Harrison, 1988). ^{39}Ar recoil invalidates the assumption inherent in age spectra and correlation plots, that the irradiation-induced ^{39}Ar is located in the same site as the ^{39}K parent and the radiogenic ^{40}Ar (Huneke and Smith, 1976). Thus, the age determined from the data is dependent on the interpretation of the mechanism for saddle formation.

To interpret correlation plots, argon data must be corrected for the analytical blank (Roddick, 1978). High atmospheric ^{40}Ar (Appendix 2, Table A2.1, A2.2 and A2.3) in the analyses indicates that the contribution from the analytical blank was substantial in many cases. As blank values of the system are unconstrained for this study, correlation plot analysis cannot be applied. However, the widespread occurrence of saddles in biotite spectra from a large range of geological settings (metamorphosed and non-metamorphosed granitic rock, regionally and contact metamorphosed pelite) (e.g. Berger, 1975; Hanson et al., 1975; Muecke et al., 1988; Lo and Onstott, 1989) implies a cause related to the structure of biotite rather than to its geologic environment and supports the ^{39}Ar recoil interpretation. Although no K-poor phase such as chlorite was detected optically in biotite in this study, this does not preclude the recoil interpretation (e.g. Muecke et al., 1988).

Huneke and Smith (1976) proposed that the total gas age (equivalent to conventional K-Ar) age provides a lower limit to the Ar retention age of the biotites with saddle spectra. Total gas ages for biotite samples showing saddle spectra range from 41.2 ± 0.6 Ma to 45 ± 0.4 Ma (Figure 6.3 and Appendix 2). The total gas ages for these samples are used in subsequent discussion. Biotite ages from pelitic rocks in the schist complex overlap with hornblende and muscovite ages within error. The biotite age for dioritic mylonite is slightly younger than that for muscovite from C-S granite mylonite, consistent with the Tc of biotite. Coexisting biotite and muscovite in post-S_2 pegmatitic granite are concordant within error.

Mylonitization can cause significant K and Ar redistribution or loss in minerals resulting in disturbed spectra (e.g. Maluski, 1978). Biotite from diorite protomylonite yielded only a slightly disturbed spectra. C-S mylonite with a U-Pb monazite crystallization age of 49.5 Ma (HP87-110) contains muscovite with a plateau age of 43.8 ± 1.2 Ma. Therefore, if mylonitization disturbed the K-Ar isotopic system, closure with respect to argon took place soon after mylonitization.

6.3.3. Fission Track

The fission track age data are summarized in Table 6.5 and the confined track length histograms are shown in Figure 6.4. Due to poor contact between the apatite grain mount and the external (mica) detector, the number of induced tracks (N_i) in sample HP87-110 is erroneously low and the calculated age is erroneously high (although still within 2σ error). This sample was not considered further. Within experimental uncertainty, the three fission track apatite ages are identical and have a weighted mean value of 44.6 ± 8 Ma. Within error, this age is identical to hornblende, muscovite and biotite argon ages. Correction of the fission track ages for partial annealing (Appendix 2) is between 0.3 and 0.7%, that is, within 2σ error. The track length histograms are all relatively narrow and all tracks are longer than 11 μm. The mean length ranges from 14.18 ± .10 to 14.72 ± .07 μm. (standard errors). Track lengths are not corrected for measurement bias towards long tracks (see Appendix 2) as this correction is only 0.5%, within standard error (Grist, personal communication 1991).

6.4. IMPLICATIONS OF AGE DATA AND FISSION TRACK LENGTHS

U-Pb data indicate two episodes of granitic magma emplacement in the Horseranch Range: late Early Cretaceous and Eocene. The presence of syn- to post-S_2 113 Ma granite in the sillimanite-orthoclase zone limits the peak of regional metamorphism in the highest grade rocks (which is post-S_2) and the development of $^2F_3$ folds to late Early Cretaceous (113 Ma) or younger.

As peak metamorphic temperatures were well above argon closure in hornblende, muscovite and biotite and fission track retention in apatite, the ages record direct cooling from approximately 525°C to 110°C. The mean fission track lengths and distributions (Figure 6.4) indicate that temperature did not exceed ca. 50°C in the last 40 Ma and that these are rapidly cooled rocks (e.g. Gleadow et al., 1986; Green et al., 1989a). The data show that mylonitization, pyroxenitic diorite and some granite intrusion and cooling from a temperature *above* 525°C to ca. 50°C took place between ca. 53 and 41 Ma and that by the middle to late Eocene, the rocks now exposed in the Horseranch Range were 2 km or less from the surface (assuming a geothermal gradient of 25 to 40°C/km).

The uniformity of $^{40}Ar/^{39}Ar$ and fission track ages indicates that Eocene cooling was rapid and synchronous throughout the area. Eocene $^{40}Ar/^{39}Ar$ and fission track

Table 6.5: A summary of the fission track count data. N_s and N_i are the numbers of counted spontaneous tracks in apatite and induced tracks in muscovite detector, respectively. ρ_s and ρ_i are the measured spontaneous and induced track densities (track/cm^2), respectively. Errors in fission track ages are reported at the 2 sigma confidence level. A weighted mean value of 11,760 ± 650 was used for the zeta parameter. Detailed count data and statistics are given in Table A2.4 (Appendix 2). Sample HP88-296 was not counted as it was too radioactive at the time of analysis to permit handling. ^ are the ages corrected for partial annealing (see Appendix 2 for explanation of correction). * indicates that sample was difficult to count due to poor contact between the apatite grain mount and the external (mica) detector. It was excluded from the calculation of the average age.

Sample	Grains Counted	N_s	N_i	ρ_s	ρ_i	ρ_s/ρ_i	Age (Ma)	Age^ (Ma)	U (ppm)
HP87-3	22	153	534	3.50×10^5	1.22×10^6	0.287 ± .026	46.2 ± 10.0	47.8 ± 10.0	15
HP87-75	31	948	3216	1.30×10^6	4.41×10^6	0.295 ± .011	47.5 ± 6.6	50.7 ± 6.6	50
HP87-110*	20	568	1898	1.20×10^6	4.01×10^6	0.299 ± .014	48.2 ± 7.2	49.7 ± 7.2	45
HP88-159	31	771	2846	8.43×10^5	3.11×10^6	0.271 ± .011	43.7 ± 6.2	45.3 ± 6.2	35

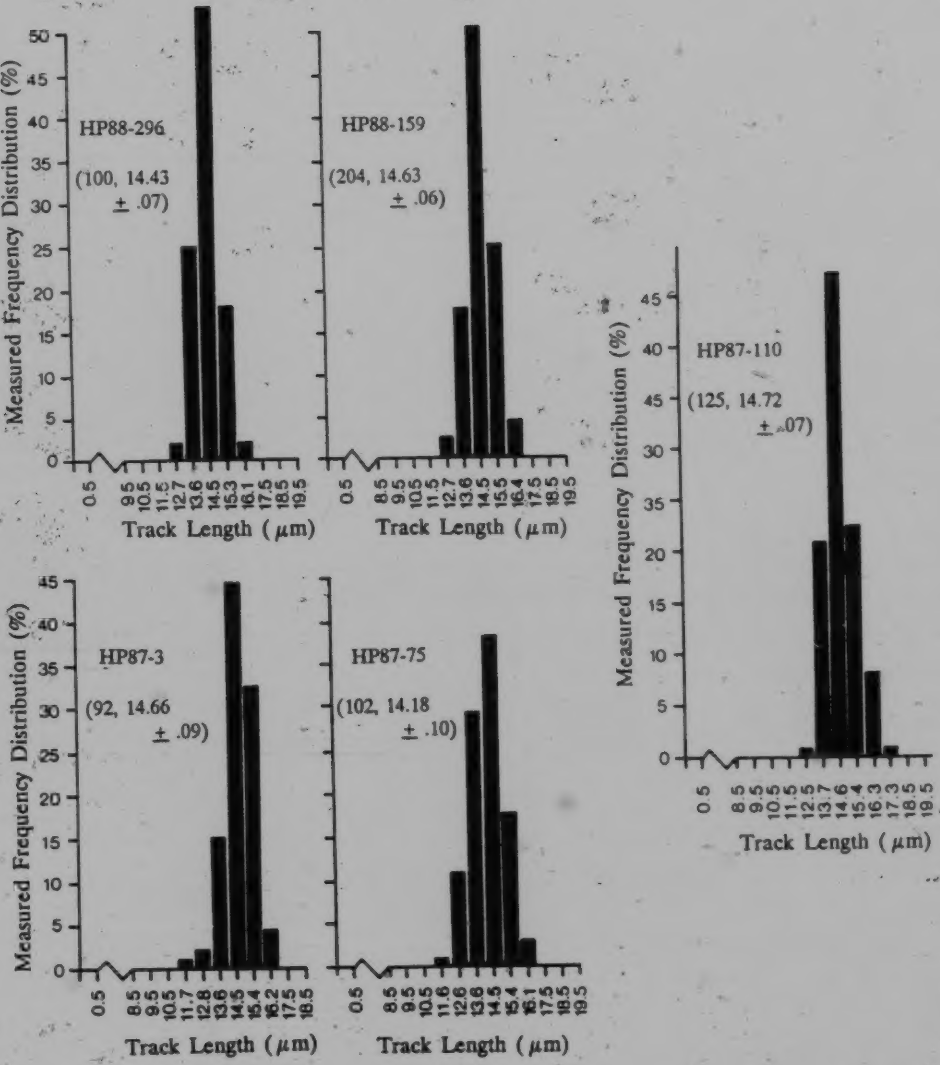

Figure 6.4: Fission track length distribution in apatite. The numbers in parentheses are the number of tracks measured, the mean track lengths and the standard (2σ) error.

cooling ages are widespread in a variety of rock types and have no spatial association with the late granite intrusions or with the mylonite zone, the potential means to reheat these rocks after regional cooling. No older (i.e. pre-Eocene) $^{40}Ar/^{39}Ar$ cooling ages are observed. Therefore, excluding the late Early Cretaceous granite pegmatite (sample HP87-139), the data are interpreted to record direct cooling from the late Early Cretaceous to the Eocene rather than Eocene resetting of Cretaceous minerals (Figure 6.5). The disturbance of the U-Pb isotopic system in monazite from granite pegmatite is interpreted to be a local phenomenon.

The 43.5 ± 0.6 Ma muscovite cooling age for granite mylonite constrains mylonitization at $T \geq 350$°C to mid-Eocene or older (i.e. pre-43 to 44 Ma). This is entirely consistent with the U-Pb zircon and monazite crystallization ages for C-S granitic mylonite and indicates that at least some of the mylonitic fabric is Eocene. The post-S_2 pyroxenitic diorite in the schist complex that yields a biotite age of 45.7 ± 0.4 Ma is interpreted to be genetically related to non-deformed diorite, gabbro, pyroxenite and hornblendite which cut both mylonitic fabric and bedding in low-grade rocks, and to pyroxenitic diorite cut by the Horseranch fault. The apparent conflict between relative timing based on field evidence and on cooling age between the pyroxenitic diorite and granitic mylonite likely reflects the fact that argon retention takes place over a range (albeit small) of temperature rather that a single temperature.

6.5. COOLING RATES AND UPLIFT RATES

Assuming that the rocks of the Horseranch Range were ca. 650°C or less at 113 Ma and ca. 525°C at 46 Ma (45.7 Ma), this corresponds to an average linear cooling rate of ca. 1.9°C/m.y. (Figure 6.5). Assuming a steady state geothermal gradient of 25 to 40°C/km, cooling by 1.9°C/m.y. corresponds to an uplift rate of ca. 0.05 to 0.08 mm/year. The term uplift rate is used here synonymously with the term exhumation rate as defined by England and Molnar (1990). This rate is interpreted to record uplift by erosion and isostatic rebound and if constant, it implies uplift of 3 to 5 km in a 67 Ma period. Uplift of sillimanite-orthoclase-muscovite schist by 3 to 5 km from depths of 15 to 21 km (see section 5.6) would place the schist at depths of 10-19 km to 12-21 km by the early Eocene. Uplift by 3 to 5 km of the staurolite-garnet schist from a depth of 12 to 15 km (section 5.6) would place the schist at a depth of 7-10 km to 9-12 km by the beginning of the Eocene. Assuming a steady state geothermal gradient of 25 to 40°C/km, depths as low as 7 km would be significantly lower than

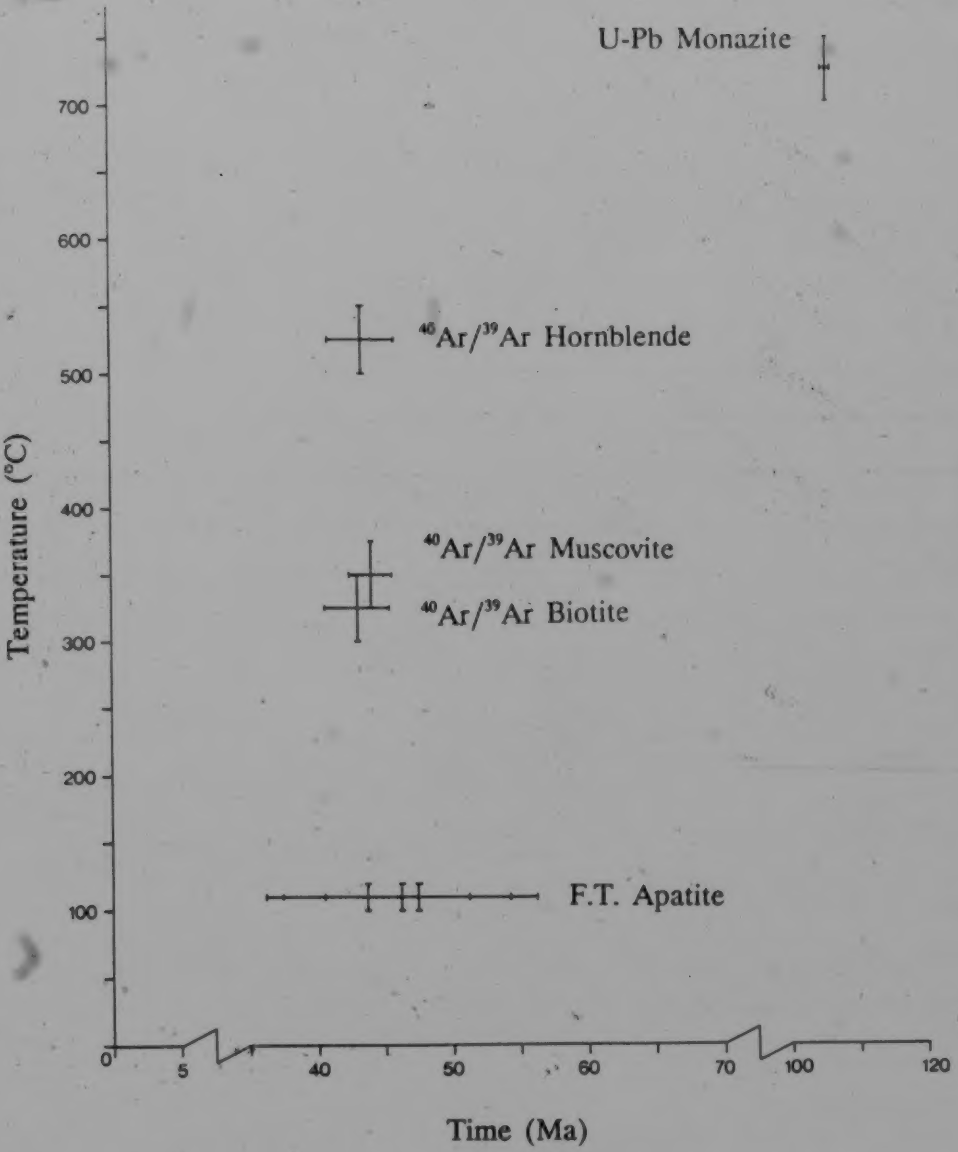

Figure 6.5: Temperature-time plot of isotopic data. Bar lengths represent maximum uncertainty: Time = range + maximum 2σ error range, Temperature = Tc ± 25 °C. The date indicated for ^{40}Ar-^{39}Ar on muscovite and biotite is the mean value. Data for biotite from pyroxenitic diorite (HP87-92) are not included.

Tc_{hb}. Therefore, the uplift rate was probably less than 0.05 to 0.08 mm/year.

Cooling in the Eocene by approximately 475°C (ie. 525°C - 50°C) in ca. 10 m.y. (45.7 Ma to 36.2 Ma, using maximum error range of the ages) in the Horseranch Range corresponds to a rate of 48°C/m.y. and implies rapid uplift (Figure 6.5). Rapid uplift results in advective heat transfer and upwards bending of isotherms (e.g. Buck et al., 1988) and therefore, 48°C/m.y. is only the rate at which the 525 to 50°C isotherms passed downwards through the rocks. An uplift rate calculated using this cooling rate and assuming a steady state geothermal gradient (horizontal isotherms) is probably a minimum estimate. Using a geothermal gradient of 25 to 40°C/km, a cooling rate of 48°C/m.y. yields an apparent uplift rate of 1.2 to 1.9 mm/year. This rate is comparable to tectonic uplift rates of 1 to 5 mm/year in the Austrian Alps (Cliff et al., 1985).

6.6. TRACK LENGTH MODELLING

To constrain the low temperature cooling rate in the Horseranch Range, fission track length data were modelled for cooling below 120°C using the GEOTRACK thermal model for fission track annealing in apatite (Green et al., 1989) which predicts a track length distribution for a given thermal history. The model assumes that spontaneous tracks are identical to induced tracks at the time of formation so that the experimentally determined description of the annealing process is applicable to geological situations (e.g. Green, 1988). The model uses the concept of "equivalent time", that is, at any given time, annealing of an already partially annealed track is dependent on temperature, time and degree of prior partial annealing, but not on the conditions that caused the prior partial annealing (Duddy et al., 1988).

The model divides the selected thermal history into a series of intervals and then uses the experimentally determined isothermal annealing model of Laslett et al. (1987) modified for variable-temperature annealing by Duddy et al. (1988) to predict the final track lengths for that interval. The final lengths for each interval are then summed to produce the overall distribution for the entire thermal history. The annealing descriptions of Laslett et al. (1987) and Duddy et al. (1988) are based on the observed mean confined track length for which there is a geometrical bias in revealing by etching (Laslett et al., 1982). Therefore, the track lengths for each interval are corrected for the geometrical bias (cf. Laslett et al., 1982) prior to the final summing to produce the net track length distribution. The net distribution is then re-biased to allow for comparison with observed data (Green et al., 1989a).

Six thermal histories were used with linear cooling rates of 5°C/m.y., 10°C/m.y. and 50°C/m.y. for temperature between 120°C and 10°C and between 120°C and 35°C, followed by maintenance at 10 or 35°C to time zero (Table 6.6). Cooling begins at 50 Ma. The effect of reducing the start time to ca. 40 Ma (as is supported by $^{40}Ar/^{39}Ar$ data) is negligible because temperature is the dominant process in fission track annealing (Green et al., 1989). Maintenance of the samples at a constant temperature following linear cooling corresponds effectively to slow cooling (<5°C/m.y.).

Figure 6.6 shows the temperature-time paths and modelled track length distributions for thermal histories 1, 2 and 3. The modelled mean track lengths are longer and narrower reflecting less annealing relative to tracks measured in this study (compare with Figure 6.4). Figure 6.7 shows temperature-time paths and modelled track length distributions for thermal histories 4, 5 and 6. The modelled distributions and mean track lengths are very similar to those of this study. The apparent lack of tailing on histograms for Horseranch apatites relative to the modelled histograms likely reflects the lack of correction of the data for track length bias (see Appendix 2). Although not a unique solution, the results for thermal histories 4 to 6 constrain the cooling rate below 120°C to ca. 10°C/m.y. or higher and indicate that the rocks were maintained at a temperature greater than 10°C and probably close to ca. 35°C. Assuming a geothermal gradient of 25°C/km to 40°C/km, 35°C corresponds to a depth of ca. 1 to 1.5 km. Therefore, modelling results support the interpretation that following Eocene uplift, the rocks now exposed in the Horseranch Range were within 2 km of the surface and indicate that subsequent uplift rates were low.

✓

Table 6.6: Time-temperature data used for fission track models.

Model	Time (Ma)	Temperature (°C)
1	50	120
	28	10
	0	10
2	50	120
	39	10
	0	10
3	50	120
	47.8	10
	0	10
4	50	120
	33	35
	0	35
5	50	120
	41.5	35
	0	35
6	50	120
	48.3	35
	0	35

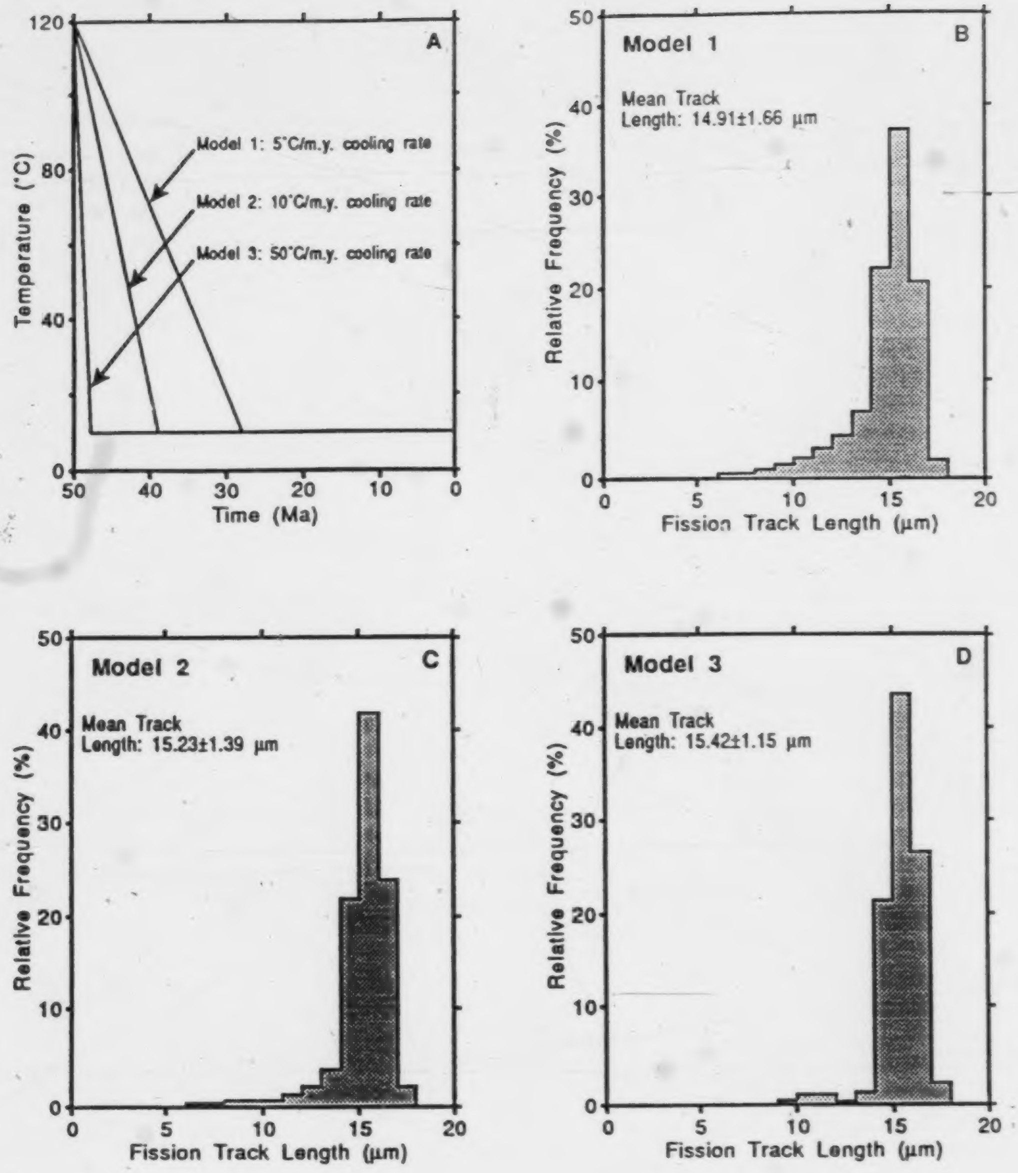

Figure 6.6: (a) Time-temperature plots for thermal histories 1, 2 and 3. (b), (c) and (d): Modelled track length distributions and mean fisson track lengths for models 1, 2 and 3, respectively. Modelled distributions are narrower, and mean lengths are greater, than analysed samples from this study (see Figure 6.4) indicating that the thermal histories of models 1 to 3 are not applicable to the samples.

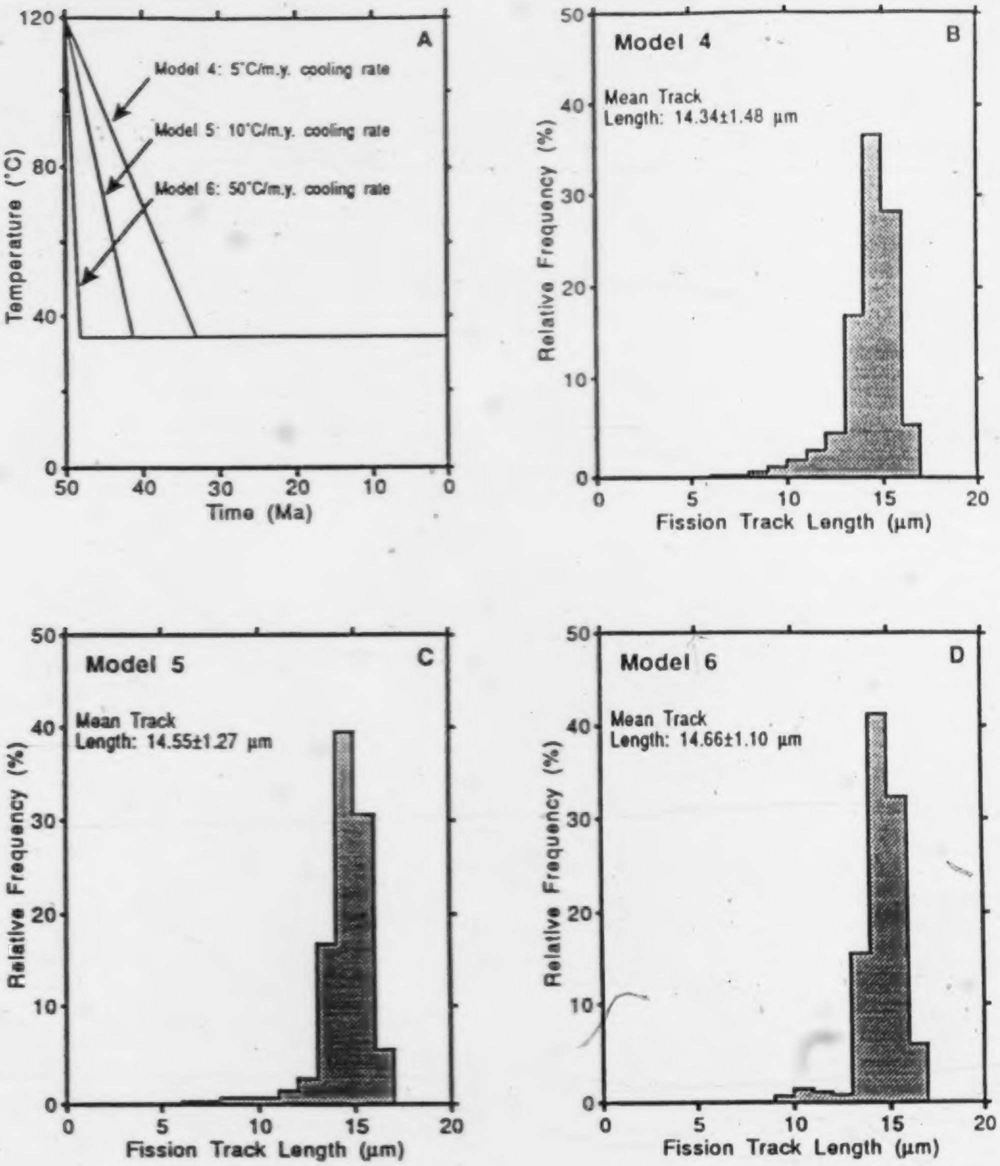

Figure 6.7: (a) Time-temperature plots for thermal histories 4, 5 and 6. (b), (c) and (d): Modelled track length distributions and mean fisson track lengths for models 4, 5 and 6, respectively. Modelled distributions and track lengths for models 5 and 6 are similar to those obtained for analysed samples (see Figure 6.4). This indicates that the samples experienced similar thermal histories to those of models 5 and 6 and limits cooling rates below 120°C to 10°C/m.y. or greater.

CHAPTER 7

TECTONIC SYNTHESIS AND REGIONAL IMPLICATIONS

7.1. PREAMBLE

Geological evidence from the nearby Swannell Ranges and from southeastern British Columbia indicates that shortening, burial, metamorphism and magmatism in the Omineca Belt during terrane accretion to North America took place largely in the Mesozoic (e.g. Parrish, 1979; Monger et al., 1982; Parrish et al., 1988). Syn-metamorphic $^1F_2$ folds, late Early Cretaceous granite magmatism and late Early Cretaceous or younger high-grade metamorphism recorded in the Horseranch Range are consistent with metamorphism and magmatism during Mesozoic crustal thickening.

Geochronological data from this study record rapid Eocene cooling of the schist complex from approximately 525 to 50°C and Eocene mylonitization. The inferred mechanism of Eocene cooling must explain the timing of $^2F_3$ folding, mylonitization and brittle faulting and be consistent with the kinematics of the mylonite zone and with regional Cretaceous to Tertiary tectonics.

7.2. REGIONAL CRETACEOUS AND TERTIARY TECTONICS IN THE NORTHERN OMINECA BELT

Gabrielse (1985) concluded that most of the dextral displacement along strike-slip faults in north-central British Columbia is mid-Cretaceous to Eocene and possibly as young as Oligocene. Of relevance to this study are the Kechika fault, for which more than 170 km and up to 280 km of mid-Cretaceous (100 to 105 Ma) to Oligocene displacement is inferred and the Northern Rocky Mountain Trench, for which 700 to > 900 km pre(?)mid-Cretaceous to Eocene or Oligocene displacement is inferred, of which 125 km took place in the Late Eocene to Oligocene (H. Gabrielse, 1985 and personal communication 1990; Evenchick, 1988). These faults are subvertical where exposed and strike approximately 325° at the latitude of the Horseranch Range (Gabrielse, 1985 and personal communication 1990). On the basis of the trends regional fold axes, the orientation of strike-slip faults and the inferred age of displacement in north-central British Columbia, Gabrielse (1985) concluded that there was a change in the regional shortening direction from northeast in pre-mid-Cretaceous time (pre-100 Ma to 105 Ma) to north or north-northwest in mid-

Cretaceous time to northeast in Late Cretaceous (post 105 to 100 Ma) and/or early Tertiary (Paleocene and younger) time (Figure 7.1).

7.3. AN OBLIQUE-NORMAL STRIKE-SLIP MODEL FOR THE HORSERANCH RANGE

The ${}^2F_3$ folds in the Horseranch Range are younger than late Early Cretaceous (113 Ma), the mylonitic fabrics are younger than ${}^2F_3$ folds and some are at least as young as Eocene (ca. 50 Ma) and strike-slip motion along the Kechika fault is mid-Cretaceous (i.e. 100 Ma to 105 Ma) to Oligocene. Therefore, ${}^2F_3$ folds may have initiated prior to the Kechika fault and mylonite zone but it is probable that the latter two structures result from the same stress field. The amount of time between ${}^2F_3$ folding and mylonitization is unknown.

Post-metamorphic folds with northwest-trending hinges (like ${}^2F_3$ folds in the Horseranch Range) are common in Proterozoic rocks of the northern Omineca Belt (e.g. Bellefontaine, 1990; Evenchick, 1988; Parrish, 1979). Although the folds could have formed in the mid-Cretaceous time with east-west-trending hinges and have rotated into parallelism with strike-slip faults, this is improbable, because it would require homogeneous penetrative dextral shear throughout the entire northern Omineca Belt. More probably, ${}^2F_3$ folds developed during pre-mid-Cretaceous (100 Ma to 105 Ma) northeast-directed shortening. This interpretation is consistent with data from this study which indicates that the ${}^2F_3$ are younger than 113 Ma.

On the basis of field and geochronometric data from this study, displacement along the mylonite zone may have predated or postdated displacement along the Kechika fault, but it was in part, synchronous. If the mylonite zone developed prior to the Kechika fault and assuming no control on the zone's orientation by pre-existing structures, it may have developed as a synthetic (dextral) Riedel shear associated with the Kechika fault (Figure 7.2). If the mylonite zone developed contemporaneously with, or after, the Kechika fault then it is unlikely a Riedel shear (see Naylor et al., 1986). Because the Horseranch Range lies north of a gentle left-stepping bend in the Kechika fault, a location where splay faults are likely to develop (e.g. Crowell, 1974), the mylonite zone may be a splay of the Kechika fault. This interpretation is preferred because it is simple, consistent with age data from this study, and requires no assumption about the absence of pre-existing structures.

Late Cretaceous and/or Early Tertiary, northeast-shortening (ca. 045°) in the northern Omineca Belt (Gabrielse, 1985) would result in northwest-directed extension

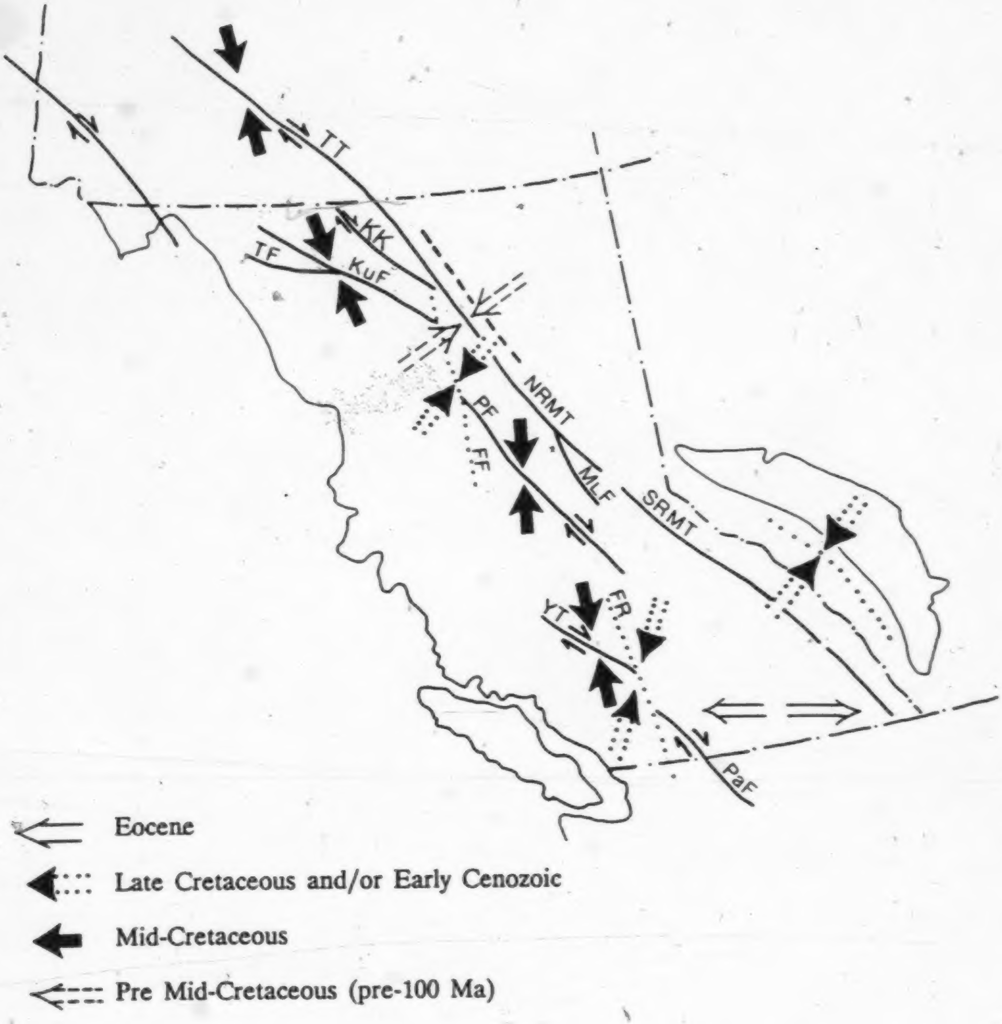
TT
KK
TF
KuF
NRMT
PF
FF
MLF
SRMT
YT
FR
PaF
Eocene
Late Cretaceous and/or Early Cenozoic
Mid-Cretaceous
Pre Mid-Cretaceous (pre-100 Ma)

Figure 7.1: Priniciple shortening component (σ_1) of regional stress field in the Omineca Belt for pre-mid-Cretaceous to Tertiary time based on timing of displacement along regional strike-slip faults. FF = Finlay fault, FR = Fraser River fault zone, KK = Kechika fault, KuF = Kutcho fault, MLF = McLeod Lake fault, NRMT = Northern Rocky Mountain Trench, PaF = Pasayten Fault, PF = Pelly fault, SRMT = Southern Rocky Mountain Trench, TF = Thibert fault, TT = Tintina fault, YF = Yalakom fault. Modified from Gabrielse (1985).

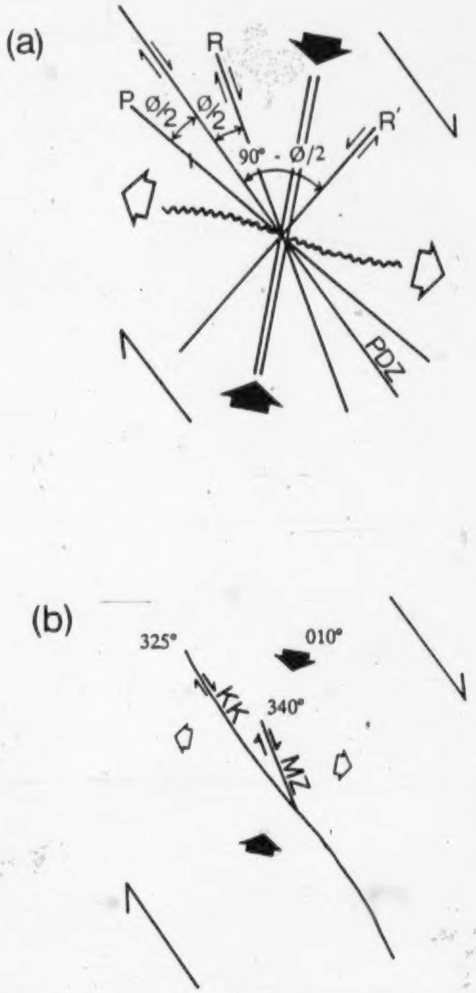

Figure 7.2: (a) Structures related to simple shear deformation modified from Sylvester (1988). PDZ = principle displacement zone, that is, the main strike-slip fault, wavy line = fold hinge trace, paired straight lines = normal fault trace, P = P shears which exhibit both strike-slip and reverse displacement, R, R' = synthetic and antithetic Riedel shears, respectively, Ø = internal angle of friction. (b) Schematic map depicting the interpretation of the mylonite zone (MZ) in the Horseranch Range as a mid-Cretaceous Riedel shear associated with the Kechika (KK) fault. This interpretation requires that the shortening direction was north-northeast (010°) and assumes no control on the orientation of the zone by pre-existing structures. Shortening and extension denoted by solid arrows and open arrows, respectively. Paired arrows denote strike-slip. Map trace of Kechika fault modified from Gabrielse (1985).

(ca. 315°). Oblique-normal strike-slip displacement along the northwest-striking (340°) mylonite zone would also result because the orientation of the zone is intermediate to the strike-slip (360°) and the extension (315°) direction (Figure 7.3). The local strike-slip displacement in the zone may be a local phenomenon or may record early strike-slip overprinted by oblique-slip displacement. This interpretation implies that oblique-normal extension may have taken place as early as Late Cretaceous. Geochronometric data from this study supports early Tertiary (i.e. Eocene) extension.

The significance of the brittle Horseranch and Deadwood faults and the inferred Southeastern fault in regional tectonics is unclear due to the uncertainty of their age and displacement. Because the Southeastern fault juxtaposes the schist complex and low-grade phyllite, it may be a ductile R shear en echelon within the mylonite zone or another splay fault. Accordingly, some oblique-slip may have taken place along the fault. If the Horseranch and Deadwood faults were initiated with the mylonite zone during mid-Cretaceous (100 Ma to 105 Ma) north-south shortening, then they are (mainly) normal faults. If they were initiated under Late Cretaceous and younger northeast-directed shortening, then they are primarily dextral strike-slip faults.

7.4. THE HORSERANCH RANGE AS A METAMORPHIC CORE COMPLEX

Metamorphic core complexes form by uplift of deep-seated crystalline rocks beneath a low-angle, ductile to brittle, normal fault (or detachment fault) and associated isostatic arching of the footwall following extensive crustal thickening. They are common phenomena in orogenic belts (e.g. Davis, 1980; Rehrig, 1986; Gibson et al., 1988; Parrish et al., 1988; Selverstone, 1988). Tertiary fabrics are commonly superimposed on Mesozoic fabrics indicating that gently dipping crustal anisotropy created by Mesozoic crustal shortening and thickening controlled the dip of Tertiary extensional faults (e.g. Rehrig, 1986; Rhodes and Hyndman, 1984; Rehrig and Reynolds, 1980; Coney and Harms, 1984). Extension is always down-dip along the detachment (e.g. Davis, 1980). The detachment juxtaposes low-grade (greenschist facies) or unmetamorphosed, brittly extended sedimentary and volcanic rocks against plutonic and high-grade (amphibolite facies) metamorphic rocks and is commonly developed on opposite sides of the complex. The upper plate rocks are chaotically tilted and structures do not correlate across the detachment which may consist of several displacement surfaces (Rehrig, 1986). In many core complexes in the United

LATE CRETACEOUS AND/OR EARLY TERTIARY

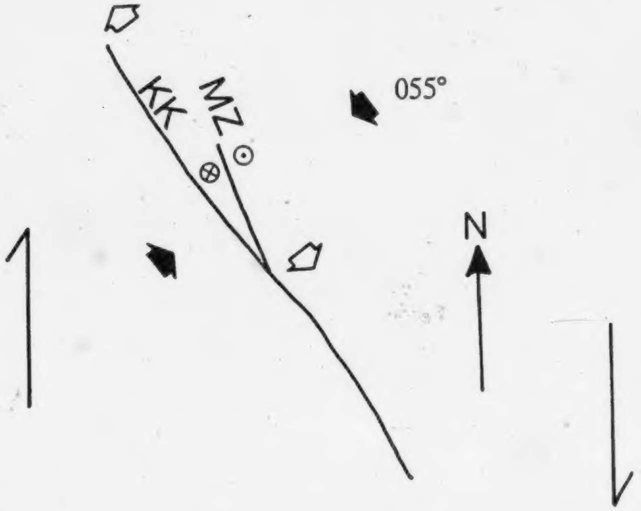

Figure 7.3: Schematic map depicting the northwest oblique-normal extension in the mylonite zone (MZ) during late Cretaceous and/or early Tertiary northeast-directed shortening (see Figure 7.1). Circled cross and dot represent motion into and out of the plane of the diagram, respectively, All other symbols as for Figure 7.2.

States, the detachment is characterized by ductile mylonite in the lower plate rocks (including granitic and sedimentary protoliths) overlain by brecciated and strongly chloritized tectonite. The top of the breccia zone is the locus of detachment (Davis, 1983). Mylonite zones are characterized by low/water rock ratios whereas chlorite breccias mark zones of hydrothermal fluid flow and alteration. In the Shuswap metamorphic core complex of southeastern British Columbia, chlorite breccia is not developed; the detachment fault originated as a single thrust surface during crustal thickening that was arched and reactivated during extension as normal detachment faults on opposite sides of the complex (e.g. Parrish et al., 1988; Carr et al., 1987). In the North American Cordillera, crustal extension and resultant uplift and rapid cooling of metamorphic core complexes took place in the Eocene (ca. 55 to 40 Ma) north of the Snake River Plain (Idaho, U.S.A.) and in the Oligocene to Miocene (ca. 35 to 16 Ma) farther south (Rehrig, 1986). Cooling rates of ca. 100°C/Ma or higher in high-grade rocks of core complexes imply uplift rates of 3 mm/year or greater (e.g. Davis and Anderson, 1987; Hyndman and Myers, 1988). Eocene cooling rates of 41°C/m.y. are reported for the Monashee complex in southeastern British Columbia (Sevigny et al., 1990).

The cause of crustal scale extension is debated. A change in the northeast Pacific plate motions in the Eocene (Engebretson et al., 1985) is thought to be the main external control on extension (Parrish et al., 1990). Ranalli et al. (1989) proposed that extension was driven by detachment of a lithospheric root formed by Late Cretaceous to Early Tertiary crustal thickening, but that far-field stresses may have also played a role. Extension in the Shushwap complex may have resulted partly from the transfer of strike-slip displacement from the Tintina-Northern Rocky Mountain Trench fault zone to the en echelon Fraser River-Straight Creek fault zone (Price, 1979; Price et al., 1985; Price and Carmichael, 1986). However, the possibility that the Fraser River - Straight Creek fault developed ca. 42 Ma, significantly after extension in the Shuswap Complex, and the absence of northwest-southeast-directed extension makes the strike-slip faulting interpretation as the single cause of extension uncertain (Parrish et al., 1990). Nevertheless, core complex formation by extension related to strike-slip faulting has been documented in the eastern Alps (Selverstone, 1988), in the Andes of southernmost Chile (Dalziel and Brown, 1989) and in the southern Appalachians (Snoke and Frost, 1990). In all these examples, the crust was thickened and heated prior to extension.

The tectonic evolution of the Horseranch Range has several similarities with metamorphic core complexes. In the Horseranch Range, a ductile normal fault which postdates crustal thickening and regional metamorphism marks juxtaposes low-grade (greenschist facies), brittly deformed, upper plate rocks against older, high-grade (amphibolite facies), ductily deformed, lower plate rocks. Structures cannot be correlated with certainty across the detachment (Chapter 3). The lower plate rocks were rapidly cooled during ductile faulting at rates comparable to some reported for core complexes. However, despite these similarities, uplift by oblique extension in the Horseranch Range contrasts strongly with normal, dip-slip extension characteristic of metamorphic core complexes (e.g. Davis, 1980; Selverstone, 1988). In addition, unlike metamorphic core complexes, the uplift of the Horseranch Range is not the result of regional extension. Therefore, the Horseranch Range is not a metamorphic core complex.

7.5. NATURE AND TIMING OF UPLIFT IN THE NORTHERN OMINECA BELT: EAST-CENTRAL BRITISH COLUMBIA TO SOUTH-CENTRAL YUKON

The timing of metamorphic cooling and the uplift mechanism(s) of the northern Omineca Belt are summarized below. In British Columbia, the areas studied in the most detail are the Sifton Range, the northern and central part of the Swannell Ranges (Chase Mountain area, Ingenika Range and Manson Creek-Germansen Landing area), the Mount Mackinnon area and the Horseranch Range (Figure 1.1). Most information regarding the timing of cooling and uplift in the Omineca Belt in the Yukon comes from south-central Yukon (see Hansen, 1990).

7.5.1. Sifton Range

In the Sifton Range, the Late Cretaceous to Eocene, ductile Sifton fault developed as a gently dipping thrust fault that connected the dextral strike-slip Northern Rocky Mountain Trench system and the Kechika fault. It accommodated Late Cretaceous to Eocene convergence south-southeast of a left-stepping bend in the Kechika fault. Evenchick (1988) inferred that the rocks were buried, heated and subsequently cooled during thrusting resulting in mid-Eocene resetting of the K-Ar system in Mesozoic minerals. This resetting must have been widespread in the Sifton Range as K-Ar cooling ages older than Eocene are reported only in garnet grade schist northeast of Spinel Lake (Hunt and Roddick, 1987, p. 197). However, biotite (170 Ma) is significantly older than coexisting muscovite (85 Ma), which may indicate that excess argon is present in this sample. Therefore, the significance of these data for regional cooling in the Sifton Range is unclear. Eocene biotite K-Ar cooling ages in gneiss is significantly older (up to 5 Ma) than muscovite in schist in the Sifton Range, which may also indicate undetected excess argon in biotite. Therefore, determination of an Eocene cooling rate for the Sifton Range is difficult. By the late Eocene, regional shortening in the Sifton Range was oriented northeast-southwest, as recorded by lamprophyric dykes with 43 to 38 Ma biotite K-Ar cooling ages (Evenchick, 1988: Figure 32).

7.5.2. Swannell Ranges

(i) Chase Mountain

On the basis of Rb-Sr muscovite dates and K-Ar muscovite and biotite dates, cooling in the northern Swannell Ranges took place between the Late Jurassic and Early Cretaceous at a rate of ca. 3 to 10°C/Ma between 500 and 220°C. Corresponding uplift rates were at least 0.1 to 0.3 mm/year (Parrish, 1979).

Cooling is interpreted to have resulted from isostatic rebound and subsequent erosion rather than from tectonic uplift (Parrish, 1979). Eocene resetting of K-Ar and Rb-Sr ages has occurred near an Eocene granitic stock south of Chase Mountain. In the vicinity of Chase Mountain, the effects of this resetting were small (Parrish, 1979).

(ii) Ingenika Range

In the Ingenika Range, 10 km northwest of Chase Mountain across a sinistral, pre-mid-Cretaceous(?)(Roots, 1954) strike-slip fault, post-metamorphic uplift has been attributed to westward thrusting along the steep Swannell fault, driven by tectonic wedging beneath the Ingenika Range during terrane accretion (Bellefontaine, 1989, 1990). The Swannell fault is interpreted to have accommodated northeast- and southwest-directed thrusting; the timing and direction of latest movement along the fault is uncertain (H. Gabrielse, personal communication 1991). K-Ar determinations on muscovite and biotite from schist in the footwall of the Swannell fault have yielded 130 ± 6 Ma and 125 ± 6 Ma, respectively (Wanless et al., 1972, recalculated using the decay constants of Steiger and Jäger, 1977). Assuming that the hanging wall rocks cooled earlier than the footwall rocks, 130 Ma is the upper age limit on post-metamorphic cooling and uplift in the Ingenika Range.

(iii) Manson Creek-Germansen Landing area

Uplift of amphibolite grade rocks of the Wolverine metamorphic core complex in the Mason Creek-Germansen Landing area is due to ductile, normal displacement along the northwest-striking, southwest-dipping Wolverine fault zone (F. Ferri, personal communication 1991). The post-metamorphic ductile fault juxtaposes the amphibolite grade rocks of the Wolverine Complex against greenschist grade rocks of the Upper Ingenika Group and Slide Mountain terrane. High-grade rocks record rapid Late Cretaceous (84 Ma) to predominantly Early Tertiary cooling whereas the low-grade rocks record Early Jurassic (174 Ma) cooling. High-angle brittle faults which appear to cut ductile fabrics in the Wolverine fault zone may be a higher level expression of the shear zone. Displacement along the Wolverine fault zone decreases northward. Based on the timing of movement along faults, extension was probably related to regional strike-slip faulting although the nature of this relationship is unclear (F. Ferri, personal communication 1991).

7.5.3. Mount Mackinnon area

In the Mount Mackinnon area, uplift and cooling are interpreted to have taken place during Tertiary northwest-southeast-directed extension along northeast-striking, gently dipping normal faults related to regional strike-slip faulting (Struik, 1989; Deville and Struik, 1990). Late northeast-striking, steeply dipping, brittle, normal faults are consistent with northwest-southeast extension. Late, probably Eocene to Miocene, felsic to mafic dykes have orientations similar to these faults.

7.5.4. South-Central Yukon

In south-central Yukon, much of the cooling and uplift is related to Triassic oblique collision and Jurassic obduction of the Slide Mountain terrane onto the margin of North America. In western Yukon and eastern Alaska, crustal thickening was succeeded by mid-Cretaceous crustal extension in the hinterland of the MacKenzie fold and thrust belt (Hansen, 1990). In south-central Yukon, the crust was not thickened to the point of instability and thus, did not extend. Rather, Cretaceous dextral, oblique subduction beneath North America caused northwest-striking, margin-parallel, dextral strike-slip faulting in this region (Hansen, 1990).

Tertiary extension in south-central Yukon is known in only a few areas, so far. Near Faro, the mid-Cretaceous Anvil batholith (ca. 100 Ma) is cut by the ductile, east- to northeast-striking, 50° south-dipping, normal Tie fault. Pigage and Jilson (1985) proposed that the Tie fault was associated with forcible intrusion of the batholith and/or with dextral strike-slip along the Tintina fault and concluded that fault is Late Cretaceous or Tertiary. Tempelman-Kluit (1977) reports normal faults which cut Cretaceous plutons in the Quiet Lake and Finlayson Lake areas. The fault traces are approximately orthogonal, trending northeast and northwest and their relative timing with respect to regional strike-slip faults is unknown.

7.5.5 Discussion

The differences in timing of regional post-metamorphic cooling in the northern Omineca Belt indicate that regional uplift was diachronous and likely subject to tectonic control by regional faults. In the Late Cretaceous, when the rocks in the northern Swannell and Sifton Ranges were cooled, those of the Horseranch Range were still at depth and therefore weak. In the regions south of the Horseranch Range which are interpreted to have been uplifted in the Tertiary, normal faulting in association with strike-slip faulting was common.

The known extent of Tertiary extension decreases northward in the Canadian Cordillera. This decrease may reflect a lack of data for the Yukon or differences in crustal rheology between northern British Columbia and the Yukon (present day coordinates) in the Tertiary. Much of southern Yukon was cool by the Late Cretaceous (Hansen et al., 1990). Thus in the Tertiary, the crustal strength must have been greater than, for example, that of amphibolite-grade rocks in the Horseranch Range or the Manson Creek-Germansen Landing area. This difference in Cretaceous crustal rheology could have caused northeast-directed Tertiary compression to partition into discrete strike-slip fault zones leaving the rocks in the panels between the faults relatively unaffected.

CHAPTER 8

CONCLUSIONS AND REMAINING QUESTIONS

8.1. CONCLUSIONS

Regional metamorphism in the Horseranch Range outlasted early syn-metamorphic tight to isoclinal folding and associated axial planar schistosity (S_2) development. The peak of metamorphism in the highest grade schists is late early Cretaceous or younger. Post-metamorphic ${}^2F_3$ folds with nor[illegible]est-trending hinges are younger than late Early Cretaceous and probably developed as a result of regional pre-mid-Cretaceous northeast-directed shortening. The mylonite zone along the western side of the range postdated these folds and is, at least partly, Eocene in age. The zone may be a dextral Riedel shear or more probably, a splay fault, that developed in association with the Kechika fault. Late Cretaceous and/or early Tertiary northeast-directed shortening caused oblique-normal strike-slip displacement along the zone, and rapid uplift and cooling of the schist complex. Uplift by oblique extension contrasts with regional dip-slip extension observed in metamorphic core complexes and therefore, the range is not a core complex.

Late Early Cretaceous (?) to the Eocene, single-stage cooling and uplift proposed in this study are compatible with results from the southern Omineca Belt but differ from the nearby Swannell and Sifton Ranges. This diachronous cooling and uplift in the Mesozoic and early Cenozoic in the northern Omineca Belt likely reflects the control of regional faults.

8.2. REMAINING QUESTIONS

1. Sphene is common in pelitic schist of the schist complex. As sphene has a U-Pb closure temperature of ≥ 600°C (Ghent et al., 1988), U-Pb analysis could provide information regarding the cooling history of the complex between peak metamorphic temperatures (i.e. 650°C in the highest grade rocks) and 500°C (Tc_{hb}). Similarly, Rb-Sr whole rock and mineral (biotite, muscovite, feldspar) analyses of schist in the complex might shed some light on the cooling history between peak metamorphic temperature and 500°C.

2. Detailed study in the poorly exposed Horseranch fault zone might yield information on the nature of displacement in the zone. Fission track dating of apatite in the

pyroxenitic diorite which is cut by the fault would constrain timing of motion along the fault.

3. Results from isotopic studies in metamorphic core complexes in the U.S.A. have revealed that the detachment, particularly the chlorite breccia zone, is a pathway for fluid flow (see Kyser and Kerrich, 1990 and the references therein). In mylonitic rocks, closed-systems conditions or isotopic buffering of fluids by rock composition prevail, whereas in chlorite breccias, fluids were either isotopically evolved or mixtures of meteoric and metamorphic fluids. The absence of strong retrogression in the mylonite zone in the Horseranch Range suggests that water-rock ratios were low or that fluids were well equilibrated with the rock, whereas chloritization of pyroxenitic diorite and brecciation and abundant calcite veining in dolomitic limestone in the Horseranch fault zone indicate open-system fluid conditions. Preliminary fluid inclusion data from quartz veins and $\delta^{18}O$ on mineral pairs implies that fluids in the schist complex were metamorphic and uniform (R. Rushton, personal communication 1991). An isotopic study of rocks in the mylonite zone and Horseranch fault zone would add to the understanding of origins and movements of fluids under extensional tectonic regimes.

4. Granites are widespread in the northern half of the range and in the mylonite zone. Their mineralogy indicates that they are peraluminous and therefore, probably had a pelitic source. The abundance of granite in the sillimanite-orthoclase-muscovite zone, the presence of enclaves of sillimanite-orthoclase-muscovite schist in granite and the presence of Precambrian inheritance in zircon in granitic mylonite (HP88-167) imply that pelitic rocks of the schist complex could have been the source of granitic melts. As there is no textural evidence for partial melting in the complex, the melting of the schist complex must have taken place at greater depth than that experienced by sillimanite-orthoclase-muscovite schist. A petrogenetic study of these granites would test this hypothesis.

5. Post-tectonic mafic to ultramafic intrusions are apparently unique to the Horseranch Range as they do not occur in other exposures of high-grade Proterozoic rocks in north-central British Columbia. These intrusions have many characteristics of zoned Alaskan-type intrusions (cf. Murray, 1973; Moores, 1972). They contain hornblende pyroxenite, are post-tectonic and display textures indicative of crystallization from a melt. Pyroxenite is present near the centre of the large body in

the northwest part of the map area, whereas diorite and gabbro are exposed at the margins suggesting compositional zoning. Murray (1973) proposed that Alaskan-type ultramafic intrusions are spatially and genetically associated with andesitic volcanic complexes and that their parent magma has an olivine-rich tholeiitic composition. Mafic and ultramafic intrusions in the Horseranch Range may be genetically related to Eocene andesitic volcanic rocks which are exposed along strike-slip faults in northern British Columbia (e.g. Wanless et al., 1978). A petrogenic study of the mafic to ultramafic intrusions would shed light on the nature of Eocene magmatism in the northern Omineca Belt.

6. Detailed structural, metamorphic and isotopic study in other fault-bounded, high-grade anticlinoria such as the Butler Range and the northern part of the Wolverine Range would provide more data on the nature and the timing of the cooling and uplift of the northern Omineca Belt to confirm the interpretation of diachronous uplift proposed here.

REFERENCES

Albee, A. L. 1965. Distribution of Fe, Mg and Mn between garnet and biotite in natural mineral assemblages. Journal of Geology, **73**: 155-164.

Albee, A. L. 1968. Metamorphic zones in northern Vermont. *In* Studies of Appalachian Geology, Northern and Maritime. *Edited by* E-An. Zen, W. S. White and J. B. Hadley. John Wiley and Sons Inc., New York, pp. 329-341.

Albee, A. L. 1972. Metamorphism of pelitic schists: reaction relations of chloritoid and staurolite. Geological Society of America Bulletin, **83**: 3249-3268.

Albee, A. L. and Ray, L. 1970. Correction factors for electron microanalysis of silicates, oxides, carbonates, phosphates and sulfates. Analytical Chemistry, **42**: 1408-1414.

Althaus, E. 1969. Experimental evidence that the reaction of kyanite to form sillimanite is at least bivariant. American Journal of Science, **267**: 273-277.

Alexander, E. C. Jr., Michelson, G. M. and Lanphere, M. A. 1978. MMHb-1: a new $^{40}Ar/^{39}Ar$ dating standard. 4th International Conference on Geochronology, Cosmochronology and Isotope Geology. United States Geological Survey, Open-File Report 79-701: 6-8.

Aleinikoff, J. N., Dusel-Bacon, C. and Foster, H. L. 1986. Geochronology of augen gneiss and related rocks, Yukon-Tanana terrane, east-central Alaska. Geological Society of America Bulletin **97**: 626-637.

Archibald, D. A., Glover, J. K., Price, R. A., Farrar, E. and Carmichael, D. M. 1983. Geochronology and tectonic implications of magmatism and metamorphism, southern Kootenay Arc and neighbouring regions, southeastern British Columbia, Part 1: Jurassic to mid-Cretaceous. Canadian Journal of Earth Science, **20**: 1891-1913.

Armstrong, R. 1988. Mesozoic and early Cenozoic magmatic evolution of the Canadian Cordillera. *In* Mesozoic and early Cenozoic magmatic evolution of the Canadian Cordillera. *Edited by* S. P. Clark (Jr.), B. C. Burchfiel and J. Suppe. Geological Society of America Special Paper 218, pp. 55-91.

Armstrong, R. 1982. Cordilleran metamorphic core complexes -from Arizona to southern Canada. Annual Reviews Earth and Planetary Sciences, **10**: 129-154.

Ashworth, J. R. and Evirgen, M. M. 1984. Garnet and associated minerals in the southern margin of the Menderes Massif, southwest Turkey. Geological Magazine, **121**: 323-337.

Atherton, M. P. 1968. The variation in garnet, biotite and chlorite composition in medium grade pelitic rocks from the Dalradian of Scotland, with particular reference to the zonation in garnet. Contributions to Mineralogy and Petrology, **18**: 347-371.

Atherton, M. P. and Smith, R. A. 1979. Chloritoid-staurolite assemblages from Barrow's Zones in Central Perthshire, Scotland. Geological Magazine, **116**: 469-476.

Avé Lallemant, H. G. and Oldow, J. S. 1988. Early Mesozoic southward migration of Cordilleran transpressional terranes. Tectonics, **7**: 1057-1075.

Bell, T. H. 1985. Deformation partitioning and porphyroblast rotation in metamorphic rocks: a radical reinterpretation. Journal of Metamorphic Geology, **3**: 109-118.

Bell, T. H. and Rubenach, M. J. 1983. Sequential porphyroblast growth and crenulation cleavage development during progressive deformation. Tectonophysics, **92**: 171-194.

Bell, T. H. and Duncan, A. C. 1978. A rationalized and unified shorthand terminology for lineations and fold axes in tectonites. Tectonophysics, **47**: T1-T5.

Bellefontaine, K. 1990. The tectonic evolution of the Ingenika Group and its implications for the boundary between the Omineca and Intermontane Belts, north-central British Columbia. M.Sc. thesis, McGill University, Montreal, Quebec, 94 p.

Bellefontaine, K. 1989. Tectonic evolution of Upper Proterozoic Ingenika Group, north-central British Columbia (94C/12). *In* Geological Fieldwork 1988. British Columbia Ministry of Energy, Mines and Petroleum Resources, Paper 1989-1, pp. 221-226.

Bence, A. E. and Albee, A. L. 1968. Empirical correction factors for the electron microanalysis of silicates and oxides. Journal of Geology, **76**: 382-403.

Berger, G. W. 1975. $^{40}Ar/^{39}Ar$ step heating of thermally overprinted biotite, hornblende and potassium feldspar from Eldora, Colorado. Earth and Planetary Science Letters, **26**: 387-408.

Berman, R. G. 1988. Internally-consistent thermodynamic data for minerals in the system Na_2O - K_2O - CaO - MgO - FeO - Fe_2O_3 - Al_2O_3 - SiO_2 - H_2O - CO_2. Journal of Petrology, **29**: 445-522.

Berthé, D., Choukroune, P., Jegouzo, P. 1979. Orthogneiss, mylonite and non-coaxial deformation of granites: the example of the South Armorican Shear Zone. Journal of Structural Geology, **1**: 31-42.

Berry, R. F. and McDougall, I. 1986. Interpretation of $^{40}Ar/^{39}Ar$ and K/Ar dating evidence from the Aileu Formation, East Timor, Indonesia. Chemical Geology (Isotope Geoscience Section), **59**: 43-58.

Bickle, M. J. and Archibald, N. J. 1984. Chloritoid and staurolite stability: implications for metamorphism in the Archean Yilgarn Block, Western Australia. Journal of Metamorphic Geology, **2**: 179-203.

Biermann, C. 1981. (100) deformation twins in naturally deformed amphiboles. Nature (London), **292**: 621-623.

Binns, R. A. 1969. Hydrothermal investigations of the amphibolite-granulite facies boundary. Geological Society of Australia Special Publication, **2**: 341-344.

Bottinga, Y. and Javoy, M. 1973. Comments on oxygen isotope geothermometry. Earth and Planetary Science Letters, **20**: 250-263.

Bottinga, Y. and Javoy, M. 1975. Oxygen isotope partitioning among the minerals in igneous and metamorphic rocks. Reviews of Geophysics and Space Physics, **13**: 401-418.

Brown, R.L., Journeay, L. S., Lane, L. S., Murphy, D. C. and Rees, J. C. 1986. Obduction, backfolding and piggyback thrusting in the metamorphic hinterland of the southeastern Canadian Cordillera. Journal of Structural Geology, **8**: 255-268.

Buck, W. R., Martinez, F., Steckler, M. S. and Cochran, J. R. 1988. Thermal consequences of lithospheric extension: Pure and Simple. Tectonics, **7**: 213-234.

Butler, R. F., Gehrels, G. E., McClelland, W. C., May, S. R. and Klepacki, D. 1989. Discordant paleomagnetic poles from the Canadian Coast Plutonic Complex: Regional tilt rather than large-scale displacement? Geology, **17**: 691-694.

Carmichael, D. M. 1969. On the mechanism of prograde metamorphic reactions in quartz-bearing pelitic rocks. Contributions to Mineralogy and Petrology, **20**: 244-267.

Carr, S. D., Parrish, R. R. and Brown, R. L. 1987. Eocene structural development of the Valhalla complex, southeastern British Columbia. Tectonics, **6**: 175-196.

Chatterjee, N. D. and Johannes, W. 1974. Thermal stability and standard thermodynamic properties of synthetic $2M_1$ - muscovite, $KAl_2(AlSi_3O_{10}(OH)_2)$. Contributions to Mineralogy and Petrology, **48**: 89-114.

Chinner, G. A. 1967. Chloritoid and the isochemical nature of Barrow's Zones. Journal of Petrology, **8**: 268-282.

Chinner C. A. 1960. Pelitic gneisses with varying ferrous/ferric ratios from Glen Clova, Angus, Scotland. Journal of Petrology, **1**: 178-217.

Cliff, R. A, Droop, G. T. R. and Rex, D. C. 1985. Alpine metamorphism in the south-east Tauern Window, Austria: 2. Rates of heating, cooling and uplift. Journal of Metamorphic Geology, **3**: 403-415.

Colby, J. W. 1968. Magic IV - A computer program for quantitative electron microprobe analysis. Advancements in X-ray analysis, **11**: 287-305.

Collerson, K. D. 1974. Descriptive microstructural terminology for high grade metamorphic tectonites. Geological Magazine, **111**: 313-318.

Coney, P. J. and Harms, T. A. 1984. Cordilleran metamorphic core complexes: Cenozoic extensional relics of Mesozoic compression. Geology, **12**: 550-554.

Copeland, P., Parrish, R. R. and Harrison, T. M. 1988. Identification of inherited radiogenic Pb in monazite and implications for U-Pb systematics. Nature (London), **333**: 760-763.

Crawford, M. L. 1977. Calcium zoning in almandine garnet, Wissahickon Formation, Philadelphia, Pennsylvania. Canadian Mineralogist, **15**: 243-249.

Crowell, J. C. 1974. Origin of Late Cenozoic basins in southern California. *In* Tectonics and Sedimentation. *Edited by* W. R. Dickinson. Society of Economic Paleontologists and Mineralogists, Special Publication 22, pp. 190-204.

Cumbest, R. J., Dury, M. R., van Roermund, H. L. M. and Simpson, C. 1989. Dynamic recrystallization and chemical evolution of clinopyroxene from Senja, Norway. Contributions to Mineralogy and Petrology, **101**: 339-349.

Dallmeyer, R. D. 1974. The role of crystal structure in controlling the partitioning of Mg and Fe^{2+} between coexisting garnet and biotite. American Mineralogist, **59**: 201-203.

Dalziel, I. W. D. and Brown, R. L. 1989. Tectonic denudation of the Darwin metamorphic core complex in the Andes of the Tierra del Fuego, southernmost Chile: Implications for Cordilleran orogenesis. Geology, **17**: 699-703.

Davis, G. H. 1983. Shear-zone model for the origin of metamorphic core complexes. Geology, **11**: 342-347.

Davis, G. H., 1980. Structural characteristics of metamorphic core complexes, southern Arizona. *In* Cordilleran Metamorphic Core Complexes. *Edited by* M. D. Crittenden, P. J. Coney and G. H. Davis. Geological Society of America Memoir 153, pp. 35-77.

Davis, G. A. and Anderson, J. L., 1987. Rapid Miocene uplift of mid-crustal mylonitic rocks, Whipple Mountains, southeastern California. Geological Society of America, Program with Abstracts, **19**: 636.

DeBethune, P., Laduron, D. and Bocquet, J. 1975. Diffusion processes in resorbed garnets. Contributions to Mineralogy and Petrology, **50**: 197-204.

Deer, W. A., Howie, R. A. and Zussman, J. 1978. An Introduction to Rock-forming Minerals, Longman Group Limited, England, 528p.

Dempster, T. J. 1985. Garnet zoning and metamorphism of the Barrovian type area, Scotland. Contributions to Mineralogy and Petrology, **89**: 30-38.

Deville, E. and Struik, L. C. 1990. Polyphase tectonic, metamorphic and magmatic events in the Wolverine Complex, Mount Mackinnon, central British Columbia. *In* Current Research, Part E. Geological Survey of Canada, Paper 90-1E, pp. 65-69.

Dutrow, B. L. and Holdaway, M. J. 1989. Experimental determination of the upper thermal stability of Fe-staurolite + quartz at medium pressures. Journal of Petrology, **30**: 229-248.

Duddy, I. R., Green, P. F. and Laslett, G. M. 1988. Thermal annealing of fission tracks in apatite 3. Variable temperature behaviour. Chemical Geology (Isotope Geoscience Section), **73**: 25-38.

Engebretson, D., Cox, A. and Gordon, R. R. 1985. Relative motion between oceanic and continental plates in the Pacific basin. Geological Society of America Special Paper **206**, 59 pp.

England, P. C. and Molnar, P. 1990. Surface uplift, uplift of rocks and exhumation of rocks. Geology, **18**: 1173-1177.

Erdmer, P. and Baadsgaard, H. 1987. 2.2 Ga age of zircons in three occurrences of Upper Proterozoic clastic rocks of the northern Cassiar terrane, Yukon and British Columbia. Canadian Journal Earth Sciences, **24**: 1919-1924.

Evans, B. W. and Guidotti, C. V. 1966. The sillimanite-potash feldspar isograd in Western Maine, U.S.A. Contributions to Mineralogy and Petrology, **12**: 25-62.

Evenchick, C. 1985. Stratigraphy, metamorphism, structure and their tectonic implications in the Sifton and Desserters Ranges, Cassiar and northern Rocky Mountains, northern British Columbia. Ph.D. thesis, Queen's University, Kingston, Ontario, 191 p.

Evenchick, C. A. 1988. Stratigraphy, metamorphism, structure and their tectonic implications in the Sifton and Deserters Ranges, Cassiar and Northern Rocky Mountains, Northern British Columbia. Geological Survey of Canada Bulletin 376, 90 p.

Evenchick, C., Parrish, R. R. and Gabrielse, H. 1984. Precambrian gneiss and late Proterozoic sedimentation in north-central British Columbia. Geology, **12**: 233-237.

Faure, G. 1986. Principles in Isotope Geology, 2nd edition, John Wiley and Sons, New York, 589 p.

Ferri, F. and Melville, D. M. 1988. Manson Creek mapping project (93N/09). *In* Geological Fieldwork 1987. British Columbia Ministry of Energy, Mines and Petroleum Resources Paper 1988-1, pp. 169-180.

Ferry, J. M. 1984. A biotite isograd in south-central Maine, U.S.A.: Mineral reactions, fluid transfer and heat transfer. Journal of Petrology, **25**: 871-893.

Ferry, J. M. and Spear, F. S. 1978. Experimental calibration of partitioning of Fe and Mg between garnet and biotite. Contributions to Mineralogy and Petrology, **66**: 113-117.

Fleck, R. J., Sutter, J. F. and Elliot, D. H. 1977. Interpretation of discordant ^{40}Ar/^{39}Ar age-spectra of Mesozoic tholeiites from Antarctica. Geochimica et Cosmochimica Acta, **41**: 15-32.

Fleischer, M. W. 1965. Some aspects of geochemistry of yttrium and the lanthanides. Geochimica et Cosmochimica Acta, **29**: 755-772.

Foster, T. Jr. 1986. Thermodynamic models of reactions involving garnet in a sillimanite/staurolite schist. Mineralogical Magazine, **50**: 427-439.

Fourcade, S. and Allègre, C. J. 1981. Trace element behaviour in granite genesis: a case study of the calc-alkaline plutonic association from the Querigut complex (Pyrenees, France). Contributions to Mineralogy and Petrology, **76**: 177-195.

Frank, E. 1983. Alpine metamorphism of calcareous rocks along a cross-section in the Central Alps: Occurrence and breakdown of muscovite, margarite and paragonite. Schewizerische Mineralogische und Petrographische Mitteilungen, **63**: 37-93.

Freer, R. 1981. Diffusion in silicate minerals and glasses: A data digest and guide to the literature. Contributions to Mineralogy and Petrology, **76**: 440-454.

French, B. W. and Eugster, H. P. 1965. Experimental control of oxygen fugacities by graphite-gas equilibriums. Journal of Geophysical Research, **70**: 1529-1539

Fritz, W. H. 1984. Uppermost Precambrian and lower Cambrian strata, Northern Omineca Mountains, north-central British Columbia. *In* Current Research, Part B. Geological Survey of Canada, Paper 84-B, pp. 245-254.

Gabrielse, H. In press. Late Paleozoic and Mesozoic terrane interactions in north-central British Columbia. Canadian Journal of Earth Sciences.

Gabrielse, H. 1985. Major dextral transcurrent displacements along the Northern Rocky Mountain Trench and related lineaments in north-central British Columbia. Geological Society America Bulletin, **96**: 1-14.

Gabrielse, H. 1975. Geology of Fort Grahame E1/2 map-area, British Columbia (94C E1/2). Geological Survey of Canada Paper 75-33, 18 p.

Gabrielse, H. 1963. McDame map-area, Cassiar District, British Columbia. Geological Survey of Canada Memoir 319, 139 p.

Gabrielse, H. and Dodds, C. J. 1982. Faulting and plutonism in northwestern Cry Lake and adjacent map areas, British Columbia. *In* Current Research, Part A. Geological Survey of Canada Paper 82-1A, pp. 321-323.

Galbraith, R. F. 1981. On statistical models for fission track counts. Mathematical Geology, **13**: 471-488.

Ganguly, J. 1972. Staurolite stability and related parageneses. Journal of Petrology, **13**: 335-365.

Ganguly, J. and Kennedy, G. C. 1974. The energetics of natural garnet solid solution. Contributions to Mineralogy and Petrology, **48**: 137-148.

Ganguly, J. and Saxena, S. K. 1984. Mixing properties of aluminosilicate garnets: constraints from natural and experimental data and applications to geothermo-barometry. American Mineralogist, **69**: 88-97.

Gapais, D. 1989. Shear structures within deformed granites: mechanical and thermal indicators. Geology, **17**: 1144-1147.

Ghent, E. D. 1975. Temperature, pressure and mixed volatile equilibria attending metamorphism of staurolite-kyanite-bearing assemblages, Esplanade Range, British Columbia. Geological Society of America Bulletin, **86**: 1654-1660.

Ghent, E. D. 1976. Plagioclase-garnet-Al_2SiO_5-quartz: a potential geobarometer-geothermometer. American Mineralogist, **61**: 710-714.

Ghent, E. D., Stout, M. Z. and Parrish, R. R. 1988. Determination of metamorphic pressure-temperature-time (P-T-t) paths. *In* Heat, Metamorphism and Tectonics, Short Course 14. *Edited by* E. G. Nisbet and C. M. R. Fowler. Mineralogical Association of Canada, pp. 155-188.

Ghent, E. D. and Stout, M. Z. 1984. TiO_2 activity in metamorphosed pelitic and basic rocks: principles and applications to metamorphism in southeastern Canadian Cordillera. Contributions to Mineralogy and Petrology, **86**: 248-255.

Ghent, E. D. and Stout, M. Z. 1981. Geobarometry and geothermometry of plagioclase-biotite-garnet-muscovite assemblages. Contributions to Mineralogy and Petrology, **76**: 92-97.

Ghent, E. D., Robbins, D. B. and Stout, M. Z. 1979. Geothermometry, geobarometry and fluid compositions of metamorphosed calc-silicates and pelites, Mica Creek, British Columbia. American Mineralogist, **64**: 874-885.

Gibson, G. M., McDougall, I. and Ireland, T. R., 1988. Age constraints on metamorphism and the development of a metamorphic core complex in Fiordland, southern New Zealand. Geology, **16**: 405-408.

Gleadow, A. J. W. 1981. Fission-track dating methods: What are the real alternatives? Nuclear Tracks, **5**: 3-14.

Gleadow, A. J. W., Duddy, I. R., Green, P. F. and Lovering, J. F. 1986. Confined fission track lengths in apatite: a diagnostic tool for thermal history analysis. Contributions to Mineralogy and Petrology, **94**: 405-415.

Goldman , D. S. and Albee, A. L., 1977. Correlation of Mg/Fe partitioning between garnet and biotite with $^{18}O/^{16}O$ partitioning between quartz and magnetite. American Journal of Science, **277**: 750-767.

Goldstein, A. G. 1988. Factors affecting the kinematic interpretation of asymmetric boudinage in shear zones. Journal of Structural Geology, **10**: 707-715.

Grambling, J. A. 1981. Kyanite, andalusite, sillimanite and related assemblages in the Truchas Peaks region, New Mexico. American Mineralogist, **66**: 702-722.

Grambling, J. A. and Williams, M. L. 1985. The effects of Fe^{3+} and Mn^{3+} on aluminium silicate phase relations in north-central New Mexico, U.S.A. Journal of Petrology, **26**: 324-354.

Grant, J. A. and Weiblen, P. W. 1971. Retrograde zoning in garnet near the second sillimanite isograd. American Journal of Science, **270**: 281-296.

Green, P. F. 1981. A new look at the statistics in fission-track dating. Nuclear Tracks, **5**: 77-86.

Green, P. F. 1988. The relationship between track shortening and fission track age reduction in apatite: combined influences of inherent instability, annealing anisotropy, length and bias and system calibration. Earth and Planetary Science Letters, **89**: 335-352.

Green, P. F., Duddy, I. R., Laslett, G. M., Hegarty, K. A., Gleadow, A. J. W. and Loverling, J. F. 1989a. Thermal annealing of fission tracks in apatite 4. Quantitative modelling techniques and extension to geological timescales. Chemical Geology (Isotope Geoscience Section), **79**: 155-182.

Green, P. F., Duddy, I. R., Gleadow, A. J. W. and Lovering, J. F. 1989b. Apatite fission track analysis as a paleotemperature indicator for hydrocarbon exploration. *In* Thermal history of sedimentary basins - methods and case histories. *Edited by* N. D. Naeser and T. H. McColluh, pp. 181-195

Green, P. F., Duddy, I. R., Gleadow, A. J. W., Laslett, G. M. and Tingate, P. R. 1986. Thermal annealing of fission tracks in apatite 1. A qualitative description. Chemical Geology (Isotope Geoscience Section), **59**: 237-253.

Gromet, L. P. and Silver, L. T. 1983. Rare-earth element distributions among minerals in a granodiorite and their petrogenetic implications. Geochimica et Cosmochimica Acta, **47**: 925-939.

Guidotti, C. V. 1970. The mineralogy and petrology of the transition from the lower to upper sillimanite zone in the Oquossoc area, Maine. Journal of Petrology, **11**: 277-336.

Guidotti, C. V. 1973. Compositional variation of muscovite as a function of metamorphic grade and assemblage in metapelites from Northwestern Maine. Contributions to Mineralogy and Petrology, **42**: 33-42.

Guidotti, C. V. 1974. Transition from staurolite to sillimanite zone, Rangeley Quadrangle, Maine. Geological Society of America Bulletin, **85**: 475-490.

Guidotti, C. V. 1984. Micas in metamorphic rocks. *In* Micas, Reviews in Mineralogy 13. *Edited by* S. W. Bailey. Mineralogical Society of America, pp. 357-468.

Guidotti, C. V. and Sassi, F. P. 1976. Muscovite as a petrogenetic indicator mineral in pelitic schists. Neues Jahrbuch fur Mineralogie Abhandlungen, **127**: 97-142.

Guidotti, C. V., Trzcienski, W. E. and Holdaway, M. J. 1983. A northern Appalachian transect - eastern townships, Quebec Maine coast to central Maine coast. *In* Regional trends in the geology of the Appalachian - Caledonian - Hercynian - Mauritanide Orogen. *Edited by* P.E. Schenk. NATO ASI Series, Series C: Mathematical and Physical Sciences 116, pp. 235-247.

Hanmer, S. 1986. Asymmetrical pull-aparts and foliation fish as kinematic indicators: Journal of Structural Geology, **8**: 111-122.

Hansen, V. L. 1989. Structural and kinematic evolution of the Teslin suture zone, Yukon: record of an ancient transpressional margin. Journal of Structural Geology, **11**: 717-733.

Hansen, V. L. 1990. Yukon-Tanana terrane: a partial acquittal. Geology, **18**: 365-369.

Hansen, V. L., Mortensen, J. K. and Armstrong, R. L. 1989. U-Pb, Rb-Sr and K-Ar isotopic constraints for ductile deformation and related metamorphism in the Teslin suture zone, Yukon - Tanana terrane, south-central Yukon. Canadian Journal of Earth Sciences, **26**: 2224-2235.

Hanson, G. N., Simmons, K. R. and Bence, A. E. 1975. $^{40}Ar/^{39}Ar$ spectrum ages for biotite, hornblende and muscovite in a contact metamorphic zone. Geochimica et Cosmochimica Acta, **39**: 1269-1277.

Harms, T. A. 1984. Structural style of the Sylvester Allochthon, northeastern Cry Lake map area, British Columbia. *In* Current Research, Part A, Geological Survey of Canada, Paper 84-1A, pp. 109-112.

Harms, T. A. 1989. Geology of the northeast Needlepoint Mountain and Erickson Mines areas, northern British Columbia (104P/4). *In* Geological Fieldwork 1988. British Columbia Ministry of Energy, Mines and Petroleum Resources, Paper 1989-1, pp. 339-345.

Harrison, T. M. 1981. Diffusion of ^{40}Ar in hornblende. Contributions to Mineralogy and Petrology, **78**: 324-331.

Harrison, T. M. 1983. Some observations on the interpretation of $^{40}Ar/^{39}Ar$ age spectra. Chemical Geology (Isotope Geoscience Section), **1**: 319-338.

Harrison, T. M., Duncan, I. and McDougall, I. 1985. Diffusion of ^{40}Ar in biotite: temperature, pressure and compositional effects. Geochimica et Cosmochimica Acta, **49**: 2461-2468.

Heizler, M. T. and Harrison, T. M. 1988. Multiple trapped argon isotope components revealed by $^{40}Ar/^{39}Ar$ isochron analysis. Geochimica et Cosmochimica Acta, **52**: 1295-1303.

Henry, D. J. and Guidotti, C. V. 1985. Tourmaline as a petrogenetic indicator mineral: an example from the staurolite-grade metapelites of NW Maine. American Mineralogist, **70**: 1-15.

Higgins, M. W. 1971. Cataclastic rocks. United States Geological Survey Professional Paper 687, pp. 7 - 11.

Holdaway, M. J. 1971. Stability of andalusite and the aluminum silicate phase diagram. American Journal of Science, **271**: 97-131.

Hollister, L. S. 1966. Garnet zoning: an interpretation based on the Rayleigh fractionation model. Science, **154**: 1647-1651.

Hollister, L. S. 1969. Contact metamorphism in the Kwoiek area of British Columbia: an end member of the metamorphic process. Geological Society of America Bulletin, **80**: 2465-2494.

Hollister, L. S. 1977. The reaction forming cordierite from garnet, the Khtada Lake metamorphic complex, British Columbia. Canadian Mineralogist, **15**: 203-266.

Hoschek, G. 1969. The stability of staurolite and chloritoid and their significance in metamorphism of pelitic rocks. Contributions to Mineralogy and Petrology, **14**: 123-162.

Huneke, J. C. and Smith, S. P. 1976. The realities of recoil: ^{39}Ar recoil out of small grains and anomalous patterns in ^{39}Ar-^{40}Ar dating. *In* 7th Proceedings of the Lunar Science Conference. Geochimica et Cosmochimica Acta, Supplement, Pergamon Press, New York, pp. 1987-2008.

Hunt, P. A. and Roddick, J. C. 1987. A compilation of K-Ar ages, Report 17. *In* Radiogenic Age and Isotopic Studies, Report 1. Geological Survey of Canada Paper 87-2, p. 143-210.

Hurford, A. J. and Hammerschmidt, K. 1985. ^{40}Ar/^{39}Ar and K/Ar dating of the Bishop Fish Canyon Tuffs: Calibration ages for fission-track dating standards. Chemical Geology (Isotope Geoscience Section), **58**: 23-32.

Hurford, A. J. and Green, P. F. 1982. A user's guide to fission track dating — calibration. Earth and Planetary Science Letters, **59**: 343-354.

Hurlburt, C. S. and Klein, C. 1971. Manual of Mineralogy (after James D. Dana). 19th edition, John Wiley and Sons, New York, 532 p.

Hyndman, D. W. and Myers, S. A. 1988. The transition from amphibolite-facies mylonite to chloritic breccia and role of the mylonite in formation of Eocene epizonal plutons, Bitterroot dome, Montana. Geologische Rundschau, **77**: 221-226.

Indares, A. and Martignole, J. 1985. Biotite-garnet geothermometry in granulite-facies rocks: the influence of Ti and Al in biotite. American Mineralogist, **70**: 272-278.

Irving, E., Woodsworth, G. J., Wynne, P. J. and Morrison, A. 1985. Paleomagnetic evidence for displacement from the south of the Coast Plutonic Complex, British Columbia. Canadian Journal of Earth Sciences, **22**: 584-598.

Kerr, P. F. 1959. Optical Mineralogy. McGraw-Hill Inc., New York, 492 p.

Kerrick, D. M. 1987. Fibrolite in contact aureoles of Donegal, Ireland. American Mineralogist, **72**: 240-254.

Kerrick, D. M. 1972. Experimental determination of the muscovite and quartz stability with $P_{H2O} < P_{TOTAL}$. American Journal of Science, **272**, 946-958.

Kerrick, D. M. and Heninger, S. G. 1984. The andalusite-sillimanite equilibrium revisited. Geological Survey of America, Abstracts with Programs, **16**: 558.

Kerrick, D. M. and Speer, J. A. 1988. The role of minor element solid solution on the andalusite-sillimanite equilibrium in metapelites and peraluminous granitoids. American Journal of Science, **288**: 152-192.

Köppel, V. and Grünenfelder, M. 1975. Concordant U-Pb ages of monazite and xenotime from the Central Alps and the timing of the high temperature Alpine metamorphism, a preliminary report. Schweizerische Mineralogische und Petrographische Mitteilungen Bulletin, **55**: 129-132.

Koziol, A. M. and Newton, R. C. 1988. Redetermination of the anorthite breakdown reaction and improvement of the plagioclase-garnet-Al_2SiO_5-quartz geobarometer. American Mineralogist, **73**: 216-223.

Kyser, T. K. and Kerrich, R. 1990. Chemistry of fluids in tectonically active crustal regions. *In* Fluids in tectonically active regimes of the continental crust, short course 18. *Edited by* B. E. Nesbitt. Mineralogical Association of Canada, pp. 195-200.

Lanphere, M. A. and Dalrymple, G. B. 1976. Identification of excess ^{40}Ar by the ^{40}Ar/^{39}Ar age spectrum technique. Earth and Planetary Science Letters, **32**: 141-148.

Laslett, G. M., Kendall, W. S., Gleadow, A. J. W. and Duddy, I. R. 1982. Bias in measurement of fission track length distributions. Nuclear Tracks, **6**: 79-85.

Laslett, G. M., Green, P.F., Duddy, I. R. and Gleadow, A. J. W. 1987. Thermal annealing of fission tracks in apatite, 2. A quantitative analysis. Chemical Geology (Isotope Geoscience Section), **65**: 1-13.

Lindh, A. and Schöberg, H. 1988. A tentative study of the U-Pb isotope system in zircons from the mylonite zone, south-east Norway. Geologiska Föreningens i Stockholm Förhandingar, **110**: 15-20.

Lister, G. S. and Snoke, A. W. 1984. S-C mylonites. Journal of Structural Geology, **6**: 617-638.

Lo, C-H. and Onstott, T.C., 1988, ^{39}Ar recoil artifacts in chloritized biotite. Geochimica et Cosmochimica Acta, **53**: 2697-2711.

Lowden, J. A. 1963. Isotopic Ages, Report 4. *In* Age determination and Geological Studies. Geological Survey of Canada Paper 63-17, p. 48

Mak, E. K., York, D., Grieve, R. A. F. and Dence, M. R. 1976. The age of the Mistastin Lake Crater, Labrador, Canada. Earth and Planetary Science Letters, **31**: 345-357

Malavieille, J. 1987. Kinematics of compressional and extensional ductile shearing deformation in a metamorphic core complex of the northeastern Basin and Range. Journal of Structural Geology, **9**: 541-554.

Maluski, H. 1978. Behaviour of biotites, amphiboles, plagioclases and K-feldspars in response to tectonic events with the ^{40}Ar-^{39}Ar radiometric method. Example of Corsican granite. Geochimica et Cosmochimica Acta, **42**: 1619-1633.

Mansy, J. L. and Gabrielse, H. 1978. Stratigraphy, terminology and correlation of Upper Proterozoic rocks in Omineca and Cassiar Mountains, north-central British Columbia. Geological Survey of Canada, Paper 77-19, 17 p.

Mattinson, J. M. 1982. U-Pb blocking temperatures and Pb loss characteristics in young zircon, sphene and apatite. Geological Society of America, Program with Abstracts, **14**: 558.

Matsuhisa, Y., Goldsmith, J. R. and Clayton, R. N. 1979. Oxygen isotopic fractionation in the system quartz-albite-anorthite-water. Geochimica et Cosmochimica Acta, **43**: 1131-1140.

McDougall, I. and Harrison, T. M. 1988. Geochronology and thermochronology by the $^{40}Ar/^{39}Ar$ method. Oxford Monographs on Geology and Geophysics No. 9. New York, Oxford University Press, 212 p.

Miller, C. F. and Mittlefehldt, D. W. 1982. Depletion of light rare-earth elements in felsic magmas. Geology, **10**: 129-133.

Miyashiro, A. 1964. Oxidation and reduction in the earth's crust with special reference to the role of graphite. Geochimica et Cosmochimica Acta, **28**: 717-729.

Miyashiro, A. 1975. Metamorphism and Metamorphic Belts. George Allen and Unwin Ltd, London, 492 p.

Monger, J. W. H. 1984. Cordilleran tectonics: a Canadian perspective. Bulletin de la Société géologique de France, **7**: 255-278.

Monger, J. W. H. and Irving, E. 1980. Northward displacement of north-central British Columbia. Nature, **285**: 289-294.

Monger, J. W. H., Price, R. A. and Tempelman-Kluit, D. J. 1982. Tectonic accretion and the origin of the two major metamorphic and plutonic welts in the Canadian Cordillera. Geology, **10**: 70-75.

Monger, J. W. H. and Price, R. A. 1979. Geodynamic evolution of the Canadian Cordillera - progress and problems. Canadian Journal of Earth Sciences, **16**: 770-791.

Moores, E. M. 1972. Geotectonic significance of ultramafic rocks. Earth-Science Reviews, **9**: 241-258

Mount, V. S. and Suppe, J. 1987. State of stress near the San Andreas fault: Implications for wrench tectonics. Geology, **15**: 1143-1146.

Muecke, G. K., Elias, P. and Reynolds, P. H. 1988. Hercynian/ Alleghanian overprinting of an Acadian terrane: $^{40}Ar/^{39}Ar$ studies in the Meguma Zone, Nova Scotia, Canada. Chemical Geology (Isotope Geoscience Section), **73**: 153-167.

Murata, K. J., Dutra, C. V., Teixeira da Costa, M. and Branco, J. J. 1958. Composition of monazites from pegmatites in eastern Minas Gerais, Brazil. Geochimica et Cosmochimica Acta, **16**: 1-14.

Murray, C. G. 1973. Zoned ultramafic complexes of the Alaskan type: feeder pipes of andesitic volcanoes. *In* Studies in Earth and Planetary Sciences. *Edited by* R. Shagam, R. B. Hargraves, W. J. Morgan, F. B. van Houten, C. A. Burk, H. D. Holland and L. C. Hollister. Geological Society of America Memoir 132, pp. 313-335.

Naeser, C. W. 1981. The fading of fission tracks in the geological environment - data from deep drill holes. Nuclear Tracks, **5**: 248-250.

Naeser, N. D., Naeser, C. W. and McCulloch, T. H. 1990. Thermal history of rocks in southern San Joaquin Valley, California: Evidence from fission-track analysis. The American Association of Petroleum Geologists Bulletin, **74**: 13-29.

Naylor, M. A., Mandl, G. and Sijpesteijn, C. H. K. 1986. Fault geometries in basement-induced wrench faulting under different initial stress states. Journal of Structural Geology, **8**: 737-752.

Newton, R. C. and Haselton, H. T. 1981. Thermodynamics of the garnet-plagioclase-Al_2SiO_5-quartz geobarometer. *In* Thermodynamics of Minerals and Melts. *Edited by* R. C. Newton, A. Navrotsky and B. J. Wood. p. 131-147.

Olimpio, J. C. and Anderson, D. E. 1978. The relationship between chemical and textural (optical) zoning in metamorphic garnets, South Morar, Scotland. American Mineralogist, **63**: 667-689.

Onstott, T. C. and Peacock, M. W. 1987. Argon retentivity of hornblendes: a field experiment in a slowly cooled metamorphic terrane. Geochimica et Cosmochimica Acta, **51**: 2891-2903.

Parrish, R. R. 1976. Structure, metamorphism and geochronology of the northern Wolverine Complex near Chase Mountain, Aiken Lake map-area, British Columbia. M.Sc. thesis, The University of British Columbia, Vancouver, British Columbia, 89 p.

Parrish, R. R. 1979. Geochronology and tectonics of the northern Wolverine Complex, British Columbia. Canadian Journal of Earth Science, **16**: 1428-1438.

Parrish, R. R. 1988. U-Pb systematics of monazite and a preliminary estimate of its closure temperature based on natural examples. Geological Association of Canada, Program with Abstracts, **13**: A94.

Parrish, R. R. 1990. U-Pb dating of monazite and its application to geological problems. Canadian Journal of Earth Sciences, **27**: 1431-1450.

Parrish, R. R., Haugerud, R. A. and Price, R. A. 1990. The Eocene tectonic transition. Oregeon to Alaska. Penrose Conference Report. Geological Society of America News and Information, May (no. 5), **12**: 124-125.

Parrish, R. R., Carr, S. D. and Parkinson, D. L. 1988. Eocene extensional tectonics and geochronology of the southern Omineca Belt, British Columbia and Washington. Tectonics, **7**: 181-212.

Parrish, R.R. and Krogh, T. E. 1987. Synthesis and purification of ^{205}Pb for U-Pb geochronology. Chemical Geology (Isotope Geoscience Section), **66**: 103-110.

Parrish, R. R., Roddick, J. C., Loveridge, W. D. and Sullivan, R. W. 1987. Uranium-lead analytical techniques at the geochronology laboratory, Geological Survey of Canada. Geological Survey of Canada Paper 87-2.

Parrish, R.R. and Roddick, J. C. 1985. Geochronology and isotope geology for the geologist and explorationist. Geological Association of Canada, Cordilleran Section, Short Course Number 4, pp. III-1 to III-15.

Passchier, C. W. and Simpson, C. 1986. Porphyroclast systems as kinematic indicators: Journal of Structural Geology, **8**: 831-843.

Perchuk, L. L. and Lavrent'eva, I. V. 1983. Experimental investigation of exchange equilibria in the system cordierite-garnet-biotite. *In* Kinetics and Equilibrium in Mineral Reactions. *Edited by* S. K. Saxena. Springer Verlag, pp. 199-240.

Petrakakis, K. 1986. Metamorphism of high-grade gneisses from the Moldanubian zone, Austria, with particular reference to garnets. Journal of Metamorphic Geology, **4**: 323-344.

Pidgeon, R. T. and Aftalion, M. 1978. Cogenetic and inherited zircon U-Pb systems in granites: Paleozoic granites of Scotland and England. *In* Crustal evolution in northwestern Britain and adjacent regions. *Edited by* D. R. Bowes. Geology Journal (Liverpool) Special Issue 10, pp. 183-220.

Pigage, L. C. and Jilson, G. A. 1985. Major extensional faults, Anvil Pb-Zn district, Yukon. Geological Society of America Abstracts with Programs, **17**: 400.

Plint, H. E. and Erdmer, P. 1989a, Structure and metamorphism in the Horseranch Range, north-central British Columbia (102P/2, 7, 10). *In* Geological Fieldwork 1988. British Columbia Ministry of Energy, Mines and Petroleum Resources Paper 1989-1, pp. 347-351.

Plint, H. E. and Erdmer, P. 1989b. Metamorphism, deformation and uplift of Proterozoic and lower Paleozoic rocks in the Horseranch Range, north-central British Columbia. Geological Society of America Abstracts with Programs, 1989, 85th Annual Cordilleran Section Meeting, **21**: 129.

Plint, H. E. and Erdmer, P. 1988. Geological studies in the Horseranch Range (104P/7, 10). *In* Geological Fieldwork 1987. British Columbia Ministry of Energy, Mines and Petroleum Resources Paper 1988-1, pp. 255-260.

Press, W. H., Flannery, B. P., Teukolsky, S. A. and Vetterling, W. T. 1986. Numerical Recipes, 818 pp. Cambridge University Press, Cambridge.

Price, R. A. 1986. The southeastern Canadian Cordillera: Thrust faulting, tectonic wedging and delamination of the lithosphere. Journal of Structural Geology, **8**: 239-254.

Price, R. A. 1979. Intracontinental ductile crustal-spreading linking the Fraser River and Northern Rocky Mountain Trench transform fault zones, south-central British Columbia and northeast Washington. Geological Society of America Abstracts with Program, **6**: 499.

Price, R. A., Monger, J. W. H. and Roddick, J. A. 1985. Cordilleran cross-section; Calgary to Vancouver. *In* Field Guides to Geology and Mineral Deposits in the Southern Canadian Cordillera. *Edited by* D. J. Tempelman-Kluit. Geological Society of America, Cordilleran Section, Vancouver, British Columbia, p 3-1 to 3-85.

Price, R. A. and Carmichael, D. M. 1986. Geometric test for Late Cretaceous - Paleogene intracontinental transform faulting in the Canadian Cordillera. Geology, **14**: 468-471.

Pupin, J. P. 1980. Zircon and granite petrology. Contributions to Mineralogy and Petrology, **73**: 207-220.

Råheim, A. and Green, D. H. 1974. Experimental determination of the temperature and pressure dependence of the Fe-Mg partition coefficient for coexisting garnet and clinopyroxene. Contributions to Mineralogy and Petrology, **48**: 179-203.

Ramsay, 1967. Folding and fracturing of rocks. New York, McGraw- Hill Book Company, 568 p.

Ranalli, G., Brown, R. L. and Bosdachin, R. 1989. A geodynamic model for extension in the Shuswap core complex, southeastern Canadian Cordillera. Canadian Journal of Earth Sciences, **26**: 1647-1653.

Rao, P. B. B. and Johannes, W. H. 1979. Further data on the stability of staurolite and quartz and related assemblages. Neues Jahrbuch fur Mineralogie Monatsheft, **1979**: 437-477.

Rast, N. and Sturt, B. A. 1957. Crystallographic and geological factors in the growth of garnets from Central Perthshire. Nature (London), **179**: 215.

Rehrig, W. A. 1986. Processes of regional Tertiary extension in the western Cordillera: Insights from the metamorphic core complexes. *In* Extensional tectonics of the southwestern United States: A perspective on processes and kinematics. *Edited by* L. Mayer. Geological Society of America Special Paper 208, pp. 97-122.

Rehrig, W. A. and Reynolds, S. J. 1980. Geologic and geochronologic reconnaisance of a northwest-trending zone of metamorphic core complexes in southern and western Arizona. *In* Cordilleran metamorphic core complexes. *Edited by* M. D. Crittenden, P. J. Coney and G. H. Davis. Geological Society of America Memoir 153, pp. 131-158.

Reynolds, P. H., Elias, P., Muecke, G. K. and Grist, A. M. 1987. Thermal history of the southwestern Meguma zone, Nova Scotia, from an ^{40}Ar/^{39}Ar and fission track dating study of intrusive rocks. Canadian Journal of Earth Sciences, **24**: 1952-1965.

Rhodes, B. P. and Hyndman, D. W. 1984. Kinematics of mylonites in the Priest River "metamorphic core complex", northern Idaho and northeastern Washington. Canadian Journal of Earth Sciences, **21**: 1161-1170.

Richardson, S. W. 1968. Staurolite stability in part of the system Fe-Al-Si-O-H. Journal of Petrology, **9**: 467-488.

Robie, R. A., Berthke, P. M., Beardsley, M. 1967. Selected X-ray crystalographic data, molar volumes and densities of minerals and related substances. United States Geological Survey Bulletin 1248.

Roddick, J. C. 1978. The application of isochron diagrams in ^{40}Ar-^{39}Ar dating: a discussion. Earth and Planetary Science Letters, **41**: 233-244.

Roddick, J. C., Loveridge, W. D. and Parrish, R. R. 1987. Precise U/Pb dating of zircon at the sub-nanogram Pb level. Chemical Geology (Isotope Geoscience Section), **66**: 111-121.

Roots, E. F. 1954. Geology and mineral deposits of Aiken Lake map-area, British Columbia. Geological Survey of Canada Memoir 274, 246 p.

Salje, E. 1986. Heat capacities and entropies and andalusite and sillimanite: The influence of fibrolitization on the phase diagram of the Al_2SiO_5 polymorphs. American Mineralogist, **71**: 1366-1371.

Sanderson, D. J. and Marchini, W. R. D. 1984. Transpression. Journal of Structural Geology, **6**: 449-458.

Schärer, U. 1984. The effect of initial ^{230}Th disequilibrium on young U-Pb ages: the Makalu case, Himalaya. Earth and Planetary Science Letters, **67**: 191-204.

Schärer, U., Xu, R-H. and Allègre, C. J. 1986. U-(Th)-Pb systematics and ages of Himalayan leucogranites, South Tibet. Earth and Planetary Science Letters, **77**: 35-48.

Schärer, U. and Allègre, C. J. 1983. The Palung granite (Himalaya): high-resolution U-Pb systematics in zircon and monazite. Earth and Planetary Science Letters, **63**: 423-432.

Selverstone, J. 1988. Evidence for east-west crustal extension in the eastern Alps: Implications for the unroofing of the Tauern Window. Tectonics, **7**: 87-105.

Sevigny, J. H., Parrish, R. R., Donelick, R. A. and Ghent, E. D. 1990. Northern Monashee Mountains, Omineca Crystalline Belt, British Columbia: Timing of metamorphism, anatexis and tectonic denudation. Geology, **18**: 103-106.

Sevigny, J. H., Parrish, R. R. and Ghent, E. D. 1989. Petrogenesis of peraluminous granites, Monashee Mountains, southeastern Canadian Cordillera. Journal of Petrology, **30**: 557-581.

Sibson, R. H. 1983. Continental fault structure and the shallow earthquake source. Geological Society of London Journal, **140**: 741-767.

Sibson, R. J. 1977. Fault rocks and fault mechanisms, Journal of the Geological Society of America, **133**: 191-213.

Simpson, C. 1985. Deformation of granitic rocks across the brittle-ductile transition. Journal of Structural Geology, **7**: 503-511.

Simpson, C. and Wintsch, R. P. 1989. Evidence for deformation-induced K-feldspar replacement by myrmekite. Journal of Metamorphic Geology, **7**: 261-275.

Sinha, A. K. and Glover, L. 1978. U/Pb systematics of zircons during dynamic metamorphism: a study from the Brevard fault zone. Contributions to Mineralogy and Petrology, **66**: 305-310.

Snoke, A. W. and Frost, B. R. 1990. Exhumation of high pressure pelitic schist, Lake Murray Spillway, South Carolina: Evidence for crustal extension during Alleghanian strike-slip faulting. American Journal of Science, **290**: 859-881.

Sonder, L. J., England, P. C., Wernicke, B. P. and Christiansen, R. L. 1987. A physical model for Cenozoic extension of western North America. *In* Continental Extension Tectonics. *Edited by* M. P. Coward, J. F. Dewey, J. F. and P. L. Hancock. Geological Society Special Publication 28, pp. 187-201.

Spear, F. S. 1989. Petrologic determination of metamorphic pressure-temperature-time paths. *In* Metamorphic pressure-temperature-time paths, Short Course in Geology 7. *Edited by* M. L. Crawford and E. Padovani. American Geophysical Union, pp. 1-50.

Spear, F. S., Kohn, M. J., Florence, F. P. and Menard, T. 1991. A model for garnet and plagioclase growth in pelitic schists: implications for thermobarometry and P-T path determinations. Journal of Metamorphic Geology, **8**: 683-696.

Spencer, J. E. 1984. Role of tectonic denudation in warping and uplift of low-angle normal faults. Geology, **12**: 95-98.

Stacey, J. S. and Kramers, J. D. 1975. Approximation of terrestrial lead isotope evolution by a two-stage model. Earth and Planetary Science Letters, **26**: 207-221.

Steiger, R. H. and Jäger, E. 1977. Subcomission on geochronology: Convention on the use of decay constants in geo- and cosmo-chronology. Earth and Planetary Science Letters, **36**: 359-362.

Streckeisen, A. 1976. To each plutonic rock its proper name. Earth Science Reviews, **12**: 1-13.

Struik, L. C. 1989. Regional geology of the McLeod Lake map area, British Columbia. *In* Current Research, Part E, Geological Survey of Canada, Paper 89-1E, p. 109-114.

Sylvester, A. G. 1988. Strike-slip faults. Geological Society of America Bulletin, **100**: 1666-1703.

Tchalenko, J. S. and Ambraseys, N. N. 1970. Structural analysis of the Dasht-e Bayaz (Iran) earthquake fractures. Geological Society of America Bulletin, **81**: 41-60.

Tempelman-Kluit, D. J. 1977. Quiet Lake (105F) and Finlayson Lake (105G) map-areas, Yukon. Geological Survey of Canada Open File 486.

Thompson, A. B. 1976. Mineral reactions in pelitic rocks: II. Calculation of some P-T-X (Fe-Mg) phase relations. American Journal of Science, **276**: 425-454.

Thompson, A. B. 1982. Dehydration melting of pelitic rocks and the generation of H_2O-undersaturated granitic liquids. American Journal of Science, **282**: 1567-1595.

Thompson, J. B. 1957. The graphical analyses of mineral assemblages in pelitic schists. American Mineralogist, **42**: 842-858.

Thompson, J. B., Tracy, R. J., Lyttle, P. T. and Thompson, J. B., Jr. 1977. Prograde reaction histories deduced from compositional zonation and mineral inclusions in garnet from the Gassetts schist, Vermont. American Journal of Science, **227**: 1152-1167.

Thompson, P. H. and Bard, J-P. 1982. Isograds and mineral assemblages in the eastern axial zone, Montagne Noire (France): implications for temperature gradients and P-T history. Canadian Journal of Earth Sciences, **19**: 129-143.

Tracy, R. J. 1982. Compositional zoning and inclusions in metamorphic minerals. *In* Characterization of metamorphism through mineral equilibria, Reviews in Mineralogy 10. *Edited by* J. M. Ferry. Mineralogical Society of America, pp. 355-397.

Tracy, R. J. 1978. High grade metamorphic reactions and partial melting in pelitic schist, west-central Massachusetts. American Mineral **61**: 150-178.

Tracy, R. J., Robinson, P. and Thompson, A. B. 1976. Garnet composition and zoning in the determination of temperature and pressure of metamorphism, central Massachusetts. American Mineralogist, **61**: 762-775.

Turner, F. G. 1981. Metamorphic Petrology Mineralogical, Field and Tectonic Aspects. 2nd edition, McGraw-Hill Book Company, New York, 524 p.

van Breemen, O., King, J. E. and Davis, W. J. 1990. U-Pb and monazite ages for plutonic rocks in the Contwoyto - Nose Lakes map area, central Slave Province, District of Mackenzie, Northwest Territories. *In* Radiogenic age and isotopic studies, Report 3. Geological Survey of Canada Paper 89-2, pp. 29-37.

Vernon, R. H. 1979. Formation of late sillimanite by hydrogen metasomatism (base-leaching) in some high-grade gneisses. Lithos, **12**, 143-152.

Wanless, R. K., Stevens, R. D., Lachance, G. R. and Delabio, R. 1978. Age determinations and geological studies, K-Ar isotopic ages, Report 13. Geological Survey of Canada Paper 77-2, pp. 21-22.

Wanless, R. K., Stevens, R. D., Lachance, G. R. and Delabio, R. N. 1972. Age determinations and geological studies, K-Ar Isotopic Ages, Report 10. Geological Survey of Canada Paper 71-2, pp. 11-27.

Wanless, R. K., Stevens, R. D., Lachance, G. R. and Delabio, R. N. 1969. Age determinations and geological studies, K-Ar Isotopic Ages, Report 9. Geological Survey of Canada Paper 69-2A, pp. 6-10.

Wayne, D. M. and Sinha, A. K. 1988. Physical and chemical response of zircons to deformation. Contributions to Mineralogy and Petrology, **98**: 109-121.

Wheeler, J. O. and McFeeley, P. 1987. Tectonic assemblage map of the Canadian Cordillera and adjacent parts of the United States of America. Geological Survey of Canada Open File Map 1561 (Sheet 1 of 2).

Wernicke, B. 1985. Uniform-sense normal simple shear of the continental lithosphere. Canadian Journal of Earth Sciences, **22**: 108-125.

Wilcox, R. E., Harding, T. P., Seely, D. R. 1973. Basic wrench tectonics. American Association of Petroleum Geology Bulletin, **57**: 74-96.

Winkler, H. G. F. 1979. Petrogenesis of Metamorphic Rocks, 5th edition. New York: Springer-Verlag, 348 p.

Wood, B. J. and Fraser, D. G. 1984. Elementary Thermodynamics for Geologists. Oxford University Press, London, 303p.

Woodsworth, G. J. 1979. Metamorphism, deformation and plutonism in the Mount Raleigh pendant, Coast Mountains, British Columbia. Geological Survey of Canada Bulletin, 295, 58 p.

Woodsworth, G. J. 1977. Homogenization of zoned garnets from pelitic schists. Canadian Mineralogist, **15**: 230-242.

Wones, D. R. and Eugster, H. P. 1965. Stability of biotite: experiment, theory and application. American Mineralogist **50**: 1228-1272

Yardley, B. W. D. 1977. An empirical study of diffusion in garnet. American Mineralogist, **62**: 793-800.

Yardley, B. W. D., Leake, B. E. and Farrow, C. M. 1980. The metamorphism of Fe-rich pelites from Connemara, Ireland. Journal of Petrology, **21**: 365-399.

Yeliseyeva, O. P. 1977. Content and distribution of uranium, thorium, yttrium and the rare-earths in accessory minerals in granitoids. Geochemistry, **9**: 37-49.

York, D. and Lopez-Martinez, M. 1986. The two-faced mica. Geophysical Research Letters, **13**: 973-975.

APPENDIX 1: Locations and detailed descriptions of samples analysed for mineral chemistry and geochronometry

General petrographic features of the main rock types in the map area are summarized in Table A1.1 and A1.2. Samples analysed for mineral chemistry and geochronometry (U-Pb, ^{40}Ar-^{39}Ar and fission track) are described below in detail. Sample localities are shown in Figure A1.1 and their coordinates, map numbers and elevations listed below. Abbreviations used are given at the front of the thesis. In sample descriptions, no distinction in feldspar type is given where optical determination is impossible and mineral chemistry was not obtained. Average grain size is given as v.f.gr. = $\leq$ 1 mm, f.gr. = 1 to 2 mm, m.gr. = >2 to 5 mm, c.gr. = > 5 mm.

SAMPLE LOCALITIES:

Sample	Northing	Easting	Map	Elevation
HP87-3	59°28’44"N	128°59’21"W	104P/7	1000m
HP87-5	59°29’26"N	128°54’29"W	104P/7	1820m
HP87-28A	59°27’07"N	128°56’03"W	104P/7	1560m
HP87-65	59°29’10"N	128°58’45"W	104P/7	1000m
HP87-75A	59°29’49"N	128°57’00"W	104P/7	1440m
HP87-78D	59°25’46"N	128°52’00"W	104P/7	1960m
HP87-78E	59°25’46"N	128°52’00"W	104P/7	1960m
HP87-79	59°25’28"N	128°52’10"W	104P/7	1940m
HP87-92	59°26’47"N	128°53’08"W	104P/7	1950m
HP97-105	59°24’70"N	128°51’30"W	104P/7	2050m
HP87-110	59°26’07"N	128°55’27"W	104P/7	1660m
HP87-139	59°25’38"N	128°51’43"W	104P/7	1970m
HP88-151	59°31’55"N	128°56’59"W	104P/10	1000m
HP88-159	59°30’31"N	128°58’26"W	104P/10	930m
HP88-167	59°30’43"N	128°57’42"W	104P/10	1350m
HP88-171	59°32’02"N	128°57’59"W	104P/10	915m
HP88-255	59°10’18"N	128°42’54"W	104P/2	1640m
HP88-272	59°11’42"N	128°43’22"W	104P/2	1280m
HP88-296	59°17’08"N	128°49’16"W	104P/7	1560m
HP88-297	59°17’08"N	128°49’16"W	104P/7	1560m
HP88-308	59°18’21"N	128°46’00"W	104P/7	1780m
HP88-324	59°21’42"N	128°46’17"W	104P/7	1635m
HP88-325	59°21’47"N	128°49’26"W	104P/7	1980m

SAMPLE DESCRIPTIONS:

Igneous rock classification after Streckeisen (1976) on the basis of point counting (min. 1000 points) of cobalte nitrate stained rock slabs.

SAMPLE HP87-3

ROCK TYPE: bi qtz monzonite protomylonite

FIELD RELATIONS: Near the western limit of exposure of the mylonite zone at the northern end of the Horseranch Range. Mylonitic foliation is parallel to that in the surrounding metasedimentary mylonites. Contacts oblique to mylonitic foliation. Moderately to well preserved granitic textures and restricted aerial extent suggest that this sample is a mylonitized intrusion.

HAND SAMPLE: Light brown to grey and cream weathering, black and white on the fresh surface; c.gr to m.gr (3 to 6 mm); moderately to strongly foliated; moderately lineated; foliation defined by bi wraps around Ksp porphyroclasts (up to approximately 1 cm diameter); lineation defined by fsp; poorly developed Type I C-S planes (terminology after Lister and Snoke, 1984). Minor, elongate bi-rich patches (enclaves?) parallel to the foliation and up to 3 cm in their longest dimension.

THIN SECTION: mc (26%), pl (37%), bi (20%), qtz (15%), sph (1%), mt (1%), ap (tr), ep (tr), zr (tr); retrograde chl after bi, minor ser after pl; mc and pl form porphyroclasts - some are zoned; minor myrmekitic intergrowths of qtz in pl developed at mc grain boundaries; granitic texture is well preserved but bi is "shredded" and qtz is partially recrystallized; qtz subgrains show undulose extinction; bi is partially replaced by chl; qtz and bi commonly present along fractures in mc; sph locally rims mt.

SAMPLE HP87-5

ROCK TYPE: sil-or-mu-gt schist

FIELD RELATIONS: In schist complex at northern end of the range, west of small pond, approximately 15 m from post-S_2 granite/schist contact.

HAND SAMPLE: Rusty to yellowish brown weathering; grey to white on the fresh surface; f.gr to m.gr (1-3 mm); schistose; crenulated (amplitude 1-2 cm; wavelength 3 cm); bi and mu define S_2.

THIN SECTION: mu (30%), qtz (30%), bi (30%), sil (5%), pl (2%), or (1%), gt (1%), ilm (1%), zr (tr), ap (tr); minor retrograde chl partially replaces gt along fractures and micas; mu and qtz form a "wormy" intergrowth and are overprinted by fb; randomly oriented fb also overprints pl, bi and qtz in the matrix; subid gt includes qtz and ilm; no S_i; bi, mu and elongate qtz subgrains define S_2.

SAMPLE HP87-28A

ROCK TYPE: hb-bi protomylonite

FIELD RELATIONS: On ridge crest, near eastern boundary of mylonite zone, contacts with mylonitic granite and schist are gradational over approximately 4 m.

HAND SAMPLE: Rusty yellow to brown weathering; dark grey with white fsp augen on the fresh surface; f.gr to m.gr.; moderately foliated to schistose, fsp augen up to 5 mm diameter locally; amp, bi and qtz-fsp aggregates define the foliation.

THIN SECTION: pl (30%), hb (25%), bi (25%), qtz (10%), ksp (8%), sph (1%), opm (1%), ap (tr), ep? (tr); subid, blue-green hb; subid pl forms porphyroclasts wrapped around by the hb-bi defined foliation; minor ribbon texture developed in qtz; sph rims opm locally.

SAMPLE HP87-65

ROCK TYPE: mylonitic sil-or-mu-gt schist

FIELD RELATIONS: In northwestern part of mylonite zone in river valley, north side of river.

HAND SAMPLE: Yellowish to greyish brown weathering; grey to black on the fresh surface; f.gr.; well developed schistosity; micas define foliation; abundant fb.

THIN SECTION: sil (40%), bi (29%), qtz (15%), ksp (15%), gt (0.5%), chl (0.5%), mu (tr), ap (tr), opm (tr), zir (tr), rt (tr); retrograde chl and rt after biotite and chl after gt; subid to xeno gt overgrows (S_2) and contains inclusion trails defined by bi and opm; schistosity is defined by bi and sil and is folded into tight to isoclinal irregular folds with axial traces commonly parallel to S_2; fb and c.gr. subid sil developed.

SAMPLE HP87-75A

ROCK TYPE: foliated mu-bi granite orthogneiss

FIELD RELATIONS: Strongly foliated granite in sil-mu-or zone of schist complex, contacts between the granite and schists are parallel to the foliation in both units, foliation in granite is parallel to that in the surrounding sil-mu-or-gt schist indicating that the granite was deformed with the schist.

HAND SAMPLE: Reddish yellow, yellow and grey weathering; creamy white on the fresh surface; f.gr.; well foliated; two-mica granite orthogneiss.

THIN SECTION: pl (33%), or (25%), qtz (22%), mu (10%), bi (10%), ap (tr), zr (tr); moderate ser after fsp; foliation defined by micas and elongated qtz subgrains; ap commonly included in fsp.

SAMPLE HP87-78D

ROCK TYPE: amphibolite

FIELD RELATIONS: Concordant amphibolite layer in schist complex exposed on cliff west of Gale Force Lake (see Figure 1-24-1, Plint and Erdmer, 1988); centre of amphibolite layer contains ophitic texture, margins are schistose; schistosity is parallel with that in the surrounding schist indicating that the schist and amphibolite were deformed together.

HAND SAMPLE: Green-brown and grey weathering; dark green to black and white on fresh surface; f.gr.; schistose.

THIN SECTION: hb (56%), bi (30%), qtz (5%), pl (8%), opm (0.5%), sph (0.5%), ap (tr); minor ser after pl; moderately developed schistosity defined by subid bi and hb;

pl forms subid to xeno grains interstitial to hb and bi and shows minor optical zoning.

SAMPLE HP87-78E

ROCK TYPE: mu-bi granite

FIELD RELATIONS: Granite cuts S_2 in sil-or-mu-gt schist and schistosity in amphibolite. Boudinaged sills along the foliation in the sil-or-mu-gt schist are traceable into the main, undeformed granite body. These observations indicated that the granite is syn- to post-tectonic with respect to the main schistosity (S_2) in the surrounding schist. Aplitic and pegmatitic phases are also present.

HAND SAMPLE: Yellowish grey weathering; grey and white on the fresh surface; m.gr. to c.gr.; massive; equigranular.

THIN SECTION: pl (33%), or (24%), qtz (21%), mu (10%), bi (10%), sil (1%), ap (1%); minor to moderate ser after pl; equigranular; hypoidiomorphic texture; mu is partially replaced by Ksp and fb; Ksp forms a wormy intergrowth with mu; pl is locally myrmekitic and perthitic.

SAMPLE HP87-79

ROCK TYPE: leucocratic, two mica-garnet, granite pegmatite,

FIELD RELATIONS: Intrudes sil-or-mu schist and cuts S_2.

HAND SAMPLE: Fresh 1-2 cm mica books from a yellowish white to rusty brown weathering; white, cream and dark brown granite pegmatite.

THIN SECTION: no thin section was examined.

SAMPLE HP87-92

ROCK TYPE: pyroxenitic diorite

FIELD RELATIONS: Intrudes sil-or-mu schist and cuts S_2.

HAND SAMPLE: Greenish-brown to greenish-black weathering; dark brown to black on the fresh surface; c.gr.; bi up to 1 cm in diameter; cpx up to 5 mm diameter.

THIN SECTION: pl (55%), bi (22%), cpx (17%), hb (2%), qtz (2%), sph (1%), ap (1%), ep (tr); green hb partly replaces cpx; equigranular, hypoidiomorphic to pegmatitic texture; pl is strongly twinned and in some cases is moderately to strongly zoned.

SAMPLE HP87-105

ROCK TYPE: hb-bi schist

FIELD RELATIONS: Concordant layer in sil-or-mu schist; schistosity in hb-bi schist is parallel to S_2 in sil-or-mu schist.

HAND SAMPLE: Greenish-brown weathering; dark green to brownish black on fresh surface; f.gr.; schistose.

THIN SECTION: hb (55%), bi (20%), qtz (15%), pl (10%), sph (tr); schistose texture, sub bi and hb define the schistosity.

SAMPLE HP87-110

ROCK TYPE: bi-mu granite mylonite

FIELD RELATIONS: Mylonitic foliation in the granite is parallel to that in the sil-or-mu schist although foliation is oblique to the granite-schist contact. This suggests that the granite was intrusive into the mylonite and deformed with the mylonite. The granite is interpreted as syn-tectonic with respect to the mylonitization.

HAND SAMPLE: Yellowish grey weathering; light grey to white on the fresh surface; m.gr. to c.gr.; strongly foliated and lineated; type I S-C planes very well developed; lineation defined by elongated fsp and qtz.

THIN SECTION: qtz (30%), pl (29%), Ksp (26%), mu (7%), bi (7%), ap (0.5%), op min (0.5%), chl (tr), zr (tr), sil (tr); minor chl after bi and ser after fsp; some mu grains show partial replacement by Ksp and fb.; mu (retrograde?) partially replaces mc along twin planes. sense of shear from S-C planes and asymmetric porphyroclast systems is dextral down-plunge of the lineation.

SAMPLE HP87-139

ROCK TYPE: pegmatitic mu-bi-gt granodiorite

FIELD RELATIONS: Granodiorite intrudes sil-mu-or-gt schist as sills along S_2 and as dikes cutting S_2.

HAND SAMPLE: Yellowish to brownish grey weathering; dark grey to white on the fresh surface; massive; pegmatitic to m.gr.; Ksp megacrysts are perthitic, some include gt; minor 3-4 mm x 1-2 mm crystals of tm; weathered surface locally oxidized.

THIN SECTION: pl (41%), qtz (25%), Ksp (13%), bi (10%), mu (10%) and chl, gt, tm, ep (1%); (% difficult to estimate due to pegmatitic nature of the sample); minor chl after bi and moderate to extensive ser after fsp; fb overprints (replaces?) mu; subhd gt moderately fractured.

SAMPLE HP88-151

ROCK TYPE: st-gt-(and) schist

FIELD RELATIONS: Pelitic layer in schist complex at inferred northern contact with overlying phl marble, approximately 4 m from 2 mica, post-S_2 granite.

HAND SAMPLE: Yellow-brown weathering; bluish grey to yellowish grey on fresh surface; f.gr.; porphyroblasts of bi, gt andl and st present; pink-weathering, xeno to subid andl porphyroblasts are up to 3 mm diameter; subid st porphyroblasts are up to 2 mm long.

THIN SECTION: mu (30%), qtz (15%), st (15%), bi (12%), gt (10%) and (10%), pl (5%), ilm (2%), ap (0.5%), tm (0.5%), fb (tr); mu and ilm define crenulated schistosity; subid bi replaces subid to xeno gt forming atoll gt; andl forms subid to xeno poikiloblasts which include all other phases and partly replace subid st; trace amounts of fb overprint bi.

SAMPLE HP88-159

ROCK TYPE: mu-bi granite mylonite

FIELD RELATIONS: Mylonitized granite from northern end of marginal mylonite zone, contacts with other rock types not exposed, granitic textures preserved.

HAND SAMPLE: Yellowish brown to grey weathering, white to cream grey on the fresh surface; m.gr; strongly foliated and lineated; Type I S-C planes are well developed; foliation defined by micas; lineation defined by elongated feldspar and quartz.

THIN SECTION: pl (32%), Ksp (30%), qtz (26%), mu (6%), bi (5%), ap (0.5%), chl (0.5%); minor chl after bi; quartz strongly subgrained; moderately sericitized feldspars form porphyroclasts; sense of shear from S-C planes and asymmetric porphyroclast systems is dextral down-plunge of the lineation;

SAMPLE HP88-167

ROCK TYPE: mu-bi granite mylonite

FIELD RELATIONS: Contacts with other rock types not exposed. Although not in the mylonite zone as mapped (see sample locality map) sample has moderately developed S-C fabric. Shear sense is dextral down lineation suggesting that the mylonitization experienced by this sample is contemporaneous with that recorded in the mylonite zone proper.

HAND SPECIMEN: Yellow to grey weathering; grey and creamy white on the fresh surface; f.gr. to m.gr.; strongly lineated; moderately developed Type I S-C fabric indicating top down-to-the-northwest shear along the lineation.

THIN SECTION: pl (32%), qtz (27%), Ksp (25%), mu (10%), bi (5%), ap (1%), chl (tr), op min (tr); moderate ser after pl and minor chl after bi; lineation defined by aligned micas and elongated qtz subgrains; Ksp and pl form porphyroclasts; myrmekitic textures locally in pl.

SAMPLE HP88-171

ROCK TYPE: st-gt schist

FIELD RELATIONS: Pelitic layer in phl marble unit.

HAND SAMPLE: Rusty- to yellow-brown weathering; bluish to yellowish grey on fresh surface; porphyroblastic; f.gr.; schistose.

THIN SECTION:

mu (30%), bi (25%), qtz (25%), st (5%), pl (5%), gt (5%), ilm (tr), ap (tr), zir (tr), fb (tr); minor retrograde chl after gt, bi and st; subid to xeno st contain stage 2 S_i defined by qtz, ilm and tm; subid to xeno, commonly poikiloblastic, gt includes qtz, ilm, bi, mu, minor ep, but contains no inclusion trails; gt is partially included in subid st; subid bi porphyroblasts have grown along and across the schistosity (S_2).

SAMPLE HP88-255

ROCK TYPE: bi-gt schist

FIELD RELATIONS: Pelitic layer in bi-gt ± ky zone of the schist complex.

HAND SAMPLE: Yellowish brown to silvery grey weathering with a phyllitic sheen, bluish grey to silvery-green grey on the fresh surface, porphyroblasts of gt 1 - 2 mm diameter; f.gr.; schistose.

THIN SECTION: mu (53%), bi (30%), qtz (10%), pl (3%), gt (2%), ilm (1%) chl (1%) zir (tr), ep (tr), ap (tr); gt, bi, mu and chl form subid to xeno porphyroblasts; Chl porphyroblasts partly replace bi and mu and cut S_2 and are interpreted to be retrograde; f.gr. intergrowths of chl, bi and mu partly replace gt; gt shows well preserved textural discontinuity (Type III garnet zonation); schistosity defined by mu, bi and lenses of qtz and fsp up to 1 mm wide and 5 mm long.

SAMPLE HP88-272

ROCK TYPE: st-gt schist

FIELD RELATIONS: Pelitic layer at the inferred southwestern margin of the schist complex.

HAND SAMPLE: Rusty-brown to yellow weathering; bluish grey to yellowish grey on the fresh surface; f.gr.; schistose.

THIN SECTION: mu (45%), qtz (33%), bi (12%), gt (5%), st (3%), tm (1%), ilm (1%), pl (tr%), ap (tr), zir (tr); subid st overgrows S_2 and partly encloses idio gt, which is truncated against the matrix schistosity (S_2); gt in the matrix is subid and contains qtz-defined stage 2 inclusion trails; muscovite and biotite define S_2; minor S_1 folds of a muscovite-biotite defined schistosity (S_1) and polygonalized quartz veinlets are preserved.

SAMPLE HP88-296

ROCK TYPE: mu-gt granite orthogneiss

FIELD RELATIONS: Foliation in the granite orthogneiss is parallel to that in the st-gt schist with which it is in contact suggesting that the orthogneiss and schist have been deformed together. The contacts between orthogneiss and schist are oblique to the foliation.

HAND SAMPLE: Yellow-cream weathering; white to creamy white on the fresh surface; f.gr.; moderately foliated granite orthogneiss; moderately developed foliation defined by mu and flattened qtz; weathered surface oxidized locally.

THIN SECTION: pl (39.5%), Ksp (22%), qtz (29%), mu (8%), gt (1%), ap (0.5%); fsp weakly to moderately sericitized; foliation is defined by mu and elongated qtz subgrains; subhd to anhd gt has commonly nucleated on ap.

SAMPLE HP88-297

ROCK TYPE: st-gt schist

FIELD RELATIONS: Pelitic layer in southwestern part of schist complex, approximately 150 m from HP88-296.

HAND SAMPLE: Rusty to yellow-brown weathering; bluish grey to yellowish grey on the fresh surface; f.gr.; schistose; subid gt and st porphyroblasts up to 3 mm in the longest dimension.

THIN SECTION: qtz (37%), bi (20%), mu (17%), st (10%), gt (10%), pl (5%), tm (1%), ilm (tr), ap (tr), zir (tr); mu, bi and ilm define S_2; gt is xeno, locally subid and contains stage 2 inclusion trails defined by qtz and ilm; st includes qtz, tm, ilm and has poorly developed Si that are defined by qtz and ilm; commonly, st has grown along mu-rich folia; subid bi porphyroblasts cut the schistosity; some have inclusion trails defined by v.f.gr. opm (gra?) that are parallel with the S_2.

SAMPLE HP88-308

ROCK TYPE: bi-gt schist in bi-gt ± ky zone of schist complex

FIELD RELATIONS: Pelitic layer in schist complex

HAND SAMPLE: Yellow-brown weathering; bluish grey to brown on the fresh surface; f.gr.; crenulated (amplitude and wavelengths ca. 8 mm); schistose.

THIN SECTION: mu (50%), bi (36%), qtz (10%), ilm (2%), gt (1%), pl (1%), tm (tr); minor retrograde chlorite after bi and gt; mu, bi and ilm define S_2; minor F_1

crenulations preserved; subid to xeno includes subid ilm and round quartz inclusions; ilm in the matrix is typically xeno with irregular "fuzzy" grain boundaries.

SAMPLE HP88-324

ROCK TYPE: ky-gt schist

FIELD RELATIONS: Pelitic to semipelitic layer exposed in the west-central part of the schist complex.

HAND SAMPLE: Rusty brown to grey weathering; white, cream and dark brown on the fresh surface; f.gr. to m.gr.; moderately schistose; subid gt porphyroblasts up to 3 mm diameter are wrapped around by the schistosity; subid ky porphyroblasts up to 2.5 cm long and 1 cm wide cut the schistosity.

THIN SECTION: qtz(35-45%), pl (25-35%), bi (10-15%), mu (3-8%), ky (1%), gt (1%), sil (tr), ap (tr), ilm (tr), sph (tr); pl moderately sericitized; garnet forms subid to xeno poikiloblasts with inclusions of qtz, bi and ilm and wrapped around by matrix foliation; ky forms subid porphyroblasts with qtz inclusions and commonly overprints mu; no inclusion trails; minor fb overprints bi and ky; foliation defined by bi, mu and ilm; ky has grown along and across the schistosity.

SAMPLE HP88-325

ROCK TYPE: sil-mu-gt-(or) schist

FIELD RELATIONS: Semi-pelitic layer in the schist complex

HAND SAMPLE: Rusty-brown to yellow-brown weathering; bluish grey to greyish brown on the fresh surface; subid garnet porphyroblasts up to 1.5 mm diameter; f.gr.; moderately schistose; quartz-feldspar vein 1 cm wide is parallel to the schistosity (S_2); schistosity defined by mu and bi; weakly crenulated.

THIN SECTION: qtz (54%), mu (25%), bi (15%), pl (3%), gt (1%), sil (1%), tm (0.5%), ilm (0.5%); pl is weakly sericitized; bi and mu define S_2; fb overprints bi; subid to xeno gt includes qtz and minor ilm and has no inclusion trails.

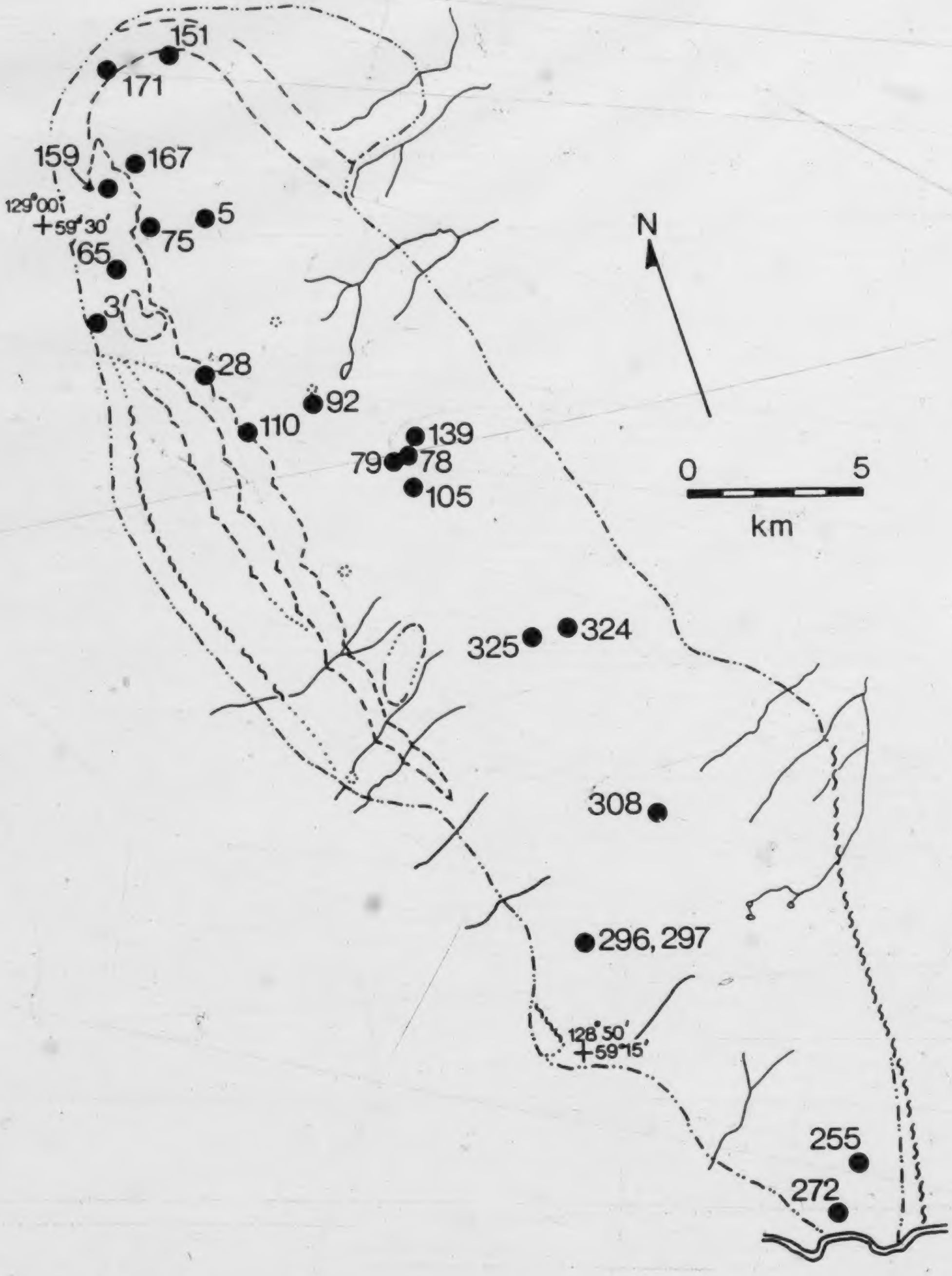
151
171
159
167
129°00'
+59°30'
5
75
65
3
28
92
110
139
79
78
105
N
0
5
km
325
324
308
296, 297
128°50'
+59°15'
255
272

Figure A1.1: Location map of samples (solid circles) analysed in the study and described in Appendix 1. All other symbols as for Figure 3.1.

Table A1.1: Summary of petrographic features of the major rock types in the map area. Numbers in brackets in mineral assemblage column refer to visually estimated percent. Minerals underlined in the foliation column are the dominant foliation-defining minerals. Metamorphic mineral zone is given in brackets after the rock type. Abbreviations are given at the front of the thesis.

Table A1.1:

ROCK TYPE	BULK COMP.	MINERALOGY	TEXTURE	PBLAST	PCLASTS/ RELICT GRAINS	FOLIATION	S_i	RETROGRADE ALTERATION	COMMENTS
KECHIKA GROUP									
chloritic phyllite (chl zone)	pelitic	chl rich layers: chl+mu(94),crb(5) qtz(.5-1),opm(.5-1) crb rich layers: crb(97),chl+mu(2) qtz(.5-1),opm(.5-1)	v.f.gr.; phyllitic	none	fossil frag. (<1%); rd. qtz grains (<.5mm) (<1%)	chl, mu; well developed planar clev.	--	none	comp. layers (chl- & crb-rich) folded with a.p. parallel to clev. (avg. 0.25 mm wide)
chloritic schist (chl zone)	dolomitic(?) & argillaceous	crb(60-70),chl(10-20),serp(tr-10), tc(tr-10),opm(10), qtz(tr)	v.f.gr.; phyllitic to schistose	none	relict dm? crystals (< 1mm) (<1%)	chl, dm(?); mod. developed scht.	--	none	----
meta-mudstone (chl zone)	calcareous & argillaceous	crb(86),qtz(10) whm+chl(2), opm(.5)	v.f.gr.; planar clev.; weak cren.	none	subrd. qtz grains (<1 mm) (<1 %)	whm, chl, phl; well developed scht.	--	none	----
biotite schist (bi zone)	semipelitic	qtz(70-85),mu(5-20) bi(10-15),ilm(1), tm(tr-.5),ep(tr)	f.gr.; schistose to grano. - elongate	subid. to xeno. bi	none	bi, mu; mod. developed scht.	--	minor chl after bi	comp. layers (mica- & qtz-rich) parallel to scht. (avg. .25 mm wide)
ATAN GROUP									
homog-geneous quartzite (bi zone)	siliceous	qtz(90-95),bi(1) pl(0-5),opm(0-1) sph(0-1),ep(0-.5) ap(tr-1),crb(tr)	f.gr.; subgrano. - elongate	none	minor rd. qtz grains	elongate qtz subgrains (< 1mm) (<1%); weak fol.	--	chl after bi; ser after pl	----

Table A1.1: (continued)

ROCK TYPE	BULK COMP.	MINERALOGY	TEXTURE	PBLAST	PCLASTS/ RELICT GRAINS	FOLIATION	S_1	RETROGRADE ALTERATION	COMMENTS
ATAN GROUP (continued)									
marble (bi zone)	calcareous	cc(80-97),pl(tr-7) trm(2),qtz(.5) sph(.5),phl(tr)	m.gr. to c.gr.; grano.	none	none	none	--	none	----
INGENIKA GROUP, Stelkuz Formation									
chl-mu-gt schist (chl-bi zone)	pelitic	qtz(42-50),chl(23-45),mu(23-45),bi(1-10),ilm(1),gt(<1-4),st(0-1),tm(.5), ep(.5),ap(tr), zir(tr)	f.gr.; schistose & cren.	subid. & locally poikiol. gt, st, bi, & mu	minor, strongly subgrained qtz grains (<1mm)(<1%)	chl, mu, bi; well developed scht.	--	minor chl after gt	1-5 mm comp. layers (chl-mu-rich & qtz-rich) parallel to scht.
hb-gt calcsilicate rock (chl-bi zone)	calcareous & siliceous	qtz(50-60),pl(25-27),hb(10-18),bi (2-5),opm(.5-1), gt(.5-1),zr(tr), ap(tr),ep(tr)	f.gr.; mod. schistose to grano. - elongate	subid. to xeno., skel. gt; subid. to xeno. hb	none	hb, bi, qtz; mod. developed fol.	--	minor chl after hb; ser after pl	----
INGENIKA GROUP, Espee Formation									
phl marble (st-gt zone)	calcareous & siliceous	crb(50-52),qtz(40-45),phl(2-3),mu (1-2),ilm(1), sph(1)	f.gr. to m.gr.; subgrano.	none	rd. qtz grains (<1mm)	phl; weak fol.	--	none	----

Table A1.1: (continued)

ROCK TYPE	BULK COMP.	MINERALOGY	TEXTURE	PBLAST	PCLASTS/ RELICT GRAINS	FOLIATION	S_1	RETROGRADE ALTERATION	COMMENTS
INGENIKA GROUP, Tsaydiz and Swannell Formations (undifferentiated)									
st-gt schist (st-gt zone)	pelitic to semipelitic	mu(20-50),qtz(15 50),bi(10-30),st (2-30),gt(0-10), pl(tr-5),ilm(tr-2), andl(0-3),ap(tr), zir(tr),fb(tr), zo(tr)	f.gr. to m.gr.; schistose, porphyrobl.	subid. to xeno. st, gt, pl, bi, & mu	none	mu, bi, qtz & fsp subgrains; well developed scht.	mod. to well developed	ser after pl; chl after bi, st, & gt	zo incl. in gt
marble (st-gt zone)	calcareous	crb(95-97),qtz(1-2),opm(1-2),mu(1) sph(1)	m.gr.; grano.	none	rd. qtz grains (<1 mm) (<1%)	none	---	iron staining on mu	----
calcsilicate rock (st-gt zone)	calcareous & siliceous	qtz(92),hb(2-3), pl(2-3),bi(1), sph(.5),opm(.5), ap(tr),gt(tr)	f.gr.; grano-elongate	subid. hb & bi	none	hb, qtz, bi, opm; mod. developed scht.	---	ser after pl; chl after bi & gt	----
granite orthogneiss (st-gt zone)	granitic	pl(37),qtz(26), Ksp(18),mu(7), gt(.5-1),ap(.5)	f.gr.; grano-elongate to mod. schistose	none	qtz,fsp (1-2 mm) (1%)	mu, qtz subgrains; mod. developed scht.	---	ser after pl	----
bi-gt schist (bi-gt±ky zone)	pelitic	mu(54-60),bi(5-40),qtz(10-20), pl(3-6),gt(0-2), ilm(1),tm(tr-1), gra(0-1),ap(tr), ep(tr),zir(tr), zo(tr)	f.gr.; schistose	subid. bi, gt, pl, mu, & chl	none	mu, bi, qtz; well developed scht.	locally mod. developed in gt & bi	chl, bi, mu after gt	zo incl. in gt locally; late chl pblasts cut S_2

Table A1.1: (continued)

ROCK TYPE	BULK COMP.	MINERALOGY	TEXTURE	PBLAST	PCLASTS/ RELICT GRAINS	FOLIATION	S_i	RETROGRADE ALTERATION	COMMENTS
INGENIKA GROUP, Tsaydiz and Swannell Formations (undifferentiated) (continued)									
ky-gt schist (bi-gt±ky zone)	semipelitic	qtz(35-40),pl(25 30),bi(10-15),mu (3-8),ky(1),gt(1), sil(tr),ap(tr), ilm(tr),sph(tr)	f.gr. to m.gr.; mod. schistose	subid. ky, bi, & mu; subid. to xeno. gt	none	bi, mu, qtz, pl; mod. developed scht.	none	minor ser after pl; minor chl after bi	
sil-mu-or -gt schist (sil-or-mu zone)	pelitic to semipleitic	bi(25-40),mu(tr-30), qtz(25-45),pl(2-3), sil(1-5),gt(1-3), or(1-2),ilm(1-2), tm(tr-2),ap(tr-1), zir(tr)	f.gr. to m.gr.; schistose	subid. sil bi, mu, gt, pl & or	none	mu, bi, qtz, pl subgrains; well developed scht.	locally mod. developed in gt, pl, & bi	chl after bi; ser & ep after pl	
psammitic schist (sil-or-mu zone)	psammitic	qtz(68-75),bi(0-20), pl±or(10-25),sph(tr-2),ap(0-1),gt(0-2), hb(0-10),opm(tr), tm(tr),zir(tr)	f.gr.; grano.-elongate to weakly foliated; locally lineated (pl, hb)	subid. bi; subid. to xeno. gt	rd. pl grains (<1-2 mm) (1-15%)	bi, qtz subgrains; mod. developed scht.	none	ser after fsp; chl after bi	hb nucleates on pl grains
impure quartzite (sil-or-mu zone)	siliceous	qtz(89-91),pl(2-4), dp(2-4),hb(1-2),sph (1-2),ap(0-1),gt(0-tr),crb(0-1)	f.gr.; subgrano. to weakly schistose	subid., skel. gt; subid. dp & hb	rd. qtz & fsp (≤ 1 mm) (10%)	dp, hb; weak to mod. developed scht.	none	ser after pl; chl after bi	hb rims dp
marble (sil-or-mu zone)	calcareous	crb(90-92),dp(1-5), qtz(2-3),pl(1-2), hb(0-1),opm(tr-3)	f.gr.; grano.; locally lineated (qtz)	subid. dp	rd, qtz & pl (≤ 1mm) grains (1 %)	none	none	ep after fsp	dp nucleates on pl grains

Table A1.1: (continued)

ROCK TYPE	BULK COMP.	MINERALOGY	TEXTURE	PBLAST	PCLASTS/ RELICT GRAINS	FOLIATION	S_i	RETROGRADE ALTERATION	COMMENTS
INGENIKA GROUP, Tsaydiz and Swannell Formations (undifferentiated) (continued)									
calcsilicate rock (sil-or-mu zone)	calcareous & siliceous	dp(5-30),pl(5-15),qtz(33-50),sph(1-2),gt(0-5),hb(0-2),bi(0-1),ep(0-1),ap(0-1),crb(0-1),opm(tr-1)	subgrano. to grano., locally lineated (dp, gt, qtz, pl)	subid. dp, gt, hb	none	dp, qtz, bi; mod. developed fol.	none	chl after bi; ser after pl	----
granite orthogneiss (sil-or-mu zone)	granitic	pl(33),or(25),qtz(22),mu(10),bi(10),ap(tr),zr(tr)	grano. - elongate to weakly schistose	none	none	mu, bi, qtz subgrains; mod. developed fol.	none	chl after bi; ser after pl	----
amphibolite (sil-or-mu zome)	mafic	hb(55-58),bi(20-30),qtz(5-15),pl(8-20),sph(tr-0.5),opm(tr-5),ap(tr)	f.gr., schistose	subid. hb, bi	none	hb, bi; well developed scht.	none	minor chl after bi; ser after pl	ophitic texture locally preserved

Table A1.2: Petrographic features for granitic rocks and nondeformed ultramafic to mafic rocks. Classification according to Steckeisen (1976). Diorite and gabbro were distinguished using an upper limit of An_{50} for plagioclase. Plagioclase composition was determined optically using the Michel-Levy method (see Kerr, 1959, p. 294). Visual estimates of percentages are given in brackets in mineral assemblage column. Mineral abbreviations are given at the front of the thesis. In all cases, cpx and opx are augite and hypersthene, respectively.

Table A1.2:

Rock Type	Mineral Assemblage	Texture	Alteration	Comments
hornblende diorite	An_{37-45} pl(40-52), hb(35-50),bi(3-10), qtz(tr-3),opm(tr-1), sph(1-2),ap(tr-2), crb(0-1),whm(tr)	f.gr. to m.gr. (2.5 to 4 mm); equigran. hypoidiom.; hb locally poik.	mod. whm after pl; minor chl after bi & hb	mod. zoning in pl in some samples
px-(hb) diorite	An_{35-37} pl(55-64), cpx (15-20),opx(0-5), bi(0-22),hb(0-2),opm (tr-10),antg(0-5),qtz (1-2),sph(0-1),ap(0-1), chl(0-2),cc(0-1),ep(tr)	f.gr. to m.gr. (1 to 5 mm); subophitic to subequigran. hypoidiom.	chl after pl & px; antg. after px & ol?; ser after pl	late cc veinlets locally; minor antg pseudomorphs after ol (?) locally
opx diorite	An_{40} pl(40),opx(20), cpx(20),hb(14),bi(3), qtz(2),opm(1)	f.gr. (1-2 mm); subequigran. hypoidiom.; hb is poik. & incl. pl, px, qtz	ser after pl	some opm rimmed by bi; hb partly replaces or rims px; hb partly replaced by bi
cpx-hb gabbro	An_{52-62} pl(15-35), cpx(30-40),hb(7-15), bi(15-35),opm(tr-5), sph(0-2),qtz(tr-1), ap(0-tr),ep(0-tr)	c.gr. (5-7 mm); subequigran. hypoidiom.	minor ser after pl; iron staining along fractures	hb & bi partly replace px; bi partly replaces hb

Table A1.2: (continued)

Rock Type	Mineral Assemblage	Texture	Alteration	Comments
pl-bearing hornblendite	hb(89), An_{40} pl(2), bi(7),sph(1),qtz(1), opm(tr)	f.gr. (1-3 mm); equigran. subhypoidiom.	minor ser after pl	bi partly replaces hb; sph present along clev. in hb
pl-bearing px hornblendite	An_{33} pl(10),hb(44), cpx(37),opx(3),opm (1),qtz(1),sph(1), bi(1)	f.gr. (1-2 mm); equigran. hypoidiomorphic	-----	bi & hb partly replace cpx
ol-px hornblendite	hb(40-42),cpx(12-34), ol(6-30),bi(1-5), aph(0-15),opx(3-8), pl(0-2),opm(1), cc(0-1)	c.gr. (5-10 mm); equigran. hypoidiom.; hb locally poik. & incl. ol & px	aph after hb & px	late cc veinlets; ol included in cpx, hb, & bi; hb & bi partly replace cpx
granite to granodiorite (syn- to post-S_2 in sil-or-mu zone)	An_{40} pl(33-45),or (13-27),qtz(26-28), mu(10),bi(5-10),ap (tr-1),zir(tr),gt (0-tr),fb(tr)	f.gr. to c.gr. (1-6 mm; most commonly 3 mm); equigran. hypoidiom. to pegmatitic	ser after pl; minor chl after bi	mu forms wormy intergrowth with qtz and is partly replaced by fb; microperthite & graphitic qtz-Ksp intergrowths in pegmatitic granite

Table A1.2: (continued)

Classification	Mineral Assemblage	Texture	Alteration	Comments
granite S-C mylonite	pl(29-32),or(26-29), qtz(25-30),mu(10), bi(5),ap(tr-1),zir (tr),gt(0-tr),fb(tr)	S-C fabric well developed; S: micas, fsp pclasts systems, qtz subgrains; C: strongly recrystl. qtz & micas; pclasts of fsp, qtz, tm, ap, gt	whm after mc & pl; minor chl after bi	mu forms "wormy" intergrowth with qtz locally; fb developed in frac. in mc pclasts; pl comp. indeterminate
mylonitized transitional granite to qtz monzonite	An_{38-40} pl(37),mc(26), qtz(15),bi(20),sph(1), mt(1),ap(tr),ep(tr), zir(tr),mz(tr)	weak S-C fabric, defined as in granite mylonite above; pclasts of fsp, qtz, ap	ser after pl; chl after bi	bi is greenish brown in ppl

APPENDIX 2: ANALYTICAL METHODS

A2.1. ELECTRON MICROPROBE

All analyses were done using an automated wavelength-dispersive ARL-SEMQ microprobes. Natural silicate and oxide standards were used. Data for garnet, staurolite, biotite, muscovite, plagioclase and orthoclase were collected at the University of Calgary (operating conditions: accelerating voltage = 15 KeV, beam current = 1.5×10^{-7} amps and beam spot size = 0.5×0.5 to 1×1 μm). Counting time for standards, unknowns and background was 20 seconds; five analyses per standard were run. Data were reduced using the methods of Bence and Albee (1968) and Albee and Ray (1970). To estimate water content in hydrous minerals, an initial water content of half that required to total the analysis to 100 wt. % was added during data reduction. The reduction was carried out iteratively until the total of the analysis was within 0.3 wt. % of 100 wt. %. Ilmenite, rutile and Al_2SiO_5 analyses were carried out at the University of Alberta (operating conditions: accelerating voltage = 15 KeV, beam current = 0.6×10^{-7} amps, beam spot size 1×1 μm). In some cases, beam was rastered over an area ranging from of 2×2 to 10×10 μm. Counting times for standards, samples and backgrounds were 40 seconds, 30 seconds and 20 seconds, respectively. Data were processed using the program MAGIC IV (Colby, 1968).

A2.2. GEOCHRONOMETRY

A2.2.1. U-Pb METHOD

(i) Theory

The following derivation and notation is taken from Faure (1986). The U-Pb method is based on the decay of ^{238}U to ^{206}Pb and ^{235}U to ^{207}Pb. Pb has 4 naturally occurring isotopes: ^{208}Pb, ^{207}Pb, ^{206}Pb and ^{204}Pb. The latter, because of its very long half-life, is treated as a stable reference isotope. The isotopic composition of Pb in U-bearing samples is given by:

$$\frac{^{206}Pb}{^{204}Pb} = \left(\frac{^{206}Pb}{^{204}Pb}\right)_i + \frac{^{238}U}{^{204}Pb}\left(e^{\lambda_1 t} - 1\right) \qquad \text{(A2.1)}$$

(A2.2) $$\frac{^{207}Pb}{^{204}Pb} = \left(\frac{^{207}Pb}{^{204}Pb}\right)_i + \frac{^{235}U}{^{204}Pb}\left(e^{\lambda_2 t} - 1\right)$$

where: $\frac{^{206}Pb}{^{204}Pb}, \frac{^{207}Pb}{^{204}Pb}$ = analytically determined isotopes of Pb,

$\left(\frac{^{206}Pb}{^{204}Pb}\right)_i, \left(\frac{^{207}Pb}{^{204}Pb}\right)_i$ = the initial isotopic ratios of Pb incorportaed into the mineral when it formed,

$\frac{^{238}U}{^{204}Pb}, \frac{^{235}U}{^{204}Pb}$ = the isotopic ratios in the mineral at the time of analysis,

λ_1, λ_2 = the decay constants of ^{238}U and ^{235}U, respectively

t = time elapsed since closure of the mineral to uranium, lead and all the intermediate daughters.

Equation A2.1 can be solved for t:

(A2.3.) $$t_{206} = \frac{1}{\lambda_1} \ln\left(\frac{\frac{^{206}Pb}{^{204}Pb} - \left(\frac{^{206}Pb}{^{204}Pb}\right)_i}{\frac{^{238}U}{^{204}Pb}} + 1\right)$$

A similar equation can also be written for t_{207} by solving equation (A2.2) for t. This method assumes that: (1) initial Pb isotope ratios are correct, (2) the decay constants are accurately known, (3) the isotopic composition of uranium is unmodified by fractionation or by spontaneous fission of ^{235}U and, if the calculated age is equated with crystallization, that (4) the mineral has remained closed to U, Pb, Th and all intermediate daughter products.

In most cases minerals have experienced some Pb loss. Provided that the Pb lost had the same isotopic composition as that which remained at the time of loss, the effect of Pb loss can be minimized by calculating the $^{207}Pb/^{206}Pb$ age. The ratio of equation (A2.1 and A2.2) is:

(A2.4) $$\left(\frac{^{207}Pb}{^{206}Pb}\right)^* = \frac{^{235}U}{^{238}U}\left(\frac{(e^{\lambda_2 t} - 1)}{(e^{\lambda_1 t} - 1)}\right)$$

Equation A2.4 is transcendental and must be solved iteratively for t until a value that solves the equation for a particular radiogenic $^{207}Pb/^{206}Pb$ (i.e. $^{207}Pb/^{206}Pb^{*}$)is found.

(ii) Analytical Techniques

Hand picking and U-Pb analyses were done by R. Parrish at the Geological Survey of Canada geochronometry laboratory in Ottawa. Zircons and monazites were hand picked from mineral separates on the basis of size, morphology and clarity. Mineral separates were washed, dried, weighed, spiked with a ^{205}Pb-^{233}U-^{235}U tracer (Parrish and Krogh, 1987) and dissolved using the technique described by Parrish et al (1987). Anion exchange columns were used for element separation (see Parrish et al., 1987). Isotopic compositions of Pb and U are measured on a Finnigan-MAT 261 variable multicollector mass spectrometer (Roddick et al., 1987; Parrish et al., 1987). The common Pb correction was made using the Stacey-Kramers (1975) growth curve assuming an age of ca. 50 Ma for all samples, except HP87-78E (100 Ma for monazite, 110 Ma for zircon) and HP87-139 (110 Ma for zircon). Total processing blanks for Pb were 12 to 18 pg and for U were 0 to 1 pg. Decay constants of Steiger and Jäger (1977) were used.

Data reduction incorporated uncertainty in measured U and Pb ratios, Pb fractionation per mass unit, amount of U and Pb blanks, Pb blank composition (see Parrish et al, 1987; Roddick, 1987). Uncertainty in the U/Pb ratio for the tracer is a constant and therefore, need only be considered for comparison with results of other laboratories.

In this study, a concordant analysis is that which substantially overlaps concordia at the 2σ error level. In this case, the mean of the intersections of the error ellipse with concordia is taken as the age and the deviation of the intersections from the mean, as the error (cf. Parrish et al., 1987).

(iii) Correction for ^{230}Th Disequilibrium

The reverse discordance observed in the monazite samples is interpreted to reflect the presence of excess or unsupported ^{206}Pb from the decay of excess ^{230}Th incorporated during crystallization from the magma (Schärer, 1984). Corrections for the effect of initial ^{230}Th disequilibrium were made to $^{207}Pb/^{206}Pb$ and $^{238}U/^{206}Pb$ dates following the method of Schärer (1984).

Initial excess or deficit of ^{230}Th in a mineral results in an excess or deficit of ^{206}Pb, respectively. This effect is strongest in young samples where radiogenic ^{206}Pb ($^{206}Pb^{*}$) derived from ^{230}Th decay is comparable to that derived from ^{238}U decay. If the magama was in radioactive equilibrium before crystallization and if the Th/U ratios of monazite and magma from which the monazite crystallized can be determined, then the relative amount of disequilibrium ^{230}Th is defined by the degree of Th-U fractionation (f) between the magma and the mineral:

$$\text{(A2.5)} \qquad f = \frac{(\mathrm{Th/U})_{\mathrm{mineral}}}{(\mathrm{Th/U})_{\mathrm{magma}}}$$

The assumption of radioactive equilibrium is not always valid (see Chapter 6 and Parrish, 1990). The $\mathrm{Th/U}_{\mathrm{magma}}$ composition is commonly assumed to be the ratio of the measured whole rock Th and U concentrations. The Th concentration of the mineral is calculated from the measured ^{208}Pb, assuming that ^{232}Th approximates the Th concentration, that the ^{235}U/^{207}Pb date approximates the age of crystallization of the mineral and a closed behaviour for Th and its daughter products (Schärer, 1984). Thus, the Th/U ratio of the mineral is taken as equivalent to the ^{232}Th/^{238}U ratio, which neglects the 0.7% contribution from ^{235}U.

An initial excess of ^{230}Th in the mineral corresponds to $f > 1$ and and initial deficit to $f < 1$. The corrected (corr.) isotopic ratio is calculated using the measured (meas.) isotopic ratio and f in the equation:

$$\text{(A2.6)} \qquad {}^{206}\mathrm{Pb}/{}^{238}\mathrm{U}_{\mathrm{corr.}} = {}^{206}\mathrm{Pb}/{}^{238}\mathrm{U}_{\mathrm{meas.}} - [(f-1)\, \lambda_{238}/\, \lambda_{230}]$$

where λ_{238} and λ_{230} are the decay constants for U^{238} (= $1.55125 \times 10^{-10} y^{-1}$) and ^{230}Th (= $0.922 \times 10^{-5} y^{-1}$), respectively. The equation for correction to ^{207}Pb/^{206}Pb ratio is:

$$\text{(A2.7)} \qquad {}^{207}\mathrm{Pb}/{}^{206}\mathrm{U}_{\mathrm{corr.}} = ({}^{235}\mathrm{U}/{}^{238}\mathrm{U})({}^{207}\mathrm{Pb}/{}^{235}\mathrm{U})_{\mathrm{meas.}}({}^{238}\mathrm{U}/{}^{206}\mathrm{Pb})_{\mathrm{corr.}}$$

Since ^{235}U/^{238}U = 137.88, substituting into equation (A2.7) and cancelling terms gives:

$$\text{(A2.8)} \qquad {}^{207}\mathrm{Pb}/{}^{206}\mathrm{Pb}_{\mathrm{corr.}} = (1/137.88)[({}^{207}\mathrm{Pb}/{}^{235}\mathrm{U})_{\mathrm{meas.}}/({}^{206}\mathrm{Pb}/{}^{238}\mathrm{U})_{\mathrm{corr.}}]$$

The corrected ratios are then used to calculate the age using the equations:

$$\text{(A2.9)} \qquad t_{206} = 1/\,\lambda_{238}\{\ln[({}^{206}\mathrm{Pb}/{}^{238}\mathrm{U})_{\mathrm{corr.}} + 1]\}$$

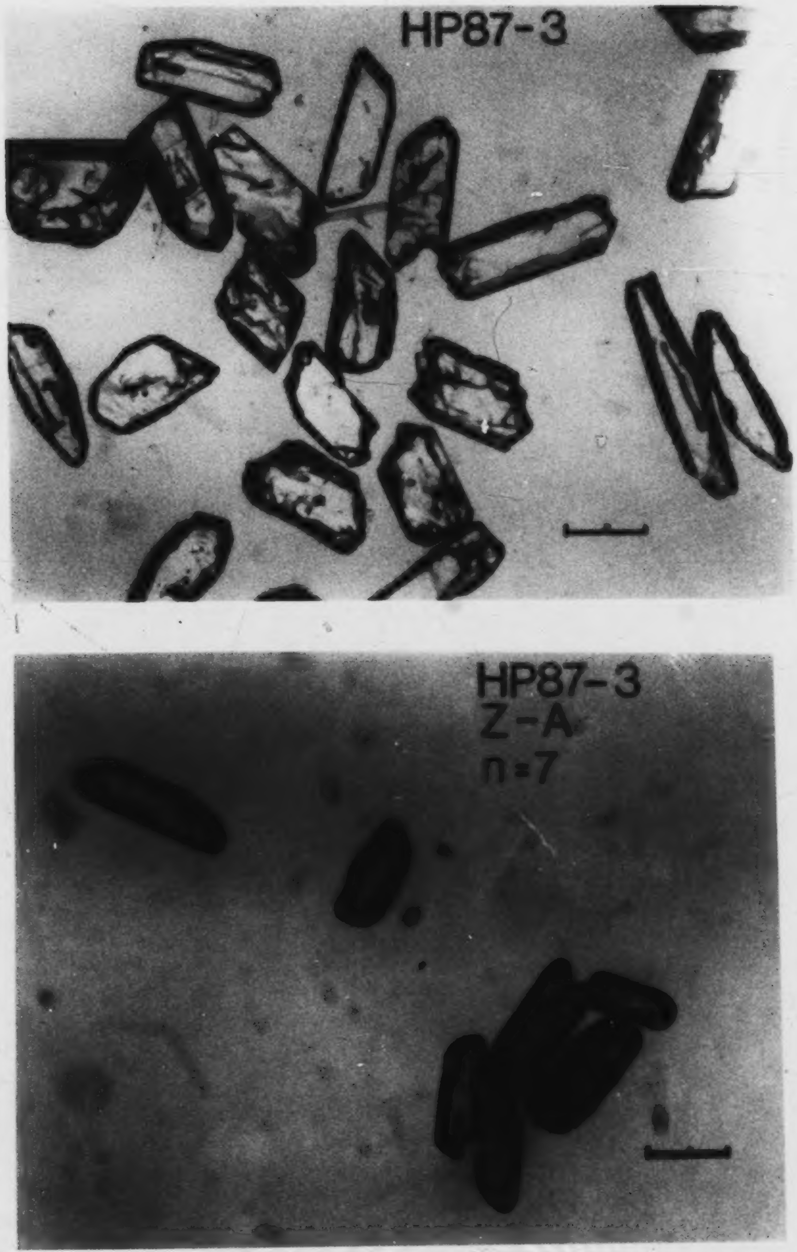

Plate A2.1: (a) Example of unabraded, high quality zircon from quartz monzonite mylonite sample HP87-3. (b), (c), and (d) show the abraded samples that were analysed. n = number of analyses. Bar scale is 2 mm.

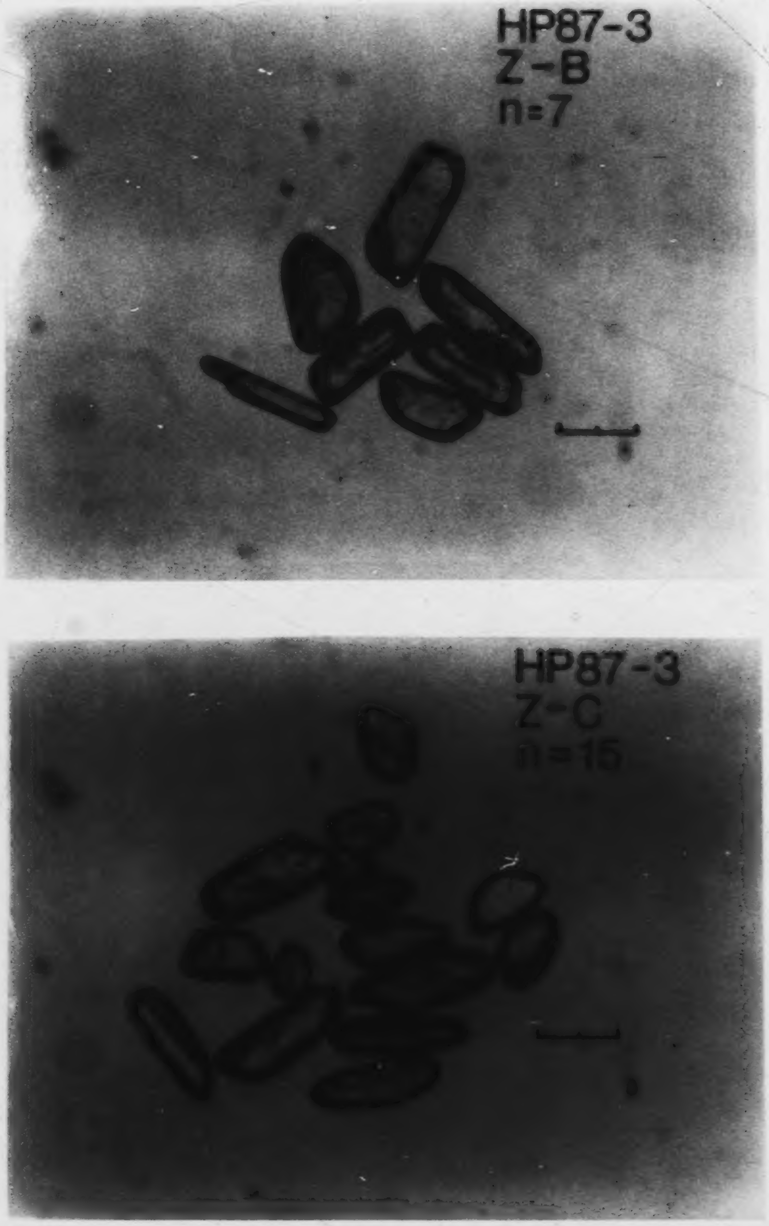
HP87-3
Z-B
n=7
HP87-3
Z-C
n=15

Plate A2.1 (continued).

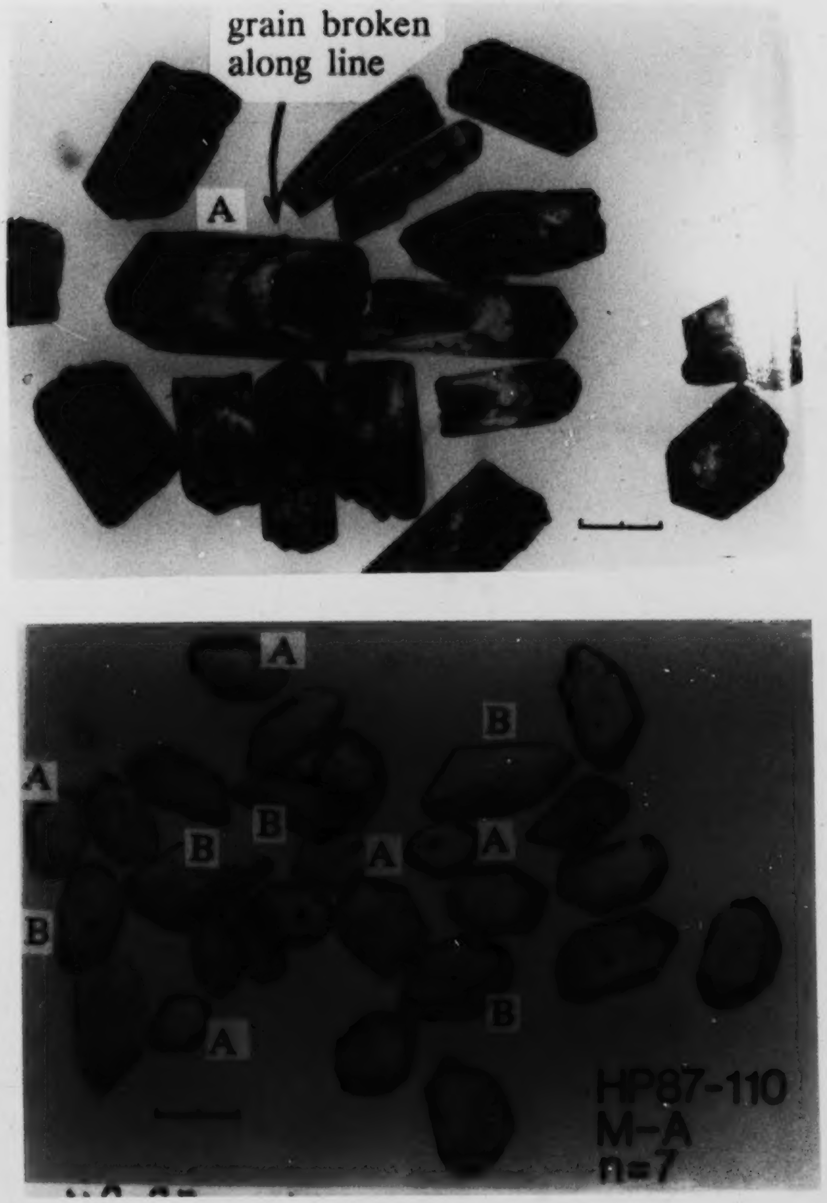
grain broken along line
A
A
B
A
B
B
A
A
B
B
A
HP87-110
M-A
n=7

Plate A2.2: (a) Zircon from C-S granite mylonite HP87-110. "A" denotes the fragment of the large grain that was analysed. Note cloudiness and poor quality of zircon grains. (b) Monazite from the same sample. "A" and "B" denote monazite fractions A and B. n = number of grains. Bar scale is 2 mm.

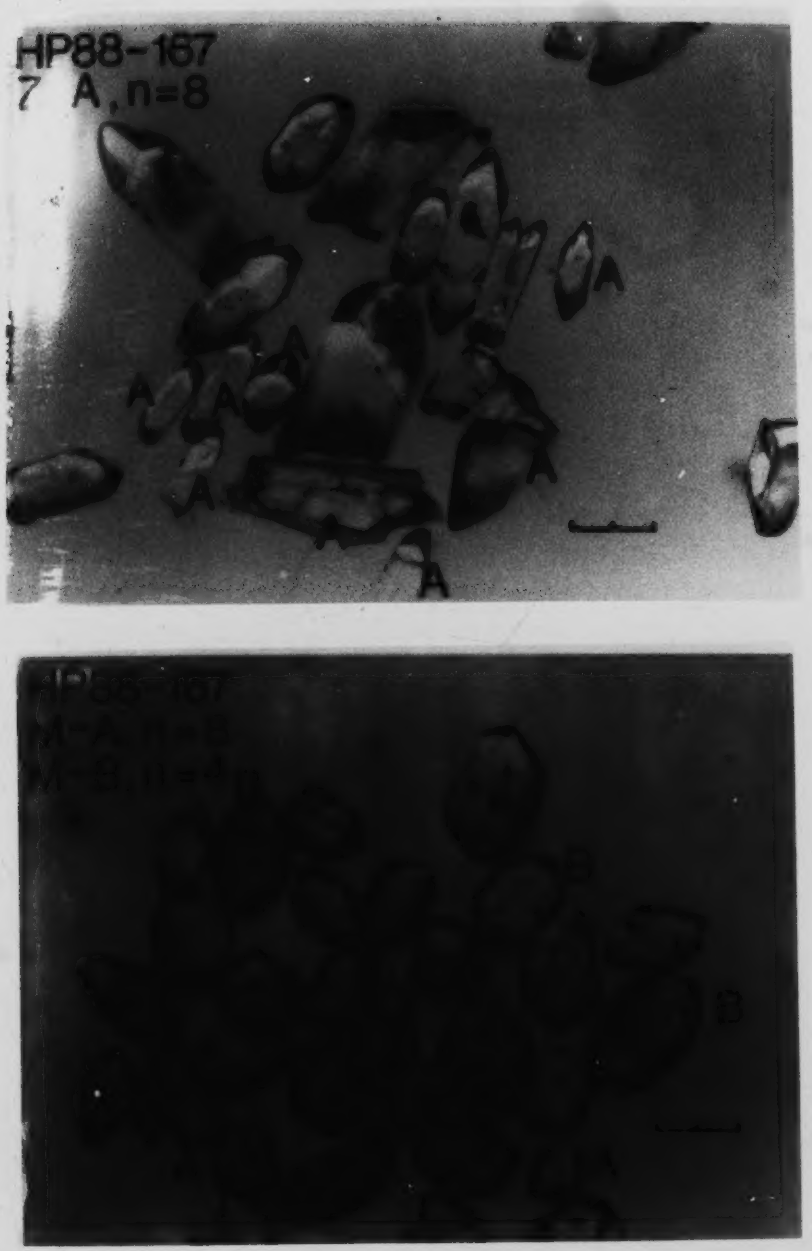
HP88-167
7 A, n=8
A
A
A
A
A
A
A
HP88-167
M-A, n=8
M-B, n=4
B
A

Plate A2.3: Zircon in C-S granite mylonite HP88-167. "A" denotes the anlaysed grains. (b) Monazite from the same sample. "A" and "B" denote monazite fractions A and B. n = number of grains. Bar scale is 2 mm.

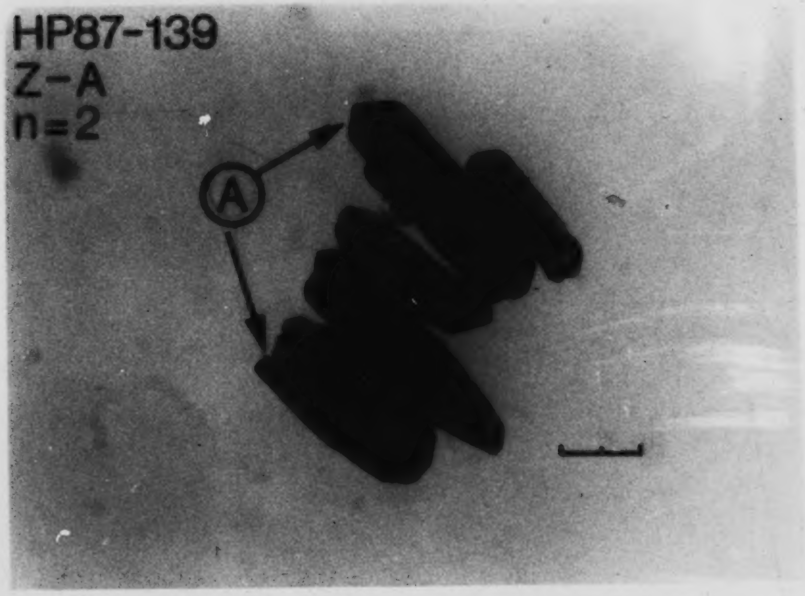
HP87-139
Z-A
n=2
A

Plate A2.4: (a) Very poor quality zircon from post-S_2 granitic pegmatite in the schist complex. "A" denotes the grains analysed.

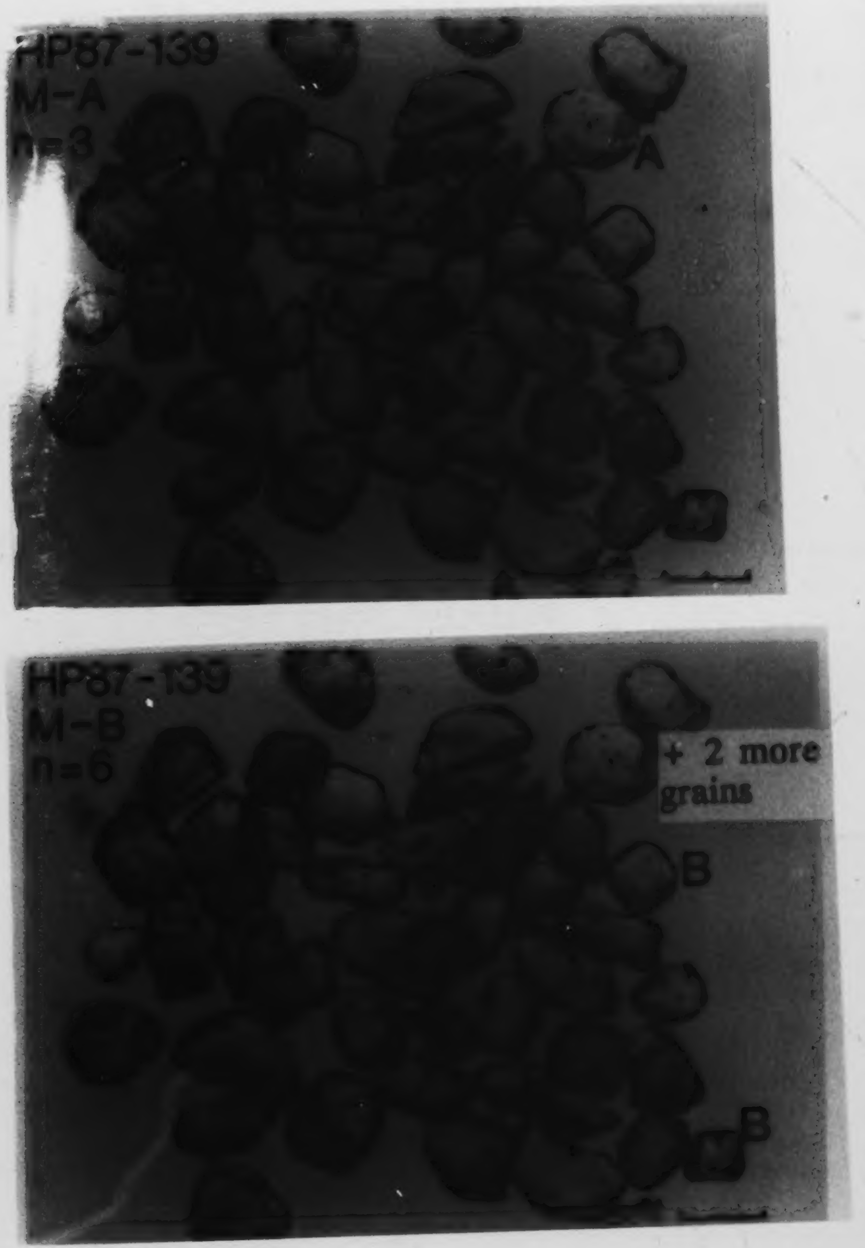
HP87-139
M-A
n=3
A
HP87-139
M-B
n=6
+ 2 more grains
B
B

Plate A2.4 (continued): (b) and (c) show monazite fractions A and B, respectively, from the same sample. n = number of grains. Bar scale is 2 mm.

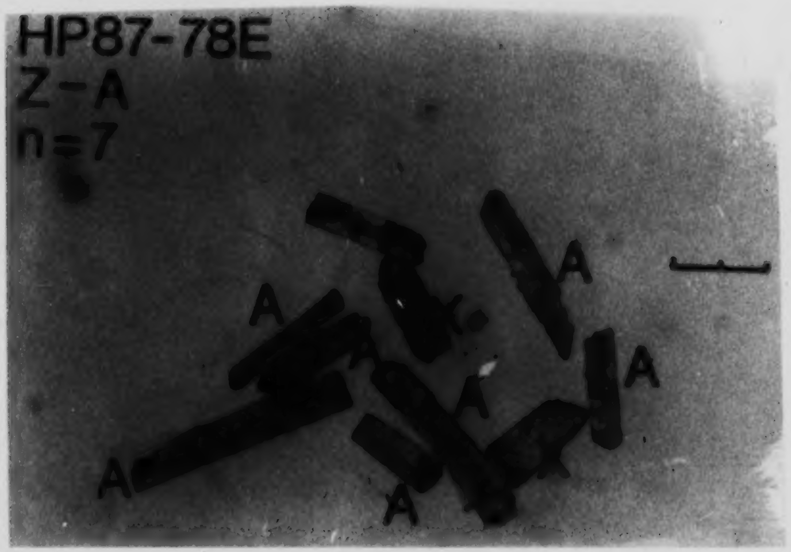
HP87-78E
Z-A
n=7
A
A
A
A
A
A
A
X

Plate A2.5: (a) Zircon from syn- to post-S_2 granite HP87-78E in the schist complex. "A" denote grains analysed. "X" and unlabelled grained were not analysed.

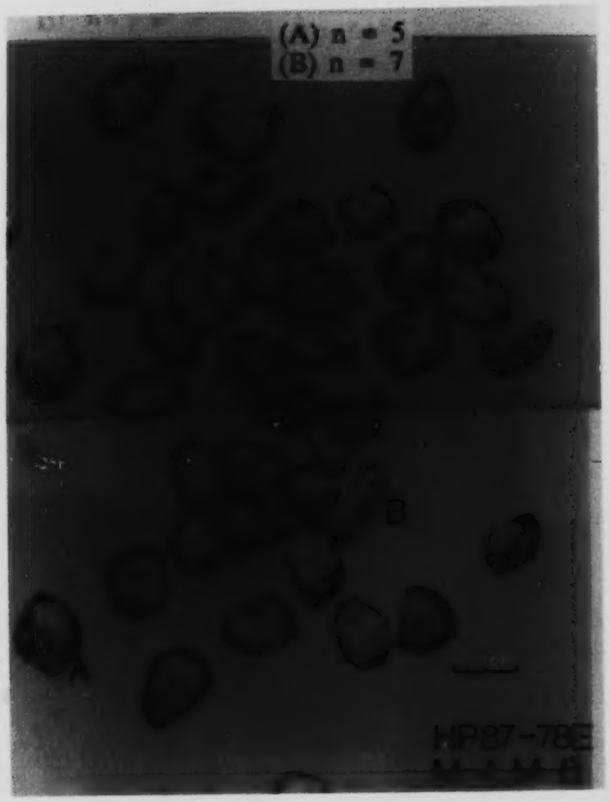
(A) n = 5
(B) n = 7
A
B
A
HP87-78E

Plate A2.5 (continued): (b) Monazite fractions from the same sample. "A" and "B" denote monazite fractions A and B. n = number of grains. Bar scale is 2 mm.

$$(A2.10) \qquad (^{207}Pb/^{206}Pb) = 1/137.88[(e^{\lambda_{235} t_{207}} - 1)/(e^{\lambda_{238} t_{206}} - 1)$$

where t_{206} and t_{207} refer to the $^{206}Pb/^{238}U$ age (eqn. A2.9) and the $^{207}Pb/^{235}U$ age, respectively (see equation A2.3). Equation (A2.10) is transcendental and is solved by the successive approximation of t until a value was obtained which solves the equation for the $(^{207}Pb/^{206}Pb)_{corr.}$ value.

A2.2.2. ^{40}Ar/^{39}Ar METHOD

(i) Theory

The following derivation and notation is taken from Faure (1986). The $^{40}Ar/^{39}Ar$ stepwise heating method is based on the formation of ^{39}Ar by the irradiation of K-bearing samples in a fast neutron flux. The $^{40}Ar^{*}/^{39}Ar$ ratio is proportional to the $^{40}Ar^{*}/^{40}K$ ratio because the $^{39}K/^{40}K$ ratio is nearly constant in nature and the amount of ^{39}Ar is dependent on the amount of ^{39}K in the samples (McDougall and Harrison, 1988). The amount of ^{39}Ar produced is given by:

$$(A2.11) \quad {}^{39}Ar = {}^{39}K \, \Delta T \int \varphi(E)\sigma(E)d(E)$$

where T = length of irradiation

$\varphi(E)$ = neutron flux density at energy E

$\sigma(E)$ = capture cross section of ^{39}Ar neutrons having energy E

The integration is carried out for the entire neutron energy spectrum.

Radiogenic argon ^{40}Ar ($^{40}Ar^{*}$) formed by the spontaneous decay of ^{40}K is also present in the sample and is given by the standard K-Ar dating age equation:

$$(A2.12) \quad {}^{40}Ar^{*} = {}^{40}K\,(e^{\lambda t} - 1)\,\frac{\lambda_e}{\lambda}$$

where λ_e = decay constant for ^{40}K by electron capture

λ = total decay constant for ^{40}K (i.e. $\lambda_e + \lambda_\beta$)

Combining (A2.11) and (A2.12), the $(^{40}Ar/^{39}Ar)_{measured}$ for an irradiated sample of age t is:

$$(A2.13) \quad \frac{^{40}Ar^{*}}{^{39}Ar} = \frac{\lambda_e}{\lambda}\left(\frac{^{40}K}{^{39}K}\right)\frac{1}{\Delta T}\,\frac{e^{\lambda t} - 1}{\int \varphi(E)\sigma(E)d(E)}$$

The quanity, $\frac{^{40}Ar^{*}}{^{39}Ar} = \frac{e^{\lambda t} - 1}{J}$

is referred to as the J-value or J. Therefore from equation (A2.13):

$$t = 1/\lambda \ \ln[{}^{40}Ar^{*}/{}^{39}Ar\ (J) + 1] \tag{A2.14}$$

and

$$J = \frac{\lambda}{\lambda_e}\left(\frac{{}^{39}K}{{}^{40}K^{*}}\right)\Delta T \int \varphi(E)\,\sigma(E)\,d(E) \tag{A2.15}$$

The value of J varies because the energy spectrum of the neutron flux and the cross-section of ^{39}Ar for capture of neutrons of varying energies experienced by a sample depends on its position in the sample holder. Therefore, several standards of known age are placed in the sample holder at known positions between the samples. As the ages of the standards are known, their J-value can be easily obtained from equation (A2.15). The J-values for the standards are plotted versus the position in the can and the required J-value for the unknown sample is extrapolated from the points of known J.

(ii) Analytical Methods

The $^{40}Ar/^{39}Ar$ analytical procedure used has been summarized by Reynolds et al. (1987) and Muecke et al. (1988). Mineral separates were wrapped in aluminum foil, shaped into thin discs and stacked inside a cadmium-lined, aluminum irradiation canister. Cadmium liners (ca. 1.0 mm thick) absorb thermal neutrons. The flux monitor, 519 Ma hornblende standard MMHb-1 (Alexander et al., 1978), was interdispersed among the samples. J-values for samples were determined from interpolation between those for standards and ranged between 0.002232 and 0.002308 for canister 72 and were 0.002495 for both samples in canister 73. The range in measures J-value for the length of canister 72 was ca. 4% and for canister 73 was negligible.

Following irradiation with fast neutrons in the McMaster nuclear reactor, Hamilton, Ontario and a cool-off period of approximately 1 to 3 months, each sample was loaded into a glass boat and placed inside a quartz extraction tube. The extraction tube is connected to a glass vaccuum line, which in turn, is connected on-line to a modified MS 10 mass spectrometer.

A multiple sample loading technique of 4 to 5 samples was used. Between each lot of samples, the line was baked-out overnight at 150°C. Successive samples were

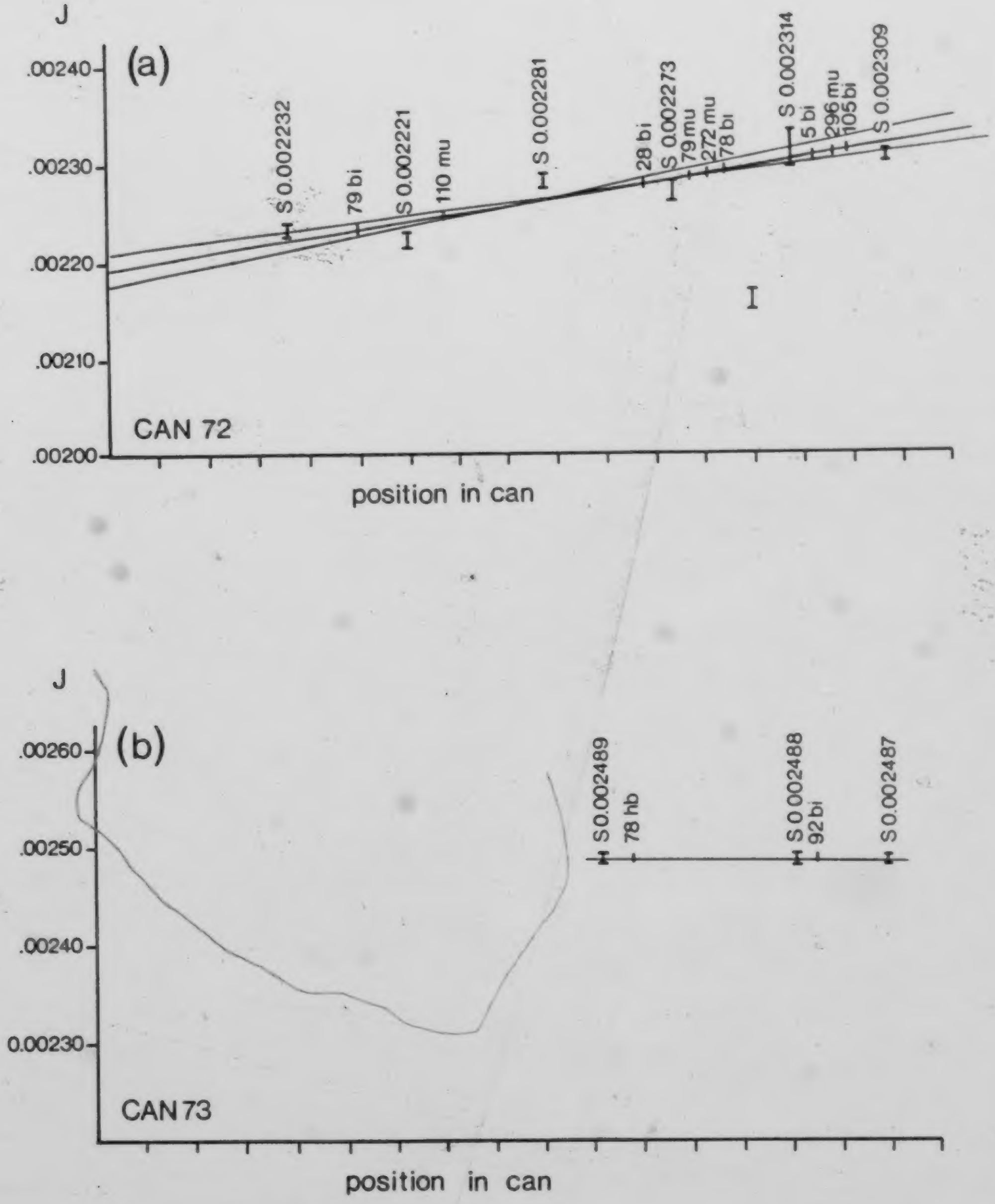

Figure A2.1: J curves for irradiation canisters numbers 72 and 73 containing samples analysed by the ^{40}Ar/^{40}Ar method. (a) Curves represent the "best fit" ± the uncertainty allowed by the data. Vertical bar in bottom right denotes 1% variation in J. Variation in can 72 is ca. 4 %. (b) No gradient is detectable in can 73.

moved into the quartz tube using magnets. The sample and quartz tube were heated in a stepwise fashion. Each heating step lasted approximately 1 hour. Biotite samples were outgassed in 50°C temperature steps between 550°C and 1000°C and in 50°C or 100°C steps between 1000°C and 1100°C. Muscovite samples and the hornblende sample were outgassed in a similar fashion except that muscovite was outgassed in 30°C temperature steps between 810°C and 1140°C and hornblende was outgassed in 25°C temperature steps between 950°C and 1125°C. Temperature in the tube was precisely controlled (to 1°C) by a thermocouple-regulated power supply. Thermal gradient is negligible across the sample region (i.e. hot zone). Gas steps were cleaned for 15 minutes by a Ti sponge getter heated to 800°C, collected on a liquid nitrogen-cooled charcoal finger, and then leaked into the mass spectrometer.

Data acquisition was fully automated. Analyses were carried out by sequentially scanning for masses 36, 37, 39 and 40. Once peaks were located, an automatic peak hoping procedure was begun and the amplified signal sent to an on-line Apple computer. The abundance of each isotope was measured a total of 15 times. The signals were digitized and the mass ratios 36/39, 37/39 and 40/39 calculated. Because the Ar ratios varied over the duration of the analysis due to static mode operation of the mass spectrometer (resulting in a "memory effect"), the ratios were linearly extrapolated back to zero time, that is, when the gas was first admitted into the mass spectrometer.

Corrections were made for the presence of interferring argon isotopes and atmospheric argon. The latter correction assumes the $^{40}Ar/^{36}Ar$ of the atmospheric Ar is 295.5. Following the analysis, an air-calibration is conducted in which atmospheric $^{40}Ar/^{36}Ar$ is measured. The difference between this value and the assumed value for atmospheric argon of 295.5 is used to derive a correction factor used in the calculation of the apparent age.

The significant interferring isotopes are Ca-derived ^{36}Ar and ^{39}Ar and K-derived ^{40}Ar (see Table 3.3 of McDougall and Harrison, 1988). These were corrected for using Ca and K-derived Ar isotopic ratios (i.e. production ratios) appropriate for the McMaster reactor (e.g. Mak et al., 1976). These values are $^{39}Ar/^{37}Ar_{Ca} = 6.51 \pm 0.31 \times 10^{-4}$, $^{36}Ar/^{37}Ar_{Ca} = 2.54 \pm 0.09 \times 10^{-4}$ and $^{40}Ar/^{39}Ar_{K} = 1.56 \pm 0.04 \times 10^{-2}$. The need for correction for interference reactions on Cl is precluded by cadmium shielding in the irradiation canister which absorbs the thermal neutrons that drive these reactions. The equation for deriving $^{40}Ar^{*}/^{39}Ar_{K}$ which takes into account the interferring isotope corrections and the atmospheric argon correction is given by McDougall and Harrison (1988, p. 83-84).

Table A2.1: ^{40}Ar/^{39}Ar analytical data for biotite. 36, 37, 39 and 40 stand for ^{36}Ar, ^{37}Ar, ^{39}Ar, and ^{39}Ar, respectively Error estimates at 1σ level. ^{37}Ar/^{39}Ar, ^{40}Ar/^{36}Ar and ^{39}Ar/^{36}Ar ratios are corrected for interferring isotopes. %IIC = interferring isotope correction which is negligible for biotite in this study. % atmos = % of ^{40}Ar* that is atmospheric.

SAMPLE: HP87-5

°C	39 mV	%39	Age Ma	% atmos	37/39	40/36	39/36	%IIC
550	11	3	38 ± 2	72	---	410	12.3	--
600	37	9	44 ± 1	45	---	662	34.1	--
650	76	19	46 ± 1	27	---	1093	71.7	--
700	51	13	44 ± 1	31	---	962	61.6	--
750	29	7	44 ± 1	52	---	572	25.5	--
800	16	4	39 ± 1	78	---	377	8.5	--
850	7	2	30 ± 3	88	---	337	5.6	--
900	28	7	41 ± 1	68	---	433	13.7	--
950	72	18	44 ± 1	56	---	532	22	--
1000	49	12	43 ± 1	69	---	427	12.6	--
1050	15	4	31 ± 2	91	---	323	3.7	--
1100	11	3	10 ± 11	99	---	299	1.3	--

Total gas age = 42 Ma, = 45 ± 0.4 Ma eliminating the last two steps.
J = 2.308 X 10^{-3}

SAMPLE: HP87-28

°C	39 mV	%39	Age Ma	% atmos	37/39	40/36	39/36	%IIC
550	12	2	26 ± 2	85	—	348	8.1	--
600	10	2	35 ± 2	51	—	584	33.5	--
650	63	13	43 ± 1	22	—	1372	100.8	--
700	76	16	43 ± 1	18	—	1683	129.9	--
750	121	25	44 ± 1	20	—	1501	110.1	--
800	52	11	42 ± 1	35	—	848	52.9	--
850	21	4	36 ± 1	62	—	478	20.6	--
900	25	5	39 ± 1	67	—	442	15.3	--
950	39	8	41 ± 1	62	—	477	17.9	--
1000	41	8	39 ± 1	68	—	436	14.5	--
1100	24	5	18 ± 4	96	—	306	2.4	--

Total gas age = 41 Ma, = 41.2 ± 0.6 Ma eliminating the last step.
J = 2.278 X 10^{-3}

Table A2.1: $^{40}Ar/^{39}Ar$ data for biotite (continued).

°C	39 mV	%39	Age Ma	% atmos	37/39	40/36	39/36	%IIC
SAMPLE: HP87-78D								
650	5	1	---*	--	---	---	-----	--
700	28	6	38 ± 1	45	---	650	38.1	--
750	62	14	43 ± 2	27	---	1104	77	--
800	76	17	44 ± 1	27	---	1080	72.8	--
850	18	4	33 ± 2	66	---	448	19	--
900	27	6	37 ± 1	68	---	436	15.6	--
950	39	9	40 ± 1	71	---	416	12.3	--
1000	63	14	42 ± 1	66	---	448	14.8	--
1100	140	31	43 ± 1	63	---	468	16.5	--

Total gas age = 42.6 ± 1.0 Ma eliminating the first step (*) lost due to analytical difficulties.
$J = 2.293 \times 10^{-3}$

°C	39 mV	%39	Age Ma	% atmos	37/39	40/36	39/36	%IIC
SAMPLE: HP87-79B								
600	17	3	42 ± 1	72	---	411	10.8	--
650	74	12	45 ± 1	25	---	1160	75.5	--
700	100	17	45 ± 1	12	---	2460	190.5	--
750	97	16	45 ± 1	10	---	3032	241.8	--
800	33	6	42 ± 1	28	---	1048	71.2	--
850	25	4	42 ± 1	47	---	632	32.2	--
900	14	2	38 ± 1	66	---	447	15.9	--
950	42	7	44 ± 1	39	---	751	41.3	--
1000	99	17	45 ± 1	43	---	692	35.3	--
1050	57	10	42 ± 1	65	---	456	15.3	--
1100	36	6	41 ± 1	78	---	378	8	--

Total gas age = 43.9 ± 0.8 Ma
$J = 2.232 \times 10^{-3}$

Table A2.1: $^{40}Ar/^{39}Ar$ data for biotite (continued).

SAMPLE: HP87-92

°C	39 mV	%39	Age Ma	% atmos	37/39	40/36	39/36	%IIC
500	1	<1	0	100	---	293	0.5	--
550	7	1	30 ± 5	96	---	309	1.9	--
600	14	3	45 ± 2	64	---	459	16.2	--
650	67	13	45 ± 1	36	---	832	52.5	--
700	96	19	46 ± 1	11	---	2683	230.1	--
750	87	17	46 ± 1	9	---	3461	308.5	--
800	77	15	46 ± 1	13	---	2313	195	--
850	29	6	45 ± 1	25	---	1188	87.3	--
900	57	11	45 ± 1	32	---	928	61.8	--
950	18	3	43 ± 1	29	---	1032	76.4	--
1000	25	5	43 ± 1	34	---	865	58.3	--
1050	37	7	45 ± 1	38	0.2	773	46.6	--

Total gas age = 45 ± 0.4 Ma
$J = 2.495 \times 10^{-3}$

SAMPLE: HP87-105

°C	39 mV	%39	Age Ma	% atmos	37/39	40/36	39/36	%IIC
550	4	<1	12 ± 6	98	---	301	2	--
600	6	1	37 ± 3	80	---	369	8.2	--
650	34	7	43 ± 1	51	---	575	26.7	--
700	58	13	45 ± 1	32	---	928	58.2	--
750	81	18	45 ± 1	31	---	939	59.1	--
800	16	3	46 ± 6	53	---	561	23.7	--
850	37	8	44 ± 2	63	---	466	16	--
900	25	5	42 ± 2	67	---	438	14.1	--
1000	144	31	42 ± 1	66	---	447	15	--
1100	57	12	31 ± 2	86	---	344	6.3	--

Total gas age = 41 ± 1.2 Ma
$J = 2.287 \times 10^{-3}$

Table A2.2: ^{40}Ar/^{39}Ar analytical data for muscovite. Error estimates at 1σ level. All symbols as for Table A2.1.

°C	39 mV	%39	Age Ma	% atmos	37/39	40/36	39/36	%IIC
SAMPLE: HP87-79								
700	5	<1	---*	--	---	----	----	--
750	22	4	44 ± 1	37	---	799	46.5	--
780	156	30	47 ± 1	12	---	2386	181.5	--
810	29	6	42 ± 1	25	---	1180	85.2	--
840	170	33	47 ± 1	11	---	2697	209.8	--
870	34	7	44 ± 1	16	---	1863	143.7	--
900	29	6	43 ± 1	29	---	1024	69.6	--
950	19	4	40 ± 1	45	---	663	37	--
1000	18	4	38 ± 2	59	---	501	22	--
1050	20	4	39 ± 2	69	---	428	14	--
1140	10	2	25 ± 3	92	---	321	4.2	--

Total gas age = 43.5 ± 0.6 Ma eliminating the first step (*) lost due to analytical difficulties (*) and the final step with high blank.
J = 2.287 X 10^{-3}

°C	39 mV	%39	Age Ma	% atmos	37/39	40/36	39/36	%IIC
SAMPLE: HP87-110								
700	10	2	28 ± 2	89	---	330	5.1	--
750	10	2	30 ± 2	79	---	374	10.5	--
810	12	2	34 ± 6	73	---	403	12.8	--
840	66	11	50 ± 1	38	---	788	39.1	--
890	136	23	43 ± 1	27	---	1112	75.9	--
940	135	23	43 ± 1	33	---	883	54.4	--
990	124	21	44 ± 1	54	---	552	23.5	--
1040	44	7	37 ± 1	85	---	349	5.8	--
1090	34	6	29 ± 3	94	---	315	2.6	--
1140	18	3	16 ± 6	98	---	301	1.5	--

Total gas age = 41 ± 1.2 Ma
J = 2.246 X 10^{-3}

Table A2.2: ^{40}Ar/^{39}Ar data for muscovite (continued).

°C	39 mV	%39	Age Ma	% atmos	37/39	40/36	39/36	%IIC
SAMPLE: HP87-272								
600	24	4	43 ± 1	66	---	449	14.6	--
650	20	3	42 ± 1	42	---	708	40.1	--
700	38	6	43 ± 1	34	---	874	54.3	--
750	80	12	45 ± 1	37	---	800	45.9	--
800	165	26	45 ± 1	22	---	1330	92.9	--
850	142	22	45 ± 1	27	---	1097	72.3	--
900	40	6	43 ± 1	43	---	683	37.1	--
950	37	6	42 ± 1	60	---	491	19.1	--
1000	22	3	39 ± 1	69	---	429	14	--
1150	74	11	43 ± 1	77	---	383	8.3	--

Total gas age = 44 ± 1.0 Ma
J = 2.29 X 10^{-3}

°C	39 mV	%39	Age Ma	% atmos	37/39	40/36	39/36	%IIC
SAMPLE: HP87-296								
650	4	<1	15 ± 6	91	---	324	7.7	--
700	6	1	29 ± 3	72	---	408	16.1	--
750	16	3	40 ± 2	52	---	563	27.3	--
780	42	9	44 ± 1	49	---	608	29.3	--
810	46	10	43 ± 1	37	---	807	48.5	--
840	32	7	43 ± 1	33	---	899	57.6	--
870	54	11	44 ± 1	31	---	950	61.5	--
900	140	29	45 ± 1	32	---	926	57.6	--
950	50	10	43 ± 1	46	---	636	32.5	--
1000	39	8	41 ± 1	66	---	450	15.4	--
1050	25	5	37 ± 1	82	---	362	7.4	--
1140	23	5	29 ± 3	94	---	314	2.5	--

Total gas age = 42 ± 0.4 Ma
J = 2.312 X 10^{-3}

Table A2.3: $^{40}Ar/^{39}Ar$ analytical data for hornblende. Error estimates at 1σ level. All symbols as for Table A2.1.

°C	39 mV	%39	Age Ma	% atmos	37/39	40/36	39/36	%IIC
SAMPLE: HP87-78D								
650	<1	2	346 ± 41	78	---	380	0.9	--
750	2	5	63 ± 9	86	---	345	3.4	--
850	<1	2	22 ± 36	94	---	314	3.8	--
950	<1	2	0	100	---	292	3.5	--
975	2	4	47 ± 11	85	6.8	349	4.9	5
1000	3	8	39 ± 4	82	14.2	360	7.3	13
1025	8	21	44 ± 2	73	13.7	405	11.1	11
1050	6	17	41 ± 2	71	13.2	417	13.1	11
1075	12	33	45 ± 1	77	12.3	386	8.8	10
1100	1	3	6 ± 14	98	11	300	3.2	58
1125	1	3	15 ± 19	97	11.8	304	2.3	26

Total gas age = 49 ± 2.2 Ma
J = 2.495 X 10^{-3}

Errors on plateau and total gas ages were calculated taking into consideration the error on the $^{40}Ar/^{39}Ar$ ratio (R) and the J-values. Consider the following,

(A2.16) $$R = \frac{39_1R_1 + 39_2R_2 + ...}{39_T}$$

where: $R = {}^{40}Ar^*/{}^{39}Ar$

39_i = the abundance of ^{39}Ar in mV where i = 1, 2, 3,...etc.

39_T = the sum of 39_i over the plateau or entire spectrum

Since $R = R(R_1, R_2, R_3$ etc.) differentiating gives:

(A2.17) $$(dR)^2 = (dR/dR_1)^2dR_1^2 + (dR/dR_2)^2dR_2^2 + ...$$
$$(dR)^2 = (39_1/39_T)^2dR_1^2 + (39_2/39_T)^2dR_2^2 + ...$$

Using the basic age equation,

(A2.18) $$t = 1/\lambda\{\ln[1 + (J)(R)]\}$$

and differentiating with respect to J and to R we get:

(A2.19) $$dt^2 = (dt/dJ)^2dJ^2 + (dt/dR)^2dR^2$$

(A2.20) $$dt^2 = [R/\lambda(1 + JR)]^2dJ^2 + [J/\lambda(1 + JR)]^2dR^2$$

Substituting R and dR from above and J, dJ determined from the flux curve into Equation A2.20, one can calculated the error (dt) on the age (t) (P. Reynolds, written communication 1991)

A2.2.3. FISSION TRACK METHOD

(i) Theory: Age Dates

Although ^{238}U decays predominantly by alpha emission to ^{206}Pb through a series of intermediate daughter isotopes, approximately one of every two million transformations take place by spontaneous fission. The ^{238}U fission particles fly apart in opposite direction, strip electrons from the host mineral lattice and form a linear damage zone or fission track. In geological samples, fission tracks are up to 15 μm

long and a few Å wide. All spontaneous fission tracks are attributed to ^{238}U decay because other fissioning isotopes have longer half lives and lower abundances and because terrestrial samples are shielded from cosmic rays (see Faure, 1986).

The number of spontaneous fission tracks depends on the uranium content of the mineral (sample) and the time duration for track accumulation. To determine the U-content, the mineral is irradiated in a nuclear reactor with a monitored dose of thermal neutrons which cause the less abundant isotope, ^{235}U, to fission and produce induced fission tracks. The ^{235}U-content is determined from the induced track density count and the thermal neutron flux and the ^{238}U-content can be determined from the known isotopic ratio of ^{235}U/^{238}U (= 7.2527×10^{-3}) (e.g. Hurford and Green, 1982). Therefore, in the way that other geochronometric methods depend on the ratio of daughter to parent isotope, the fission track method depends on the ratio of spontaneous to induced tracks.

The basic fission track equation is:

$$t = \frac{1}{\lambda_D} \ln\left(1 + \frac{\lambda_D \phi \sigma I g \rho_s}{\lambda_f \rho_i}\right) \tag{A2.21}$$

where:

λ_D = total decay constant for ^{238}U, 1.55125×10^{-10} y^{-1}

λ_f = spontaneous fission decay constant for ^{238}U

I = ^{235}U/^{238}U isotope abundance ratio = 7.2527×10^{-3}

σ = thermal neutron fission cross section for ^{235}U = 580.2×10^{-24} cm^2

ρ_s / ρ_i = spontaneous/induced fission track density ratio in the sample

g = geometry factor (0.5 for the external detector method)

ρ_i, g, ϕ, I and σ are related to the irradiation process. The product $(\phi)(\sigma)$ represents the number of fission reactions induced by thermal neutrons per atom of ^{235}U where ϕ is the neutron flux and σ is the probability per atom of the reaction taking place. Thermal neutrons are generated as fission neutrons in the reactor core and are slowed down in a moderator by neutron scattering. The neutrons become thermalized upon reaching a state of thermal equilibrium with the moderator. The cadmium ratio (Cd) is a measure of how well the neutron flux is thermalized. If it is well thermalized (high Cd) fission of ^{238}U and ^{232}Th will not occurr. The McMaster reactor in Hamilton, Ontario, used in this study, is well thermalized (see below).

The main error sources in the calculated fission track date are: (1) uncertainty in the neutron dose, (2) uneven U-distribution in the sample, (3) partial track annealing and (4) statistical error in counting tracks. The first two error sources can be addressed by the external detector method (EDM) (Gleadow, 1981) and the zeta method (Hurford and Green, 1982), respectively. Annealing and counting errors can be addressed by track length studies (see below).

At the Dalhousie Laboratory, Halifax, Nova Scotia, the induced track density in apatite is determined by the external detector method. Apatite grains are mounted on a glass slide, polished to expose an internal surface and etched in nitric acid to reveal spontaneous tracks. The spontaneous track lengths are measured (see below) and then the etched mount is placed in contact with a low-uranium external mica detector. Four uranium glass dosimeters (CN1 in this study) with external mica detectors are also included at discrete intervals within the irradiation package to monitor the neutron flux. During irradiation, fission is induced in ^{235}U in apatite; some of the fission fragments enter the mica detector and produce induced tracks which are revealed by etching.

Spontaneous and induced tracks are counted in matching areas from the planar surface of the apatite crystal so that inhomogenity in U distribution in and between apatite grains is not a problem. Commonly, 10 to 25 grains per analysis are counted to calculate an age. Spontaneous tracks on the etched internal surface of the apatite grain result from the two-way movement of the fission fragments above and below the etched surface (4π geometry), whereas induced tracks result from one-way movement of the fission particles (2π geometry) from the apatite into the detector. Therefore, to compare spontaneous and induced tracks, a geometry correction factor (g) is required, which under correct etching conditions, is equal to 0.5 for the apatite-mica pair.

The values for λ_D, σ and I are well known. Experimental determinations of λ_f differ by as much as 20% but are commonly near 8.5×10^{-17} or 7.0×10^{-17} y^{-1}. At the present, ϕ can not be measured accurately. In order to avoid the need for absolute dosiometry and for a correct value of λ_f, the zeta method is used. Equation (A2.12) is re-written as:

(A2.22) $$t = \frac{1}{\lambda_D} \ln\left(1 + \lambda_D \zeta \left(\frac{\rho_s}{\rho_i}\right) g \rho_d\right)$$

where

(A2.23) $$\zeta = \frac{\left(e^{\lambda_D t_{std}} - 1\right)}{\lambda_D \left(\frac{\rho_s}{\rho_i}\right)_{std} \rho_d g}$$

Table A2.4: (a) Individual grain data for Fish Canyon Tuff standard. N = number of tracks counted in the standard where N_i = number of induced tracks and N_s = number of spontaneous tracks. Quads = number of grid quadrants counted. N_D = number of induced tracks counted in the glass dosimeter (CN1). The pooled age is determined by averaging the sum the individual crystal (apatite grain) ages. The mean age is determined using the sum of the count data for all the crystals.

Crystal	N_s	N_i	Quads	N_s/N_i	ρ_s	ρ_i	U (ppm)	Age (Ma)
1	11	52	25	0.212	2.82E+05	1.33E+06	15	33.5 ± 11.4
2	4	21	25	0.190	1.02E+05	5.38E+05	6	30.2 ± 16.7
3	1	39	25	0.026	2.56E+04	9.98E+05	11	4.1 ± 4.1
4	6	21	25	0.286	1.54E+05	5.38E+05	6	45.3 ± 21.3
5	6	42	20	0.143	1.92E+05	1.34E+06	15	22.7 ± 10.1
6	10	51	25	0.196	2.53E+05	1.31E+06	15	31.1 ± 11.0
7	14	55	25	0.255	3.58E+05	1.41E+06	16	40.3 ± 12.5
8	8	43	20	0.186	2.65E+05	1.38E+06	16	29.5 ± 11.6
9	4	24	20	0.167	1.28E+05	7.68E+05	9	26.4 ± 14.4
10	5	42	25	0.119	1.28E+05	1.08E+06	12	18.9 ± 9.1
11	9	32	25	0.281	2.30E+05	8.19E+05	9	44.6 ± 17.2
12	5	24	25	0.208	1.28E+05	6.14E+05	7	33.0 ± 16.4
13	8	53	25	0.151	2.05E+05	1.36E+06	15	23.9 ± 9.3
14	16	45	25	0.356	4.10E+05	1.15E+05	13	56.3 ± 17.0
15	6	44	20	0.136	1.92E+05	1.41E+06	16	21.6 ± 9.6
16	3	30	25	0.100	7.68E+04	7.68E+05	9	15.9 ± 9.7
17	4	48	25	0.083	1.02E+05	1.23E+06	14	13.2 ± 7.0
18	10	46	25	0.217	2.56E+05	1.18E+06	13	34.5 ± 12.3
19	14	66	25	0.212	3.58E+05	1.69E+06	19	33.6 ± 10.2
20	6	40	25	0.150	1.54E+05	1.02E+06	12	23.8 ± 10.6
21	7	22	15	0.318	2.99E+05	9.39E+05	11	50.4 ± 22.2
22	7	30	25	0.233	1.79E+05	7.68E+05	9	37.0 ± 15.8
23	5	26	25	0.192	1.28E+05	6.66E+05	8	30.5 ± 15.1
24	7	52	25	0.135	1.79E+05	1.33E+06	15	21.4 ± 8.8
25	2	17	25	0.118	5.12E+04	4.35E+05	5	18.7 ± 14.0
26	5	44	25	0.114	1.28E+05	1.13E+06	13	18.0 ± 8.6
27	4	31	25	0.129	1.02E+05	7.94E+05	9	20.5 ± 11.0
28	10	61	25	0.164	2.56E+05	1.56E+06	18	26.0 ± 9.1
29	6	37	25	0.162	1.54E+05	9.47E+05	11	25.7 ± 11.5
30	6	43	25	0.140	1.54E+05	1.10E+06	13	22.1 ± 9.8
31	5	40	25	0.125	1.28E+05	1.02E+06	12	19.8 ± 9.5
	214	1221			1.84E+05	1.05E+06		

SUMMARY OF STATISTICS:

Variance of $(N_s)^{1/2}$ = 0.4388
Variance of $(N_i)^{1/2}$ = 1.0665
Correlation coefficient (R) for N_i = 0.6243
Chi^2 = 26.48441 with 30 degrees of freedom (Test Pass)
Probability of greater value = 0.6501943

AGE CALCULATION:

Zeta factor used = 11560 ± 890
Glass Dosimeter = CN1
N_D counted = 2600
ρ_D for glass = $2.750 \times 10^6 \pm 0.539 \times 10^5$
Area of 1 Quad = 1.5625×10^{-6} cm^2
Pooled N_s/N_i = 0.175 ± 0.013
Mean N_s/N_i = 0.178 ± 0.013

POOLED AGE = 27.8 ± 3.0 Ma

MEAN AGE = 28.2 ± 3.0 Ma

Table A2.4b (continued): Individual grain data for Fish Canyon Tuff standard.

Crystal	N_s	N_i	Quads	N_s/N_i	ρ_s	ρ_i	U (ppm)	Age (Ma)
1	10	65	25	0.154	2.56E+05	1.66E+06	19	25.3 ± 8.8
2	5	53	25	0.094	1.28E+05	1.36E+06	15	15.5 ± 7.4
3	5	43	25	0.116	1.28E+05	1.10E+06	13	19.1 ± 9.2
4	3	30	25	0.100	7.68E+04	7.68E+05	9	16.4 ± 10.0
5	9	49	25	0.184	2.30E+05	1.25E+06	14	30.2 ± 11.2
6	7	32	25	0.219	1.79E+05	8.19E+05	9	35.9 ± 15.3
7	3	30	25	0.100	7.68E+04	7.68E+05	9	16.4 ± 10.0
8	2	44	25	0.045	5.12E+04	1.13E+06	13	7.5 ± 5.4
9	8	45	25	0.178	2.05E+05	1.15E+06	13	29.2 ± 11.5
10	9	33	25	0.273	2.30E+05	8.45E+05	10	44.7 ± 17.2
11	8	49	25	0.163	2.05E+05	1.25E+06	14	26.8 ± 10.5
12	6	33	20	0.182	1.92E+05	1.06E+06	12	29.9 ± 13.5
13	7	47	25	0.149	1.79E+05	1.20E+06	14	24.5 ± 10.1
14	3	37	25	0.081	7.68E+04	9.47E+05	11	13.3 ± 8.1
15	9	40	25	0.225	2.30E+05	1.02E+06	12	36.9 ± 14.0
16	9	41	25	0.220	2.30E+05	1.05E+06	12	36.0 ± 13.6
17	9	28	25	0.321	2.30E+05	7.17E+05	8	52.7 ± 20.6
18	1	31	20	0.032	3.20E+04	9.92E+05	11	5.3 ± 5.4
19	8	35	20	0.229	2.56E+05	1.12E+06	13	37.5 ± 15.0
20	7	37	25	0.189	1.79E+05	9.47E+05	11	31.1 ± 13.1
21	7	30	25	0.233	1.79E+05	7.68E+05	9	38.3 ± 16.4
22	10	40	25	0.250	2.56E+05	1.02E+06	12	41.0 ± 14.9
23	8	51	25	0.157	2.05E+05	1.31E+06	15	25.8 ± 10.0
24	8	29	20	0.276	2.56E+05	9.28E+05	11	45.3 ± 18.4
25	6	36	25	0.167	1.54E+05	9.22E+05	10	27.4 ± 12.3
26	7	42	25	0.167	1.79E+05	1.08E+06	12	27.4 ± 11.4
27	8	44	25	0.182	2.05E+05	1.13E+06	13	29.9 ± 11.7
28	6	38	25	0.158	1.54E+05	9.73E+05	11	25.9 ± 11.6
29	9	52	25	0.173	2.30E+05	1.33E+06	15	28.4 ± 10.5
	197	1164			1.79E+05	1.06E+06		

SUMMARY OF STATISTICS:
Variance of $(N_s)^{1/2}$ = 0.3001
Variance of $(N_i)^{1/2}$ = 0.4712
Correlation coefficient (R) for N_i = 0.3324
Chi^2 = 22.92657 with 28 degrees of freedom (Test Pass)
Probability of greater value = 0.7367067

AGE CALCULATION:
Zeta factor used = 11970 ± 950
Glass Dosimeter = CN1
N_D counted = 2600
ρ_D for glass = $2.750 \times 10^6 \pm 0.539 \times 10^5$
Area of 1 Quad = 1.5625×10^{-6} cm^2
Pooled N_s/N_i = 0.169 ± 0.013
Mean N_s/N_i = 0.173 ± 0.013

POOLED AGE = 27.8 ± 3.1 Ma

MEAN AGE = 28.4 ± 3.1 Ma

Table A2.4b: Individual grain data for Horseranch apatites. All symbols as in part (a).

HP87-3: granite monzonite mylonite

Crystal	N_s	N_i	Quads	N_s/N_i	ρ_s	ρ_i	U (ppm)	Age (Ma)
1	12	18	9	0.667	8.53E+05	1.28E+06	15	106.9 ± 40.3
2	2	22	15	0.091	8.53E+04	9.39E+05	11	14.7 ± 10.9
3	7	15	9	0.467	4.98E+05	1.07E+06	12	75.0 ± 34.6
4	5	20	10	0.250	3.20E+05	1.28E+06	15	40.3 ± 20.3
5	4	12	9	0.333	2.84E+05	8.53E+05	10	53.7 ± 31.1
6	11	32	15	0.344	4.69E+05	1.37E+06	16	55.3 ± 19.6
7	28	79	25	0.354	7.17E+05	2.02E+06	23	57.1 ± 13.0
8	3	9	9	0.333	2.13E+05	6.40E+05	7	53.7 ± 35.9
9	6	22	9	0.273	4.27E+05	1.56E+06	18	43.9 ± 20.4
10	4	25	10	0.160	2.56E+05	1.60E+06	18	25.8 ± 14.0
11	8	48	10	0.167	5.12E+05	3.07E+06	35	26.9 ± 10.4
12	8	25	9	0.320	5.69E+05	1.78E+06	20	51.5 ± 21.1
13	5	12	9	0.417	3.56E+05	8.53E+05	10	67.0 ± 35.9
14	6	27	9	0.222	4.27E+05	1.92E+06	22	35.8 ± 16.3
15	3	10	10	0.300	1.92E+05	6.40E+05	7	48.3 ± 31.9
16	6	22	10	0.273	3.84E+05	1.41E+06	16	43.9 ± 20.4
17	4	16	9	0.250	2.84E+05	1.14E+06	13	40.3 ± 22.6
18	7	25	25	0.280	1.79E+05	6.40E+05	7	45.1 ± 19.5
19	7	23	10	0.304	4.48E+05	1.47E+06	17	49.0 ± 21.4
20	9	36	25	0.250	2.30E+05	9.22E+05	10	40.3 ± 15.2
21	5	25	9	0.200	3.56E+05	1.78E+06	20	32.3 ± 15.9
22	3	11	25	0.273	7.68E+04	2.82E+05	3	43.9 ± 28.7
	153	534			3.50E+05	1.22E+06		

SUMMARY OF STATISTICS:
Variance of $(N_s)^{1/2}$ = 0.6585
Variance of $(N_i)^{1/2}$ = 1.7775
Correlation coefficient (R) for N_i = 0.8558
Chi^2 = 15.65918 with 21 degrees of freedom (Test Pass)
Probability of greater value = 0.7884844

AGE CALCULATION:
Zeta factor used = 11760 ± 650
Glass Dosimeter = CN1
N_D counted = 2600
$_D$ for glass = 2.750 X 10^6 ± 0.539 X 10^5
Area of 1 Quad = 1.5625 X 10^{-6} cm^2
Pooled N_s/N_i = 0.287 ± 0.026
Mean N_s/N_i = 0.297 ± 0.026

POOLED AGE = 46.2 ± 5.0 Ma

MEAN AGE = 47.8 ± 5.0 Ma

Table A2.4b (continued): Individual grain data for Horseranch apatites.

HP87-75: granite orthogneiss

Crystal	N_s	N_i	Quads	N_s/N_i	ρ_s	ρ_i	U (ppm)	Age (Ma)
1	52	181	25	0.287	1.33E+06	4.63E+06	53	46.3 ± 7.8
2	15	77	9	0.195	1.07E+06	5.48E+06	62	31.4 ± 9.1
3	20	63	9	0.317	1.42E+06	4.48E+06	51	51.1 ± 13.5
4	47	173	25	0.272	1.20E+06	4.43E+06	50	43.8 ± 7.6
5	17	54	9	0.315	1.21E+06	3.84E+06	44	50.7 ± 14.4
6	60	157	25	0.382	1.54E+06	4.02E+06	46	61.5 ± 10.0
7	17	47	9	0.362	1.21E+06	3.34E+06	38	58.2 ± 16.8
8	21	63	9	0.333	1.49E+06	4.48E+06	51	53.7 ± 13.9
9	14	69	9	0.203	9.96E+05	4.91E+06	56	32.7 ± 9.8
10	18	58	9	0.310	1.28E+06	4.12E+06	47	50.0 ± 13.8
11	30	73	9	0.411	2.13E+06	5.19E+06	59	66.1 ± 14.8
12	65	214	25	0.304	1.66E+06	5.48E+06	62	48.9 ± 7.5
13	56	165	25	0.339	1.43E+06	4.22E+06	48	54.6 ± 9.0
14	19	45	9	0.422	1.35E+06	3.20E+06	36	67.9 ± 19.0
15	22	59	9	0.373	1.56E+06	4.20E+06	48	60.0 ± 15.4
16	36	147	20	0.245	1.15E+06	4.70E+06	53	39.5 ± 7.7
17	23	59	9	0.390	1.64E+06	4.20E+06	48	62.7 ± 15.9
18	47	140	25	0.336	1.20E+06	3.58E+06	41	54.1 ± 9.6
19	26	67	9	0.388	1.85E+06	4.76E+06	54	62.4 ± 14.9
20	68	156	25	0.436	1.74E+06	3.99E+06	45	70.1 ± 11.0
21	47	184	25	0.255	1.20E+06	4.71E+06	54	41.2 ± 7.1
22	14	48	9	0.292	9.96E+05	3.41E+06	39	47.0 ± 14.5
23	45	181	25	0.249	1.15E+06	4.63E+06	53	40.1 ± 7.1
24	30	168	20	0.179	9.60E+05	5.38E+06	61	28.8 ± 6.0
25	39	174	25	0.224	9.98E+05	4.45E+06	51	36.1 ± 6.7
26	17	70	9	0.243	1.21E+06	4.98E+06	57	39.1 ± 10.8
27	19	58	9	0.328	1.35E+06	4.12E+06	47	52.7 ± 14.3
28	16	69	9	0.232	1.14E+06	4.91E+06	56	37.4 ± 10.6
29	20	96	15	0.208	8.53E+05	4.10E+06	47	33.6 ± 8.5
30	11	53	9	0.208	7.82E+05	3.77E+06	43	33.5 ± 11.3
31	17	48	9	0.354	1.21E+06	3.41E+06	39	57.0 ± 16.4
	948	3216			1.30E+06	4.41E+06		

SUMMARY OF STATISTICS:
Variance of $(N_s)^{1/2}$ = 2.1619
Variance of $(N_i)^{1/2}$ = 7.1554
Correlation coefficient (R) for N_i = 0.8850
Chi^2 = 41.27089 with 30 degrees of freedom (Test Pass)
Probability of greater value = 8.250255E-02

AGE CALCULATION:
Zeta factor used = 11760 ± 650
Glass Dosimeter = CN1
N_D counted = 2600
ρ_D for glass = $2.750 \times 10^6 \pm 0.539 \times 10^5$
Area of 1 Quad = 1.5625×10^{-6} cm^2
Pooled N_s/N_i = 0.295 ± 0.011
Mean N_s/N_i = 0.303 ± 0.013

POOLED AGE = 47.5 ± 3.3 Ma

MEAN AGE = 48.8 ± 3.6 Ma

Table A2.4b (continued): Individual grain data for Horseranch apatites.

HP87-110: granite mylonite

Crystal	N_s	N_i	Quads	N_s/N_i	ρ_s	ρ_i	U (ppm)	Age (Ma)
1	12	44	9	0.273	8.53E+05	3.13E+06	36	43.9 ± 14.5
2	14	41	9	0.341	9.96E+05	2.92E+06	33	55.0 ± 17.3
3	47	147	25	0.320	1.20E+06	3.76E+06	43	51.5 ± 9.1
4	45	145	25	0.310	1.15E+06	3.71E+06	42	50.0 ± 9.0
5	22	73	10	0.301	1.41E+06	4.67E+06	53	48.5 ± 12.1
6	12	58	10	0.207	7.68E+05	3.71E+06	42	33.4 ± 10.8
7	25	75	15	0.333	1.07E+06	3.20E+06	36	53.7 ± 12.8
8	55	164	25	0.335	1.41E+06	4.20E+06	48	54.0 ± 9.0
9	14	62	9	0.226	9.96E+05	4.41E+06	50	36.4 ± 11.0
10	18	64	9	0.281	1.28E+06	4.55E+06	52	45.3 ± 12.4
11	15	54	9	0.278	1.07E+06	3.84E+06	44	44.8 ± 13.3
12	18	47	9	0.383	1.28E+06	3.34E+06	38	61.6 ± 17.5
13	19	73	10	0.260	1.22E+06	4.67E+06	53	41.9 ± 11.1
14	62	218	25	0.284	1.59E+06	5.58E+06	63	45.8 ± 7.1
15	22	59	10	0.373	1.41E+06	3.78E+06	43	60.0 ± 15.4
16	15	49	9	0.306	1.07E+06	3.48E+06	40	49.3 ± 14.8
17	18	82	10	0.220	1.15E+06	5.25E+06	60	35.4 ± 9.4
18	52	167	25	0.311	1.33E+06	4.28E+06	49	50.1 ± 8.5
19	44	151	25	0.291	1.13E+06	3.87E+06	44	46.9 ± 8.5
20	39	125	25	0.312	9.98E+05	3.20E+06	36	50.2 ± 9.7
	568	1898			1.20E+06	4.01E+06		

SUMMARY OF STATISTICS:

Variance of $(N_s)^{1/2}$ = 2.2097
Variance of $(N_i)^{1/2}$ = 6.5440
Correlation coefficient (R) for N_i = 0.9797
Chi^2 = 7.186661 with 19 degrees of freedom (Test Pass)
Probability of greater value = 0.9931496

AGE CALCULATION:

Zeta factor used = 11760 ± 650
Glass Dosimeter = CN1
N_D counted = 2600
ρ_D for glass = $2.75 \times 10^6 \pm 0.539 \times 10^5$
Area of 1 Quad = 1.5625×10^{-6} cm^2
Pooled N_s/N_i = 0.299 ± 0.014
Mean N_s/N_i = 0.297 ± 0.011

POOLED AGE = 48.2 ± 3.6 Ma

MEAN AGE = 47.9 ± 3.3 Ma

Table A2.4b (continued): Individual grain data for Horseranch apatites.

HP87-159: granite mylonite

Crystal	N_s	N_i	Quads	N_s/N_i	ρ_s	ρ_i	U (ppm)	Age (Ma)
1	14	32	9	0.438	9.96E+05	2.28E+06	26	70.4 ± 22.9
2	35	104	25	0.337	8.96E+05	2.66E+06	30	54.2 ± 11.1
3	53	146	25	0.363	1.36E+06	3.74E+06	43	58.4 ± 10.0
4	24	93	20	0.258	7.68E+05	2.98E+06	34	41.6 ± 9.8
5	18	50	15	0.360	7.68E+05	2.13E+06	24	57.9 ± 16.3
6	43	143	25	0.301	1.10E+06	3.66E+06	42	48.4 ± 8.9
7	28	115	25	0.243	7.17E+05	2.94E+06	33	39.2 ± 8.6
8	23	112	25	0.205	5.89E+05	2.87E+06	33	33.1 ± 7.8
9	12	37	10	0.324	7.68E+05	2.37E+06	27	52.2 ± 17.6
10	17	100	25	0.170	4.35E+05	2.56E+06	29	27.4 ± 7.4
11	31	104	15	0.298	1.32E+06	4.44E+06	50	48.0 ± 10.2
12	25	123	25	0.203	6.40E+05	3.15E+06	36	32.8 ± 7.4
13	39	118	25	0.331	9.98E+05	3.02E+06	34	53.2 ± 10.3
14	29	116	25	0.250	7.42E+05	2.97E+06	34	40.3 ± 8.7
15	31	110	25	0.282	7.94E+05	2.82E+06	32	45.4 ± 9.6
16	36	142	25	0.254	9.22E+05	3.64E+06	41	40.9 ± 8.0
17	20	48	9	0.417	1.42E+06	3.41E+06	39	67.0 ± 18.3
18	11	46	9	0.239	7.82E+05	3.27E+06	37	38.5 ± 13.1
19	20	83	15	0.241	8.53E+05	3.54E+06	40	38.8 ± 9.9
20	40	146	25	0.274	1.02E+06	3.74E+06	43	44.1 ± 8.3
21	14	71	15	0.197	5.97E+05	3.03E+06	34	31.8 ± 9.5
22	27	104	20	0.260	8.64E+05	3.33E+06	38	41.8 ± 9.4
23	29	107	20	0.271	9.28E+05	3.42E+06	39	43.7 ± 9.5
24	15	58	10	0.259	9.60E+05	3.71E+06	42	41.7 ± 12.3
25	23	93	25	0.247	5.89E+05	2.38E+06	27	39.9 ± 9.6
26	23	74	15	0.311	9.81E+05	3.16E+06	36	50.1 ± 12.3
27	20	87	20	0.230	6.40E+05	2.78E+06	32	37.1 ± 9.4
28	12	43	9	0.279	8.53E+05	3.06E+06	35	45.0 ± 14.9
29	16	56	15	0.286	6.83E+05	2.39E+06	27	46.0 ± 13.3
30	8	40	9	0.200	5.69E+05	2.84E+06	32	32.3 ± 12.6
31	35	145	25	0.241	8.96E+05	3.71E+06	42	38.9 ± 7.7
	771	2846			8.43E+05	3.11E+06		

SUMMARY OF STATISTICS:
Variance of $(N_s)^{1/2}$ = 1.1403
Variance of $(N_i)^{1/2}$ = 3.9401
Correlation coefficient (R) for N_i = 0.8846
Chi^2 = 23.25201 with 30 degrees of freedom (Test Pass)
Probability of greater value = 0.8047593

AGE CALCULATION:
Zeta factor used = 11760 ± 650
Glass Dosimeter = CN1
N_D counted = 2600
ρ_D for glass = $2.750 \times 10^6 \pm 0.539 \times 10^5$
Area of 1 Quad = 1.5625×10^{-4} cm^2
Pooled N_s/N_i = 0.271 ± 0.011
Mean N_s/N_i = 0.276 ± 0.011

POOLED AGE = 43.7 ± 3.1 Ma

MEAN AGE = 44.5 ± 3.2 Ma

Zeta (ζ) is the calibration factor for a given glass dosimeter which is determined by irradiating the dosimeter with samples of known fission track age (t_{std}). ρ_d is the induced fission track density in the mica detector covering the glass dosimeter during irradiation. Zeta calibration factors must be determined using mean values based on a large number of determinations with carefully chosen age standards. They depend on mineral type, the procedure of track investigation and the experience of the analyst (e.g. Green, 1981; Hurford and Green, 1982).

The error estimates on the track length measurements that are reported in the text are errors on the mean of the distribution or "standard errors". Standard error is defined as:

$$\text{standard error} = \sigma_d/(N_T - 1)^{1/2} \tag{A.24}$$

where σ_d = the standard deviation of the track length distribution
N_T = total number of track lengths measured

(Press et al., 1986). Effectively, standard error is the statistical error on the mean of the measured track lengths.

(ii) Theory: Track Lengths

Between temperatures of ca. 120 and 50°C, fission tracks anneal such that track lengths shorten and track length distributions broaden (e.g. Gleadow et al., 1986; Green et al., 1986). Therefore, track lengths and their distribution may provide information on the rate of cooling of the sample through the partial annealing zone. Horizontal tracks which do not intersect the surface, lie in a plane parallel to the etched surface and have been etched due to intersection with another track or fracture are measured. These are easily identified by their optical properties in transmitted and reflected light. Generally, 100 track counts are sufficient to characterize the track length distribution.

Track length measurements in apatite are subject to error from anisotropic track length reduction (which is slowest parallel to the C-axis) and from bias in etching, observing and measuring the tracks, as the longest tracks are the most readily etched and identified (e.g. Green, 1988; Laslett et al., 1982). The total error from these sources is < 0.5% and track lengths were not corrected for these errors (A. Grist, personal communication, 1991). In conventional fission track analysis, Poissonian errors are assumed to be applicable to the track length densities because radioactive decay is a random process (Green, 1981). Non-poissonian distributions indicate that errors other than the random fluctuation of radioactive decay rate are present. Non-poissonian error sources for the EDM include error due to grain populations of mixed ages, poor contact between mineral and external detector, counting of track-like defects and incorrect matching of sample and detector after irradiation (Green, 1981). Green (1981) gives several methods for including non-Poissonian errors in fission track dating.

(ii) Analytical Techniques

The external detector method was used to obtain fission track ages of apatites. Irradiations were carried out in the McMaster University Nuclear Reactor in Hamilton, Ontario (900 seconds in site 9D, Cd ratio at this site = 54-58 for Cu, i.e well thermalized at this site). The flux gradient was monitored using pieces of dosimeter glass CN1 with a mean track length of 15.191 μm and a composition of 72.7% SiO_2, 5.1% CaO, 1.4% Al_2O^{23}, 36 ppm ^{238}U and $^{238}U/^{235}U = 137.88$) which was placed above and below the samples. Fish Canyon Tuff apatite standard (Hurford and Hammerschmidt, 1985) was used to determine the zeta calibration factor (ζ) for the dosimeter glass. Between 20 and 31 grains were counted for each sample. Count data were subjected to a Chi-squared test to check for variation beyond that predicted by Poissonian statistics (Galbraith, 1981; Green, 1981). As all data passed the test, ages and error estimates were calculated by conventional methods (Green, 1981). Fission track lengths were measured on horizontal, confined tracks using a drawing tube fitted to the microscope and a digitizing table.

A2.3. INSTRUMENTAL NEUTRON ACTIVATION ANALYSES

INAA analyses were carried out at the XRAL Activation Services laboratory, Ann Arbor, Michigan. The following description is summarized from that provided by the laboratory.

Whole rock samples were crushed and milled to between -80 and -200 mesh. The rock powder is then weighed out in a high-purity polyethelyne vial and capped and placed in a neutron field for 15 minutes to 1 hour. The amount of neutrons passing through the area is monitored by a nickel-chrome foil placed next to the vial during the irradiation. The amount of neutrons is generally 1×10^{20} neutrons/cm^2/s. Following irradiation, the samples are allowed to cool-off for at least 7 days. Only the elements which decay by gamma-ray emission (i.e.those having long half lives) are present at the end of 7 days.

The irradiated sample is placed on a gamma-ray detector for a set period of time and the gamma-ray emissions counted over a range of energies. The elements are then quantified based on the irradiation time, the amount of neutrons present, the sample weight, the length of the post-irradiation "cool-off" period, the detector efficiency and the neutron absorbing properties of the element in question. Standards with known elemental concentrations are analysed with the sample during irradiation.

APPENDIX 3: Numerical expressions for geothermometers and geobarometers

INTRODUCTION

A key to the abbreviations used here is given at the beginning of the thesis. A numerical expression is not given for the calibration of Thompson (1976) because temperature was determined using the linear relationship defined by the graph of K_D versus temperature in Figure 1 of Thompson (1976).

The general formula for geothermobarometry is:

(A3.1) $0 = \Delta G = \Delta H - T\Delta S + (P-1)\Delta V + RT\ln K_D$ in the ideal case (i.e $\gamma = 1$)

and

(A3.2) $0 = \Delta G = \Delta H - T\Delta S + (P-1)\Delta V + RT\ln K_D + RT\ln K\gamma$

in the non-ideal case (see equation 4.3, Wood and Fraser, 1978)

where:

T = temperature in Kelvin
P = pressure in bars
R = gas constant = 1.987 cal/(mol)(K)
K_D = distribution coefficient
$K\gamma$ = ratio of activity coefficients

For common metamorphic pressures (i.e. 3 to 10 kb), (P-1) = P and equations (A3.1) and (A3.2) become:

(A3.3) $0 = \Delta G = \Delta H - T\Delta S + P\Delta V + RT\ln K_D$

and

(A3.4) $0 = \Delta G = \Delta H - T\Delta S + P\Delta V + RT\ln K_D + RT\ln K\gamma$

GARNET-BIOTITE GEOTHERMOMETER

Ferry and Spear (1978)

Ferry and Spear (1978) define K_D as:

$K_D = (Mg/Fe)_{gt}/(Mg/Fe)_{bi}$

On the basis of their experimental work,

$H = 3R(2109) - P\Delta V$ (cal) where P = 2070 bars
$T\Delta S = 3R(0.782)$ (e.u.)

Using ΔV = 0.057 cal/bar (Robie et al., 1967), equation (A3.3) becomes:

(A3.5) $0 = \Delta H - T\Delta S + P\Delta V + 3RT\ln K_D$

where:

ΔH = 12454 cal
ΔS = 4.662 e.u.
ΔV = 0.057 cal/bar
P = pressure of interest in bars
T = temperature in Kelvin

Perchuk and Lavrent'eva (1983)

Perchuk and Lavrent'eva define K_D as:

$K_D = (Mg/Fe)bi/(Mg/Fe)gt$

On the basis of their experimental work, Perchuk and Lavrent'eva (1983) determined:

$\Delta H = -7843.7 - 6000\ \Delta V$ cal
$\Delta S = -5.699$ cal
$\Delta V = -0.0577$ cal/bar or -0.0246 cal/bar

Substituting these values into equation (A3.3) we get:

$$T = 7843.7 + 0.0246(P-6000)/5.699 + R\ln K_D \tag{A3.6}$$

or

$$T = 7843.7 + 0.0577(P-6000)/5.699 + R\ln K_D \tag{A3.7}$$

where:
P = is pressure of interest in bars
T = temperature in Kelvin

Ganguly and Saxena (1984)

Ganguly and Saxena (1984) define K_D in the same manner as Perchuk and Lavrent'eva (1983). However, the following derivation uses the same definition of K_D as Ferry and Spear (1978). According to Ganguly and Kennedy (1974), the nonideality in a quaternary garnet solid solution model, using a simple mixture and neglecting multicomponent interactions, can be expressed as:

$$RT\ln \gamma_{alm}/\gamma_{pyr} = W_{alm\text{-}pyr}(X_{pyr} - X_{alm}) + (W_{alm\text{-}gro} - W_{pyr\text{-}gro})(X_{gro}) + (W_{alm\text{-}spe} - W_{pyr\text{-}spe})(X_{spe}) \tag{A3.8}$$

According to Ganguly and Saxena (1984),

$$W_{pyr\text{-}gro} - W_{alm\text{-}gro} = 3000 \text{ cal/mol of cation} \tag{A3.9}$$

$$W_{pyr\text{-}spe} - W_{alm\text{-}spe} = 3000 \text{ cal/mol of cation} \tag{A3.10}$$

(A3.11) $W_{alm\text{-}pyr} = 200[Mg/(Mg + Fe^{2+})]_{gt} + 2500[Fe^{2+}/(Fe^{2+} + Mg)]_{gt}$

Therefore (A3.8) becomes:

(A3.12) $RT\ln K(\gamma_{alm}/\gamma_{pyr}) = W_{alm\text{-}pyr}(X_{pyr} - X_{alm}) - 3000\,(X_{gro} + X_{spe})$

Note: As Ferry and Spear (1978) used $alm_{90}pyr_{10}$ in their experiments, Ganguly and Saxena (1984) subtract 0.8 from $(X_{pyr} - X_{alm})$

Combining (A3.4), (A3.5), and (A3.11) and (A3.12), we get:

(A3.13) $T = 2089 + 0.00956P + (B)/\ 0.7821 - \ln K_D$

where $B = \{200[Mg/(Mg + Fe^{2+})] + 2500\,[Fe^{2+}/(Fe^{2+} + Mg)]\}\,[(X_{Mg} - X_{Fe}) - 0.8]/$
$R - 1510(X_{gro} + X_{spe})$

Newton and Haselton (1981)

Newton and Haselton (1981) define K_D in the same manner as Ferry and Spear (1978) and state that:

$W_{pyr\text{-}gro} = 3300 - 1.5T$ cal/mol of cation (T in Kelvin)

and assume all other Margules mixing parameters to be zero. Applying this correction for Ca in garnet, equation (A3.6) becomes:

(A3.14) $RT\ln(\gamma_{alm}/\gamma_{pyr}) = -\,(3300 - 1.5T)(X_{gro})$

Combining (A3.4), (A3.5), and (A3.14) we get:

(A3.15) $T = 2089 + 0.00956 + (1661 - 0.755T)(X_{gro})/\ 0.7821 - \ln K_D$

Indares and Martignole (1985)

Indares and Martignole (1985) suggest two different corrections to the Ferry and Spear (1978) calibration. Model A of Indares and Martignole (1985) applies the Ca-correction of Newton and Haselton (1981) in addition to Indares and Martignole (1985) empirically derived correction for Ti and Al in biotite. Model B of Indares and Martignole differs from Model A in that it applies Ganguly and Saxena's correction for Ca and Mn in garnet.

Indares and Martignole (1985) determined that:

(A3.16) $RT\ln[(\gamma^{bi})_{Fe}/(\gamma^{bi})_{Mg}] = m(X^{bi})_{Al} + n(X^{bi})_{Ti}$

where:

$m = -\,464$ (Model A) or -1590 (Model B)
$n = -6767$ (Model A) or -1451 (Model B)

For Model A, combining (A3.5), (A3.14), and (A3.16) we get:

(A3.17) $T = 12{,}454 + 0.057P + 3[m(X^{bi})_{Al} + n(X^{bi})_{Ti}]$
$-\ 3[-(3300 - 1.5T)(X_{gro})]/4.662 + 5.961(\ln K_D)$

For Model B, combining (A3.5), (A3.9), (A3.10), and (A3.16) we get:

(A3.18) $$T = 12{,}454 + 0.057P + 3[m(X^{bi})_{Al} + n(X^{bi})_{Ti}] -3[-(3000(X_{gro} + X_{spe})]/4.662 - 5.961(\ln K_D)$$

GARNET-PLAGIOCLASE-Al_2O_5-QUARTZ GEOBAROMETRY

There are several formulations published for the garnet-plagioclase-Al_2SiO_5-quartz geobarometer.

Formulation 1: Ghent, 1976; Ghent et al., 1979

From equation (A3.1) for P and T of interest,

(B3.1) $$0 = \Delta H/2.303RT - \Delta S/2.303R + \Delta V(P-1)/2.303RT + \log K_D$$
where P is in bars.

or

(B3.2) $$0 = A/T - B + C\,(P-1)/T + \log K_D$$

where $A = \Delta H/2.303R$
$B = \Delta S/2.303R$
$C = \Delta V/2.303R$
$K_D = (X_{gro})^3/(X_{anor})^3$

From Ghent (1976):

(a) for sillimanite: $A = -2551.4$, $B = -7.1711$, $C = -0.2842$

(b) for kyanite: $A = -3272$, $B = -8.3969$, $C = -0.3448$

(c) for andalusite: $A = -2817.2$, $B = -7.4351$, $C = -0.2678$

Ghent et al. (1979) empirically determined $\log K\gamma = 0.4$ for pelites from the Mica Creek area, British Columbia. Therefore, combining A3.2 and B3.2 we get:

(B3.3) $0 = A/T - B + C(P-1)T + \log K_D + (-0.4)$

Formulation 2: Newton and Haselton (1981), Koziol and Newton (1988)

The second commonly used formulation of the garnet-plagioclase-Al_2SiO_5-quartz geobarometer is:

(B3.4) $0 = \Delta G^\circ + RT\ln K_{eq} + P\Delta V$ (Newton and Haselton, 1981)

where: P = pressure in bars
T = temperature in Kelvin
$K_{eq} = a_{gro}/a_{anor}$

$$\Delta\bar{V} = \text{partial molar volume change at one bar}$$
$$= \bar{V}_{products} - \bar{V}_{reactants}$$

$$G^o = \text{Gibbs energy change at one bar}$$
$$= -P^o \Delta V^o$$

where P^o is the pressure of the end member reaction at T and V^o is the endmember reaction volume change.

Therefore, equation (B3.5) becomes:

(B3.5) $$P = P^o \Delta V^o - RT\ln K_{eq} / \Delta V$$

This is the formulation used by Newton and Haselton (1981) and Koziol and Newton (1988).

The partial molar volumes ($\bar{V}$) for anorthite, Al_2SiO_5, and quartz are constants. From Berman (1988):

$\bar{V}_{an}$ = 2.409 cal/bar

$\bar{V}_{qtz}$ = 0.542 cal/bar

$\bar{V}_{ky}$ = 1.054 cal/bar

$\bar{V}_{sil}$ = 1.193 cal/bar

$\bar{V}_{and}$ = 1.232 cal/bar

The partial molar volume of grossular deviates from molar volume at $X_{gro} < 0.4$. For the end-member reaction, it is approximately:

$\bar{V}_{gro}$ = 2.995 cal/bar (Koziol and Newton, 1988, Table 3)

Therefore,

$$\Delta V^o_{sil} = [0.542 + 2(1.193) + 2.995] - [3(2.409)]$$
$$= -1.3044 \text{ cal/bar}$$
$$\Delta V^o_{ky} = [0.542 + 2(1.054) + 2.995] - [3(2.409)]$$
$$= -1.5815 \text{ cal/bar}$$

Because the partial molar volume of grossular deviates from molar volume at $X_{gro} <$ 0.4, ΔV_{gr} for the sample in question must be determined using the molar volume curve of (Ca, Fe, Mg) garnets (Figure 1, Newton and Haselton, 1981). Newton and Haselton also provide an analytical expression that may be used for determining $\bar{V}_{gr}$ (see page 138 of Newton and Haselton, 1981). $\bar{V}_{gr}$ is determined graphically in this study.

Newton and Haselton (1981) provide the following analytical expression for the calculation of a_{gro} and a_{anor}:

$$a_{gro} = (\gamma_{gro})^3 (X_{gro})^3$$

where: $\ln\gamma_{gro} = W_{gro\text{-}pyr}[(X_{pyr})_2 + (X_{pyr})(X_{alm})]/RT$
$W_{gro\text{-}pyr} = 3300 - 1.5T$ (T in Kelvin)

$$a_{anor} = \frac{[X_{anor}(1 + X_{anor}2)]}{4} \exp \frac{(1 - X_{anor})^2}{RT}(2050 + 9392X_{anor})$$

P^o can be expressed in the form $P^o = a + bT$. Newton and Haselton (1981) determined that:

$P^o_{sil} = 23.60T - 600$ (°C, bars)
$P^o_{ky} = 23.20T - 2100$ (°C, bars)

However, P^o_{sil} expression is incorrect and should be:

$P^o_{sil} = -1.17 + 0.0238T$ (°C, kb) (E. Froese, 1984, in Ganguly and Saxena, 1984)

Koziol and Newton (1988) determined:

$P^o_{sil} = \{[-0.000187][2(T^2)]\} + 23.41T - 25$ (°C, bars)
$P^o_{ky} = 22.80(T) - 1093$ (°C, bars)

PLAGIOCLASE-BIOTITE-GARNET-MUSCOVITE GEOBAROMETRY

Using an ionic solution model, Ghent and Stout (1981) define K_D for reaction (19) and (20) (see Chapter 5) as:

$K_D(1) = [(X_{anor})^3 (X_{phl})^3]/\{[(X^{mu})_K (X^{mu})_{Al}^2] [(X_{pyr})^3] [(X_{gro})^3]\}$

$K_D(2) = [(X_{anor})^3 (X_{ann})^3]/\{[(X^{mu})_K (X^{mu})_{Al}^2)] [(X_{alm})^3] [(X_{gro})^3]\}$

where Al is Al^{vi}.

Equilibrium constant equations were derived using P and T determined by the Ghent et al. (1979) calibration of the garnet-plagioclase-Al_2SiO_5-quartz geobarometer and the Ferry and Spear (1978) calibration of the garnet-biotite geothermometer. Linear least squares equations of a plot of T (Kelvin) versus ($-RT\ln K_D - P\Delta V$) yields the following equilibrium constant equations:

(B3.6) $0 = -8{,}888.4 - 16.675T + 1.738P + RT\ln K_D(1)$

(B3.7) $0 = 4124.4 - 22.061T + 1.802P + RT\ln K_D(2)$

(Ghent and Stout, 1981). Substitution of an independently determined temperature in Kelvin into (B3.6) and (B3.7) yields pressures within several hundred bars of one another.

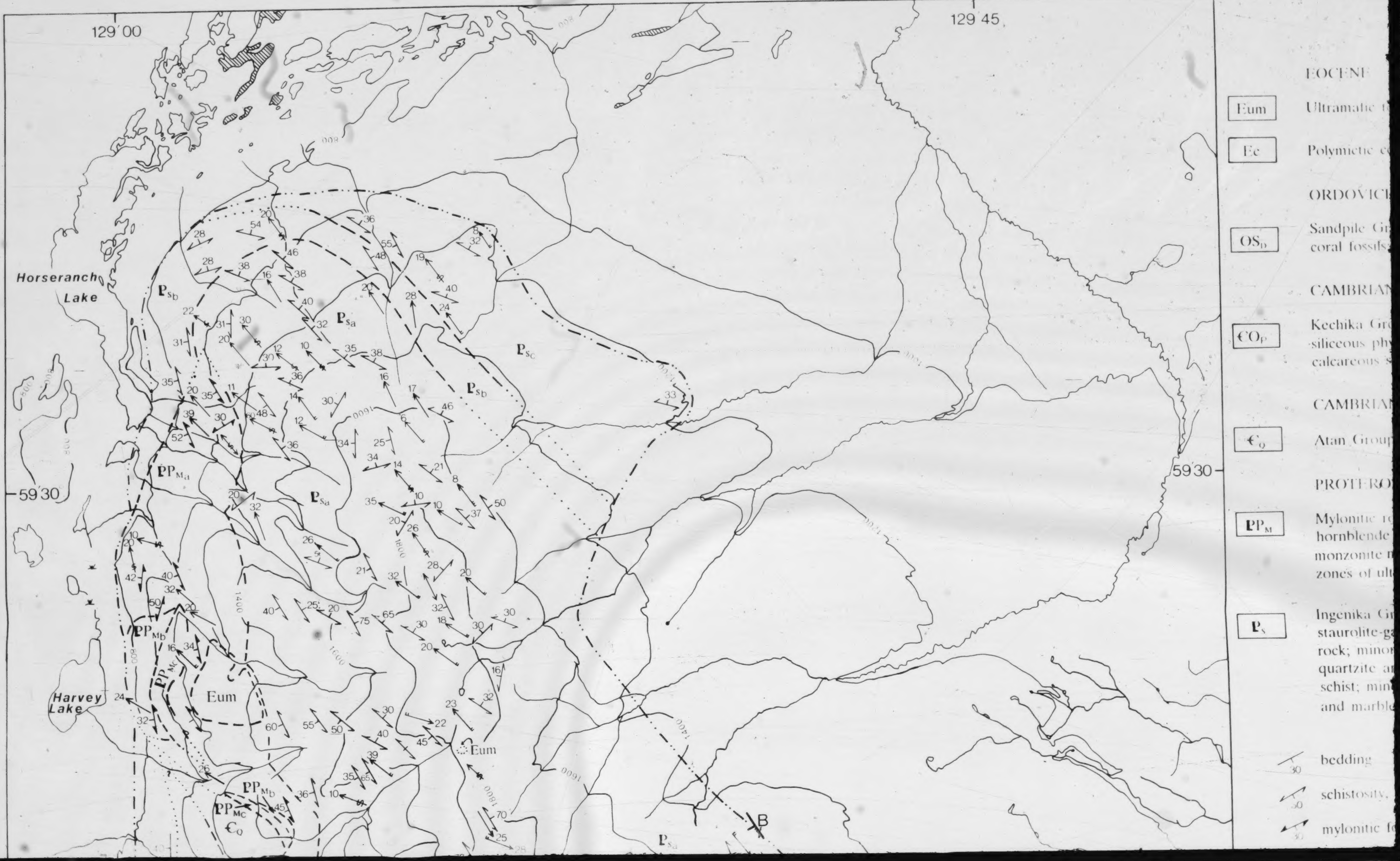

129°00
129°45
Horseranch Lake
Harvey Lake
59°30
59°30
Ps b
Ps a
Ps c
PP Ma
PP Mb
PP Mc
Eum
Є0
B
EOCENE
Eum Ultramatic
Ec Polymictic co
ORDOVICI
OS b Sandpile Gr coral fossils
CAMBRIAN
ЄOp Kechika Gr siliceous phy calcareous s
CAMBRIAN
Є0 Atan Group
PROTERO
PP M Mylonitic ro hornblende monzonite m zones of ult
Ps Ingenika Gr staurolite-ga rock; minor quartzite a schist; min and marble
bedding
schistosity,
mylonitic fo

LEGEND

EOCENE

Eum Ultramafic to mafic intrusions: hornblende pyroxenite, gabbro, diorite

Ec Polymictic conglomerate with quartz, silstone, phyllite and minor granitic clasts

ORDOVICIAN AND SILURIAN

OS Sandpile Group: aphanitic, grey dolostone; dolomitic limestone with minor, thin chert beds and rugose coral fossils; dolostone breccia.

CAMBRIAN AND ORDOVICIAN

O Kechika Group: silvery grey to green grey, calcareous, chloritic phyllite; pink to white, muscovitic, siliceous phyllite; green, chlorite schist; aphanitic, locally fossil-bearing meta-mudstone; black, calcareous slate.

CAMBRIAN

€ Atan Group: homogeneous, white to pink quartzite; minor biotite schist; minor metacarbonate schist.

PROTEROZOIC AND/OR CAMBRIAN (?)

$\mathrm{PP_M}$ Mylonitic rocks: (a) C-S, granitic protomylonite to mylonite; laminated quartzite mylonite; diopside-hornblende metacarbonate mylonite; mylonitic sillimanite schist; minor micaschist; (b) quartz monzonite mylonite; (c) dioritic to gabbroic protomylonite to mylonite with minor centimetre scale zones of ultramylonite.

P Ingenika Group: (a) Swannell and Tsaydiz Fms. (?): sillimanite-orthoclase-muscovite-garnet schist; staurolite-garnet schist; semipelitic to psammitic schist; quartzite; diopside-garnet marble; calcsilicate rock; minor amphibolite, (b) Espee Fm. (?): tan-weathering phlogopite marble with quartz clasts; minor quartzite and pelitic schist, locally staurolite-garnet schist; (c) Stelkuz Fm. (?): chlorite-muscovite-garnet schist; minor layers of semipelitic to psammitic schist, hornblende-garnet calcsilicate schist, quartzite and marble.

30 bedding

60 schistosity, cleavage

30 mylonitic foliation

geologic contact: approximate, inferred

fault (exposed, inferred)

limit of exposure

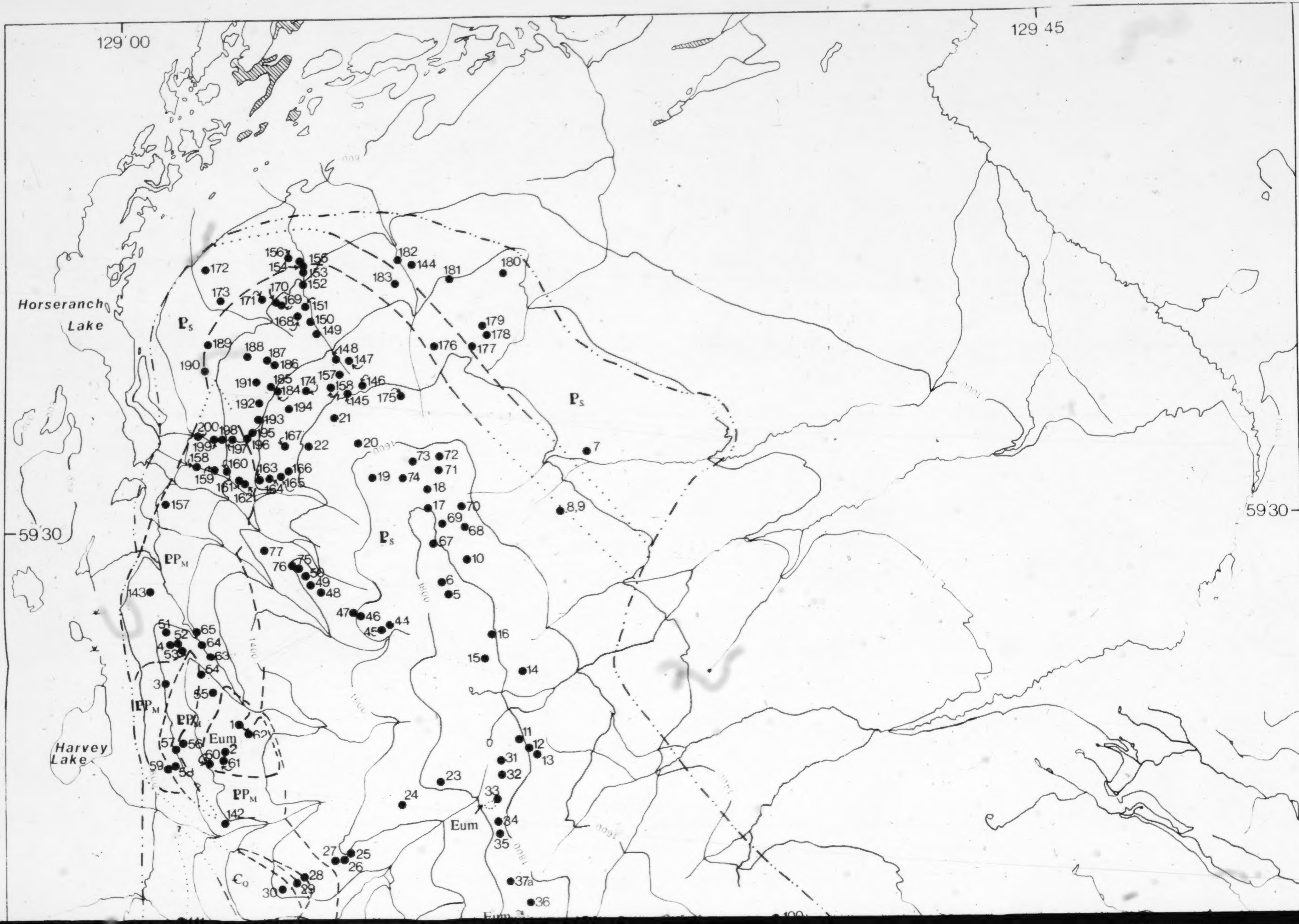
129°00
129 45
59°30
59°30
Horseranch Lake
Harvey Lake
P$_S$
PP$_M$
Eum
€$_Q$

SAM

HORSE

LEGEND

EOCE

Eum Ultrar

Ec Polyn

ORD

OS$_D$ Sand

CAM

€O$_P$ Kech

CAM

€$_Q$ Atan

PRO

PP$_M$ Mylo

P$_S$ Inger

SAMPLE LOCALITY MAP FOR THE HORSERANCH RANGE, NORTH-CENTRAL BRITISH COLUMBIA

LEGEND

	EOCENE
Eum	Ultramafic to mafic intrusions
Ec	Polymictic conglomerate
	ORDOVICIAN AND SILURIAN
$\bar{O}S_D$	Sandpile Group
	CAMBRIAN AND ORDOVICIAN
$\text{€}O_P$	Kechika Group
	CAMBRIAN
€_Q	Atan Group
	PROTEROZOIC AND/OR CAMBRIAN (?)
PP_M	Mylonite
P_S	Ingenika Group

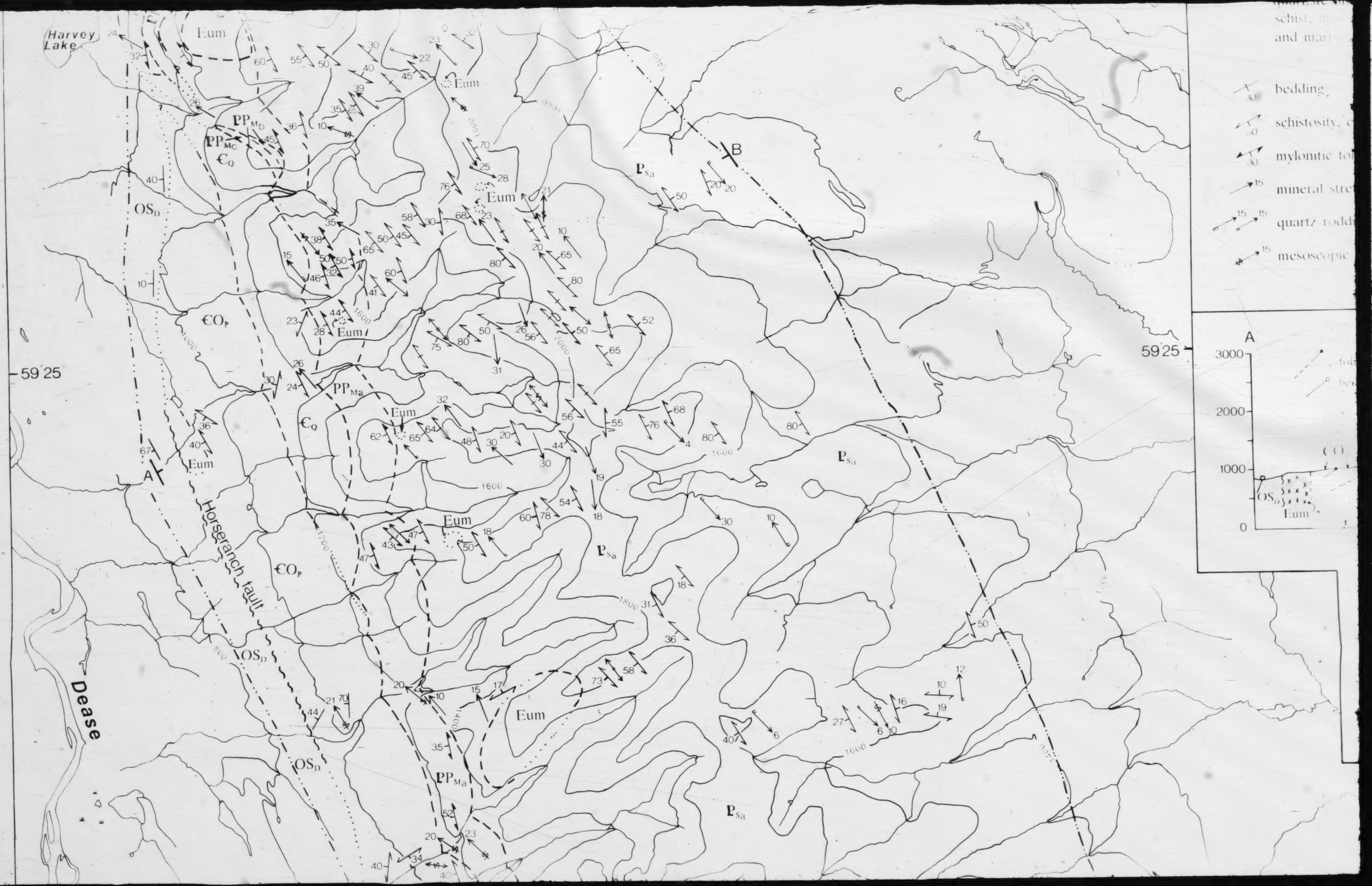
Harvey Lake
Dease
Horseranch fault
Eum
PP_Mb
PP_Mc
PP_Ma
€Q
€O_P
OS_D
P_Sa
A
B
59°25
1600
1800
1200
2000
1000
800
bedding,
schistosity,
mylonitic
mineral stre
quartz roddi
mesoscopic
schist,
and mar
3000
2000
1000
0
€Q
OS_D
Eum

schist, minor layers of semipelitic to psammitic schist, hornblende-garnet calcsilicate schist, quartzite and marble.

bedding

schistosity, cleavage

mylonitic foliation

mineral stretching lineation

quartz rodding, $^2F_3$ crenulation hinges

mesoscopic fold hinges - mainly $^2F_3$ in P_S

geologic contact: approximate, inferred

fault (exposed, inferred)

limit of exposure

abrupt metamorphic grade change

Ⓕ fossil locality

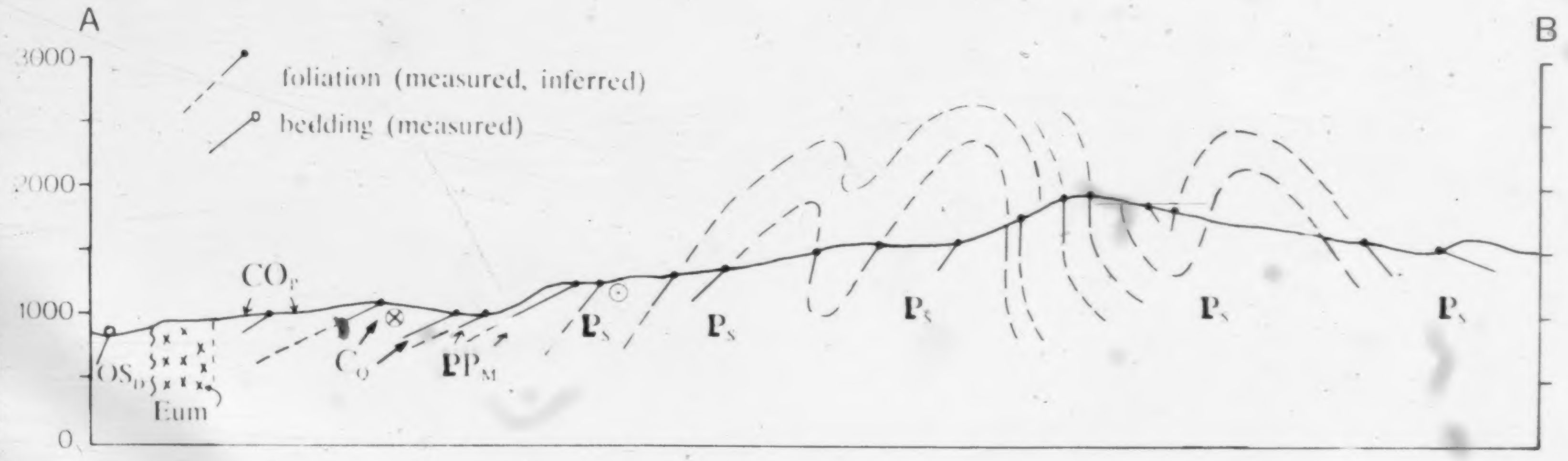

A
B
3000
2000
1000
0
foliation (measured, inferred)
bedding (measured)
CO_P
OS_D
Eum
C_Q
PP_M
P_S
P_S
P_S
P_S
P_S

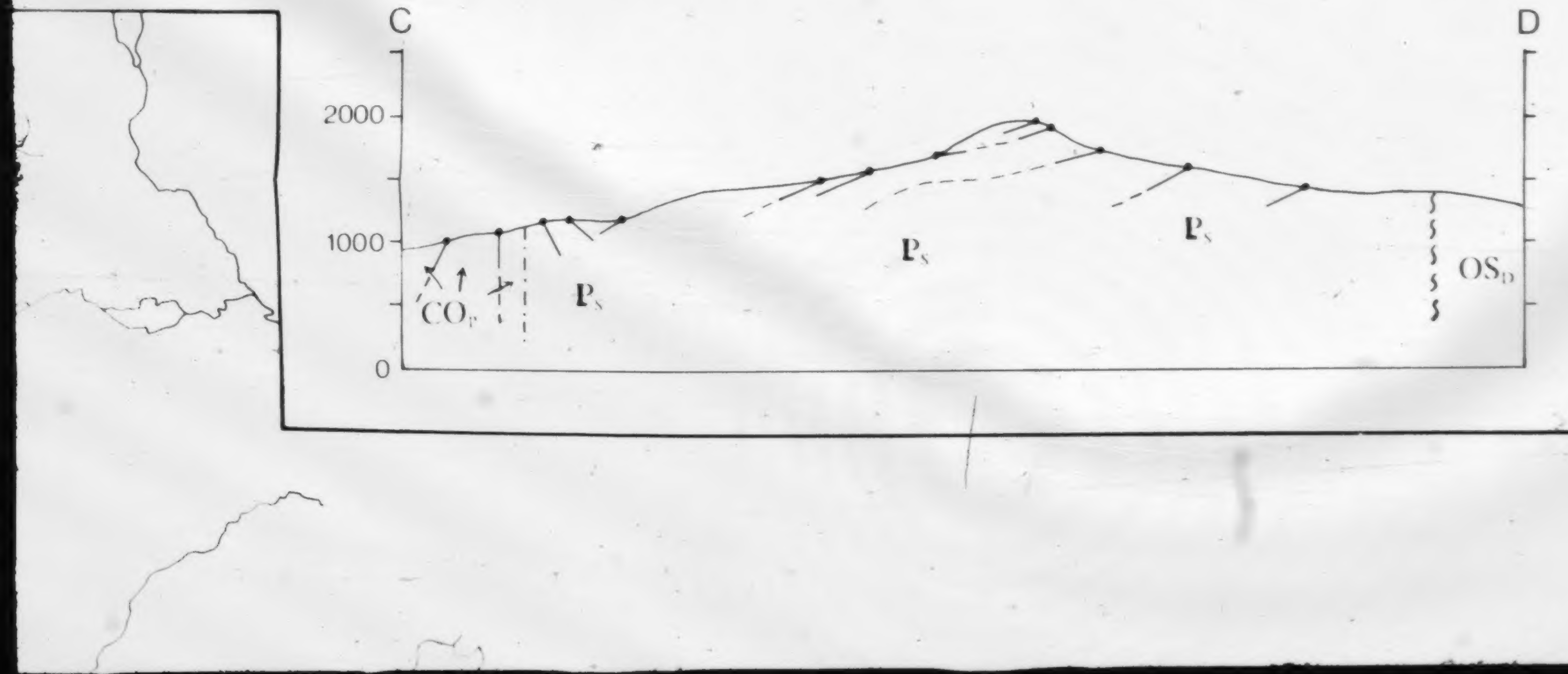

C
D
2000
1000
0
CO_P
P_S
P_S
P_S
OS_D

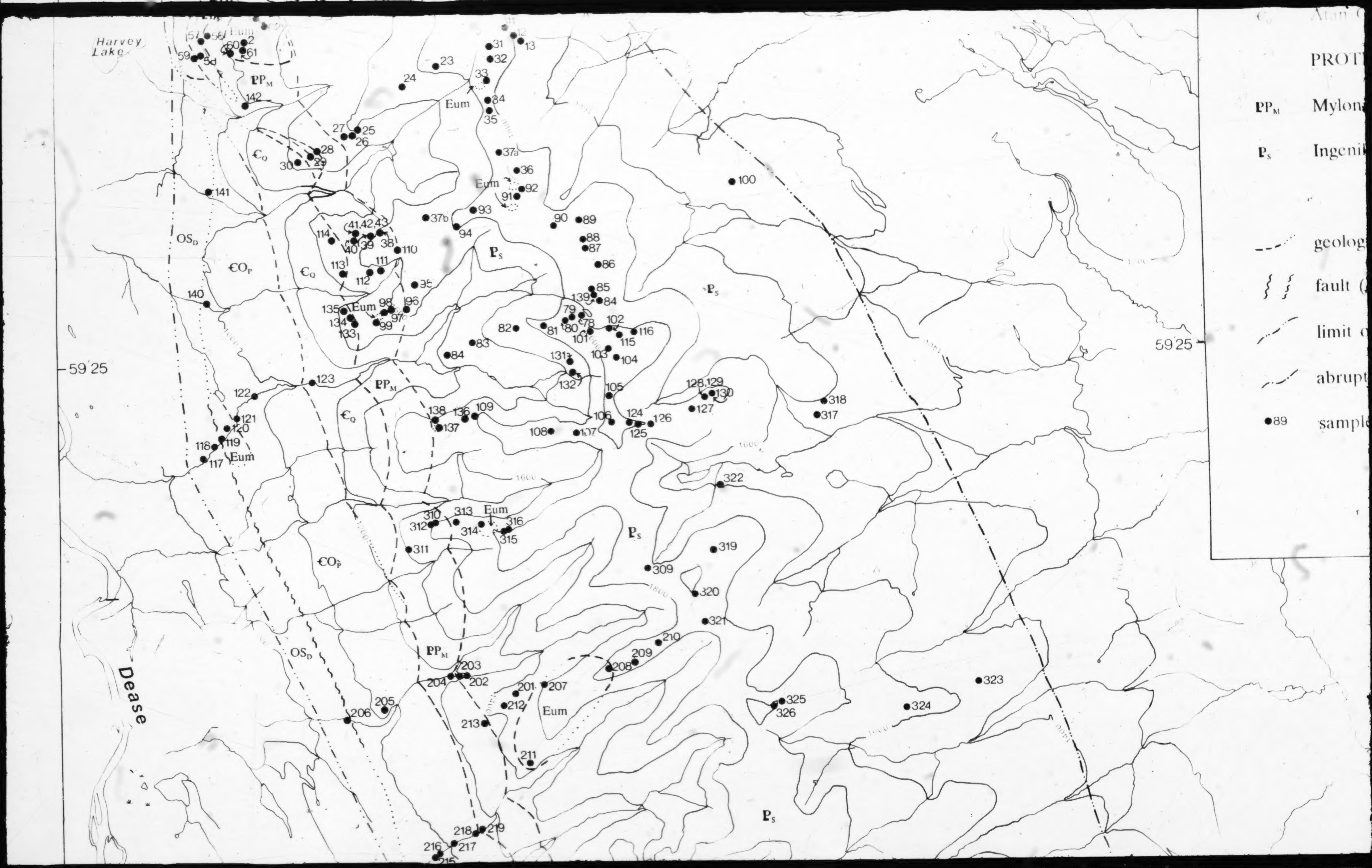
Harvey Lake
Dease
59 25
59 25
PROT
PP_M Mylon
P_s Ingeni
geolog
fault (
limit o
abrupt
•89 sampl
Eum
PP_M
€Q
€O_P
OS_D
P_s
1600
1800

Є$_A$ Atan Group

PROTEROZOIC AND/OR CAMBRIAN (?)

PP$_M$ Mylonite

P$_S$ Ingenika Group

geologic contact: approximate, inferred

fault (exposed, inferred)

limit of exposure

abrupt metamorphic grade change

●89 sample locality (numbers abrreviated, e.g. 89 = HP87-89)

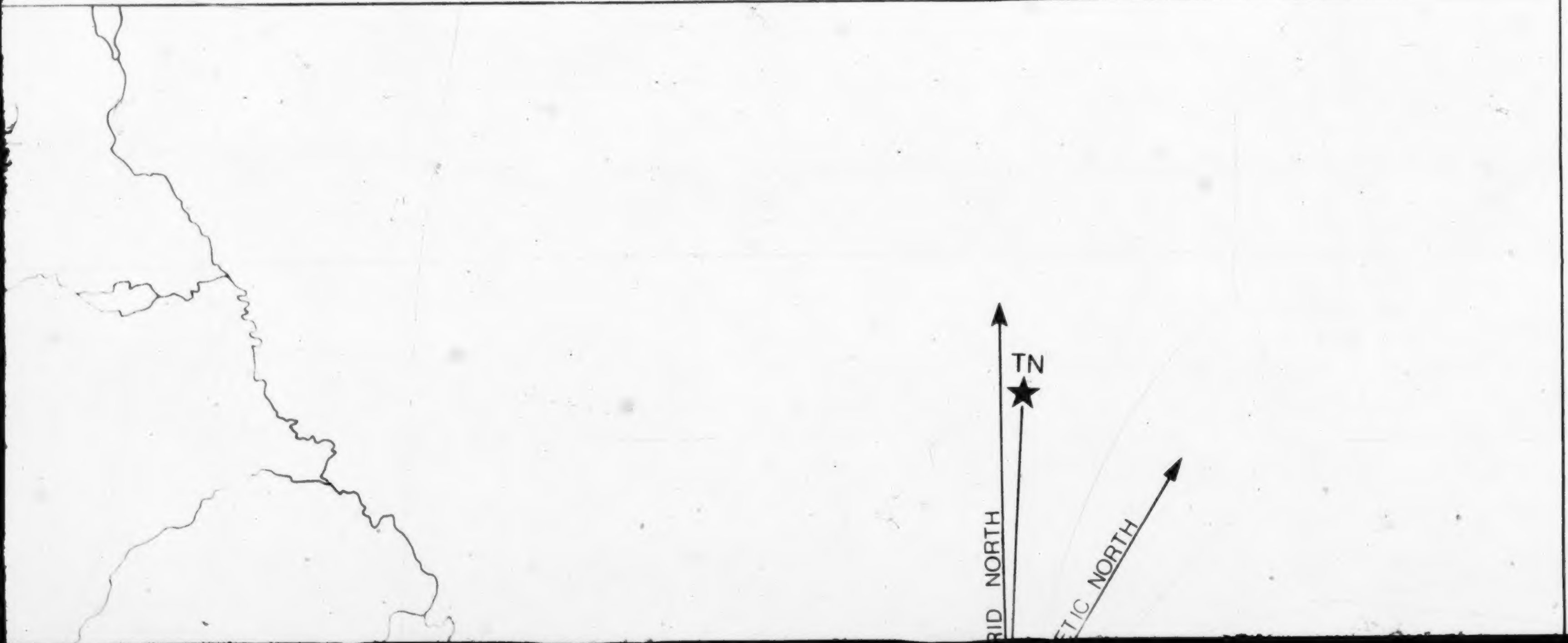

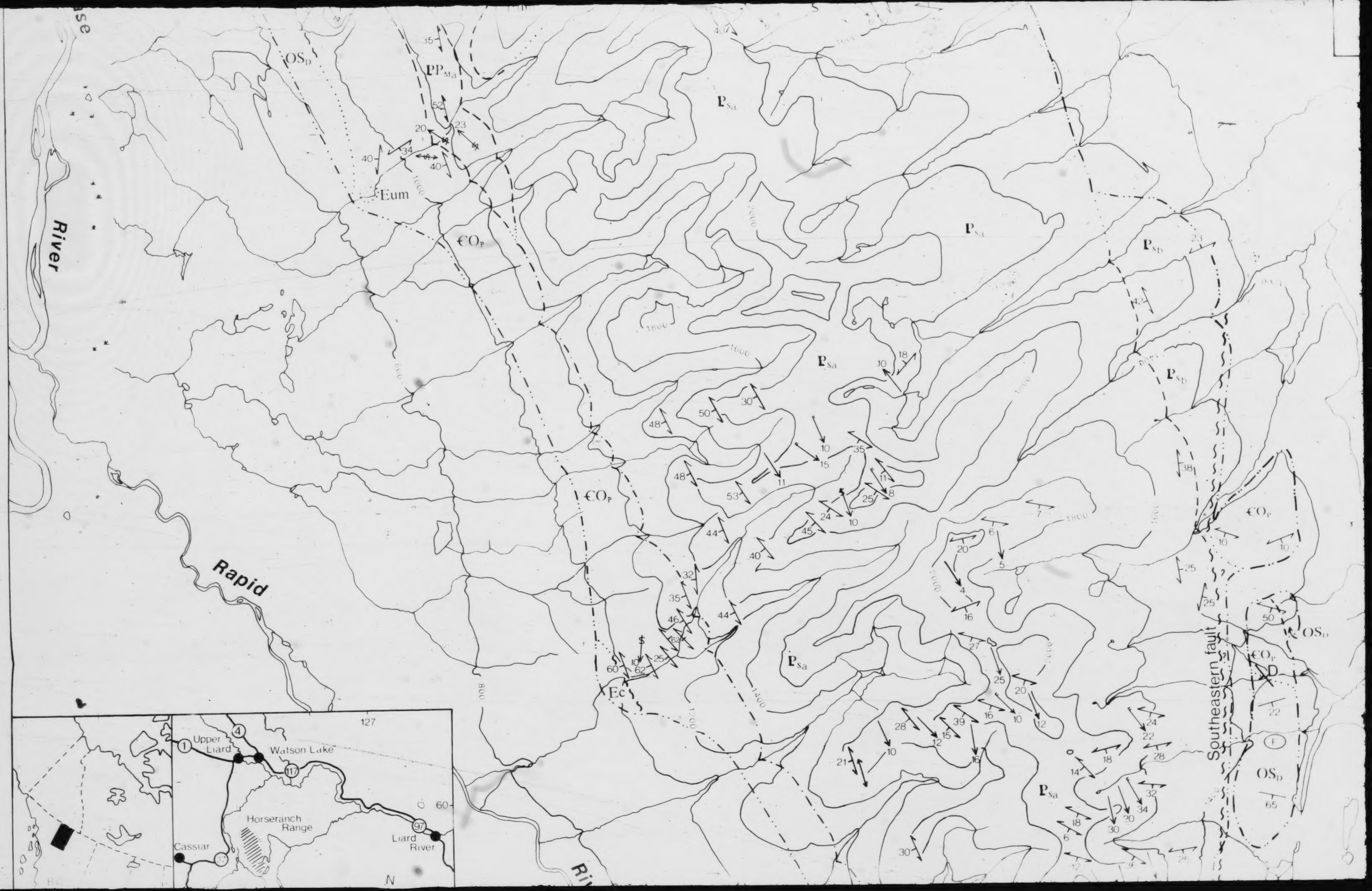
ase
River
Rapid
Riv
OSD
PPMa
Eum
COP
Psa
Psb
Ec
Southeastern fault
D
F
1800
1600
1400
1200
800
Upper Liard
Watson Lake
Horseranch Range
Cassiar
Liard River
127
60
N
BC
1
4
117
97
37

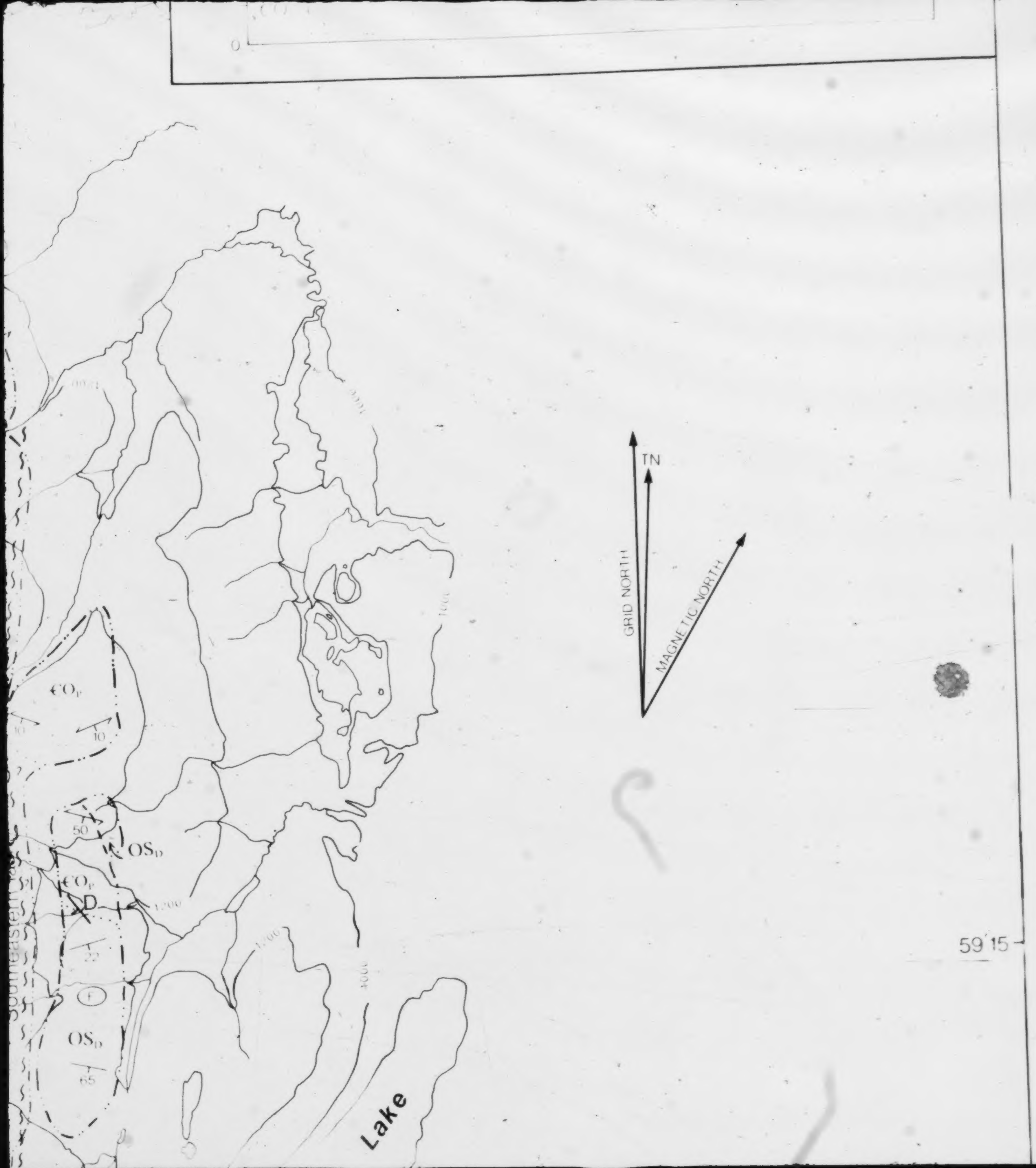
0
TN
GRID NORTH
MAGNETIC NORTH
€O_P
10
10
50
OS_D
€O_P
D
1200
22
F
OS_D
65
Southeastern
1000
Lake
59°15'

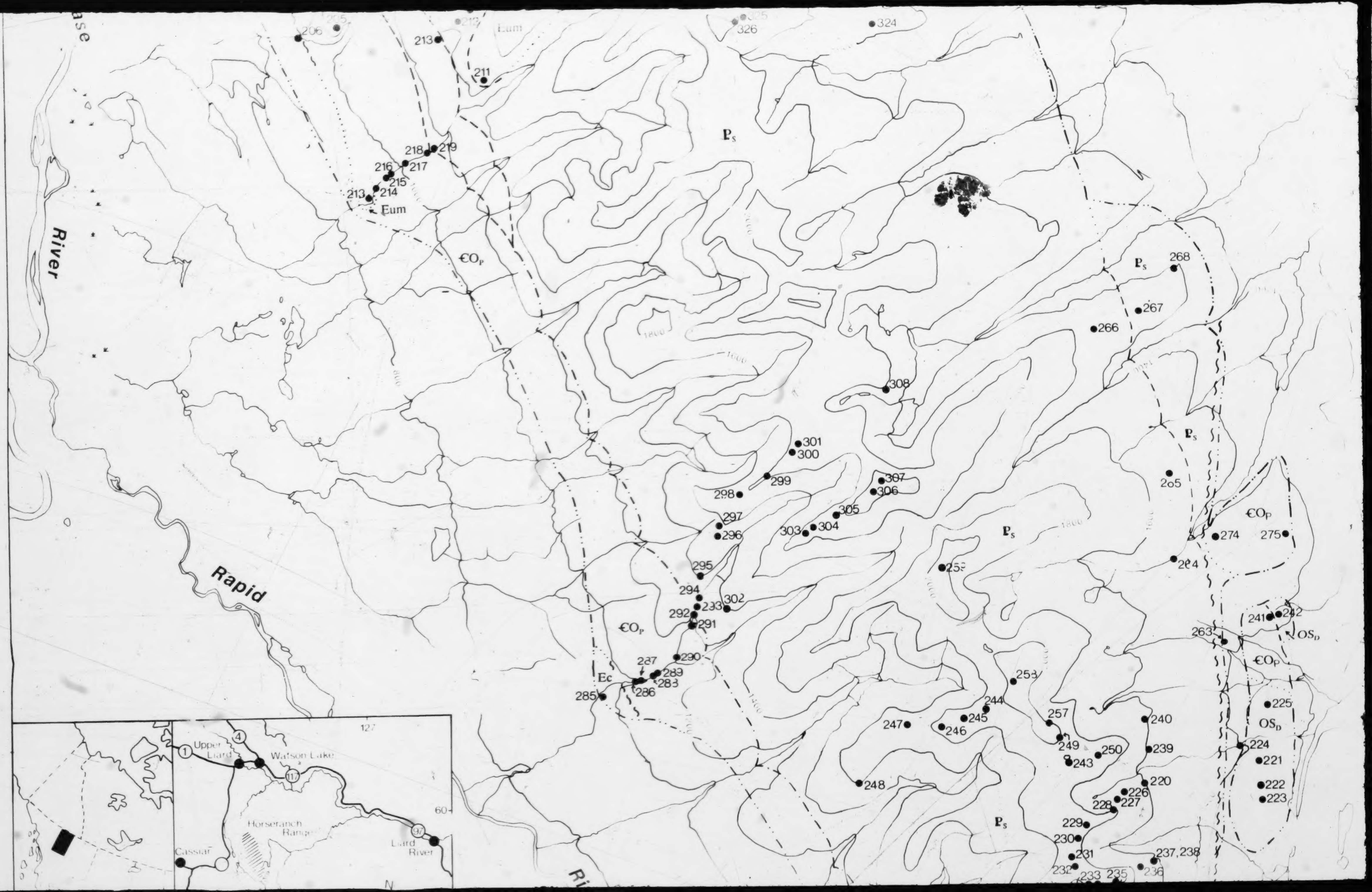

ase
River
Rapid
Ri
Eum
Eum
€O_P
€O_P
€O_P
€O_P
Ec
P_s
P_s
P_s
P_s
P_s
OS_D
OS_D
1800
1600
1400
1200
800
205
206
212
213
211
218
219
216
217
215
213
214
325
326
324
268
267
266
308
301
300
299
298
307
306
305
303
304
297
296
295
294
293
292
291
302
290
287
289
286
283
285
259
265
274
275
264
241
242
263
258
244
245
246
247
257
249
250
243
240
239
220
226
227
228
229
230
231
232
233
235
236
237, 238
248
225
224
221
222
223
127
Upper Liard
1
4
Watson Lake
117
60
Horseranch Range
97
Liard River
Cassiar
N

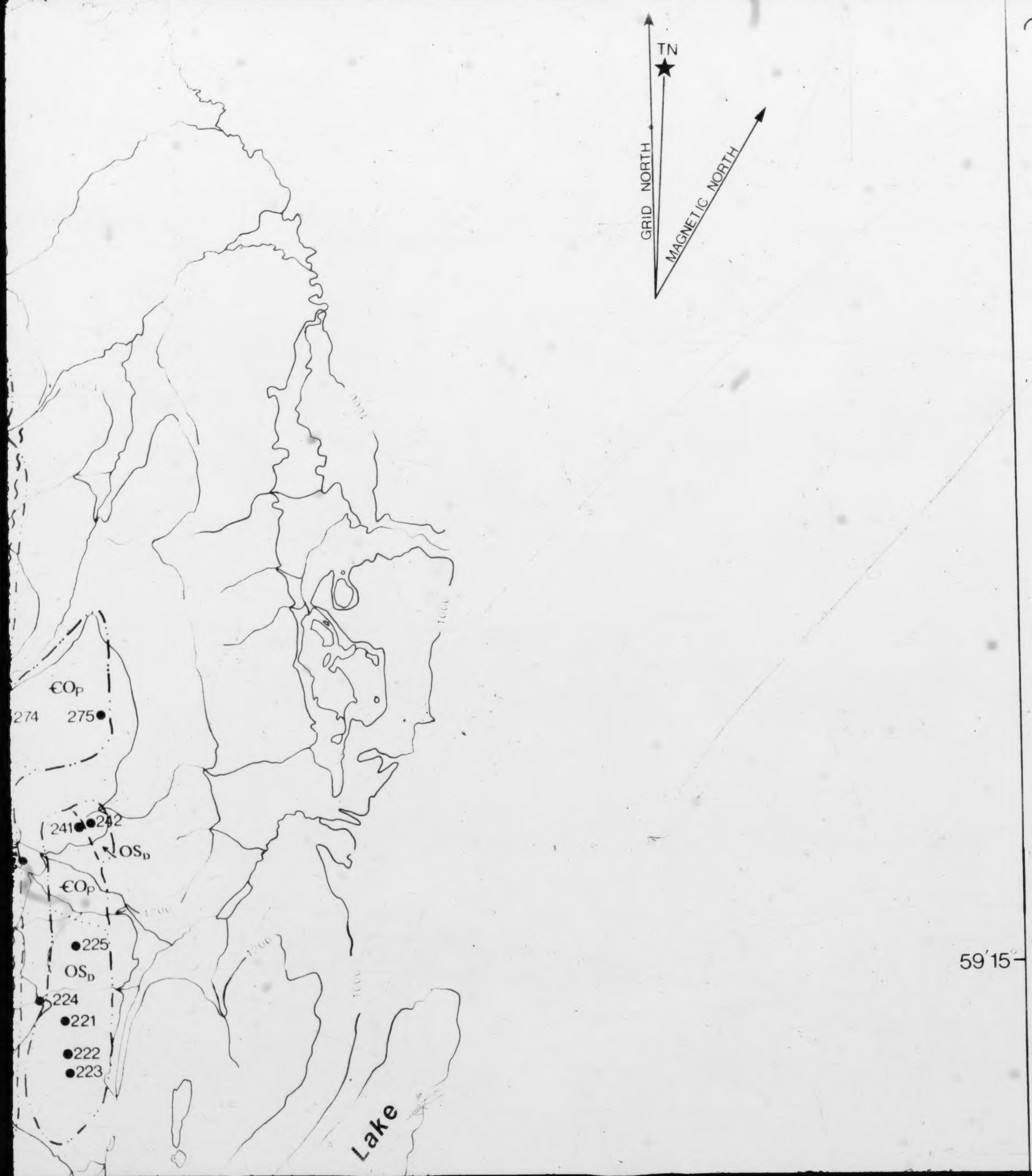
TN
GRID NORTH
MAGNETIC NORTH
€O_P
274
275
241
242
OS_D
€O_P
225
OS_D
224
221
222
223
Lake
59′15

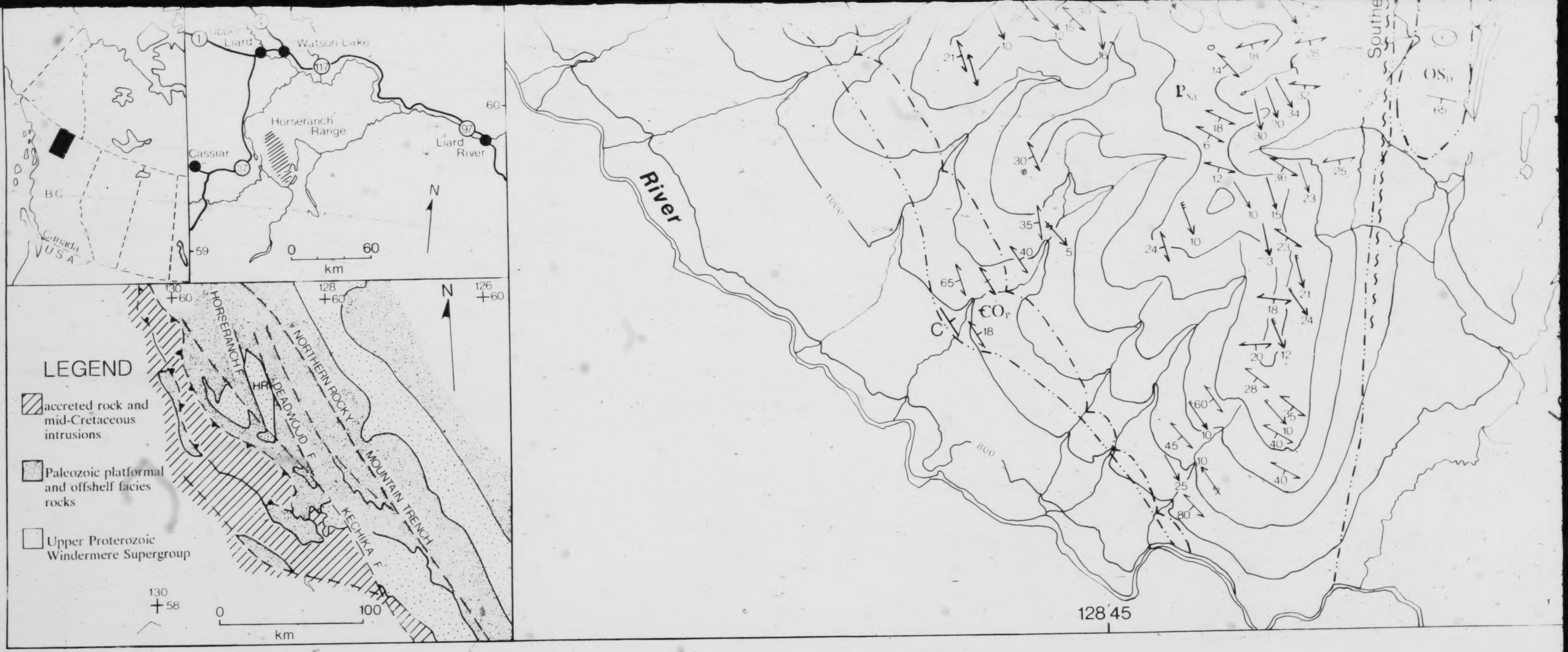Upper Liard
Watson Lake
Horseranch Range
Cassiar
Liard River
60
59
0 60
km
N
BC
Canada
USA
1
4
117
97
37
HORSERANCH F
HR
DEADWOOD F
NORTHERN ROCKY MOUNTAIN TRENCH
KECHIKA F
130 +60
128 +60
126 +60
130 +58
0 100
km
LEGEND
▨ accreted rock and mid-Cretaceous intrusions
▩ Paleozoic platformal and offshelf facies rocks
☐ Upper Proterozoic Windermere Supergroup
River
1000
800
€O_r
C
P_sa
OS_b
Southe
128°45

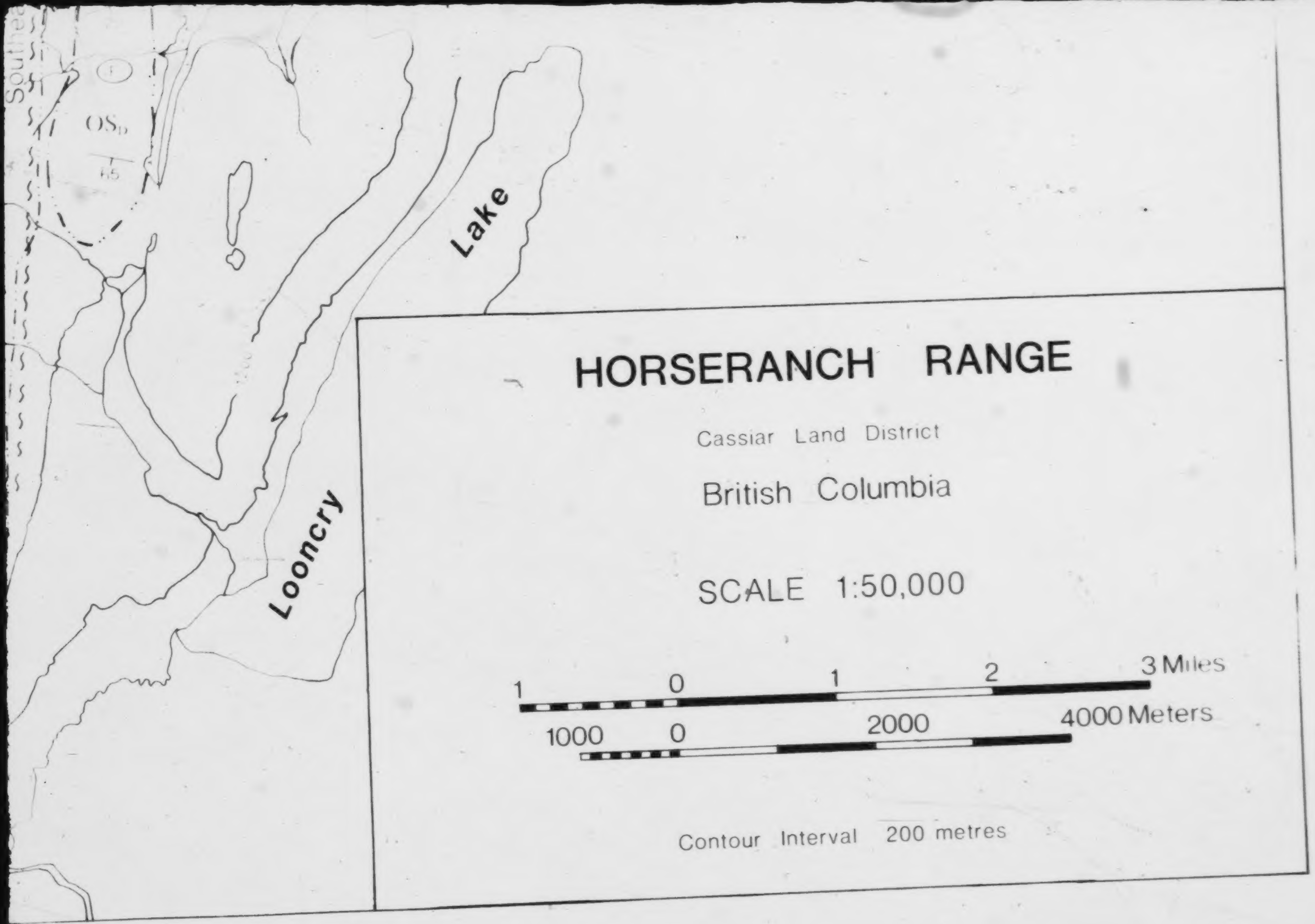
OS
Looncry
Lake

HORSERANCH RANGE

Cassiar Land District

British Columbia

SCALE 1:50,000

1 0 1 2 3 Miles

1000 0 2000 4000 Meters

Contour Interval 200 metres

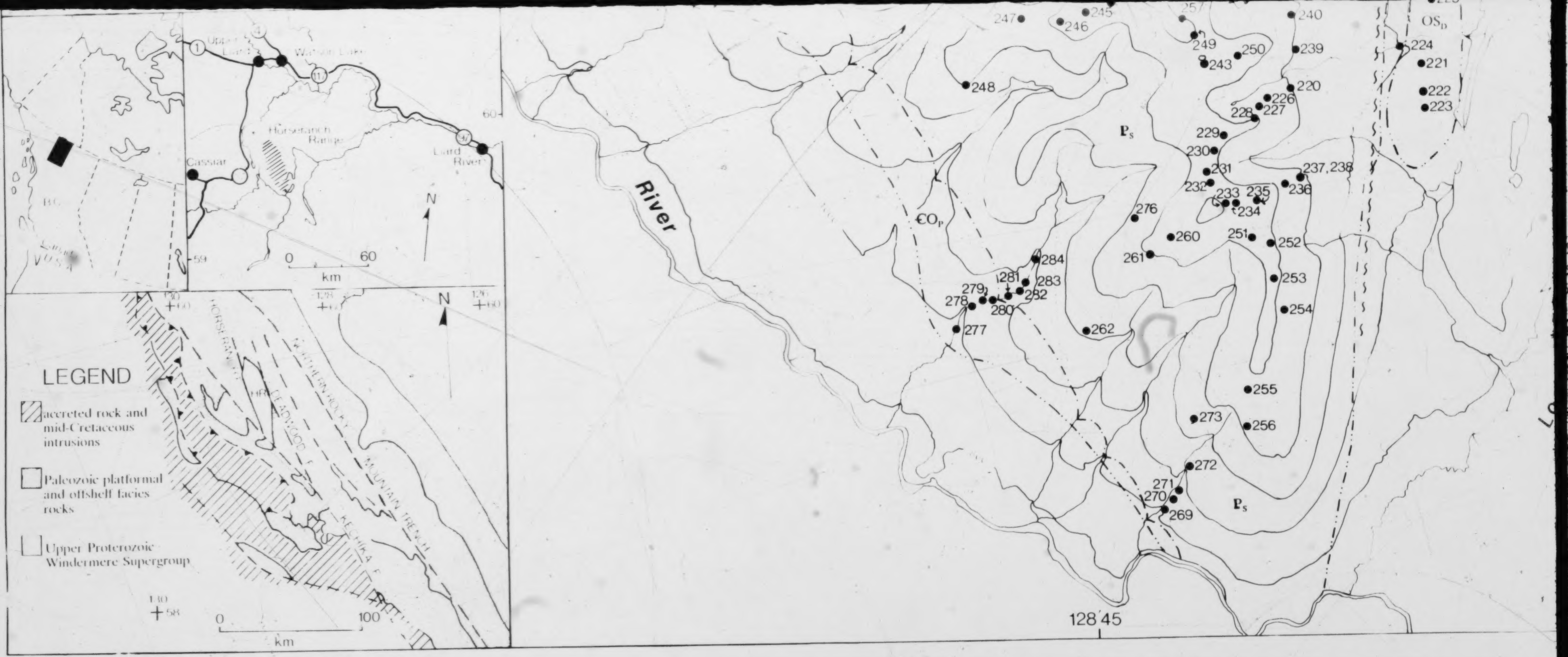
LEGEND
accreted rock and mid-Cretaceous intrusions
Paleozoic platformal and offshelf facies rocks
Upper Proterozoic Windermere Supergroup
Upper Liard
Watson Lake
Horseranch Range
Cassiar
Liard River
B.C.
U.S.A.
60
59
0
60
km
N
130 60
128 60
126 60
130 58
0
100
km
HORSERANCH
HR
LEAD/COOD F.
NORTHERN ROCKY MOUNTAIN TRENCH
KECHIKA F.
River
€O_P
P_S
OS_D
128 45
220
221
222
223
224
226
227
228
229
230
231
232
233
234
235
236
237, 238
239
240
243
245
246
247
248
249
250
251
252
253
254
255
256
257
260
261
262
269
270
271
272
273
276
277
278
279
280
281
282
283
284

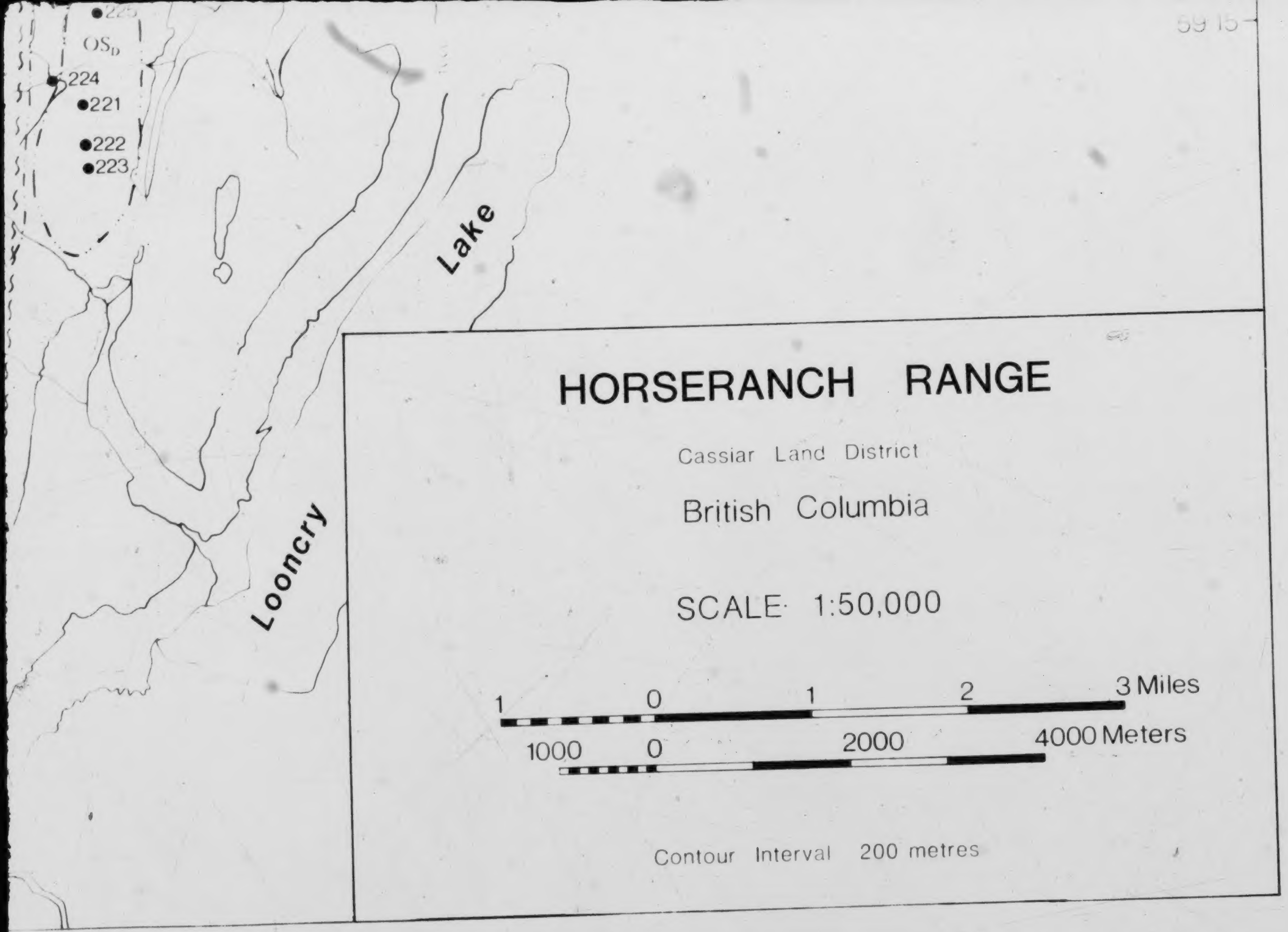
59 15
225
OSD
224
221
222
223
Lake
Looncry
1
0
1
2
3 Miles
1000
0
2000
4000 Meters

HORSERANCH RANGE

Cassiar Land District

British Columbia

SCALE 1:50,000

Contour Interval 200 metres